Elastic Strain Engineering in Silicon and Silicon-Germanium Nanomembranes

By

Deborah Marie Paskiewicz

A dissertation submitted in partial fulfillment of

the requirements for the degree of

Doctor of Philosophy

(Materials Science)

at the

UNIVERSITY OF WISCONSIN-MADISON

2012

Date of final oral examination: 11/14/12

The dissertation is approved by the following members of the Final Oral Committee:

Max G. Lagally, Professor, Materials Science and Engineering

Mark A. Eriksson, Professor, Physics

Thomas F. Kuech, Professor, Chemical and Biological Engineering

Paul G. Evans, Associate Professor, Materials Science and Engineering

Irena Knezevic, Associate Professor, Electrical and Computer Engineering

Abstract

Elastic Strain Engineering in Silicon and Silicon-Germanium Nanomembranes

Deborah M. Paskiewicz

Under the supervision of Professor Max G. Lagally

At the University of Wisconsin-Madison

Strain in crystalline materials alters the atomic symmetry, thereby changing materials properties. Controlling the strain (its magnitude, direction, extent, periodicity, symmetry, and nature) allows tunability of these new properties. Elastic strain engineering in crystalline nanomembranes (NMs) provides ways to induce and relax strain in thin sheets of single-crystalline materials without exposing the material to the formation of extended defects. I use strain engineering in NMs in two ways: (1) elastic strain sharing between multiple layers using the crystalline symmetry of the layers to induce unique strain distributions, and (2) complete elastic relaxation of single-crystalline alloy NMs. In both cases, NM strain engineering methods enable the introduction of unique strain profiles or strain relaxation in ways not compatible with conventional bulk processing, where strain destroys the long-range crystallinity.

Elastically strain-shared NMs are fabricated by releasing multi-layer thin film heterostructures from the original host substrate. If one layer of the original heterostructure contains strain, the strain will share between the layers of the freestanding NM. The extent of strain sharing will depend on the relative thicknesses, the ratio of the elastic moduli between

the materials, and elastic symmetry of the layers. I calculate strain distributions in flat NMs between layers with 2-fold and 4-fold elastic symmetry. I verify my calculations with experimental proof of two examples: (1) strain sharing between biaxially isotropic layers, Si/SiGe/Si(001), and (2) strain sharing between biaxially anisotropic layers, Si/SiGe/Si(110).

Strain engineering in NMs is also used to relax strain elastically in thin materials that are difficult to fabricate with conventional bulk crystal growth techniques. The SiGe alloy is one such material. Thin films of SiGe grow uniformly and elastically strained on Si substrates. I release the SiGe layer from the Si growth template with NM fabrication processes and allow the SiGe allow to relax elastically to the appropriate bulk lattice constant. I confirm the high structural quality and strain uniformity of these new materials, and demonstrate their use as substrates for technologically relevant epitaxial films by growing strained Si layers and thick, lattice-matched SiGe alloy layers on them. I compare the structural quality of epitaxial films grown on SiGe NMs to those grown on plastically relaxed SiGe substrates.

Acknowledgements

I would like to thank all the people whose assistance and support have made this work possible. My research advisor, Max Lagally, has provided me with the encouragement and advice needed to carry out my thesis research and grow professionally. Thank you for helping me develop my research skills and creating an environment where I was free to work on many projects. I also appreciate the scientific guidance and professional advice of Professors Paul Evans, Mark Eriksson, and Kevin Turner. All of which helped me advance my research and shape my career path.

Thanks to all of the Lagally group members, past and present, who have provided feedback on my research and helped me with experiments. I'd especially like to thank Don Savage for assistance in the lab and many valuable discussions. I appreciate all the conversations, both research and non-research related, with my officemates Arnold Kiefer, Anna Clausen, José Sánchez-Pérez, Boy Tanto, and RB Jacobson. Thank you to Anna for teaching me TEM sample prep, and José for helping me fix the MBE more times than we can count.

Thank you to all of the staff members and scientists who assisted me with the experimental work in this thesis. In particular, staff at the Wisconsin Center for Applied Microelectronics (WCAM) for cleanroom training and staff at the Materials Science Center (MSC) for help with the materials characterization (XRD, TEM, and Raman) needed for this work. I thank Martin Holt at the Nanoprobe station at the Advanced Photon Source for helping me collect the data for the x-ray microdiffraction experiments, and Paul Evans for letting me

use some of his beam time to do so. Thank you to Soitec, and in particular George Celler, for providing SOI(110).

I acknowledge fellowship support from the following programs: the Rae and Anne Herb UW Materials Science Program Fellowship, the National Defense Science and Engineering Graduate (NDSEG) Fellowship, and the National Science Foundation Graduate Research Fellowship (NSFGRF). Funding for this research was also provided by the DOE.

Lastly, thank you to my family for your encouragement and emotional support through the many highs and lows I have experienced while in school. A special thank you to my husband, David, for your constant support and patience during these years, and for making me laugh every day.

Table of Contents

Introduction

Motivation

Strain modifies many important materials properties. In semiconductors, most salient features are affected by strain, including electronic band structure [1-3], electronic transport [4], optoelectronic properties [5], phonon structure [6], and kinetics and thermodynamics of atom motion and structure [7]. In oxides, the existence and extent of structural phases are sensitive to strain: magnetic, dielectric, and superconducting complex oxides can have extremely large responses to applied stresses and fields [8]. In thin-film technology, the stress state of the deposited film controls materials properties from optical reflectance to resistivity [9, 10]. One would like to harness the strain to obtain unique properties not present in the relaxed material. Thermodynamics limits the success: the strain term in the free energy of a material quickly leads to the formation of extended defects [11], which can limit expected new properties or enhanced performance [12-14].

A recent development, crystalline nanomembranes (NMs), offers a new platform for creating strained materials that have unique properties. Crystalline NMs are extremely flexible, compliant, and very thin (less than 5nm to 500nm), with aspect ratios of thickness to lateral dimension of the order of 10^5 or greater. These features allow introduction of strain and materials integration in ways not possible with thick materials, enabling a panoply of entirely new properties. Use of NMs has already significantly altered the landscape as it relates to strain in semiconductors. For example, elastically strain-sharing NMs enable large-area, dislocation-free, uniformly strained silicon [15, 16], a development of considerable importance

for enhancing charge carrier mobilities, for creating very-high-speed flexible electronics [17, 18], and for modifying band gaps and creating new types of electronic heterostructures and superlattices [19-21]. There is also potential for NM fabrication in other material systems, such as III-V semiconductors [22], III-nitrides [23] and various oxide materials [24, 25], all of which exhibit changes in materials properties with strain [3, 26-28]. What has not been recognized, however, is that strain engineering of NMs offers the opportunity to make uniformly strained materials that cannot be made any other way, and elastically relaxed, nominally defect-free materials that conventionally contain significant amounts of crystalline defects. By taking advantage of the anisotropies in elastic constants of the components of the strained-NM system, I can engineer unique strain distributions that are not possible within the limitations of plastic relaxation processes. Thin, strained films released from the original substrates will elastically relax, removing strain intrinsic to the thin-film deposition process. I provide here examples in which strain engineering in Group IV, Si and SiGe, NMs has enabled tunability of *elastic* strain in materials; the strain profiles are created without the formation of extended defects at any point in the fabrication process.

Structure of Dissertation

In Chapter 1, I provide background information on the Si, SiGe, and Ge materials used in the strain engineered NMs for this work. I discuss bulk crystal growth processes, heteroepitaxial growth, and how strain modifies important materials properties. The theory behind the experimental techniques used for measuring strain in the strain engineered Group IV NMs is also reviewed.

Chapter 2 includes the fabrication of NMs and various ways in which to induce and control strain in NMs. Elastic strain sharing between multi-layer NMs with isotropic materials is presented first to introduce elastic strain sharing. Then, I discuss a general treatment of elastic strain sharing in functional NM systems to demonstrate the influence of elastic anisotropies on the resulting strain distributions. I show that the strain distributions in flat strain shared NMs can be controlled and optimized by tuning the relative thicknesses and elastic symmetry of the layers within the multi-layer NMs.

The fabrication of elastically relaxed SiGe NMs is presented in Chapter 3. Thin layers of SiGe grown on Si substrates are released and transferred to new host substrates in NM form. The average strain states as measured with x-ray diffraction and Raman spectroscopy indicate that the $Si_{1-x}Ge_x$ NMs are elastically relaxing to the bulk lattice constant appropriate to the composition of the alloy. I also measured the uniformity of the strain in the transferred SiGe NMs with ~1μm lateral resolution with micro-Raman spectroscopy.

I use the elastically relaxed and transferred SiGe NMs as substrates for growth of strained Si/relaxed SiGe epitaxial heterostructures. This work is discussed in Chapter 4. I measured uniformity of the crystalline tilt and the strain in the Si layer of the heterostructures grown on SiGe NM substrates. I compare the uniformity of these samples to similar heterostructures grown on plastically relaxed SiGe substrates and discuss the different mechanisms for strain and crystalline tilt variations in the heterostructures grown on the two different substrates.

Chapter 5 summarizes the work presented in this dissertation and how it applies to future NM strain engineering research. Specific suggestions to improve the feasibility of using SiGe NMs as growth substrates are provided.

Appendix A provides details on the linear anisotropic elastic theory used to calculate strain distributions in multilayer NMs. I discuss details of the data analysis for the micro-Raman spectroscopy measurements and micro/nano x-ray diffraction measurements in Appendices B and C, respectively.

References

1. Y. Sun, S. E. Thompson, T. Nishida, Physics of Strain Effects in Semiconductors and Metal-Oxide-Semiconductor Field-Effect Transistors. *J. Appl. Phys.* 101 (2007) 104503.

2. M. V. Fischetti, Z. Ren, P. M. Solomon, M. Yang, K. Rim, Six-Band K•P Calculation of the Hole Mobility in Silicon Inversion Layers: Dependence on Surface Orientation, Strain, and Silicon Thickness. *J. Appl. Phys.* **94** (2005) 1079-1095.

3. M. Grundmann, O. Stier, D. Bimberg, InAs/GaAs Pyramidal Quantum Dots: Strain Distribution, Optical Phonons, and Electronic Structure. *Phys. Rev. B* **52** (1995) 11969-11981.

4. F. Schäffler, High-Mobility Si and Ge Structures. *Semicon. Sci. Technol.* **12** (1997) 1515-1549.

5. Y. Sun, S. E. Thompson, T. Nishida, *Strain Effect in Semiconductors: Theory and Device Applications* Springer: New York (2010).

6. J. M. Nieto, F. Comas, Polar Optical Phonons in a Semiconductor Quantum-Well: The Complete Matching Problem. *Physica B* **388** (2007) 153-158.

7. F. Liu, F. Wu, M. G. Lagally, Effect of Strain on Structure and Morphology of Ultrathin Ge on Si(001). *Chem. Rev.* **97** (1997) 1045-1061.

8. J. Cao, J. Wu, Strain Effects in Low-Dimensional Transition Metal Oxides. *Mat. Sci. Eng. R* **71** (2011) 35-52, and references therein.

9. J. A. Thornton, D. W. Hoffman, The Influence of Discharge Current on the Intrinsic Stress in Mo Films Deposited Using Cylindrical and Planar Magnetron Sputtering Sources. *J. Vac. Sci. Technol. A* **3** (1985) 576-579.

10. S. Tamulevičius, Stress and Strain in Vacuum Deposited Thin Films. *Vacuum* **51** (1998) 127-139.

11. J. W. Matthews, A. E. Blakeslee, Defects in Epitaxial Multilayers: I. Misfit Dislocations. *J. Cryst. Growth* **27** (1974) 118-125.

12. M.-W. Chu, I. Szafraniak, R. Scholz, C. Harnagea, D. Hesse, *et al.,* Impact of Misfit Dislocations on the Polarization Instability of Epitaxial Nanostructured Ferroelectric Perovskites. *Nat. Mater.* **3** (2004) 87.

13. D. Monroe, Y. H. Xie, E. A. Fitzgerald, P. J. Silverman, G. P. Watson, Comparison of Mobility-Limiting Mechanism in High-Mobility $Si_{1-x}Ge_x$ Heterostructures. *J. Vac. Sci. Technol. B* **11** (1993) 1731-1737.

14. A. Borak, S. Tsujino, C. Falub, M. Scheinert, L. Diehl, *et al.* Recent Results on the Road to a Si/SiGe Quantum Cascade Laser. *Mater. Res. Soc. Symp. Proc.* 832 (**2005)** F4.2.1.

15. M. M. Roberts, L. J. Klein, D. E. Savage, K. A. Slinker, M. Friesen, *et al.,* Elastically Relaxed Free-Standing Strained-Silicon Nanomembranes. *Nat. Mater.* **2006**, *5,* 388-393.

16. S. A. Scott, M. G. Lagally, Elastically Strain-Sharing Nanomembranes: Flexible and Transferable Strained Silicon and Silicon-Germanium Alloys. *J. Phys. D Appl. Phys.* **40** (2007) R75-R92.

17. H.-C. Yuan, M. M. Kelly, D. E. Savage, M. G. Lagally, G. K. Celler, *et al.,* Thermally Processed High-Mobility MOS Thin-Film Transistors on Transferable Single-Crystal Elastically Strain-Sharing Si/SiGe/Si Nanomembranes. *IEEE T. Electron Dev.* **55** (2008) 810-815.

18. Y. Sun, E. Menard, J. A. Rogers, H.-S. Kim, S. Kim, *et al.,* A. Gigahertz Operation in Flexible Transistors on Plastic Substrates. *Appl. Phys. Lett.* **88** (2006) 183509.

19. M. H. Huang, C. S. Ritz, B. Novakovic, D. Yu, Y. Zhang, *et al.,* Mechano-Electronic Superlattices in Silicon Nanoribbons. *ACS Nano* **3** (2009) 721-727.

20. C. Deneke, R. Songmuang, N. Y. Jin-Phillipp, O .G. Schmidt, The Structure of Hybrid Radial Superlattices. *J. Phys. D Appl. Phys.* **42** (2009) 103001.

21. Z. Liu, J. Wu, W. Duan, M. G. Lagally, F. Liu, Electronic Phase Diagram of Single-Element Silicon "Strain" Superlattice. *Phys. Rev. Lett.* **105** (2010) 016802.

22. D. L. Owen, D. Lackner, O .J. Pitts, S. P. Watkins, P. M. Mooney, In-Place Bonding of GaAs/InGaAs/GaAs Heterostructures to GaAs(001). *Semicond. Sci. Technol.* **24** (2009) 035011.

23. S. W. Seo, K. K. Lee, S. Kang, S. Huang, W. A. Doolittle, *et al.,* GaN Metal-Semiconductor-Metal Photodetectors Grown on Lithium Gallate Substrates by Molecular-Beam Epitaxy. *Appl. Phys. Lett.* **79** (2001) 1372-1375.

24. S. P. Albu, A. Ghicov, J. M. Macak, R. Hahn, P. Schmuki, Self-Organized, Free-Standing TiO_2 Nanotube Membranes for Flow-Through Photocatalytic Applications. *Nano. Lett.* **7** (2010) 221901.

25. J.-J. Chen, S. Jang, J. F. Ren, Y. Li, H.-S. Kim, *et al.,* Selective and Nonselective Wet Etching of $Zn_{0.9}Mg_{0.1}$/ZnO. *J. Electron. Mater.* **35** (2006) 516-519.

26. W.-J. Yin, S. Chen, J.-H. Yang, X.-G. Gong, Y. Yan, *et al.,* Effective Bandgap Narrowing of Anatase TiO_2 by Strain Along a Soft Direction. *Appl. Phys. Lett.* **96** (2010) 221901.

27. Y. S. Nam, S. W. Lee, K. S. Baek, S. K. Chang, J.-H. Song, *et al.,* Anisotropic Optical Properties of Free and Bound Excitons in Highly Strained *A*-plane ZnO Investigated with Polarized Photoreflectance and Photoluminescence Spectroscopy. *Appl. Phys. Lett.* **92** (2008) 201907.

28. W. Shan, A. J. Fischer, J. J. Song, G. E. Bulman, G. E. Kong, *et al.,* Optical Studies of GaN and GaN/AlGaN Heterostructures on SiC Substrates. *Appl. Phys. Lett.* **69** (1996) 740-743.

Chapter 1 Si/SiGe Thin Film Heterostructures

Silicon and silicon-germanium alloys play an important role in Group IV electronics and photonics. The ability to tune the lattice constant of SiGe by varying composition has led to extensive efforts in the strain engineering of Si, Ge, and SiGe in order to enhance electronic transport properties like charge carrier mobility, induce new effects not seen in the bulk forms of Si or Ge, such as the electro-optic effect in strained Si, and create charge confinement in heterostructures. Conventionally, strain is controlled through lattice mismatch and crystalline-defect formation. In this chapter I review heteroepitaxial growth in the Si/SiGe system and plastic strain relaxation mechanisms. I also discuss significant electrical, mechanical, and optical properties of Si and SiGe and how these properties change with strain.

1.1 Crystalline structure and materials properties of Si, SiGe, and Ge

Si and Ge crystallize in the diamond cubic structure or face-centered cubic lattice with a two-atom basis. The basis atoms are tetragonally bonded with one atom centered at (0,0,0) and the other at (¼, ¼, ¼) as shown in Figure 1-1A. There is an approximately 4.2% lattice mismatch between Si and Ge with a_{Si} = 5.431Å and a Ge = 5.658Å. The alloy, $Si_{1-x}Ge_x$, can be formed over the entire composition range and forms a random solid solution. The phase diagram and lattice constant as a function of composition for $Si_{1-x}Ge_x$ are shown in Figures 1-1B and 1-1C, respectively. The lattice constant difference between SiGe alloys and Si (or Ge) makes it difficult to integrate these materials in heterostructures in large amounts, but provides a nice way to strain engineer these materials in thin-film form, as will be seen in later sections.

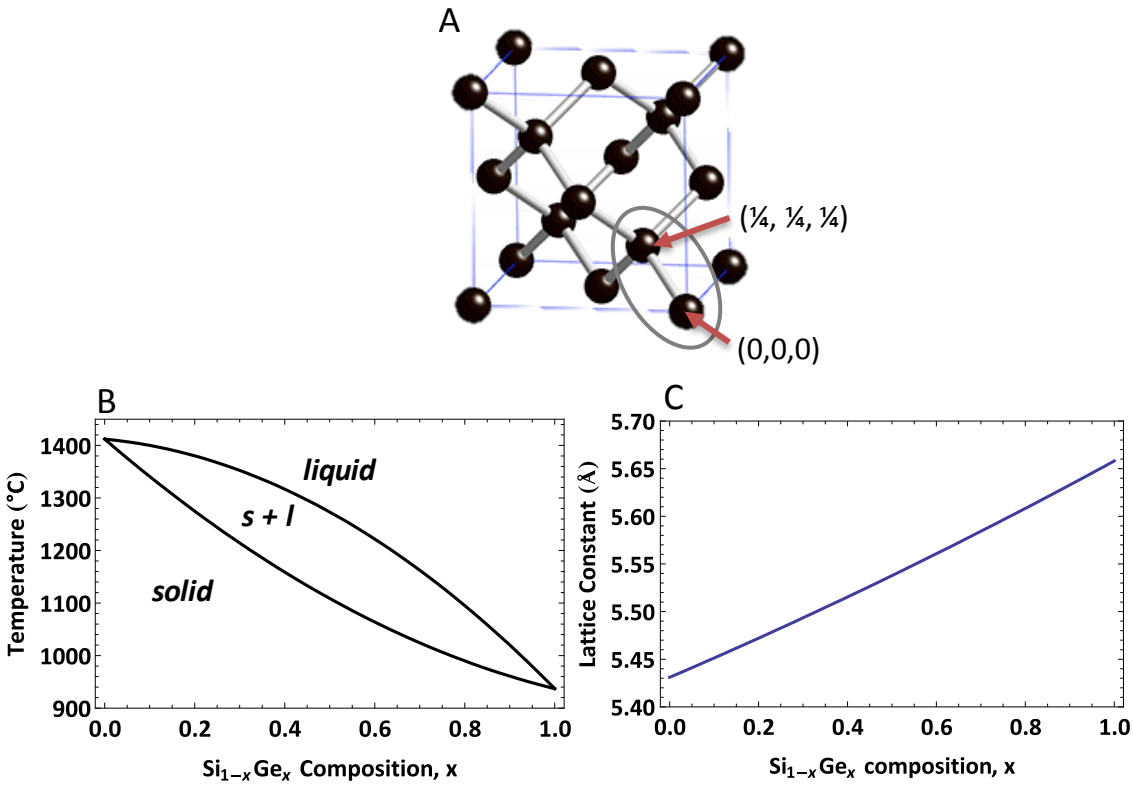

Figure 1-1. (A) Crystalline structure of Si, SiGe and Ge. The diamond cubic structure shown has a 2-atom basis (circled atoms) sitting on a face-centered cubic lattice. One atom is located on (0,0,0) and the other at (¼,, ¼, ¼). (B) The phase diagram for $Si_{1-x}Ge_x$ alloys. Si and Ge are miscible over the entire composition range and form a random solid solution. There is a large two-phase region between the liquidus and solidus curves. (C) Lattice constant of $Si_{1-x}Ge_x$ alloys. The lattice constant as a function of Ge composition is: $a_{SiGe} = 5.431 + 0.2x + 0.027x^2$ [1]. The alloy lattice constant deviates slightly from Vegard's law (weighted linear combination of Si and Ge lattice constants).

The cubic symmetry of the crystalline structure of Si, SiGe, and Ge makes the elastic properties four-fold symmetric, but the materials are not isotropic. The elastic properties of these materials will be important when considering strain sharing between layers of different compositions or crystalline orientations. For instance, consider the symmetry of three different

low-index crystalline planes; the atomic configurations for the {001}, {110}, and {111} planes are shown in the insets of Figures 1-2D, E, and F.

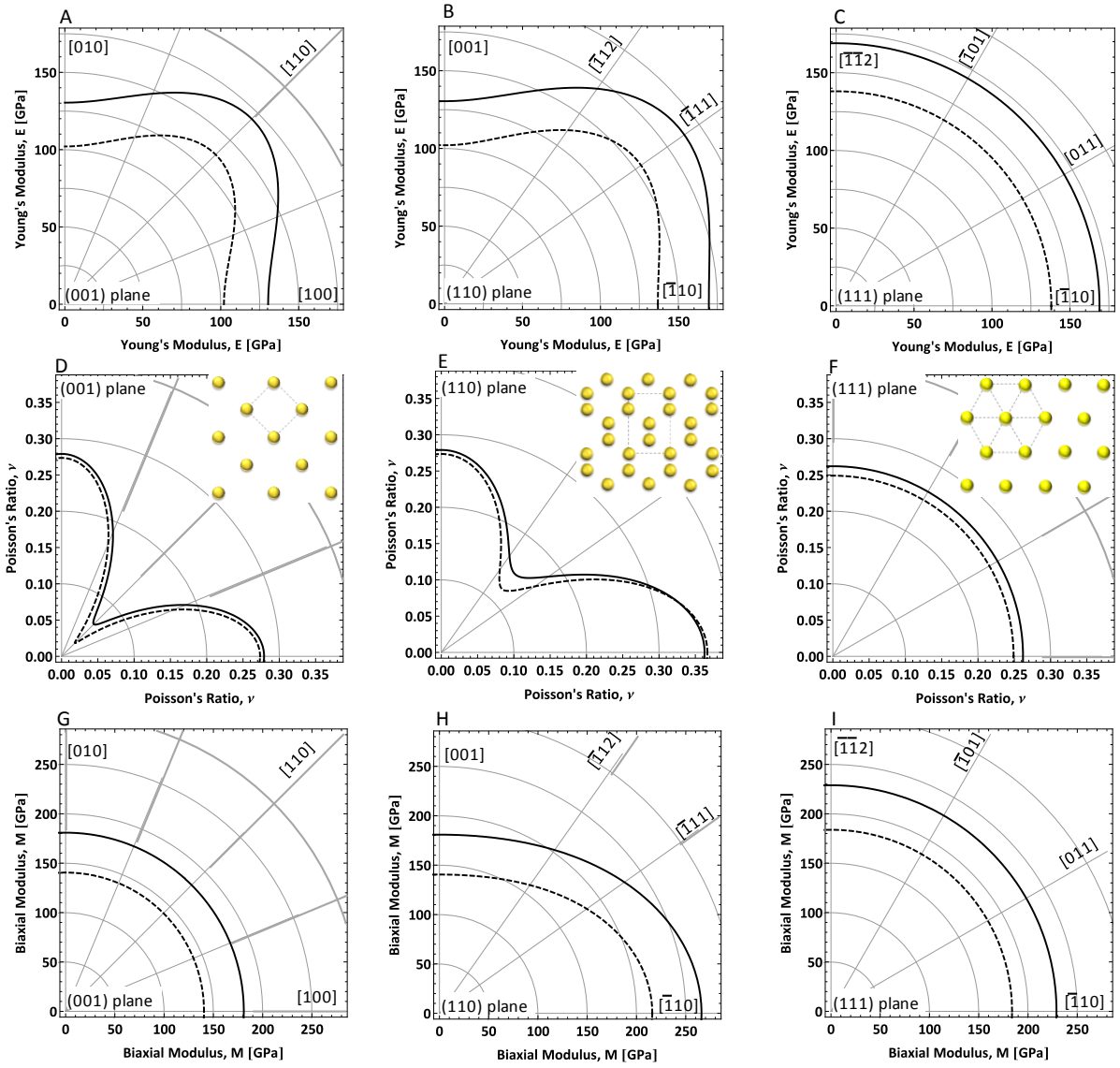

Figure 1-2. Variation of select elastic constants in the {001}, {110}, and {111} planes for Si and Ge. (A-C) Young's (elastic) modulus, (D-F) Poisson's ratio (in the plane noted), and (G-I) biaxial modulus. The elastic constants for $Si_{1-x}Ge_x$ are a weighted linear combination based on the composition. The insets show the atomic arrangement in the respective planes.

The Young's (elastic) modulus (E), Poisson's ratio (ν), and biaxial modulus [M = E/(1-ν)] are plotted as functions of in-plane direction for the three crystalline planes. The Young's modulus and biaxial modulus represent how the material will respond to uniaxial and equibiaxial stress, respectively. The elastic-constant symmetry is the same as that of the atomic configuration in the plane; the {001} plane has four-fold symmetry, the {111} plane has six-fold symmetry (the elastic constants in this plane are isotropic), and the {110} plane has two-fold symmetry. These elastic constants are derived from basic elastic properties and the fundamental compliance tensors for Si and Ge [2]. For details please see Appendix A.

Probably the most important properties of any semiconductor, including Si, SiGe, and Ge, are the electronic band structure and the band gap, E_g. The valance band maximum, or highest filled energy state, is at the gamma point (center of the Brillouin zone) for both Si and Ge. The conduction band minimum (lowest empty energy state) for Si is six-fold degenerate and lies along the <001> direction at the Δ point. The conduction band minimum for Ge is 4-fold degenerate and lies along the <111> direction at the edge of the Brillouin zone or the L point (Figure 1-3B). E_g = 1.12eV and 0.67eV for Si and Ge, respectively. As will be seen in later sections of this chapter, strain can be applied to change the crystalline symmetry of Si (and Ge) and thus change the electronic band structure and band gap. Figure 1-3C shows the band gap of $Si_{1-x}Ge_x$ as a function of Ge composition for relaxed alloys and for alloys strained to the Si lattice constant. For the unstrained alloy, there is an abrupt change in the band gap at x~0.85. This is when the SiGe alloy becomes more Ge-like: the conduction band minimum changes from the Δ

valley to the L valley. The variation in band structure and band gap is important in designing Si/SiGe heterostructures for devices. This will be discussed in more detail in section 1.4.

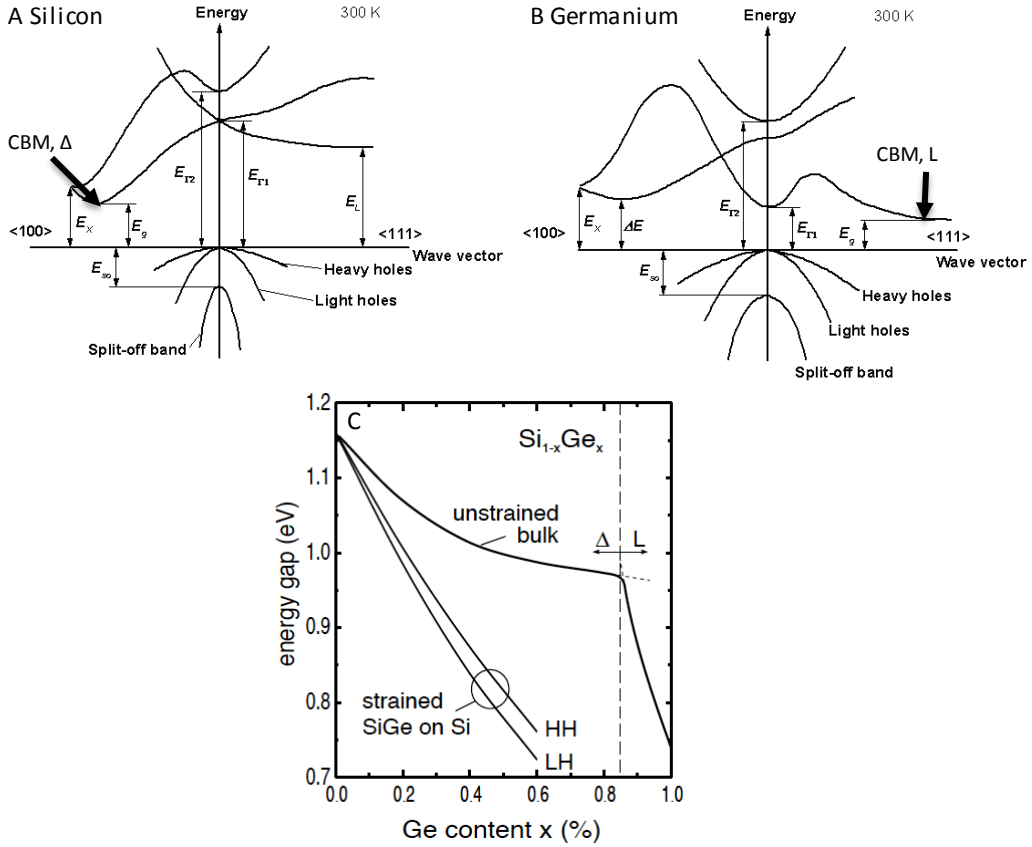

Figure 1-3. Electronic band structure for (A) Si and (B) Ge [3]. (C) The band gap for $Si_{1-x}Ge_x$ as a function of composition for unstrained bulk SiGe and for SiGe strained to the Si lattice constant [4]. The strained curve has two lines because the valance band degeneracy is removed with strain; the light hole (LH) and heavy hole (HH) bands split in energy.

1.2 Bulk crystal growth

I will briefly review two of the more common methods for single-crystal growth of bulk Si: Czochralski growth and float zone growth. Both involve growing single crystals from highly

purified melted materials. I will discuss how bulk single-crystalline growth is different for SiGe alloys and the difficulties associated with it. Please consult other reviews [5-7] for more details on these processes and descriptions of less commonly used single-crystalline growth techniques.

1.2.1 Silicon

Czochralski growth

Single crystals of Si are most commonly produced with Czochralski (CZ) growth. Highly purified Si (99.999999999%) is heated to ~1500°C in a fused silica crucible in an inert gas atmosphere. A single-crystal Si 'seed' is brought into contact with the molten Si and is subsequently slowly pulled (while rotating) from the melt causing the crystalline material to grow. The melt solidifies at the solid/liquid interface because a temperature gradient is achieved by thermal conduction through the solid and with increasing surface area of the crystal [5]. The resulting crystalline material is a large cylindrical ingot, or boule. This process is shown in Figure 1-4. Si boules can be grown as large as 450mm (~18in.) in diameter and up to ~2m long. Wafers are produced by slicing the boule along desired crystallographic directions.

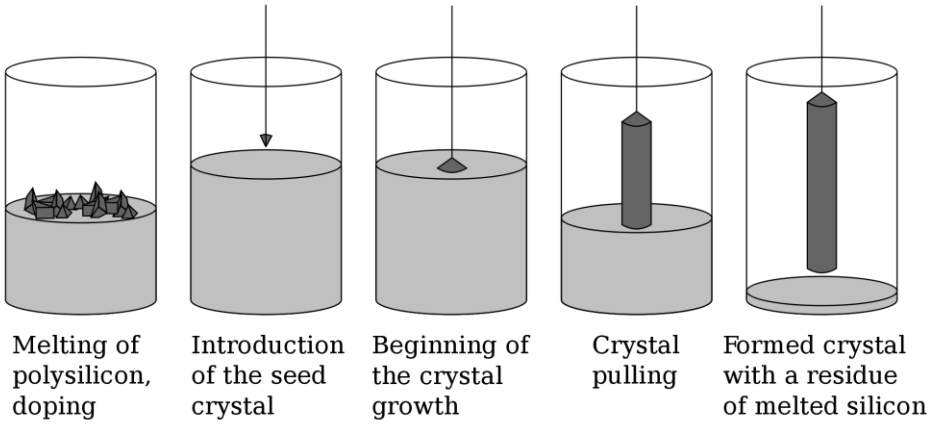

Figure 1-4. CZ growth process [8]. From left to right: (1) Highly pure Si is melted in a fused silica crucible. (2) The single-crystalline Si seed is put into contact with the melt. (3) The boule begins to grow. (4) The seed crystal is rotated while pulling the crystal to ensure uniformity of the material and limit thermal gradients in the melt. (5) The boule is removed from the melt and cooled very slowly to prevent thermal shock.

There are many factors that go into producing highly pure, defect-free wafers of Si. For instance, the rate at which the seed crystal is pulled from the melt will determine if growth is even possible, or if the crystalline material will be highly defective. If the pull rate is too high, proper temperature gradients cannot be achieved to solidify the melt. If the pull rate is too slow, high densities of vacancies at the liquid/solid interface tend to agglomerate. Dislocation densities and the formation of other crystalline defects are also sensitive to the pull rate. Typical pull rates for Si are ~1mm/min. In addition to crystalline defects, the impurity concentration must be kept to a minimum. In CZ growth, the main impurity is oxygen; oxygen dissolves into the melt through contact with the fused-silica crucible. One way to limit impurity incorporation is to use magnetic fields around the crucible to steer ionic impurities in the melt away from the liquid/solid interface.

Float zone growth

In float zone growth, a portion of a polycrystalline Si rod is melted with high power radio frequency coils in an inert gas atmosphere. The coils produce eddy currents within the Si, which induce Joule heating to melt a small portion of the Si. Only solid Si supports the portion of the rod that is melted: the melted material never comes into contact with a crucible. The melted region starts near a crystalline seed and the coils are swept along the length of the rotating rod to crystallize the remaining material. This process can be repeated several times to segregate impurities from the majority of the crystal. Many impurities have segregation coefficients in Si of less than one (at thermodynamic equilibrium), so they would prefer to stay in the molten region rather than become incorporated in the solid crystal. Float zone growth (or float zone refining) has produced Si with carrier concentrations as low as ~$10^{11}/cm^3$ [5] (the intrinsic carrier concentration at room temperature in Si = ~$10^{10}/cm^3$).

1.2.2 Silicon-Germanium

There are two major issues in creating bulk single-crystalline SiGe alloy from melt: (1) lack of a lattice-matched seed crystal, and (2) segregation of Si and Ge in the solidification process. I showed in section 1.1 that the lattice constant of SiGe changes nearly linearly with composition. This means that when growing SiGe of any composition there will be a lattice mismatch with the Si (or Ge) seed crystal. For reasons that will soon be apparent, defect-free, single crystalline $Si_{1-x}Ge_x$ seeds are not available for a large portion of the composition range. This lattice mismatch between the alloy and the seed crystal is eventually relieved by the

formation of extended defects (i.e., dislocations). The crystalline defects destroy long-range order in the crystal and can significantly alter the materials properties [9]. Crystalline-defect formation associated with strain relaxation and how defects affect the materials properties will be discussed in more detail in sections 1.3.3 and 1.4.3, respectively.

The second reason that bulk crystalline growth of SiGe is difficult (segregation of Si and Ge during solidification) can be explained by examining the phase diagram. For example, let us examine what happens as we cool a 50/50 mix of Si and Ge starting from a liquid (T > 1300°C). At T ~1250°C we hit the liquidus curve on the phase diagram [(1) in Figure 1-5]. At that same temperature a solid forms with a composition of ~20% Ge [(2) in Figure 1-5]. This makes sense as Si has a higher melting point and will solidify more readily at this temperature range. At this point the solid SiGe is at a composition much different from that of the original melt, thus the melt has to change composition as well. If the mixture is in true equilibrium, the new melt composition should be ~80% Ge because the solid SiGe composition has 30% more Si than the original melt [(3) in Figure 1-5]. The temperature needs to drop further to solidify the new melt (T ~1100°C) and the new solid SiGe composition will be ~55% [(4) in Figure 1-5]. In reality, growth of bulk crystalline SiGe is a continually changing process. If growth is allowed to proceed without interference, the composition of the solid SiGe will gradually increase as the crystal forms. As mentioned before, the changing composition leads to strain build up and eventually crystalline defect formation. I have illustrated an extreme case where segregation of the Si and Ge result in very large differences in the liquid and solid compositions. Crystal growth of SiGe from the liquid phase is easier for compositions closer to pure Si or pure Ge.

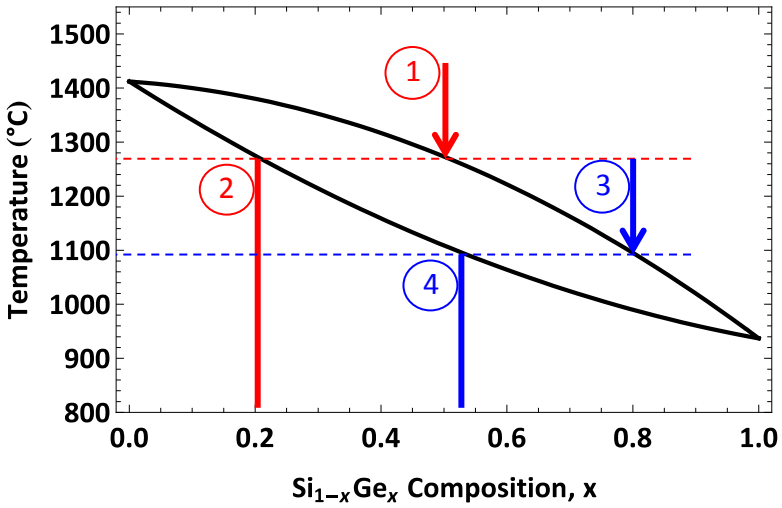

Figure 1-5. Phase diagram of $Si_{1-x}Ge_x$. (1) Start with a melt with a 1:1 ratio of SiGe. (2) At a temperature of ~1250°C the mixture will start to solidify at $Si_{0.8}Ge_{0.2}$. The large difference in liquid and solid compositions is set by the large two-phase region of the diagram. (3) In equilibrium, the liquid mixture will have 30% less Si than the initial mixture, making the new melt composition 80% Ge. The new liquid mixture has a different melting point and temperature must be lowered to solidify the new melt. (4) At ~1100°C the mixture will solidify at ~55% Ge.

One way to circumvent the issue of continuously changing SiGe composition during crystal growth is to continually 'feed' Si into the melt to maintain a constant Si:Ge ratio [10]. If the melt composition is maintained, the solid composition will be different from the melt, but consistent. In theory, this method should produce uniform SiGe crystals if the system is in true equilibrium. There are a few problems in maintaining equilibrium in the system. The first is that the SiGe composition is very sensitive to temperature. Even small changes in temperature will lead to compositional variations over the width and length of the boule. Because it is difficult to maintain a constant temperature for large-diameter crystals, the boule diameter of crystalline SiGe is often limited to ~25mm for melt growth techniques [11].

The second issue is that it is difficult to maintain the melt composition near the solid/liquid interface. Because Si solidifies more readily than Ge, there is typically a higher ratio of Ge atoms near the interface than in the rest of the melt. Depending on the pull rate, Ge diffusion may not be fast enough for the melt to maintain an equilibrium composition, resulting in a gradient in the liquid composition. This means that at any given point in the melt there is a different solidification/freezing temperature (liquidus curve). There also exists a temperature gradient from the solid interface into the melt. If at any point in the melt the temperature drops below the liquidus curve temperature for a particular composition, constitutional supercooling occurs [12]. This is illustrated in Figure 1-6. The liquid starts to solidify away from the growth front and often results in polycrystalline growth. To avoid constitutional supercooling very low pull rates are used (~mm/hr to ~mm/day) so that the compositional gradient in the melt is small [11]. The low pull rates, segregation of species, small crystal diameters, and lack of lattice-matched seed crystals make crystalline growth of SiGe from the liquid state very difficult and not cost effective (very low pull rates and low crystalline quality).

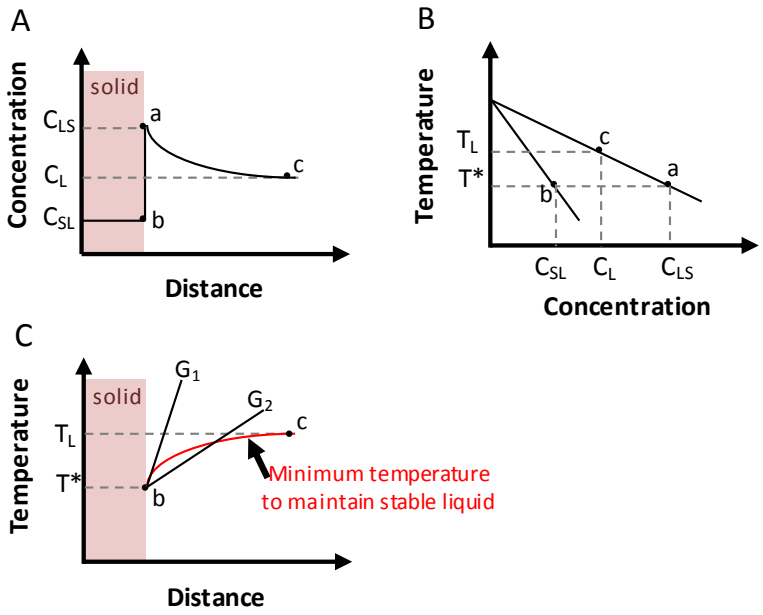

Figure 1-6. Example of constitutional supercooling [after 12]. (A) Profile of the concentration within the solid (shaded region) and within the liquid. The solid is at concentration b, the liquid is at concentration a at the solid/liquid interface, and the concentration of the liquid goes to c. (B) Phase diagram. To maintain a liquid at concentration C_L, the minimum temperature is T_L. The temperature at the solid/liquid interface is at T*. (C) Temperature profile along the growth direction. The solid/liquid interface is at temperature T* and the minimum temperature to maintain a liquid for concentration C_L is T_L. There will be a temperature profile starting from the solid/liquid interface. The minimum temperature needed to maintain a liquid with the concentration profile shown in A is shown as the red solid line. If the temperature dips below this line at any point along the growth direction, crystals will start to form ahead of the solid/liquid interface and constitutional supercooling occurs (G_2). If the temperature along the growth direction is above the red line then crystal growth should proceed normally.

Aside from the wide range of issues associated with crystal growth of SiGe from melt, there is still a need for single-crystalline, defect-free SiGe substrates. Solution-based crystal growth techniques [13-16], are attractive because alloy crystal growth occurs below the melting

temperature, such that segregation of the constituent species is less of an issue. I will describe the traveling heater (or traveling solvent) method here, but many solution-based growth techniques follow similar principles. In the traveling heater method (THM), a seed crystal, usually the same size, composition, and lattice constant as the material to be grown, is separated from the polycrystalline material by a solvent. The solvent is usually metallic for Si and Ge growth and melts at a lower temperature than the alloy to be grown [16]. Much like the float zone method, a heater is passed along the length of the system where the polycrystalline material mixes with the melted solvent material. Eventually supersaturation of the solute occurs and the material crystallizes at the solution/seed crystal interface (see Figure 1-7). Crystals fabricated with this method are typically heavily doped with the metallic solvent.

The THM has been used to grow $Si_{1-x}Ge_x$ crystals with a wide range of compositions [14]. The main issue is fabrication of an adequate seed crystal. For this technique to work well the seed crystal must have the same size, composition, and lattice constant as the crystal to be grown, and must be defect-free to obtain the highest quality crystalline material. SiGe crystals made by any of the liquid crystal growth techniques will suffer from the problems enumerated above. In all cases, the starting material to make the SiGe seed crystals is either Si or Ge and thus all the SiGe seeds will contain crystalline defects associated with strain relief. The method used to make the SiGe seed will determine the density of defects. For these reasons it is important to find alternative ways, like nanomembrane fabrication, to make defect-free relaxed SiGe substrates.

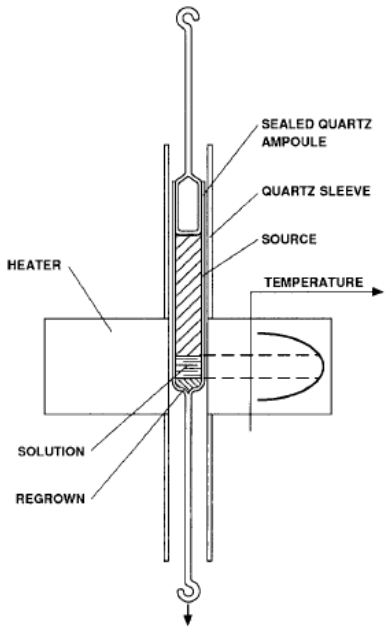

Figure 1-7. The traveling heater method (THM) for bulk crystalline growth [16]. The solution is molten and in contact with the solid polycrystalline source material. The source material will supersaturate in the molten solution and condense at the crystalline interface. The crystal/solution/source material apparatus is pulled through the heater to grow the crystal.

1.3 Heteroepitaxial growth

Epitaxy is single-crystalline growth of thin films. A "template" substrate is required with an atomic structure similar to that of the film. In heteroepitaxy, the material composition of the substrate is different from that of the growing film. There is always a lattice mismatch associated with heteroepitaxial growth in the Si/Ge system. As previously discussed, Si and Ge have a ~4.2% lattice mismatch and the lattice constant of the SiGe alloy varies with composition. Here the mismatch strain of a film epitaxially grown on a given substrate is defined as:

$$\varepsilon_m = \frac{a_{sub} - a_{film}}{a_{film}}. \quad (1\text{-}1)$$

Using this definition a SiGe film grown on a Si substrate will be compressively strained ($-\varepsilon_m$) and a similar film grown on a Ge substrate will be tensilely strained ($+\varepsilon_m$). The mismatch strain is key in understanding strain engineering and the difficulties associated with heteroepitaxy in the Si/Ge system.

In this section I will briefly discuss heteroepitaxial growth of Si, SiGe, and Ge. I will review the possible growth modes and techniques for growing heterostructures in the Si/Ge system, mismatch strain relief mechanisms, and various ways to control crystalline defects associated with strain relaxation.

1.3.1 Growth modes

Thin-film growth proceeds one of three ways (shown in Figure 1-8): Frank-van der Merwe (layer-by-layer growth), Volmer-Weber (3D-island growth), or Stranski-Krastanov (layer-by-layer followed by 3D-island/nanocrystal growth). Heteroepitaxal films within the Si/Ge system grow in either the Frank-van der Merwe growth mode [Figure 1-8A] (low mismatch strains, < ~1%) or the Stranski-Krastanov growth mode [Figure 1-8C] (high mismatch strains > ~1%) depending on the magnitude of the lattice mismatch strain, thickness of the film, and other kinetic factors, like growth conditions. In both cases, the initial growth is planar, but in Stranski-Krastanov growth, the surface starts to roughen to provide a degree of elastic strain relaxation in the film while maintaining overall coherency. The kinetic factors during growth

(growth rate, temperature, pressure, *etc*.) may alter the magnitude of the mismatch strain transition from Frank-van der Merwe-like growth to Stranski-Krastanov-like growth [17,18].

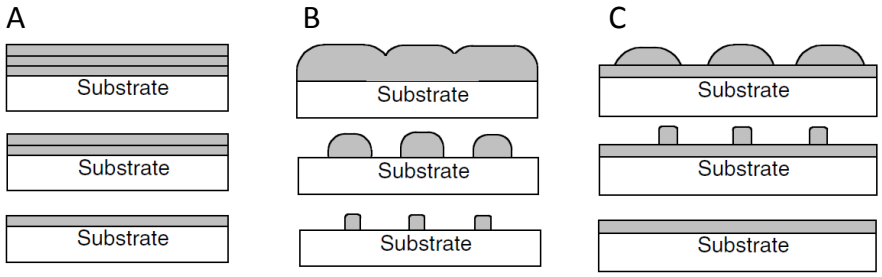

Figure 1-8. Thermodynamic-limit growth modes [19]. (A) Layer-by-layer growth (Frank-van der Merwe): film grows in complete layers. (B) Island growth (Volmer-Weber): film forms three-dimensional islands that may coalesce during growth. (C) Stranski-Krastanov growth: the film grows layer-by-layer to a certain thickness (wetting layer) followed by three-dimensional island growth.

1.3.2 Epitaxial-growth techniques

As stated in section 1.2, epitaxy is the primary way to grow high-crystalline-quality SiGe alloys. I will review the two techniques used in this work to grow epitaxial thin films of Si, SiGe, and Ge: solid-source molecular beam epitaxy (MBE) and ultra-high vacuum chemical vapor deposition (UHVCVD). Both are well-established techniques and further details can be found elsewhere [20, 21].

MBE

In solid-source molecular beam epitaxy (MBE), heated source materials (here Si and Ge) evaporate into an ultra-high vacuum (UHV) [$<10^{-9}$ torr] growth chamber. The evaporated atoms then condense onto an atomically clean heated substrate (~400-600°C for Si substrates, 200-400°C for Ge substrates) to form the epitaxial thin film. Si and Ge are often evaporated from an

electron beam (e-beam) source. The e-beam is created by passing current through a metal filament and accelerating the emitted electrons though an electric field. The filament is usually located under the material to be evaporated so as not to interfere with growth. A magnetic field is used to steer the e-beam onto the source material. The flux coming off the sources is emitted in all directions and thus the source material is deposited on anything that is in line-of-sight of the source within the growth chamber (see Figure 1-9).

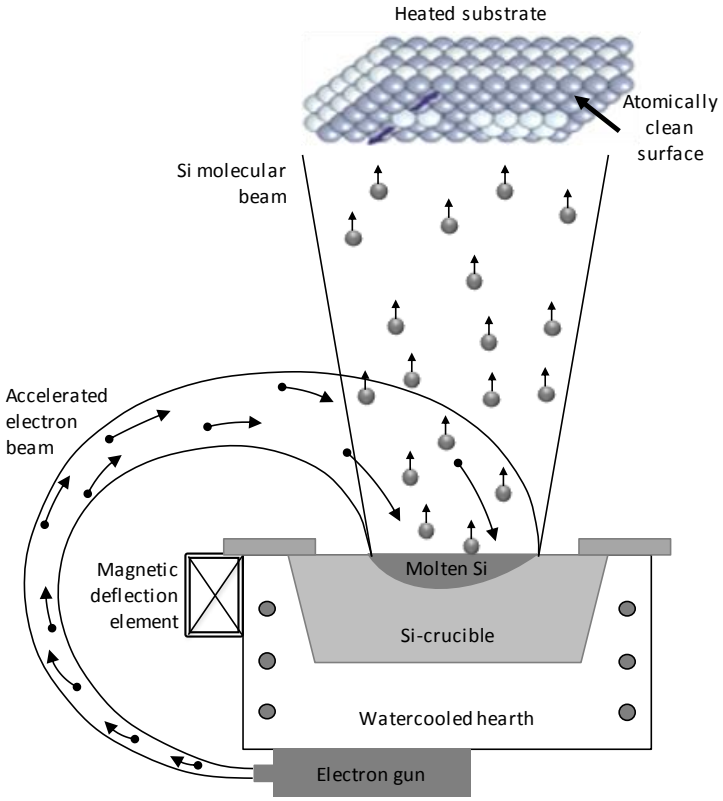

Figure 1-9. Solid-source e-beam MBE process [after 22]. The electrons are emitted from a filament housed under the Si source material. The electrons are accelerated through an electric field and deflected in a magnetic field to form the e-beam and steer it onto the source material. The e-beam controls the heating of the source material. The source material is evaporated in all directions. The atoms reaching the surface of the substrate material condense onto the atomically clean, heated substrate where the epitaxial film is grown.

MBE sources may also be evaporated from Knudsen cells (K-cells) or effusion cells. Here the source material is completely melted within a heated crucible. Growth proceeds in a similar way to evaporating material from e-beam cells. In the Si/Ge MBE at the University of Wisconsin-Madison, e-beam sources are used to evaporate the Si and Ge source materials and the samples are heated resistively by passing current through the Si substrates (sample size = 42mm x 8mm).

MBE growth rates are predominantly controlled by the source flux, which is determined by the temperature of the source and the distance between the source and the substrate. Typical growth rates for MBE will vary from system to system (0.5 – 30nm/min) based on the size of the chamber, base pressure, size of the source, etc. [20]. The base pressure is kept low (≤ 10^{-10} torr) to avoid impurity incorporation in the epitaxial thin films and to ensure that the evaporant atoms have long scattering mean free paths (>1m). This means that the flux getting to the sample is easily determined by the geometry of the chamber (if the source flux is known) and growth can be stopped abruptly by inserting a shutter between the source and the sample. Growth rates in the UW MBE system are 2 – 5 nm/min, with a base pressure of ~2 x10^{-11} mbar when the chamber walls are cooled with liquid nitrogen. The cool chamber walls act to condense particulates and prevent components near the sources from getting hot enough to outgas during growth.

One advantage of MBE is that the kinetic factors of growth (growth rate, material composition, growth temperature) are independent of one another. This makes MBE uniquely suited to study the influence of the surface on heteroepitaxy for different growth rates,

temperatures, and film compositions. The only limits placed on growth temperature are the ability to grow epitaxial films with low impurity concentrations (low) and control roughening of the film surface (high). As previously mentioned, the transition from Frank-van der Merwe-like growth to Stranski-Krastanov-like growth in SiGe films can be kinetically controlled. An example of how growth temperature controls surface effects is shown in the atomic force microscopy (AFM) images in Figure 1-10 where similar SiGe films were grown on Si substrates with MBE at different substrate temperatures. The SiGe film grown at the higher growth temperature shows signs of strain driven roughening (Stranski-Krastanov), and the film is smooth (Frank-van der Merwe) when grown at the lower growth temperature. The ability to tune the growth rate, growth temperature, and film compositions independently makes MBE a great research tool; however, the low throughput (low growth rates, limited number of wafers growing simultaneously) does not make it in general a viable commercial process.

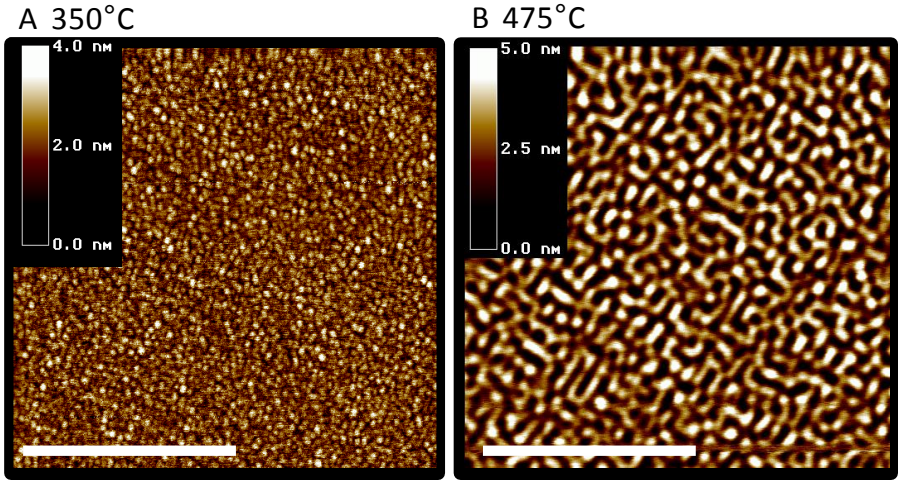

Figure 1-10. AFM images of the surface of 25nm $Si_{0.62}Ge_{0.38}$ films grown on bulk Si with low-temperature MBE. (A) Growth temperature = 350°C, and (B) growth temperature = 475°C. The film grown at the higher temperature shows signs of strain driven roughening, while the film grown at the lower temperature does not. The length scale bars are 1µm. Images courtesy of C. White.

UHVCVD

Ultra-high-vacuum chemical vapor deposition (CVD) produces epitaxial films by passing reactive gases over the surface of heated substrates. For Si/Ge growth, silane (SiH_4) and germane (GeH_4) [other gases used include Si_2H_6, Ge_2H_6, and SiH_2Cl_2] react with an atomically clean Si substrate. The SiH_4 (or GeH_4) decomposes at the surface of the Si substrate where the Si (or Ge) incorporates into the film by attaching to dangling bonds on the surface. The remaining H reacts with other free H to create H_2 or attaches itself to surrounding free Si bonds on the surface (creating a H-terminated surface). There are several possible reactions for SiH_4 with the surface of the substrate, depending on the number of available bonding sites and the growth regime [21]. As shown below in Figure 1-11C, growth is not performed at ultra-high-vacuum ($<10^{-9}$ torr). The ultra-high vacuum label comes from the base pressure of the reaction chamber. Low water and other contaminant partial pressures prevent oxygen and impurity incorporation in the epitaxial films.

The CVD growth rate is dependent on the rate at which the gases reach the substrate, the decomposition of the reactant gases at the growth surface, and on H desorption from the surface. When working at low carrier gas partial pressures and high temperatures the growth rate is limited by the arrival and decomposition of reactant gases at the surface. At high temperature, H readily leaves the surface, exposing many active sites for growth (Figure 1-11A). The growth rate is site limited at higher partial pressures and low temperatures, where H desorption from the surface determines the growth rate. Hydrogen desorption is slower at low temperatures and limits the growth rate because there are fewer available growth sites (Figure

1-11B). The growth rate trend as a function of substrate temperature is shown in Figure 1-11C for Si. At low temperatures the growth rate is largely independent of pressure, and at high temperatures the growth rate is less dependent on temperature. Although SiGe growth takes place at low temperatures (550-650°C) to limit strain driven roughening (see Figure 1-10 above) and plastic relaxation via dislocations (see later sections), the growth is usually reactant limited because H leaves Ge atoms more readily than Si atoms; there is a layer of Ge that segregates to the surface during alloy growth and this will shift the boundary between growth regimes to lower temperatures for alloy growth.

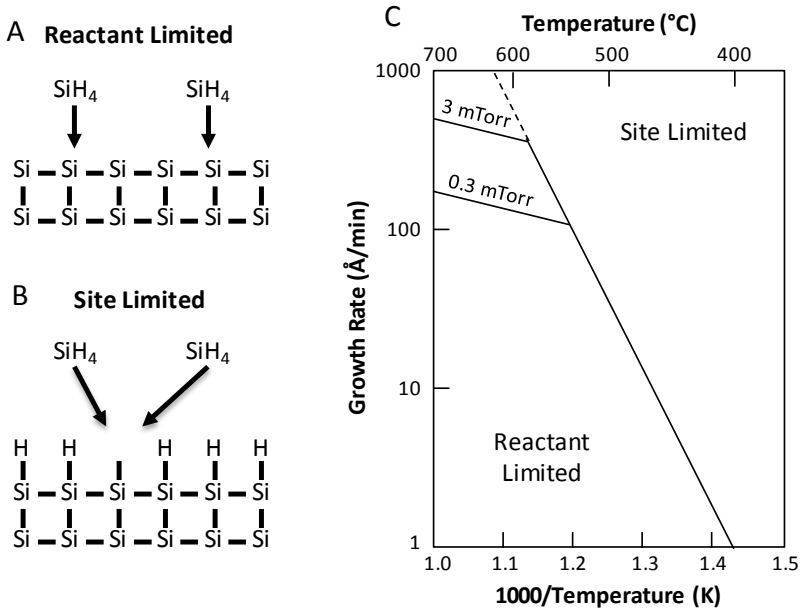

Figure 1-11. Schematic diagrams of (A) reactant limited and (B) site limited Si CVD growth. The rate at which the reactant gases (SiH_4) reach the surface and decompose determine the growth rate in (A). The growth rate is limited by H desorption from the surface in the site limited regime (B). (C) Plot of growth rate trend vs. temperature. At high temperatures the growth rate is not a strong function of temperature and varies with the partial pressure of SiH_4. The growth rate is a strong function of temperature in the site-limited regime where the growth rate is controlled by H desorption from the surface (temperature sensitive). Figures after [20].

The Si/Ge UHVCVD reactor at UW uses SiH_4 and GeH_4 reactant gases with H as the carrier gas. Doping of the semiconductor films is possible with diborane (B_2H_6 for acceptor or p-type dopants) and phosphine (PH_3 for donor or n-type dopants). The base pressure of the UHVCVD chamber is $4x10^{-10}$ torr, but growth takes place ~2-3 mtorr. Pure-Si growth rates range from 2-3nm/min and are largely based on the temperature of the substrate [growth typically takes place in site-limited regime described above (growth temp < 700°C)]. SiGe alloy growth takes place in the reactant limited regime and growth rates range from 10-20nm/min. The samples (sample size = 42mm x 8mm) are also resistively heated.

The fundamental differences in the growth mechanisms make MBE and UHVCVD useful for different reasons. In MBE, the kinetic factors of growth are largely independent such that effects of growth temperature can be tested independently of flux arrival rate. This is not the case for SiGe growth in UHVCVD. Conversely, maximum single-crystalline epitaxial growth rates in CVD can reach ~0.1 - 1μm/min [23] and growth will take place anywhere the reactant gases reach the heated substrate surface; growth does not require direct line-of-sight from the source material to the substrate surface as is the case for MBE. This means that more wafers can be grown on at one time in a given space allowing for much higher throughput than a similar MBE process. These features make CVD a more viable commercial process (higher throughput) and MBE a useful research tool.

1.3.3 Plastic strain relaxation

Mismatch or lattice strain in SiGe epitaxial films grown on Si substrates is accommodated one of three ways: fully strained to Si lattice constant (*i.e.*, pseudomorphic

growth), (2) partially *elastically* relaxed *via* Stranski-Krastanov growth (strain driven surface roughening or coherent-nanocrystal formation), or (3) partially or fully *plastically* relaxed *via* dislocation formation. Schematic diagrams of these three states are show in Figure 1-12. I will focus on plastic strain relaxation via misfit dislocation formation in this section.

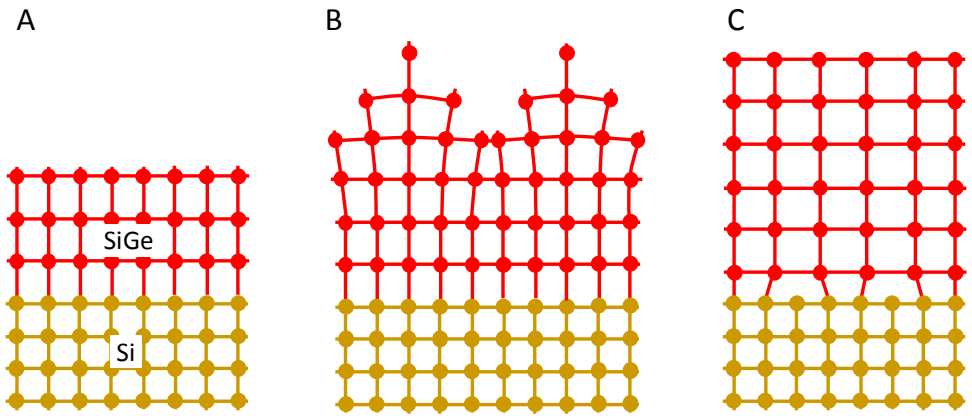

Figure 1-12. Strain states and relaxation mechanisms for SiGe films grown on relaxed Si substrates. (A) Pseudomorphic layer-by-layer growth. The SiGe is strained to the Si in-plane lattice constant. (B) Stranski-Krastanov growth: layer-by-layer followed by three-dimensional-nanocrystal growth. The three-dimensional growth allows some elastic strain relaxation near the top of the islands. (C) Plastic relaxation of mismatch strain via misfit dislocations at the growth interface.

In general, SiGe grown on Si relaxes via misfit dislocation formation at the film/substrate interface. The misfit segments relax a portion of the mismatch strain. Since dislocations cannot begin or end within a crystal, the misfit segments must propagate to the edge of the crystal or create threading arms that allow the dislocation to open to the surface of the film. The latter case is more favorable as the film surface is most often the closest free interface. Each misfit segment has two threading arms that reach the surface of the film. The misfit dislocations in the SiGe/Si system are Shockley partial dislocations ($\mathbf{b} = {}^{1}/_{6}\langle 112\rangle$) that form along {111} glide planes. A partial dislocation is the displacement of the crystal lattice by less than a lattice

translation vector and thus results in the formation of a stacking fault. There are two types of Shockley partial dislocations, 30° and 90°, categorized by the angle between the Burgers vector, **b,** and the line direction created on the surface, **u** (intersection of the {111} glide plane with the surface). Typically, relaxation of SiGe takes place by consecutive glide of 30° and 90° partial dislocations. The order of glide is determined by the substrate orientation and sign of strain (compressive *vs*. tensile). The favored, or leading, dislocation (30° or 90°) avoids creating a high-energy stacking fault between the two partial dislocations. If the stacking sequence is ABCABC, the stacking fault ABC|BCA is energetically favored over ABC|CAB. In compressive films grown on (001)-oriented diamond-lattice substrates [SiGe on Si(001)] or tensile films grown on (110)- or (111)-oriented diamond-lattice substrates [Si on SiGe(110) or SiGe(111)] the 30° partial leads, and in tensile films grown on (001)-oriented diamond substrates [Si on SiGe(001)] or compressive films grown on (110)- or (111)-oriented diamond substrates [SiGe on Si(110) or Si(111)] the 90° partial leads [24].

If the 30° and 90° partials are narrowly dissociated or undissociated (glide separated by less than a few atomic layers), a perfect dislocation results (**b** = ½<110>): displacement of the lattice by a full lattice translation vector in a {111} plane. A perfect dislocation in the diamond cubic system is often called a 60° dislocation (corresponding to the angle between **b** and **u**). The equilibrium distance between partial dislocations (and therefore whether the misfit dislocation can be considered “perfect” or not) is set by the resolved lattice mismatch stress acting on the dislocation and the energy cost associated with the stacking fault created

between the two partial dislocations. The resolved stress, σ_a, acting on a misfit dislocation with Burgers vector **b** is given by the Schmid factor, S:

$$\sigma_a = \sigma_o S = \sigma_o \cos\lambda \cos\phi, \tag{1-2}$$

where λ is the angle between **b** and the direction normal to the dislocation line direction **u**, ϕ is the angle between the glide plane and the interface normal, and σ_o is the lattice mismatch stress, given by:

$$\sigma_o = 2G\varepsilon_m \frac{1+\upsilon}{1-\upsilon}, \tag{1-3}$$

where G is the shear modulus and v is Poisson's ratio [26]. The Schmid factor is determined only by the crystalline orientation of the substrate and is nonzero for misfit dislocations that glide along planes that are inclined with respect to the surface. In general $S_{90} > S_{60} > S_{30}$, meaning that 90° partial dislocations have the most resolved mismatch stress, and therefore, relieve the most mismatch stress in the film. This also means that when the 30° partial dislocation leads [SiGe grown on Si(001)] the trailing 90° partial follows closely because it experiences a larger resolved stress; the closely spaced or undissociated partials result in a perfect 60° misfit dislocation. Conversely, when the 90° partial leads [SiGe grown on Si(111) or Si(110)] the larger resolved stress leads to dissociated partial dislocations, leaving stacking faults in the plastically relaxed films. No dislocation glide occurs on planes that are perpendicular to the surface (as is the case for two of the four {111} planes in (110)-oriented films, see Figure 1-13] because there is no resolved stress acting on dislocations in those planes. Lack of dislocation glide in all {111} planes can result in anisotropic in-plane plastic relaxation in strained films [27-29].

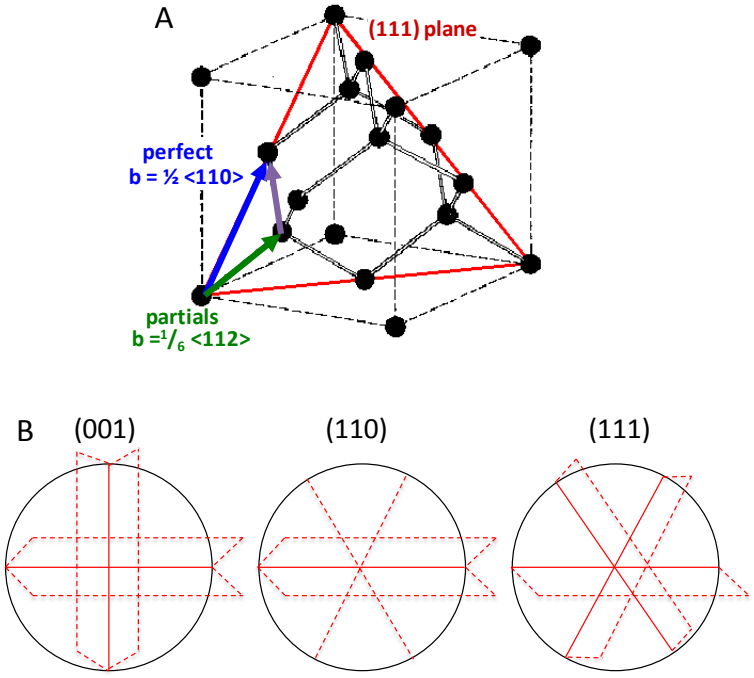

Figure 1-13. (A) Diamond cubic crystal structure with (111) glide plane (red), 30° (green), 60° (blue), and 90° (purple) dislocation Burgers b vectors highlighted. (B) Schematic illustration of {111} glide planes on (001)-, (110)-, and (111)-oriented surfaces. The solid lines show the line direction of dislocations in a given {111} plane (dashed lines): the intersection of the glide planes with the surface [after 25].

1.3.4 Critical thickness

The thickness of a strained epitaxial film must be considered to determine the state of plastic relaxation of the film. The thickness at which the film starts to form misfit dislocations to relax the strain is the critical thickness. Films thinner than the critical thickness will accommodate strain elastically (Figure 1-12A). The concept of critical thickness is most easily understood in the framework of Matthews and Blakeslee (MB) [30], i.e., under equilibrium

conditions. The MB model derives the critical thickness in terms of forces on an existing threading dislocation in the film/substrate with isotropic elastic theory (Figure 1-14).

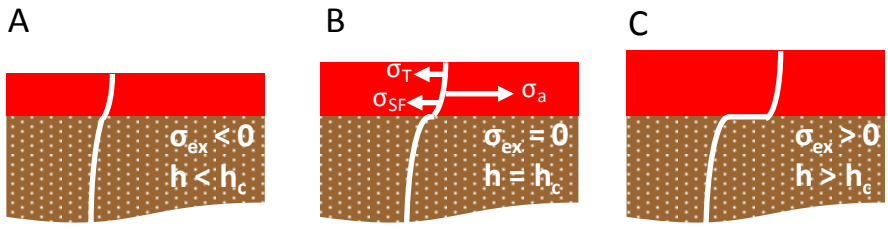

Figure 1-14. Schematic illustration of the equilibrium model for critical thickness [after 26]. (A) An existing threading dislocation will propagate through the film without forming a misfit segment when the excess stress on the threading arm in the film is less than zero, $h < h_c$. (B) A misfit segment will start to form when the excess force on the threading arm in the film equals zero ($h = h_c$). (C) The misfit segment will propagate along the interface to relieve stress in the film when the excess stress is greater than zero, $h > h_c$.

In order for the threading dislocation to propagate along the film/substrate interface and create a misfit dislocation there has to be an excess force on the threading arm within in the film. The excess stress on the threading arm in the film is determined by: (1) the resolved lattice mismatch stress, σ_a, which drives misfit dislocation formation to relieve strain in the film, (2) the dislocation line tension, σ_T, created by the formation of the misfit segment, and (3) a restoring force due to the energy cost of creating a stacking fault, σ_{SF} (= 0 for perfect dislocations). The net or excess stress on the threading dislocation in the film is [26]:

$$\begin{aligned}\sigma_{ex} &= \sigma_a - \sigma_T - \sigma_{SF} \\ &= \left(2GS\varepsilon_m \frac{1+\upsilon}{1-\upsilon}\right) - \left[Gb\cos\phi \frac{1-\upsilon\cos^2\theta}{4\pi h(1-\upsilon)} \ln\left(\frac{\alpha h}{b}\right)\right] - \left(\frac{\gamma}{b}\right)\end{aligned} \qquad (1\text{-}4).$$

The resolved lattice mismatch stress was defined in the previous section. Here *b* is the magnitude of the Burgers vector, θ is the angle between **b** and **u**, *h* is the thickness of the film, *α* is a factor added to account for the dislocation core energy (α ≈ 2 for SiGe/Si and can range from 1-4 for semiconductors), and *γ* is the stacking fault energy (γ_{Si} = 65 mJ/m^2 [31]). The restoring force contribution from formation of a stacking fault was not in the original MB model but was later added to account for the energy needed to create a stacking fault [26]. When the excess stress on the threading arm in the film is less than zero, (h is small) the energy of the system increases with formation of misfit dislocations and therefore it is more energetically favorable for the film to accommodate the mismatch strain elastically (Figure 1-12A). The thickness at which the excess stress equals zero is the critical thickness (Figure 1-14B), or the thickness at which misfit dislocations start to propagate along the film/substrate interface because the energy in the system decreases with misfit dislocation formation. The equilibrium critical thickness for SiGe grown on Si(001) is shown as the solid line in Figure 1-15A; this result assumes any misfit segments are 60° perfect dislocations such that γ = 0.

In reality, there are very few dislocations in the initial Si substrate and extra energy is needed to nucleate the dislocations at the Si substrate/SiGe film interface. This nucleation energy is unknown, but the critical thickness can be determined experimentally: this is called the *kinetic* critical thickness because it is controlled by kinetic factors such as growth rate and temperature [32]. Several models have been developed for the kinetic critical thickness [32-34], but experimental results seem to be most reliable, as growth conditions can significantly alter the kinetic critical thickness. It is important to note that any experimentally determined critical

thickness is limited by the technique used to detect dislocations or strain relaxation [35]. Figure 1-15A shows the kinetic critical thickness measured for SiGe films grown on Si at 550°C with MBE.

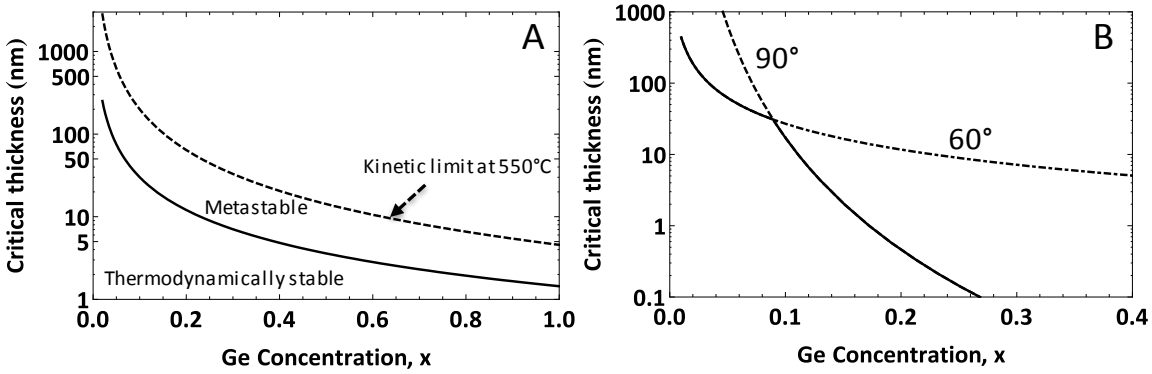

Figure 1-15. Critical thickness for SiGe grown on Si. (A) SiGe on Si(001). The solid line defines the critical thickness as derived by the MB model [30]. The dashed line is the kinetic critical thickness measured for SiGe alloy grown on Si with MBE at 550°C [32]. (B) SiGe on Si(110). For low mismatch strains (low Ge concentrations) the formation of 60° perfect dislocations is preferred. It is not until higher mismatch strains that the 90° partials dissociate and nucleate separate from the 30° partials, forming stacking faults in the film.

The critical thickness for SiGe grown on Si(110) substrates is also shown in Figure 1-15B. There are two lines, one for relaxation via 60° perfect dislocations and one for relaxation via 90° partial dislocations. As mentioned previously, for SiGe grown on Si(110) or Si(111) the 90° partial leads the 30° partial and the two are often dissociated. The larger resolved lattice mismatch stress on the 90° partial leads to a greater driving force for formation (σ_a), however, there is now a restoring force associated with the stacking fault (σ_{SF}) that opposes formation of the dislocation. For low mismatch strains (low Ge concentrations) it is energetically favorable for 60° perfect dislocations to form, and at higher mismatch strains 90° partial dislocations

form. The critical thickness of SiGe grown on Si(110) is determined by the lowest predicted critical thickness (solid line in Figure 1-15B). The intersection of the two critical thickness plots is very sensitive to the stacking fault energy [31].

1.3.5 Growth on compliant substrates

A compliant substrate is one that will deform or accommodate some the mismatch strain in the film/substrate system. Instead of the epitaxial film accommodating all of the mismatch strain in the system, the substrate will accommodate some of the strain as the film is growing. This lowers the magnitude of the strain in the epitaxial layer and thus increases the critical thickness for dislocation formation. Consider, for instance, a very thin freestanding Si substrate (< 1000nm thick). Fabrication methods for this type of substrate are outlined in Chapter 3. When SiGe is grown on the compliant Si substrate some of the compressive strain in the SiGe is transferred as tensile strain to the Si substrate (see Chapter 2 for details about elastic strain sharing). The mismatch strain in the system is unchanged, but the strain in the SiGe is reduced. Figure 1-16A shows the strain in a $Si_{0.6}Ge_{0.4}$ layer as a function of alloy thickness grown on different-thickness compliant Si substrates. The magnitude of strain in the SiGe layer decreases with increasing alloy thickness and with decreasing Si layer thickness. This is a direct result of strain sharing with the compliant Si substrate: as the SiGe layer thickness increases more of the strain is transferred to the 'substrate', rather than all of it remaining in the SiGe epitaxial layer. This strain sharing increases the kinetic critical thickness of the alloy. Figure 1-16B shows the expected increase in critical thickness for alloys grown on a 10-, 100-, and 1000-nm thick compliant Si substrates. The inset shows the percentage increase in critical

thickness over the kinetic critical thickness of SiGe grown on bulk Si at 550°C in MBE (Figure 1-16A). The critical thickness increases ~3% for a 50% alloy when grown on a 1000-nm thick SiNM, but increases by a factor of 5 when grown on a 10-nm thick SiNM. This concept has been experimentally shown by Mooney et al. [36], who grew SiGe on both sides of a freestanding Si pedestal (supported in its center by a post of SiO_2). The total SiGe thickness (= top and bottom layer thicknesses) was thicker than the kinetic critical thickness for dislocation formation while the SiGe remained coherent with the freestanding Si.

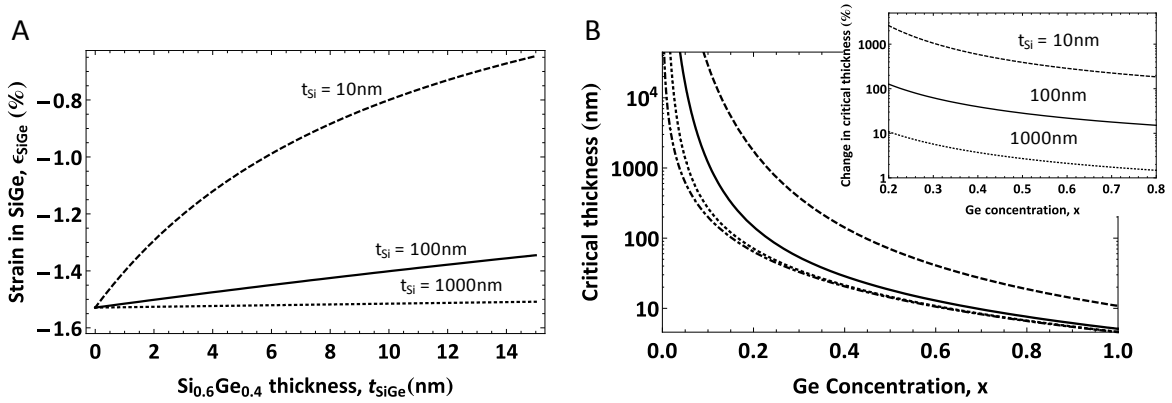

Figure 1-16. (A) Strain in a $Si_{0.6}Ge_{0.4}$ layer grown on a 10-nm (dashed), 100-nm (solid), and 1000-nm thick (dotted) freestanding compliant Si substrate as a function of alloy thickness. Initially the strain in the alloy will equal the mismatch strain because the alloy will be much thinner (few atomic layers) than the compliant Si substrate. As the SiGe gets thicker the strain will be shared between the two layers, resulting in a reduction of strain in the alloy. (B) The measured critical thickness for $Si_{1-x}Ge_x$ layers grown at 550°C in MBE on a rigid Si substrate (dot-dashed) [32]. The calculated critical thickness of SiGe alloys grown on 1000-nm (dotted), 100-nm (solid) and 10-nm (dashed) thick compliant substrates assuming dislocation formation initiates at the SiGe/Si interface. The inset plots the change in critical thickness in percentage from alloy grown on a rigid substrate to alloy grown on various thickness compliant substrates.

The above only considers a reduction in the mismatch film stress (σ_a) with growth on compliant substrates, which leads to an increase in the critical thickness. There can also be a change in the dislocation line tension (σ_T) when growing strained films on compliant substrates. The thinness of the substrate may allow dislocations to be "injected" into the substrate to relieve strain in the film. This happens because the dislocation line tension is reduced at the free surface. Ideally the line tension approaches zero for truly freestanding compliant substrates, resulting in a film critical thickness of zero (for formation of perfect dislocations). There is some energy associated with injecting dislocations into the unstrained substrate, which adds a term to the excess stress equation (Eq. 1-4) that is dependent on the thickness of the compliant substrate. The reduction in the dislocation line tension and the stress injected into the substrate with dislocation formation will be dependent on the exact configuration of the compliant substrate: the thickness, composition, and interface quality. The balance between the reduction in line tension and increase in stress in the substrate will determine the new critical thickness. There are many variations on how compliant substrates may affect the critical thickness of strained films [37-39], but as truly compliant substrates are difficult to realize very few experimental results exist [36, 40].

1.3.6 Plastically relaxed SiGe substrates

Up to now, I have focused on strained SiGe epitaxial growth on Si substrates but, as will be seen in section 1.4, growing strained Si on relaxed SiGe is important for altering the electronic properties of Si. Considering the issues with creating single-crystalline bulk SiGe (section 1.2.2), epitaxial growth is used to make relaxed SiGe substrates for growth of strained

Si. This means that the SiGe is relaxed via misfit dislocation formation and that the resulting density of threading dislocations that reach the surface of the SiGe (and consequently the strained Si layer) is a function of the number of misfit dislocations needed to relax the film. For typical electrical devices, the threading dislocation density (TDD) must be less than $10^5/cm^2$; this TDD does not significantly alter the electrical properties of the material for bulk-like (> 50nm) devices. For highly sensitive optical and quantum electronic devices the TDD should approach that of electronic-grade semiconductor wafers (< $10^4/cm^2$) for optimum performance (see section 1.4). The misfit dislocation density needed to relax a strained film is directly proportional to the mismatch strain; high-Ge-concentration alloys (ε_m ~1%) grown on Si require a misfit dislocation every ~20nm to relax the mismatch strain fully. High misfit dislocation densities mean that misfit segments cannot propagate very far before intersecting another segment. A threading dislocation results at the intersection of misfit segments, thus the higher the density of intersecting misfit dislocations the higher the TDD. Several techniques have been developed to reduce the TDD in plastically relaxed SiGe films grown on Si. I will briefly describe three such techniques here: (1) graded buffer layer substrates, (2) aspect ratio trapping, and (3) the Ge condensation technique. Similar methods have also been implemented in the III-V semiconductor system with comparable results.

Graded buffer layer substrates

The first method is growth of step graded (i.e., multiple layers with increasing Ge concentration) buffer layers of SiGe all grown past their kinetic critical thickness for dislocation formation, such that each sequential alloy layer is fully relaxed via misfit dislocations. The slow

grading of Ge composition in the alloy layers results in the misfit dislocations being distributed through the thickness of the graded layers. There are fewer misfit segments at each growth interface, thus allowing them to propagate further before intersecting another dislocation. This limits the number of threading arms that can reach the top relaxed SiGe layer and hence the strained Si cap layer [41]. Using grading rates ~10%/μm, TDDs ~10^6/cm^2 are common. The grading rate and desired Ge composition determine the required thickness for the graded buffer layer substrates (i.e., 30% relaxed alloy requires a 3-μm thick buffer layer). Often, an additional 1-2μm of constant-composition alloy is grown on top of the graded region to create a more uniform substrate before growing the desired heterostructure. The graded region, together with the constant-composition region, can be several microns thick and take a full day to grow.

Relaxed SiGe fabricated with the graded buffer layer technique suffers from dislocation pile-ups, creating a very rough surface called crosshatch, local variations in the strain relaxation of the SiGe alloy, and variation in the crystalline tilt (mosaic structure). The dislocation pile-ups are a result of the nucleation mechanism for new dislocations: a modified Frank-Read mechanism (MFR) [41]. New dislocations tend to form at the intersection between two orthogonal misfit segments with the same Burgers vector. This pushes threading dislocations into the substrate (or lower layers of the graded heterostructure), thus creating rough interfaces. Because new dislocations form near existing dislocations (creating pile-ups), relaxation tends to be non-uniform over the sample area. The pile-ups also lead to a small degree of tilt variation over the sample area often referred to as mosaic tilt because of the

block-like structure created [42]. Figure 1-17 shows examples of some of the inhomogeneities in relaxed graded SiGe. While the surface roughness can be chemical-mechanically polished away [43], the mosaic tilt and strain variations remain.

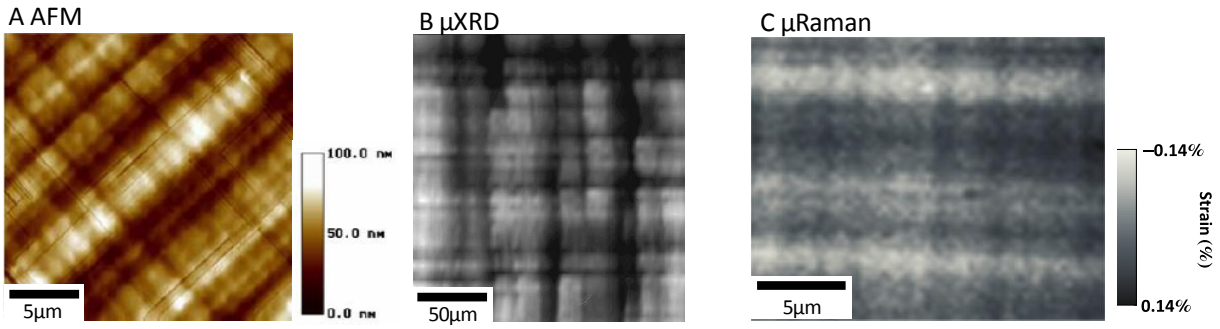

Figure 1-17. Inhomogeneities in relaxed graded $Si_{0.7}Ge_{0.3}$. (A) AFM of crosshatch surface roughness [44]. (B) X-ray microdiffraction showing mosaic tilt. The light regions are set at a (004) Bragg condition and the dark regions are tilted by up to 0.2° from the light regions [45]. (C) Micro-Raman map of strain variation in the top SiGe layer.

Aspect ratio trapping

The second method, referred to as aspect ratio trapping, involves growth of SiGe in small areas of a patterned SiO_2/Si substrate. Small areas (areas range from a few nanometers to few microns in size) of the Si substrate are exposed via patterning and etching of the SiO_2 capping layer. The pattern forms high-aspect-ratio trenches and the SiGe alloy grows on the Si at the bottom of these trenches. The dislocations formed at the SiGe/Si interface thread through the film as described above, but the threads can terminate at the sidewalls of the SiO_2/SiGe interface (Figure 1-18A). This leaves dislocation-free material above the trench for device fabrication. The drawback to this technique is that the SiGe layer is not formed over a continuous wafer, but in small blocks. Epitaxial lateral overgrowth has been used to form larger

areas for device fabrication, however, crystalline defects are often formed where two growth fronts meet [46].

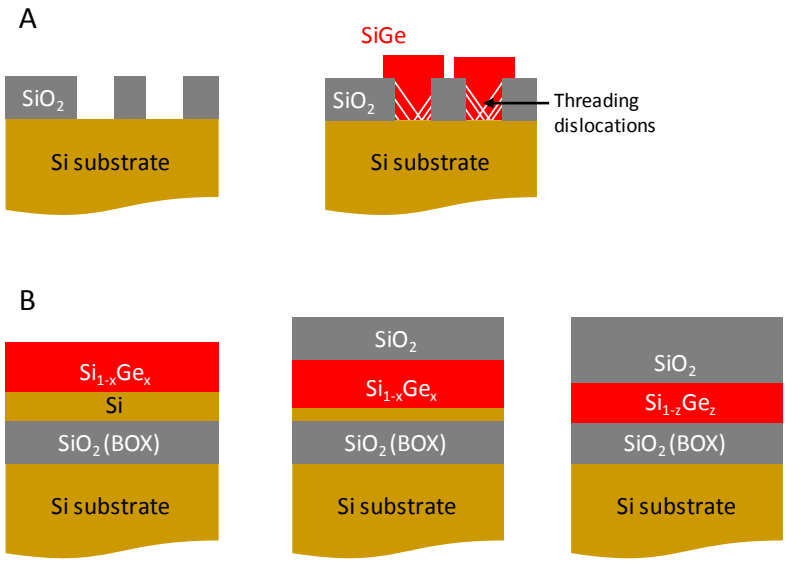

Figure 1-18. (A) Aspect ratio trapping. Small areas are patterned and etched into a SiO_2 film (or some other mask layer) on a Si substrate. SiGe is epitaxially grown on the exposed portions of the Si. Threading dislocations are trapped at the SiGe/SiO_2 sidewall interfaces leaving dislocation-free material above. (B) Ge condensation technique. A pseudomorphic $Si_{1-x}Ge_x$ film is grown on an SOI substrate. The heterostructure is oxidized: the Si is preferentially oxidized while the Ge diffuses into the Si template layer of the SOI. The final composition and thickness of the new $Si_{1-z}Ge_z$ is set by the oxidation time (where z > x). The $Si_{1-z}Ge_z$ plastically relaxes during the high-temperature oxidation.

Ge condensation

The last approach I will discuss, referred to as Ge condensation [47, 48], involves growth of a low-Ge-concentration SiGe alloy layer on a silicon-on-insulator (SOI) substrate followed by thermal oxidation. The initial SiGe layer is grown below the critical thickness for dislocation formation. During oxidation of the SiGe alloy, the Si preferentially oxidizes, driving the Ge farther into the film to create a higher-concentration, thinner alloy layer. The high

temperatures in the oxidation step encourage strain relaxation of the alloy via misfit dislocations. It is thought that the high-temperature step will cause dislocations to distribute uniformly over the sample resulting in uniform strain relaxation. The very thin layers and high TDDs do not make these substrates ideal for device processing.

1.4 Changes in materials properties with strain

Strain in a material changes the lattice constant and crystalline symmetry, and thereby creates a material with new properties relative to the unstrained, but chemically identical, material. The ability to alter the strain (its magnitude, direction, extent, periodicity, symmetry, and nature) allows tunability of these new properties. In Si and SiGe, the electronic band structure [49, 50], electronic transport [4, 51], optoelectronic properties [52, 53], phonon structure [54], and kinetics and thermodynamics of atom motion and structure [55] are all affected by strain. Here I will review how strain engineering in Si and SiGe alters a few of these properties and some negative effects of plastic strain relaxation in such heterostructures.

1.4.1 Electronic band structure

It is common practice to apply strain to Si and SiGe to alter the electronic properties of the material; almost all current CMOS technologies include strained Si to enhance the operating speed of devices. The enhancement in electronic performance is a result of changes in the electronic band structure of Si and Ge (Figure 1-2). When the crystalline symmetry of Si is changed with strain, the six-fold degenerate conduction band minimum and two-fold degenerate valence band maximum spilt and shift in energy. The extent of the energy splitting

and direction of the energy shift is dependent on the magnitude, direction, and symmetry of the applied strain [51, 52, 56]. I will limit my discussion to biaxially strained Si induced by epitaxial lattice mismatch. The four in-plane conduction band valleys shift up in energy and the two out-of-plane valleys shift down in energy with biaxial tensile strain. The energy split limits intervalley electron scattering, thus increasing the electron mobility. The light-hole and heavy-hole states of the valence band also split in energy, reducing scattering and thereby in principle increasing hole mobility. The valence band states, however, also warp (change shape) with strain, resulting in a change in the hole effective mass [40, 56]. For small biaxial tensile strains, the net result of the change in effective mass and splitting of the valence band is a reduction in the hole mobility (Figure 1-19C [57]). At higher strains, the net effect is an increase in hole mobility.

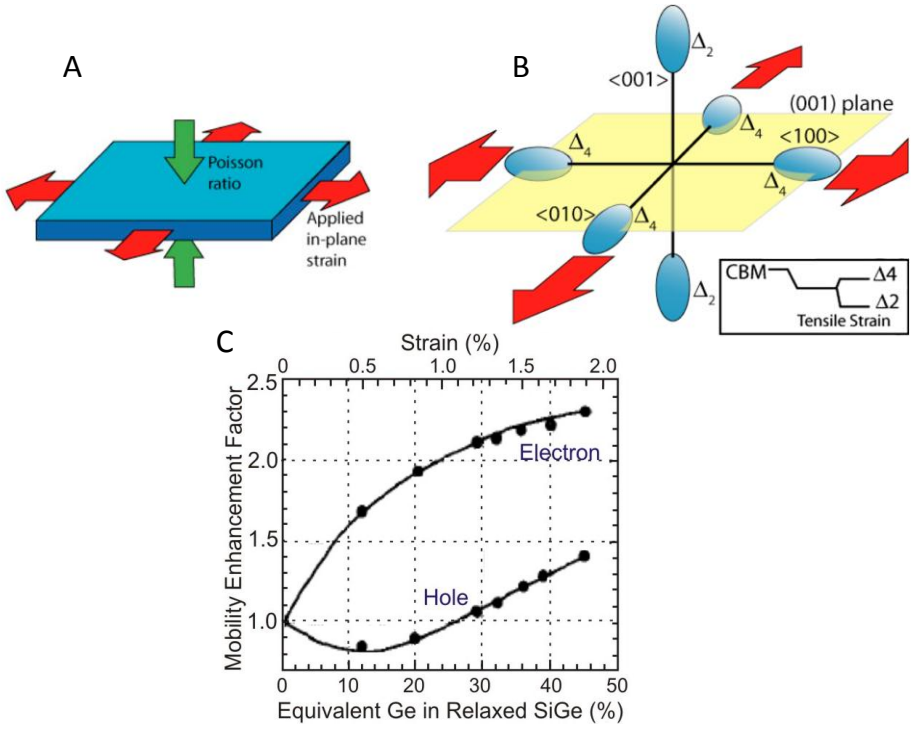

Figure 1-19. (A) Biaxial tensile strain in Si causes the in-plane lattice constant to increase and the out-of-plane lattice constant to decrease. (B) These lattice constant changes result in a splitting of the degeneracy of the conductions band valleys. The in-plane valleys move to a higher energy and the out-of-plane valleys move to a lower energy. The valence band maximum also splits. Figures A and B are reprinted from [37]. (C) The charge carrier mobility enhancement as a function of biaxial tensile strain in Si [57].

In addition to altering the charge carrier mobility in Si and SiGe, strain engineering will change the band gap and band alignment in heterostructures. The desired result is charge carrier confinement in a single layer to enhance electronic device performance. The SiGe band gap for relaxed and biaxially compressively strained alloys was shown in Figure 1-2 and the biaxially strained Si band gap is shown in Figure 1-20C. For Si/SiGe heterostructures the band offsets will shift in the conduction band and valence band depending on the relative strain state of the layers; the Si/SiGe interface will have a type I band alignment when SiGe is compressively

strained with respect to Si (Figure 1-20A) and a type II band alignment when Si is tensilely strained with respect to SiGe (Figure 1-20B).

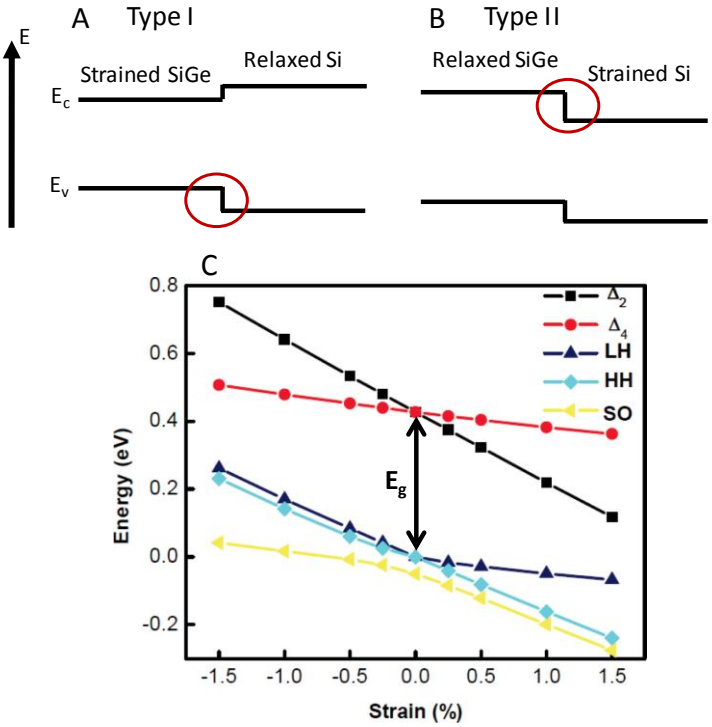

Figure 1-20. Band alignments in Si/SiGe heterostructures for (A) compressively strained SiGe grown on relaxed Si (type 1 band alignment) and (B) tensilely strained Si grown on relaxed SiGe (type II band alignment). In (A) the majority of the band offset is in the valence band, and in (B) the majority of the band offset is in the conduction band. (C) Energy shifts and splitting of the conduction band minimum and valence band maximum in biaxially strained Si [56].

Two examples where strain engineering at Si/SiGe interfaces is important are heterojunction bipolar transistors (HBTs) and two-dimensional electron gases (2DEGs). In HBTs, the band offset between the compressively strained SiGe and the relaxed Si decreases the potential barrier between the Si emitter and the SiGe base, thus increasing the current gain of the device (Figure 1-21A). In 2DEGs, a positive gate bias pulls the conduction band minimum

below the Fermi level to create a 2D sheet of electrons. The electric potential confines electrons near the strained Si/SiGe interface to reduce scattering, leading to very high electron mobilities [58] (Figure 1-21B). The latter is used to make single-electron devices for the development of quantum computing [59, 60].

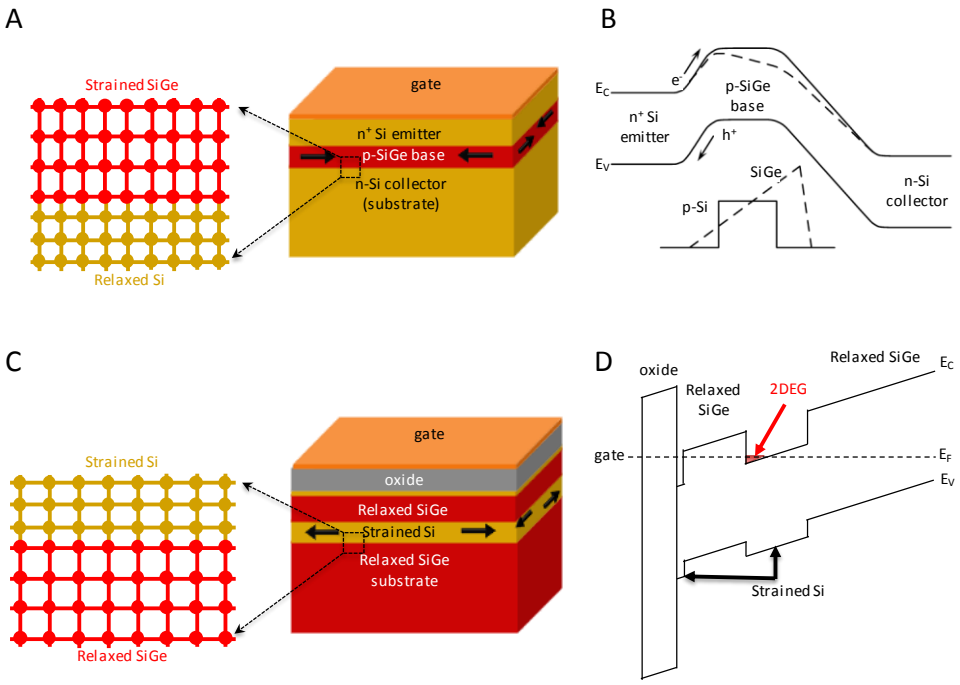

Figure 1-21. Examples of strain engineering in Si/SiGe heterostructures. (A) HBT heterostructure with relaxed Si in the emitter and collector regions and compressively strained SiGe in the base. (B) The energy band diagram for an HBT [61]. The SiGe base reduces the potential barrier (dashed line) to inject electrons into the base. A graded SiGe base (increasing Ge composition) creates an accelerating potential for electrons, thus increasing the current gain of the device. (C) Tensilely strained Si quantum well 2DEG heterostructure. (D) A gate bias is applied to pull the conduction band minimum of the confined strained Si below the Fermi level of the heterostructure, thus creating a 2DEG in the strained-Si quantum well.

1.4.2 Optical properties

Si and SiGe are not typically thought of as optical materials as they have an indirect band gap and do not emit light efficiently. It is advantageous to make optical devices from Si and SiGe to integrate such devices into mainstream Si microelectronics. The application of strain and proper heterostructure design can change optical properties such as absorption and birefringence and aid in the design of light emitters, detectors, and waveguides in Group IV devices. For instance, by combining materials with varying band gaps, a wider range of wavelengths from the solar spectrum can be absorbed to make highly efficient solar cells [62]; the detectable wavelengths of photodetectors can be tuned by altering the band gap with strain; and there has even been research toward making a Group IV quantum cascade laser by implementing heterostructure strain engineering [63].

Changes in the optical properties of Si and SiGe have proven useful in the development of Group IV optical components. The application of anisotropic strain in Si breaks the crystalline symmetry to induce a linear electro-optic effect in Si [53]: an effect prohibited by the inversion symmetry of bulk Si crystals. When the inversion symmetry of the cubic Si lattice is distorted with anisotropic strain, the index of refraction varies linearly with an externally applied electric field. This effect is useful to fabricate amplitude modulators in Si. Birefringence in Si and SiGe can also be tuned with strain to solve phase matching between optical devices [64, 65]. The ability to tune strain dynamically (and therefore the index of refraction) in Si alleviates strict tolerances on waveguide fabrication.

1.4.3 Adverse effects of crystalline defects on materials properties

When utilizing strain-induced changes in materials properties it is important to consider how crystalline defects associated with strain relaxation may affect device operation. In early studies of the influence of dislocations in single-crystalline semiconductors on electrical and optical properties, the resistivity of Ge increased, the lifetime of photo-generated carriers decreased, and lightly doped n-type Ge turned p-type all with increasing dislocation density [9]. Today it is known that impurities and native point defects play an important role in creating dislocations that can change the optical and electrical properties in semiconductors. Dislocations, by definition, locally alter the crystalline symmetry and disrupt the local bonds in the crystal. The result is a series of dangling bonds and an elastic strain field around the dislocation core, both of which can create generation and recombination states (donor and acceptor trap states) within the band gap of semiconductors. The dangling bonds often getter impurities and/or majority charge carriers, creating trap states within the band gap, rendering dopant atoms electrically inactive, or generating a locally charged region that can scatter minority carriers. The trap states within the band gap change the operation of most semiconductor devices, creating large noise currents, and can ultimately destroy the intended operation. In optical devices, the trap states can change the absorption and luminescence wavelengths of the materials, but often create non-radiative recombination states. Details of how dislocations (and other crystalline defects) change the electrical and optical properties of semiconductors can be studied with photoluminescence, optical absorption, deep level transient spectroscopy (DLTS), and electron spin resonance (ESR) to name a few [9]. The

structural characteristics of dislocations in crystalline materials in general have been studied with transmission electron microscopy (TEM), [66] and specifically, in Si-based systems with low-energy electron microscopy (LEEM) [37, 67].

For most applications there is a maximum allowed dislocation density, below which device performance is not significantly altered. The threshold is highly application specific. For instance, a common metric for microelectronic-grade Si wafers is $10^4/cm^2$. In high-performance technologies still in development (single-electron quantum qubits), a single dislocation in the device area may significantly alter device operation. Therefore, it is important to monitor the dislocation density when fabricating strained materials. Higher dislocation densities ($>\sim10^4/cm^2$) can be monitored by measuring the strain state of materials (section 1.5). Low dislocation densities ($<\sim10^4/cm^2$) can be detected with techniques like defect etching, x-ray topography, and electron beam induced current (EBIC) imaging [performed in a scanning electron microscope (SEM)] [9].

1.5 Experimental techniques for measuring strain

1.5.1 X-ray diffraction

X-ray diffraction (XRD) is widely used to measure lattice constants and film thicknesses in single-crystalline thin-film heterostructures. Diffraction of x-rays from atomic planes in a crystalline lattice gives a measurement of the plane spacing, d, according to Bragg's law:

$$2d\sin\theta = \lambda \tag{1-5}$$

where θ is half of the diffraction angle of the x-rays and λ is the wavelength. For planes parallel to the surface, the incident x-ray angle is equal to half of the diffracted x-ray angle (Figure 1-22A); these are called on-axis reflections. To measure atomic spacing for planes that are not parallel to the surface, the incident angle must be offset by the tilt angle of the planes (Figure 1-22B); these are called off-axis reflections. For thin films (t < 500nm), the x-rays will also diffract off of the surfaces and interfaces of the film. The interference of such diffraction results in thickness fringes, the presence of which indicates smooth, coherent interfaces. For multilayer heterostructures the thickness fringes of multiple layers interfere to create a complex diffraction pattern. These are often fit to simulations to extract exact lattice constants and thicknesses of individual layers.

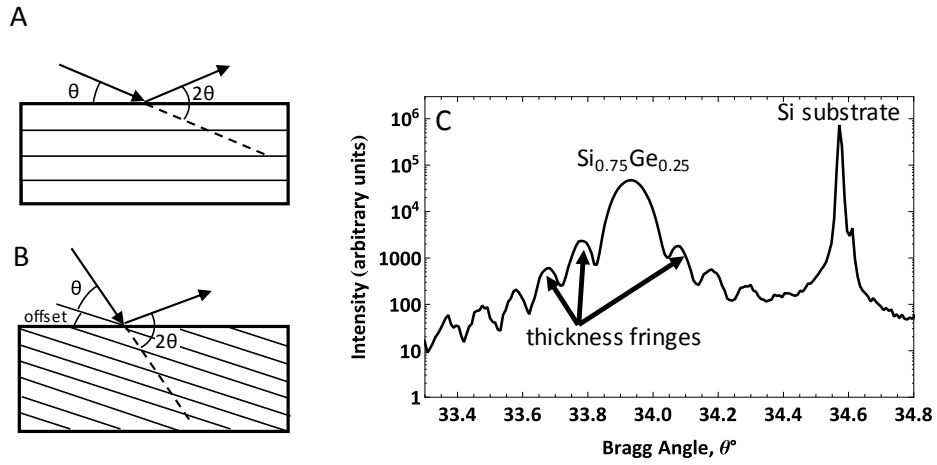

Figure 1-22. (A) Diffraction from atomic planes parallel to the surface: on-axis diffraction. (B) Diffraction from atomic planes not parallel to the surface: off-axis diffraction. (C) θ/2θ line scan around the on-axis reflection for a 52nm SiGe film grown pseudomorphically on a bulk Si substrate. The out-of-plane lattice spacing is larger for the SiGe film (smaller Bragg angle). Assuming that the SiGe layer is compressed to the in-plane Si lattice constant, the difference between the out-of-plane lattice constants of the alloy and the substrate allow me to calculate the SiGe composition.

It is typically more convenient to talk about x-ray diffraction results in reciprocal space ($Å^{-1}$) rather than real space (Å). Taking into account the forbidden reflections due to crystalline symmetry (allowed reflections are determined by the structure factor [68]), a 2-D cut of reciprocal space of the diamond crystalline structure is shown in Figure 1-23A.

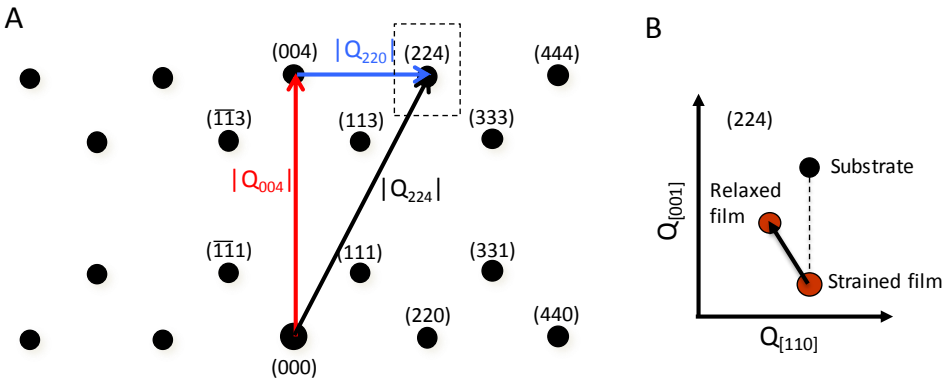

Figure 1-23. (A) Illustration of reciprocal space for the diamond cubic structure containing the [001] and [110] directions. Each diffraction condition corresponds to a unique set of crystallographic planes (labeled). The magnitude of the reciprocal-lattice vector for each reflection is $|Q_{hkl}|$. (B) Representation of a pseudomorphic compressively strained film grown on a substrate near the (224) reflection. The in-plane reciprocal lattice unit is the same for the strained film and the substrate and the out-of-plane lattice constant is larger for the film than for the substrate (decrease in reciprocal-lattice vector), indicating a compressively strained film. If the film plastically relaxes via dislocation formation, the reciprocal-lattice vector for the film decreases in the in-plane direction (increase in real-space lattice) and increases in the out-of-plane direction (decrease in real-space lattice).

Each reflection is labeled with the corresponding lattice planes. For pseudomorphic heterostructures created via epitaxial growth, the in-plane lattice constant of the film and substrate (Figure 1-23B) will be the same while the out-of-plane lattice constant may be larger (compressive films) or smaller (tensile films) than the relaxed lattice constant of the film. In

reciprocal space a larger (smaller) lattice constant is reflected as a smaller (larger) reciprocal lattice unit. When a pseudomorphic film starts to relax plastically the in-plane lattice constant of the film will no longer correspond to that of the substrate; a compressive (tensile) film will expand (contract) towards its relaxed lattice constant.

I use XRD to measure both on-axis and off-axis reflections in SiGe/Si heterostructures with a high-resolution PANalytical X'Pert PRO XRD system. The incident x-rays ($CuK_{\alpha 1}$ radiation used here, $\lambda = 1.5406$Å) are passed through a hybrid monochromator and the diffracted x-rays are detected using a triple-crystal analyzer (resolution = 12 arcseconds). The incident x-ray beam size is ~1mm x 1cm for nearly normal-incidence diffraction conditions. Strain in SiGe/Si thin-film heterostructures is routinely measured to within ±0.05%; however, this value may increase for very thin films (broader peaks in reciprocal space) or samples smaller than the area of the incident x-ray beam (less intense diffraction).

1.5.2 X-ray micro/nanodiffraction

Much like the lab-source x-ray diffraction measurement described above, x-ray microdiffraction (μXRD) is a measurement of lattice constant based on Bragg diffraction. In μXRD, however, the x-ray beam is focused down to a sub-micron spot size. Changes in lattice constant, heterostructure composition, and crystalline tilt can be mapped at the local scale because of the small spot size of the x-rays. Because of the small measurement area, x-rays generated from a highly brilliant synchrotron source are needed to collect useable signals. I used the Hard X-ray Nanoprobe operated by the Center for Nanoscale Materials at the Advanced Photon Source (station 26ID) at Argonne National Laboratory for my μXRD

measurements. The 10keV x-rays (λ = 1.2398Å) are focused down to a ~50nm spot size with a Fresnel zone plate optic. The angular divergence of the x-rays through the zone plate is 0.2367°.

The geometry of the μXRD setup is slightly different from that of a traditional lab source XRD measurement. Instead of having a collimated beam of x-rays incident on the sample at a fixed angle, the focusing of the x-rays in μXRD generates a range of incident angles. The diffracted x-rays are measured on an area detector to collect data from all of the diffracted x-rays at one time. This setup is shown in Figure 1-24.

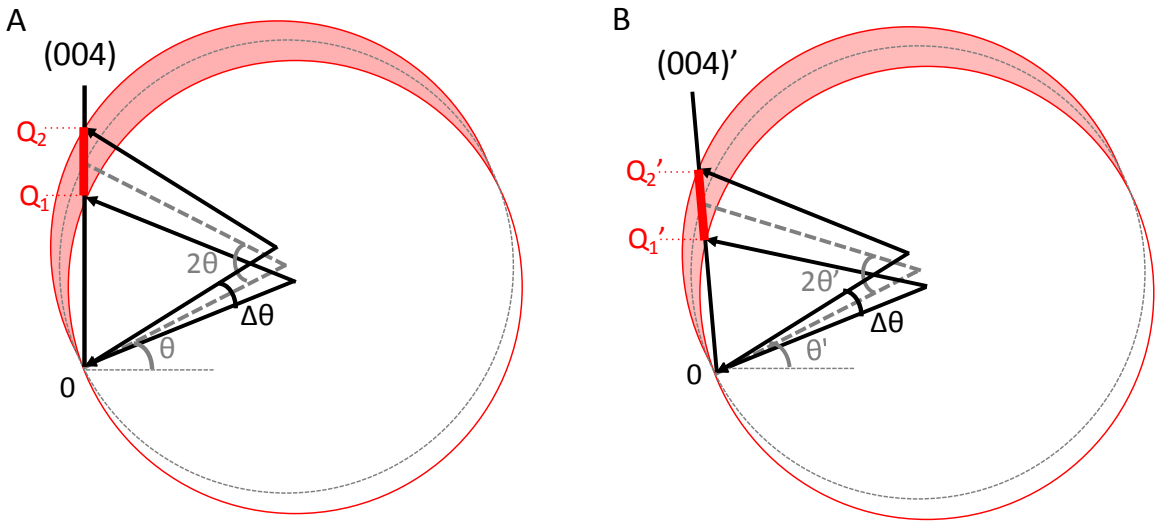

Figure 1-24. Reciprocal-space representation of the geometry of a μXRD setup for diffraction near the (004) reflection of diamond cubic materials. The incident angle θ has an angular divergence of Δθ. This divergence generates a series of Ewald spheres (shaded region) between the two extremes: θ – Δθ and θ + Δθ. (A) For areas of the crystal with the (004) planes perpendicular to the surface normal, the area detector is represented by the thick line between Q_1 and Q_2. (B) For areas of the crystal with the (004) planes tilted with respect to the surface, the effective incident angle has changed to θ' and the detector is measuring between Q_1' and Q_2'.

In a lab source XRD measurement, the single incident angle and detection angle are swept over a range to collect data like that shown in Figure 1-22C. Crystalline tilt is easy to measure with an area detector because the diffracted intensity will move around on the detector corresponding to small tilts in the crystallographic direction. Figure 1-24B shows what happens in reciprocal space for tilt in the scattering plane and what is measured for small tilts of the crystal. Using this idea, 2-D maps of crystalline tilts can be generated (similar to Figure 1-17B). For more details please see Appendix C and Chapter 4.

1.5.3 Micro-Raman spectroscopy

Raman spectroscopy measures the polarizability of molecules, or the tendency of the electron cloud around a molecule to create a charge distribution. Laser light in the UV to optical wavelength ranges is scattered off the sample and the inelastically scattered radiation is collected to measure vibrational modes. The inelastically scattered light is different in energy (from the incident light) by the excitement or de-excitement of a vibrational mode. The light interacts with an electron from a filled state (valence band), exciting it to a higher energy state (to empty state in conduction band) [1 in Figure 1-25]. The excited electron interacts with a phonon, reducing its energy by the amount needed to excite the phonon mode [ω_j] (or increases in energy by the amount needed to de-excite the phonon mode) [2 in Figure 1-25]. The excited electron then recombines with the core hole and emits light at a new frequency, $\omega_s = \omega_i \pm \omega_j$ (3 in Figure 1-25). The scattered radiation one vibration higher in energy is known as anti-Stokes scattering and one vibration lower in energy is known as Stokes scattering. Micro-Raman spectroscopy uses a microscope objective to focus the laser light onto a small area of

the sample. The spot size is set by the numerical aperture and magnification of the objective lens.

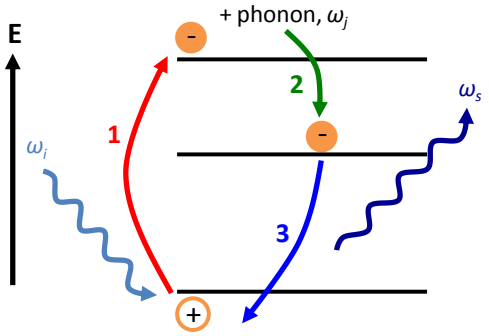

Figure 1-25. Schematic diagram of the Raman scattering process.

In solid crystalline materials the vibrations measured are optical phonon modes. For relaxed Si, there are three degenerate optical phonon modes, however not all modes may be excited in a given Raman measurement. The angle of incidence of the laser with respect to the crystalline orientation of the sample and the polarization of the incident light will determine which phonon modes are excited. When linearly polarized light hits a sample the electrons in the sample are distorted by the electric field. Even when the light is polarized in one direction the electron cloud reacts in all directions, thus changing the polarization of the scattered light. For normal incidence, Equation 1-6 [69] describes selection rules or scattering efficiency for crystalline materials.

$$I = C\sum_j \left| e_i \cdot R_j \cdot e_s \right|^2 \qquad (1\text{-}6)$$

Here C is a constant, $\mathbf{e_i}$ is a vector indicating the incident light polarization, $\mathbf{e_s}$ is the direction of polarization for the scattered light, and $\mathbf{R_j}$ is the Raman tensor for the phonon j. For a diamond

cubic structure, assuming the coordinate system x = [100], y = [010], z = [001], the Raman tensors are [70]:

$$R_x = \begin{pmatrix} 0 & 0 & 0 \\ 0 & 0 & d \\ 0 & d & 0 \end{pmatrix} \quad R_y = \begin{pmatrix} 0 & 0 & d \\ 0 & 0 & 0 \\ d & 0 & 0 \end{pmatrix} \quad R_z = \begin{pmatrix} 0 & d & 0 \\ d & 0 & 0 \\ 0 & 0 & 0 \end{pmatrix} \tag{1-7}$$

Table 1-1 describes the polarization selection rules as calculated by Equation 1-6 for (001)- and (110)-oriented diamond cubic surfaces for normal incidence Raman. For (001)-oriented diamond cubic materials only one phonon mode is measured, which corresponds to the longitudinal optical phonon mode.

Table 1-1. Polarization selection rules for backscattering from (001)- and (110)-oriented surfaces.

Polarization		Visible		
e_i	e_s	R_x	R_y	R_z
(001) surface				
[100]	[100]	--	--	--
[100]	[010]	--	--	x
[-110]	[-110]	--	--	x
[110]	[-110]	--	--	--
(110) surface				
[-110]	[001]	x	x	--
[-110]	[-110]	--	--	x
[001]	[001]	--	--	--

When crystalline materials are strained, the phonon modes shift in energy to reflect a change in the lattice; a higher energy is required to excite phonon modes in compressively strained material and a lower energy is required for tensilely strained material. The change in energy needed to excite each phonon mode is determined by the magnitude and direction of

strain. The change in energy of the three optical phonon modes in strained diamond cubic materials is determined by the eigenvalues (λ) of Equation 1-8 [69].

$$\begin{vmatrix} p\varepsilon_{xx} + q(\varepsilon_{yy} + \varepsilon_{zz}) - \lambda & 2r\varepsilon_{xy} & 2r\varepsilon_{xz} \\ 2r\varepsilon_{xy} & p\varepsilon_{yy} + q(\varepsilon_{xx} + \varepsilon_{zz}) - \lambda & 2r\varepsilon_{yz} \\ 2r\varepsilon_{xz} & 2r\varepsilon_{yz} & p\varepsilon_{zz} + q(\varepsilon_{xx} + \varepsilon_{yy}) - \lambda \end{vmatrix} = 0 \qquad (1\text{-}8)$$

$$\lambda_j = \omega_j^2 - \omega_o^2 \, or \, \Delta\omega = \omega_j - \omega_o = \frac{\lambda_j}{2\omega_o} \qquad (1\text{-}9)$$

Here p, q, and r are material constants known as the phonon deformation potentials, ε_{ij} are the strain tensor components using the same xyz directions as described for the Raman tensors, and ω_o is the unstrained Raman frequency. The phonon deformation potentials for Si, SiGe, and Ge have been determined experimentally [71-74]. There is a wide range of phonon deformation potentials reported in the literature. A discussion of the phonon deformation potentials used in this work is in Appendix B. Table 1-2 lists the shift in Raman frequency for the longitudinal optical (LO) phonon mode in diamond cubic materials under biaxial and uniaxial strain conditions in (001)-oriented materials.

Table 2. Frequency shifts for LO Raman modes for three strain configurations for (001)-oriented diamond cubic materials. Here c_{ij} are the elastic constants from the stiffness tensor, v is Poisson's ratio, and $\tilde{p} = \frac{p}{\omega_o^2}, \tilde{q} = \frac{q}{\omega_o^2}, and \tilde{r} = \frac{r}{\omega_o^2}$ are the normalized phonon deformation potentials.

	Strain tensor	Shift in LO Raman mode
Biaxial strain	$\varepsilon = \begin{pmatrix} \varepsilon_o & 0 & 0 \\ 0 & \varepsilon_o & 0 \\ 0 & 0 & -\frac{2c_{12}}{c_{11}}\varepsilon_o \end{pmatrix}$	$\Delta\omega_{LO} = \omega_o\left(\tilde{q} - \tilde{p}\frac{c_{12}}{c_{11}}\right)\varepsilon_o$
Uniaxial strain [100]	$\varepsilon = \begin{pmatrix} \varepsilon_o & 0 & 0 \\ 0 & -\nu\varepsilon_o & 0 \\ 0 & 0 & -\nu\varepsilon_o \end{pmatrix}$	$\Delta\omega_{LO} = -\frac{\omega_o}{2}\left(\tilde{q}(\nu-1) + \tilde{p}\,\nu\right)\varepsilon_o$
Uniaxial strain [110]	$\varepsilon = \begin{pmatrix} \frac{1}{2}\varepsilon_o(1-\nu) & \varepsilon_o(1+\nu) & 0 \\ \varepsilon_o(1+\nu) & \frac{1}{2}\varepsilon_o(1-\nu) & 0 \\ 0 & 0 & -\nu\varepsilon_o \end{pmatrix}$	$\Delta\omega_{LO} = -\frac{\omega_o}{2}\left(\tilde{q}(\nu-1) + \tilde{p}\,\nu\right)\varepsilon_o$

The wavelength of the incident radiation will determine the sampling depth of the Raman signal and the Raman signal intensity is proportional to the number of vibrational modes excited. Crystalline solids absorb light according to the wavelength; the approximate penetration depth, d_p, of a light with wavelength, λ, in a material with a wavelength dependent absorption coefficient, α, is [69]:

$$d_p = \frac{2.3}{2\alpha} \qquad (1\text{-}10).$$

Using this approximation, the penetration depth for Si and Ge as a function of wavelength is shown in Figure 1-26. The sampling depth is an important parameter when measuring thin-film heterostructures; the wavelength of incident light will determine which part the sample (near surface or averaged through several microns) the Raman signal is scattered from.

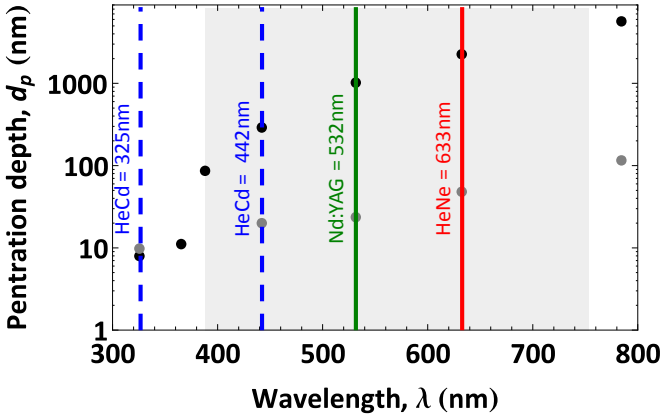

Figure 1-26. Approximate penetration depth of Si (black) and Ge (gray) as a function of wavelength according to Eq. 1-10. I used the absorption coefficient, α, as a function of wavelength at 300K [75, 76]. The shaded region represents visible wavelengths.

1.6 Chapter summary

Lattice mismatched thin-film Si/SiGe heterostructures are important in the strain engineering of Si and SiGe; changing the crystalline symmetry with strain alters the electronic band structure, resulting in changes in the electrical and optical performance of Si and SiGe devices. Strain is incorporated with heteroepitaxial growth, but is limited to thin-film structures because strain-relieving crystalline defects form in bulk-like materials. In high densities, these crystalline defects can alter the electrical and optical responses of the materials by creating trap states within the semiconductor band gap. The crystalline defect densities in plastically strain-relaxed materials can be controlled with various epitaxial growth techniques. The strain state and distribution in Si/SiGe heterostructures is monitored by measuring lattice constants of the materials with XRD or changes in phonon energies with Raman spectroscopy. The properties of strained Si and SiGe heterostructures outlined in this chapter will be used to create elastically strain engineered Si and SiGe nanomembrane materials.

1.7 References

1. J. P. Dismukes, L. Ekstrom, R. J. Pfaff, Lattice Parameter and Density in Germanium-Silicon Alloys, *J. Phys. Chem.* **68** (1964) 3021.

2. J. J. Wortman, R. A. Evans, Young's Modulus, Shear Modulus, and Poisson's Ratio in Silicon and Germanium. *J. Appl. Phys.* **36** (1965) 153-156.

3. http://www.ioffe.ru/SVA/NSM/

4. F. Schäffler, High-Mobility Si and Ge Structures. *Semicond. Sci. Technol.* **12** (1997) 1515-1549.

5. S. A. Campbell, *The Science and Engineering of Microelectronic Fabrication, 2nd Ed*. Oxford University Press: New York (2001).

6. M. Yildiz, A Combined Experimental and Modeling Study for the Growth of Si_xGe_{1-x} Single Crystals by Liquid Phase Diffusion (LPD). PhD Dissertation: Univ. of Victoria (2005).

7. J. Schilz, V. N. Romanenko, Bulk Growth of Silicon-Germanium from Solid Solutions. *J. Mater. Sci.: Mater. Electron*. **6** (1995), *6*, 265-279.

8. http://en.wikipedia.org/wiki/Czochralski_process

9. D. B. Holt, B. G. Yacobi, *Extended Defects in Semiconductors: Electrical Properties, Device Effects and Structures.* Cambridge University Press: Cambridge (2007).

10. N. V. Abrosimov, S. N. Rossolenko, W. Thieme, A. Gerhardt, W. Schröder, Czochralski Growth of Si- and Ge-rich SiGe Single Crystals. *J. Cryst. Growth* **174** (1997) 182-186.

11. I. Yonenaga, Growth and Fundamental Properties of SiGe Bulk Crystals. *J. Cryst. Growth* **275** (2005) 91-98.

12. S. Kou, *Transport Phenomena and Materials Processing*. John Wiley & Sons: New York (1996).

13. H. Miyata, S. Adachi, Y. Ogata, T. Tsuru, Y. Muramatsu, *et al.,* Crystallographic Investigation of Homogeneous SiGe Single Crystals Grown by the Traveling Liquidus-Zone Method. *J. of Cryst. Growth* **303** (2007) 607-611.

14. T. Honda, M. Suezawa, K. Sumino, Growth and Characterization of Bulk Si-Ge Crystals. *Jpn. J. Appl. Phys.* **35** (1996) 5980.

15. M. Yildiz, S. Dost, B. Lent, Growth of Bulk SiGe Single Crystals by Liquid Phase Diffusion. *J. Cryst. Growth* **280** (2005) 151-160.

16. A. Borshchevsky, J.-P. Fleurial, Growth of Heavily-Doped SiGe from Metallic Solutions. *J. Cryst. Growth* **128** (1993) 331-337.

17. J. C. Bean, L. C. Feldman, A. T. Fiory, S. Nakahara, and I. K. Robinson, Ge_xSi_{1-x}/Si Strained-Layer Superlattice Grown by Molecular Beam Epitaxy. *J. Vac. Sci. Technol., A* **2** (1984) 436-440.

18. M. Halbwax, D. Bouchier, V. Yam, D. Débarrie, L. H. Nguyen, *et al.,* Kinetics of Ge Growth at Low Temperature on Si(001) by Ultrahigh Vacuum Chemical Vapor Deposition. *J. Appl. Phys.* **97** (2005) 064907.

19. B. Tillack, P. Zaumseil, "Strained Si and SiGe Epitaxy," in *Silicon Heterostructure Handbook: Materials, Fabrication, Devices, Circuits, and Applications of SiGe and Si Strained-Layer Epitaxy.* Ed. J. D. Cressler, Taylor & Francis: Boca Raton, FL (2006) 33-44.

20. J. C. Bean, "Growth Techniques and Procedures," in *Germanium Silicon: Physics and Materials*, ed. R. Hull, J. C. Bean, Academic Press: San Diego, CA (1999) 1-48.

21. D. W. Greve, "Ge_xSi_{1-x} Epitaxial Growth and Application to Integrated Circuits," in *Thin Films: Advances in Research and Development*, ed. M. H. Francombe, J. L. Vossen, Academic Press: San Diego, CA (1998) 2-82.

22. M. Oehme, E. Kasper, "2.4 MBE Growth Techniques," in *Silicon Heterostructure Handbook: Materials, Fabrication, Devices, Circuits, and Applications of SiGe and Si Strained-Layer Epitaxy.* Ed. J. D. Cressler, Taylor & Francis: Boca Raton, FL (2006) 85-94.

23. M. Hammond, "Silicon Epitaxy by Chemical Vapor Deposition," in *Handbook of Thin-Film Deposition Processes and Techniques – Principles, Methods, Equipment and Applications (2nd Edition)*, ed. K. Seshan, William Andrew Publishing: Norwich, NY (2002) 45-110.

24. E. P. Kvam and R. Hull, Surface Orientation and Stacking Fault Generation in Strained Epitaxial Growth. *J. of Appl. Phys.* **73** (1993) 7407-7411.

25. R. Hull, J. C. Bean, L. Peticolas, Y. H. Xie, Y. F. Hsieh, Growth of Ge_xSi_{1-x}/Si Alloys on Si (100), (110) and (111) Surfaces. *Mat. Res. Soc. Symp. Proc.* **220** (1991) 153-159.

26. R. Hull, "Misfit Strain and Accommodation in SiGe Heterostructures," in *Germanium Silicon: Physics and Materials*, ed. R. Hull, J. C. Bean, Academic Press: San Diego, CA (1999) 102-168.

27. K. Arimoto, J. Yamamamka, K. Nakagawa, K. Sawano, Y. Shiraki, *et al.,* Growth Temperature Dependence of Lattice Structures of SiGe/Graded Buffer Structures Grown on Si(110) Substrates by Gas-Source MBE. *J. Cryst. Growth* **301** (2007) 343-348.

28. V. Destefanis, D. Rouchon, J. M. Hartmann, A. M. Papon, L. Baud, *et al.,* Structural Properties of Tensily Strained Si Layers Grown on SiGe (100), (110), and (111) Virtual Substrates. *J. Appl. Phys.* **106** (2009) 043508.

29. R. Hull, J. C. Bean, L. Peticolas, D. Bahnck, Growth of Ge_xSi_{1-x} Alloys on Si(110) Surfaces. *Appl. Phys. Lett.* **59** (1991) 964.

30. J. W. Matthews, A. E. Blakeslee, Defects in Epitaxial Multilayers: I. Misfit Dislocations. *J. Cryst.*

Growth. **27** (1974) 118–125.

31. R. Hull, J. C. Bean, L. J. Peticolas, D. Bahnck, B. E. Weir, *et al.*, Quantitative Analysis of Strain Relaxation in Ge_xSi_{1-x}/Si(110) Heterostructures and an Accurate Determination of Stacking Fault Energy in Ge_xSi_{1-x} Alloys. *Appl. Phys. Lett.* **61** (1992) 2802.

32. D. C. Houghton, Strain Relaxation Kinetics in $Si_{1-x}Ge_x$/Si Heterostructures. *J. Appl. Phys*. **70** (1991) 2136-2151.

33. R. People, J. C. Bean, Calculation of Critical Thickness versus Lattice Mismatch for Ge_xSi_{1-x}/Si Strained-Layer Heterostructures. *Appl. Phys. Lett.* **47** (1985) 322-324.

34. J. Menendez, Analytical Strain Relaxation Model for $Si_{1-x}Ge_x$/Si Epitaxial Layers. *J. Appl. Phys.* **105** (2009) 063519.

35. I. J. Fritz, Role of Experimental Resolution in Measurements of Critical Layer Thickness for Strained-Layer Epitaxy. *Appl. Phys. Lett.* **51** (1987) 1080-1082.

36. P. M. Mooney, G. M. Cohen, J. O. Chu, C. E. Murray, Elastic Strain Relaxation in Free-Standing SiGe /Si Structures. *Appl. Phys. Lett.* **84** (2004) 1093-1095.

37. C. Euaruksakul, Strain-Band Structure Relationship in Strained Silicon Nanomembranes. PhD Dissertation: Univ. of Wisconsin-Madison (2009).

38. W. A. Jesser, J. H. van der Merwe, P. M. Stoop, Misfit accommodation by compliant substrates. *J. Appl. Phys.* **85** (1999) 2129-2139.

39. J. E. Ayers, Compliant Substrates for Heteroepitaxial Semiconductor Devices: Theory, Experiment, and Current Directions. *J. Electron. Mater.* **37** (2008) 1511-1523.

40. E. M. Rehder, C. K. Inoki, T. S. Kuan, and T. F. Kuech, SiGe Relaxation on Silicon-on-Insulator Substrates: An Experimental and Modeling Study. *J. Appl. Phys.* **94** (2003) 7892-7903.

41. P. M. Mooney, Strain Relaxation and Dislocations in SiGe/Si Structures. *Mater. Sci. Eng.* **R17** (1996) 105-146.

42. P. M. Mooney, F. K. LeGoues, J. Tersoff, J. O. Chu, Nucleation of Dislocations in SiGe Layers Grown on (001)Si. *J. Appl. Phys.* **75** (1994) 3968- 3977.

43. M. T. Currie, S. B. Samavedam, T. A. Langdo, C. W. Leitz, E. A. Fitzgerald, Controlling Threading Dislocation Densities in Ge on Si Graded SiGe Layers and Chemical-Mechanical Polishing. *Appl. Phys. Lett.* **72** (1998) 1718-1720.

44. M. M. Kelly, Elastic Strain Sharing in Silicon/Silicon Germanium Nanomembranes. PhD Dissertation: Univ. of Wisconsin-Madison (2007).

45. P. M. Mooney, J. O. Chu, SiGe Technology: Heteroepitaxy and High-Speed Microelectronics. *Annu.*

Rev. Mater. Sci. **30** (2000) 335-362.

46. J. G. Fiorenza, J.-S. Park, J. M. Hydrick, J. Li, J. Z. Li, *et al.*, Aspect Ratio Trapping: a Unique Technology for Integrating Ge and III-Vs with Silicon CMOS. *ECS Trans.* **33** (2010) 963-976.

47. T. Tezuka, N. Sugiyama, S. Takagi, Fabrication of Strained Si on Ultrathin SiGe-on-Insulator Virtual Substrate with a High-Ge Fraction. *Appl. Phys. Lett*. **79** (2001) 1798-1800.

48. V. Terzieva, L. Souriau, F. Clemente, A. Benedetti, M. Caymax, *et al.,* The Challenges of Ge-Condensation Technique. *ECS Trans*. **3** (2006) 1023-1031.

49. Y. Sun, S. E. Thompson, T. Nishida, Physics of Strain Effects in Semiconductors and Metal-Oxide-Semiconductor Field-Effect Transistors. *J. Appl. Phys.* **101** (2007) 104503.

50. M. V. Fischetti, Z. Ren, P. M. Solomon, M. Yang, K. Rim, Six-Band K•P Calculation of the Hole Mobility in Silicon Inversion Layers: Dependence on Surface Orientation, Strain, and Silicon Thickness. *J. Appl. Phys.* **94** (2005) 1079-1095.

51. M. Chu, Y. Sun, U. Aghoram, S. E. Thompson, Strain: A Solution for Higher Carrier Mobility in Nanoscale MOSFETs. *Annu. Rev. Mater. Res.* **39** (2009) 203-209.

52. Y. Sun, S. E. Thompson, T. Nishida, *Strain Effect in Semiconductors: Theory and Device Applications* Springer: New York, (2010).

53. R. S. Jacobsen, K. N. Andersen, P. I. Borel, J. Fage-Pedersen, L. H. Frandsen, *et al.* Strained Silicon as a New Electro-Optic Material. *Nature* **441** (2006) 199-202.

54. J. Zi, K. Zhang, X. Xie, Phonon Spectra of Strained Si and Ge. Phys. Rev. B 45 (1992) 9447-9450.

55. F. Liu, F. Wu, M. G. Lagally, Effect of Strain on Structure and Morphology of Ultrathin Ge on Si(001). *Chem. Rev.* **97** (1997) 1045-1061.

56. D. Yu, Y. Zhang, F. Liu, First-Principles Study of Electronic Properties of Biaxially Strained Silicon: Effects on Charge Carrier Mobility. *Phys. Rev. B* **78** (2008) 245204.

57. K. Rim, K. Chan, L. Shi, D. Boyd, J. Ott, *et al.*, Fabrication and Mobility Characteristics of Ultra-Thin Strained Si Directly on Insulator (SSDOI) MOSFETs. *Int. El. Devices Meet.* (2003) 3.12.8-3.12.10.

58. T. M. Lu, D. C. Tsui, C.-H. Lee, C. W. Liu, Observation of Two-Dimensional Electron Gas in Si Quantum Well with Mobility of 1.6×10^6 cm^2/Vs. *Appl. Phys. Lett.* **94** (2009) 182102.

59. C. B. Simmons, J. R. Prance, B. J. Van Bael, T. S. Koh, Z. Shi, *et al.*, Tunable Spin Loading of T1 and Silicon Spin Quibit Measured by Single-Shot Readout. *Phys. Rev. Lett*. **106** (2011) 156804.

60. M. A. Eriksson, M. Friesen, S. N. Coppersmith, R. Joint, L. J. Klein, *et al*., Spin-based Quantum Computing in Silicon. *Quantum Inf. Process.* **3** (2004) 133-146.

61. J. D. Cressler, "SiGe HBTs: Device Physics," in *Silicon Heterostructure Handbook: Materials, Fabrication, Devices, Circuits, and Applications of SiGe and Si Strained-Layer Epitaxy*. ed. J. D. Cressler, Taylor & Francis: Boca Raton, FL (2006) 391-409.

62. G. Sun, F. Chang, R. A. Soref, High Efficiency Thin-Film Crystalline Si/Ge Tandem Solar Cell. *Opt. Express* **18** (2010) 3746—3753.

63. A. Borak, S. Tsujino, C. Falub, M. Scheinert, L. Diehl, *et al.,* Recent Results on the Road to a SiGe Quantum Cascade Laser. *Mater. Res. Soc. Symp. Proc.* **832** (2005) F4.2.1.

64. K. K. Tsia, S. Fathpour, B. Jalali, Electrical Tuning of Birefringence in Silicon Waveguides. *Appl. Phys. Lett.* **92** (2008) 061109.

65. M. Robillard, P. E. Jessop, D. M. Bruce, S. Janz, R. L. Williams, *et al*., Strain-Induced Birefringence in $Si_{1-x}Ge_x$ Optical Waveguides. *J. Vac. Sci. Technol. B* **16** (1998) 1773-1776.

66. M. De Graef, Introduction to Conventional Transmission Electron Microscopy. Cambridge University Press: Cambridge (2003).

67. P. Sutter, M. G. Lagally, Quantitative Determination of Dislocation-Induced Strain at the Surface of (001) Silicon-on-Insulator. *Phys. Rev. Lett.* **82** (1999) 1490-1493.

68. C. Kittel, Introduction to Solid State Physics, 8th Ed. John Wiley & Sons: Hoboken, NJ (2005).

69. I. De Wolf, Micro-Raman Spectroscopy to Study Local Mechanical Stress in Silicon Integrated Circuits. *Semicond. Sci. Technol.* **11** (1996) 139.

70. R. Loudon, The Raman Effect in Crystals. *Adv. Phys.* **13** (1964) 423.

71. E. Anastassakis, A. Cantarero, M. Cardona, Piezo-Raman Measurements and Anharmonic Parameters in Silicon and Diamond. *Phys. Rev. B* **41** (1990) 7529.

72. F. Cerdeira, C. J. Buchenauer, F. H. Pollak, M. Cardona, Stress-Induced Shifts of First Order Raman Frequencies of Diamond-and Zinc-Blende-Type Semiconductors. *Phys. Rev. B* **5** (1972) 580-593.

73. F. Pezzoli, E. Bonera, E. Grilli, M. Guzzi, S. Sanguinetti, *et al.,* Phonon Strain Coefficients in $Si_{1-x}Ge_x$ Alloys. *J. Appl. Phys.* **103** (2008) 093521.

74. S. Nakashima, T. Mitani, M. Ninomiya, K. Matsumoto, Raman Investigation of Strain in Si/SiGe Heterostructures: Precise Determination of the Strain-Shift Coefficient of Si Bands. *J. Appl. Phys.* **99** (2006) 053512.

75. H. R. Philipp, E. A. Taft, Optical Constant of Germanium in the Region 1 to 10eV. *Phys. Rev.* **113** (1959) 1002-1005.

76. G. E. Jellison, Jr., F. A. Modine, Optical Absorption of Silicon Between 1.6 and 4.7eV at Elevated Temperatures. *Appl. Phys. Lett.* **41** (1982) 180-182.

Chapter 2 Fabrication of nanomembrane materials and incorporating strain

2.1 Freestanding nanomembranes

Nanomembranes are thin (5-500nm thick) sheets of single-crystalline material that can be released from a handling substrate by dissolving the substrate or a sacrificial release layer (see Figure 2-1 below). Freestanding NMs have large aspect ratios (~10^3 – 10^5:1 width:thickness) and, for this reason, will typically exhibit different properties than their bulk counterparts. For instance, materials that are normally very rigid, brittle, and opaque in bulk form may be flexible and transparent in NM form. I will focus on Group IV semiconductor NMs, but NMs can be made from any material given the correct configuration.

2.1.1 Fabrication

Si NMs are available as a commercial product: silicon-on-insulator (SOI). The top Si layer, or template layer, of the SOI is bonded to a thick Si wafer, or handle substrate, via a SiO_2 layer (150nm - 3μm thick) [Figure 2-1A]. Here the SiO_2, or buried oxide (BOX), is the sacrificial release layer. The NM is patterned with photo- or electron-beam lithography and plasma etching to define the final shape of the NM and small etchant access holes (optional based on overall size of NM) [Figure 2-1B]. The Si NM (template layer) is released from the handle substrate by preferentially etching the BOX layer in hydrofluoric acid (HF) [Figure 2-1C]. Once the SiO_2 layer is completely etched, the Si NM settles onto the handling substrate where it loosely bonds via

van der Waals forces to the original handle substrate. At this point there are two methods for transferring the Si NM to new host substrates: wet transfer and dry transfer.

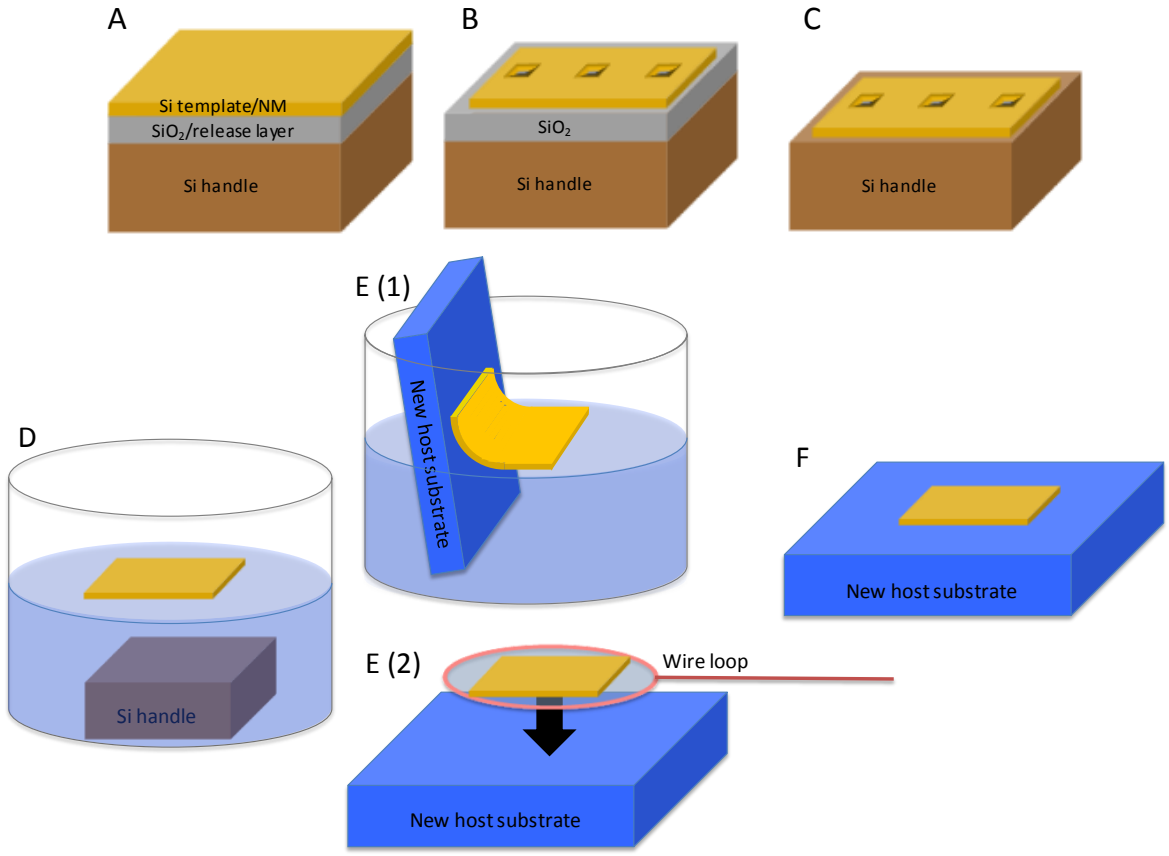

Figure 2-1. Nanomembrane fabrication and wet transfer process. (A) Starting NM material: thin NM (Si) bonded/deposited/grown onto a handle substrate (Si) via a release layer (SiO_2). (B) The shape and size of the NM is patterned with photo- or e-beam lithography and plasma etching. Etchant access holes are shown here but are not needed for all applications. (C) The release layer is selectively etched (HF for a SiO_2 release layer) and the NM settles onto the original handle substrate. (D) The NM and substrate are transferred to water. The surface tension of the water will force the NM to release from the original host substrate. Si NMs will float on the surface of the water because they are hydrophobic from the selective etchant step. (E) The NM can be transferred onto the new host substrate one of two ways: (1) scooping the NM onto the new substrate, or (2) picking up the NM within a wire loop and placing it onto the new substrate. (F) The final result is a flat NM transferred to the new host substrate.

Wet transfer

When the SiNM settled on the handle substrate is transferred to water the SiNM often comes off the substrate and floats in the water [Figure 2-1D]. The SiNM floats because both sides of the NM have been H-terminated while in the HF etchant, leaving the surfaces hydrophobic. The NM can then be transferred to a new host substrate one of two ways. (a) The NM can be scooped out of the water with the new host substrate by dipping the new host substrate in the water and lifting the NM out [Figure 2-1E (1)]. This method works best if the new host substrate is hydrophilic because the surface is wet and the NM will wick up substrate as shown schematically in Figure 2-1E. (b) The second way to transfer a NM in water is to use the surface tension of the water to hold the NM in a wire loop [Figure 2-1E (2)]. The NM can then be transferred to any new surface by touching the loop down onto the new surface and wicking the water away with a tissue [1]. In both cases the NM must be annealed to remove excess water at the interface between the NM and the new host substrate and to encourage covalent bonding at the interface. The annealing temperature must be ramped very slowly (<100°C/10min). If temperature is increased rapidly, gas products will not be able to diffuse and will cause bubbles to form at the NM/substrate interface (more details in next section). In some cases the NM may break to let the gas escape [2]. I use wet transfer techniques exclusively for this work.

Dry transfer

After the sacrificial layer has been removed and the SiNM has settled on the handling substrate, the SiNM may be picked up with another material referred to here as the "stamping" material. Here the stamp can be anything the NM bonds to more strongly that the original handle substrate: PDMS [3], SU8 [4], heat transfer tape [5], PI film [6]. If the stamping material is the new host substrate, the SiNM can remain there or it can be transferred to another host substrate by stamping the SiNM onto the new substrate and removing the stamp material. The key to the dry transfer technique is that the NM must have stronger adhesion to the new substrate material than to the stamping material. This technique has been shown for many different stamping materials elsewhere [3-6] and will not be discussed further here.

2.1.2 Bonding

In most cases, the bond between the NM and the final host substrate is very important for further processing. This will become apparent later when I describe the process for epitaxial growth on transferred NMs. In general, bonding two rigid or quasi-rigid objects involves bringing the surfaces into intimate contact and fusing them together. This means that the two surfaces must be very smooth to maximize the contact area between the two objects. Pressure is often applied to increase the contact area and heat is applied to encourage chemical bonding at the interface of the two materials. For example, clean semiconductor wafers of the same material bond with careful application of pressure and temperature [7, 8]. The strength of the bonded interface depends on the contact area and the similarity of materials to be bonded. For

the purposes of this work I will briefly discuss hydrophilic Si-Si bonding of nanomembranes. For a more complete review of the adhesion of SiNMs please see [9].

Nanomembranes, in general, bond very easily without the application of pressure because they are thin and compliant. They bend and conform to rough surfaces and particulates, thus maximizing surface-to-surface contact to encourage bonding. This is in contrast to bonding two rigid bodies, where pressure is often needed to maximize the surface-to-surface contact area. In wafer bonding, for example, small particles and rough interfaces between two wafers can leave large voids where the wafers will not bond properly. The area of the void is dependent on the size of the particle/asperity and the thickness of the object being bonded. Thinner objects will conform more readily and leave smaller unbonded areas [8, 10]. That being said, it is still important to ensure that the NM and the new substrate surface are clean before joining the materials to maximize the bonded area.

The application of heat is necessary to encourage chemical bonding of the NM with the new host substrate. In this work, the Si NMs are H-terminated from the HF etching of the SiO_2 release layer and the new host substrates are often hydrophilic Si (SiO_2 terminated from chemical cleaning). Because NM bonding is done in air there will always be at least several monolayers of water at the interface of the NM and the new substrate (more if a 'wet' NM transfer is used). When heated, the water at the NM/Si substrate interface will react with the Si to form SiO_2 and H_2 [7]. If this reaction occurs very quickly (quick temperature ramp), the trapped H_2 gas will form bubbles at the interface causing delamination of the NM (Figure 2-2A). A quick temperature ramp above 100°C will also likely cause water vapor at the interface,

another source of trapped gas. When the annealing temperature is ramped slowly, the H_2 (and water vapor) have time to diffuse into the Si and along the interface, thus preventing the formation of bubbles and delamination (Figure 2-2B). The adhesion strength between the surfaces is also related to the maximum annealing temperature. For these reasons, once the NMs have been transferred they are annealed to 500°C with a temperature ramp ≤ 10°C/min. The annealing step results in flat, well-bonded Si NMs (Figure 2-2C).

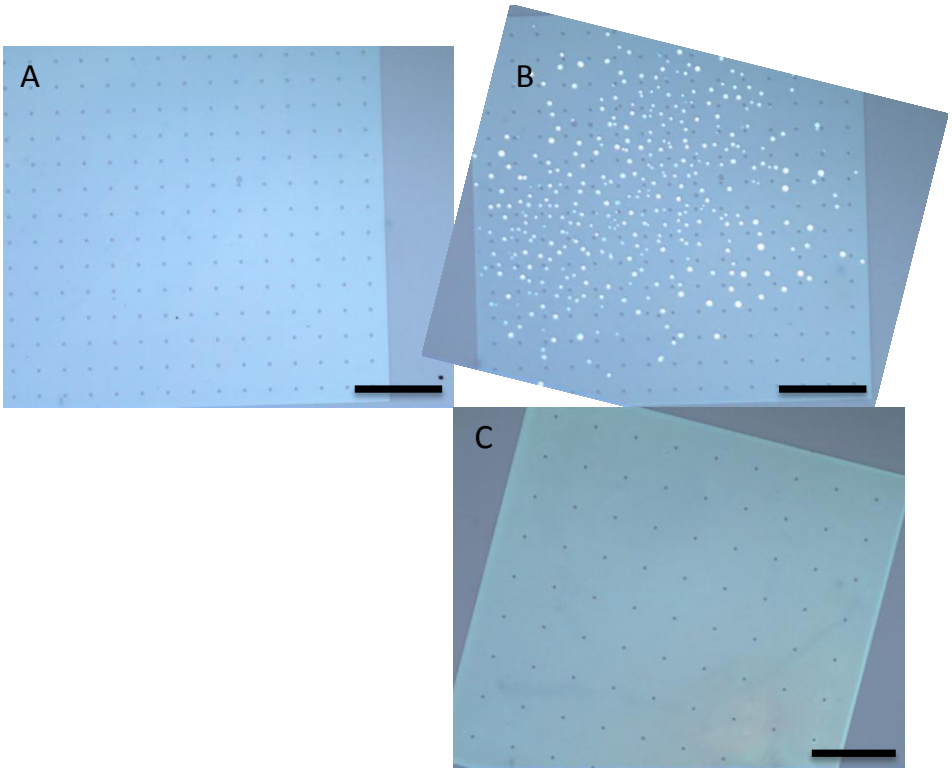

Figure 2-2. Optical micrographs of SiGe NMs after transfer to hydrophilic Si. (A) ~50nm $Si_{0.8}Ge_{0.2}$ NM after wet transfer and annealing to ~100°C (~5°C/min ramp). (B) The same NM after an additional rapid thermal annealing step at 550°C (~200°C/min ramp). The bright areas are bubbles (delaminated areas) at the NM/substrate interface. (C) ~50nm $Si_{0.74}Ge_{0.26}$ NM after wet transfer and annealing to ~550°C (~10°C/min ramp). There are no signs of delamination on the NM. Both NMs have an array of etchant access holes spaced 60µm apart (A and B) and 100µm apart (C). The scale bar is 200µm for all images.

2.2 Ways to induce strain in NMs

The thinness of nanomembranes makes them uniquely suited to strain engineering: the controlled introduction or relaxation of elastic strain to enhance or change materials properties. NMs can accommodate more strain than similar materials in bulk form before failing (breaking, dislocating, etc.). I will discuss a few ways in which NMs can be strain engineered and why these techniques are unique to NM systems.

2.2.1 Deformation of the handle substrate/NM system

As outlined in the previous section, NMs can be transferred to any new host substrate. This includes substrates that are easily deformed such as flexible plastics and soft polymers. If the transferred NMs are properly bonded to the new host substrate (via either heating to encourage chemical bonding or use of an adhesive), deforming the substrate will in turn deform the NM. The most obvious example of this is by mechanically bending the substrate. Bending an object induces tensile strain on the convex surface and compressive strain on the concave surface with a plane of neutral strain in the center. Because the NM is typically much thinner than the substrate, the NM strain will be approximately equal to the strain on the surface of the substrate. The radius of curvature of the bent substrate controls the strain in the NM. If two bulk-like materials were bonded and bent similarly, there would be a strain distribution through the thickness of both materials (Figure 2-3B). In the case of the NM/substrate system, the NM is a small proportion of the total thickness so the majority of the strain variation in the system is in the substrate (Figure 2-3A). This technique was used to strain Ge NMs transferred onto

polyimide films [6] and induce uniaxial strain in Si transferred to flexible substrates. The latter were used to monitor changes in MOSFET performance [11] and measure the splitting of the conduction band [12] as a function of uniaxial strain. One issue with this technique is that the NM/substrate system must remain bent to maintain the strain in the NM; the substrate must be plastically deformed to hold the strain, otherwise releasing the substrate will relax the strain in the system. The advantage of mechanical bending is that changing the radius of curvature can dynamically vary the strain in the system.

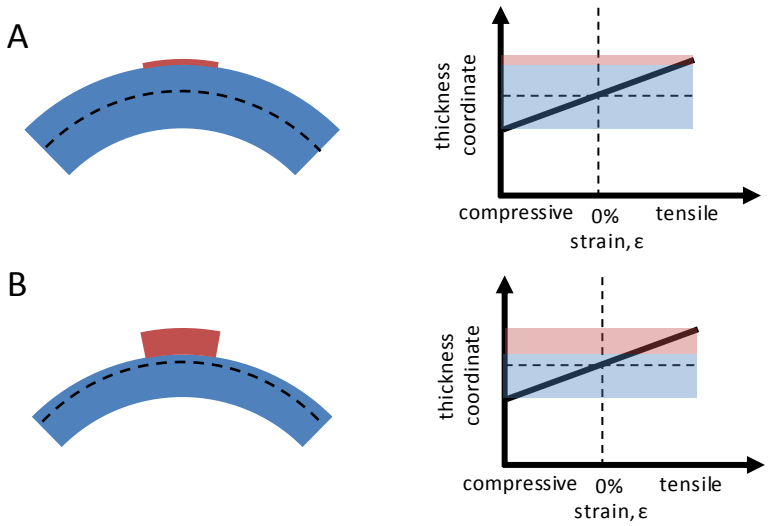

Figure 2-3. Schematic diagrams illustrating the strain profiles in bilayer bent objects. The dashed lines indicate the neutral plane, ε = 0. (A) A thin NM (top layer) bonded to a thick flexible substrate. The neutral plane (dashed line) is near the center of the substrate and there is only a small variation in strain (solid line) through the thickness of the NM. (B) A thick film on a thinner substrate. The total thickness here is the same as in A, so a similar curvature will produce a similar strain profile. The strain variation through the "film" is greater because the top layer is a larger proportion of the total thickness of the bilayer system.

Another example of inducing strain in NMs through substrate deformation is with thermal expansion mismatch. It is well known that bonding materials with different thermal expansion coefficients will induce strain in one or both of the materials with a temperature change. The mismatch strain in the system with a temperature change of ΔT is [13]:

$$\varepsilon_m = (\alpha_s - \alpha_f)\Delta T, \quad (2\text{-}1)$$

where α_s and α_f are the thermal expansion coefficients of the substrate and the film, respectively. If the 'film' material is much thinner than that of the substrate, the mismatch strain is accommodated entirely by the film or NM. Bonding materials with different thermal expansion coefficients is particularly problematic because bonding typically takes place at elevated temperatures. For instance, wafer bonding of Si and Ge results in plastic strain relaxation (delamination and cracking) [7] because there is a factor of two difference between the thermal expansion coefficients [14]. Bonding a Si NM onto a Ge substrate, however, results in smooth uniform interfaces because the thin NM easily accommodates any strain in the system [5]. The magnitude of the mismatch strain in the NM/substrate system will depend not only on the thermal expansion coefficients, but also on the temperature at which the NM is bonded to the substrate. The bonding temperature will determine the initial temperature of the system; the mismatch strain will be determined from this initial temperature.

It is important that the NM be bonded well to the host substrate in either of the cases described above. Any slipping at the interface between the substrate and the NM will change the strain in the NM; slipping at the interface will change the mismatch strain in the system. Delamination of the NM from the substrate is often a sign of failure in the system: the point at

which plastic deformation of the system commences because the magnitude of strain exceeds the elastic limit.

2.2.1 Freestanding multilayer structures

Another way to induce strain into nanomembranes is to incorporate a strained (stressor) layer in a multilayer NM. The multilayer NM may have multiple unstrained layers, but must contain at least one stressor layer (may contain more than one). The stressor layer can in principle be introduced by epitaxial growth, non-epitaxial growth, or membrane bonding. In each case, the strain in the stressor layer originates from different sources: a lattice mismatch provides a fixed strain in the stressor layer for epitaxially grown films [15, 16], there is a fixed amount of intrinsic strain in amorphous or polycrystalline films deposited *via* non-epitaxial growth techniques [17-19], and in membrane bonding the strain in the stressor layer can be introduced before bonding by controllable mechanical deformation [20] or differences in thermal expansion upon annealing [13]. The multilayer NM is released in the same way as an unstrained, single-layer NM. Upon release, the multilayer NM comes to mechanical equilibrium. A balanced NM (net moment = 0) will share the strain between the layers: for multilayer NMs with compressively (tensilely) strained layers, the entire heterostructure will expand (retract) inducing a tensile (compressive) strain in the initially unstrained layers. If the strain through the thickness of the multilayer is not balanced the heterostructure may stretch and bend/curl when released. Controlling the strain in these multilayer NMs will be discussed in detail in the following sections.

2.3 Isotropic elastic strain sharing in freestanding multilayer NMs

I mentioned in the previous section that strain can be induced in NMs in several ways. One way is to incorporate a strained layer into a multilayer NM. I will consider elastic strain sharing between layers in *isotropic* materials systems in this section. For simplicity I will discuss two systems. (1) Curled heterostructures: bilayer NMs where one layer is strained and the other is unstrained before release. (2) Balanced heterostructures: trilayer NMs where the middle layer is strained and the outer two layers are unstrained and similar before release. In both cases, all layers are considered coherent (epitaxial layers) or fully adherent (non-epitaxial layers) such that there is no defect formation or slipping at the interfaces. The mismatch strain between the layers, defined as the difference in strain between two adjacent layers (Eq. 2-2), is therefore constant no matter what the state of the system (released or unreleased).

$$\varepsilon_m = \varepsilon_2 - \varepsilon_1 \tag{2-2}$$

2.3.1 Curled heterostructures

Curling or bending in strained NMs is a result of unbalanced strain through the thickness of the NM. I will consider a bilayer NM. The initial state of the system is that all the strain is in one layer (layer 2 as shown in Figure 2-4) and there is no strain in the other layer (layer 1). This state is a consequence of the substrate holding the bilayer in place. After release from the substrate, the bilayer will come to mechanical equilibrium. There is some degree of stretching and bending once the bilayer is released. Strain sharing between the layers results in stretching: some of the compressive (tensile) strain transfers as tensile (compressive) strain to the initially

unstrained layer. The unbalanced strain through the thickness causes the bilayer NM to bend to relieve some of the strain from stretching. The tensilely strained layer will retract and the compressively strained layer will expand. This is shown for a compressively strained stressor layer and tensilely strained stressor layer in Figure 2-4.

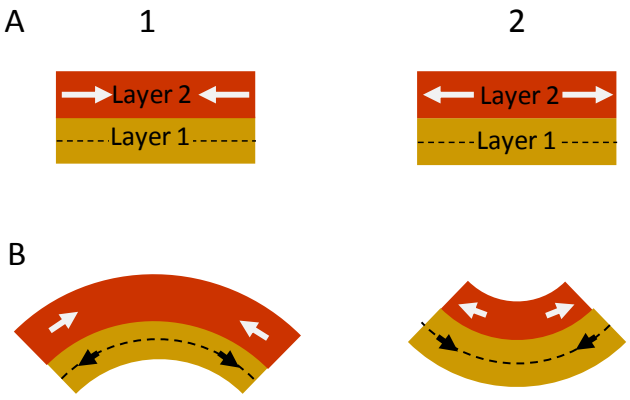

Figure 2-4. (A) Initial state of a bilayer system for a compressive film (1) and a tensile film (2). All of the strain in the system is in layer 2. The handle substrate is holding the bilayer in this state. (B) After the bilayers are released they are allowed to reach mechanical equilibrium. Tensilely strained layers want to retract and compressively strained layers want to expand, causing the bending illustrated. The arrows represent the magnitude and direction of average strain in that layer. The dashed line is defined as z = 0, where z is the distance coordinate through the thickness of the bilayer.

The amount of stretching and bending is controlled by the thicknesses of the layers and the elastic constants of the layers. Thick layers are more resistant to bending than thin layers, and stiffer materials are more resistant to bending than soft materials. Considering that there was an initial mismatch strain between the layers (ε_m from Eq. 2-2) and defining the z = 0 position to be the midplane of layer 1 (dashed line in Figure 2-4), the in-plane strain as a function of z through the thickness of the bilayer will be [13]:

$$\varepsilon_{\parallel}(z) = \begin{cases} \varepsilon_o - \kappa z \ for \frac{-1}{2} t_1 < z < \frac{1}{2} t_1 \\ \varepsilon_o - \kappa z + \varepsilon_m \ for \frac{1}{2} t_1 < z < \frac{1}{2} t_1 + t_2 \end{cases} \quad (2\text{-}3)$$

where ε_o is the strain at the midplane of layer 1 and κ is the curvature of the bilayer (1/κ = radius of curvature). Using this strain profile, the curvature, κ, and midplane strain of layer 1, ε_o, can be calculated by minimizing the total potential energy in the system. This is derived in [13, 21]; only the results are presented here.

$$\kappa = \left(\frac{6\varepsilon_m}{t_1} \eta\Sigma \right)(1+\eta)\left[1 + 4\eta\Sigma + 6\eta^2\Sigma^2 + 4\eta^3\Sigma^3 + \eta^4\Sigma^4\right]^{-1} \quad (2\text{-}4)$$

$$\varepsilon_o = (-\varepsilon_m \eta\Sigma)(1+\eta^3\Sigma)\left[1 + 4\eta\Sigma + 6\eta^2\Sigma^2 + 4\eta^3\Sigma^3 + \eta^4\Sigma^4\right]^{-1} \quad (2\text{-}5)$$

The curvature, κ, and midplane strain of layer 1, ε_o, are functions of the ratio of thicknesses of the layers, $\eta = t_2/t_1$, and the ratio of the biaxial moduli, $\Sigma = M_2/M_1$. The in-plane strain as a function of the normalized out-of-plane position for different thickness ratios and the curvature for different mismatch strains are shown in Figure 2-5A and B, respectively. The curvature is a maximum (minimum radius of curvature) near $t_2/t_1 \sim 0.5$. For thickness ratios lower and higher than this, one of the layers is much thicker than the other. This reduces the curvature because the elastic properties of the system are dominated by one layer. There is less of a bending moment because the strain variation though the thickness is reduced: the majority of the bilayer is either strained ($t_2 > t_1$) or unstrained ($t_2 < t_1$). Therefore more stretching (strain sharing) occurs than bending.

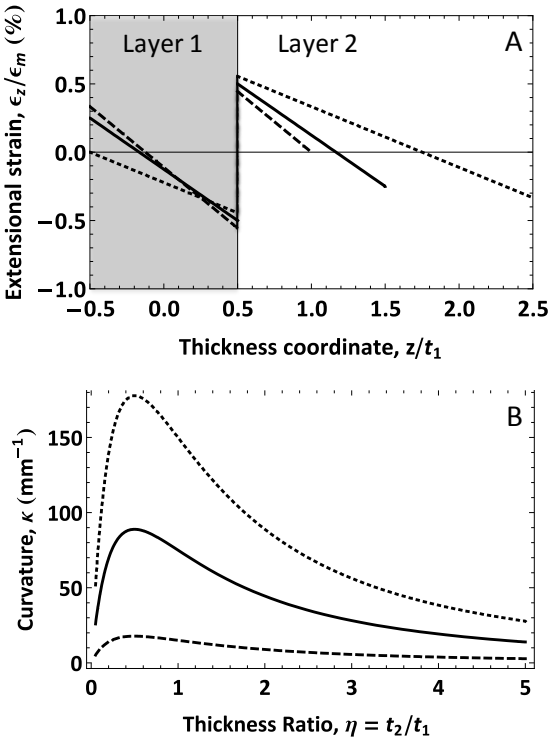

Figure 2-5. (A) Normalized strain as a function of normalized out-of-plane position in bilayer films for three different thickness ratios: η = 0.5 (dashed), 1.0 (solid), 2.0 (dotted). The shaded region represents the strain variation in layer 1. (B) Curvature as a function of thickness ratio for three different mismatch strains: ε = -0.1% (dashed), -0.5% (solid), -1.0% (dotted). The ratio of biaxial moduli, Σ = 1 for all of these plots. The thickness of layer 1 was held constant t_1 = 50nm for both plots. The in-plane strain is isotropic because I am assuming isotropic materials properties.

2.3.2 Balanced heterostructures

Balancing the strain through the thickness of the multilayer NM prevents bending of strained NMs. The easiest way to implement this is to add a balancing layer to the bilayer NM, thus creating a trilayer NM where the outer two layers are identical (Figure 2-6). Initially all the strain is in the middle layer and the trilayer is pinned this way by the substrate. After release from the substrate the trilayer can strain share. The strain through the thickness of the NM is

balanced such that only strain sharing (stretching) occurs: some of the compressive (tensile) strain in the stressor layer transfers as tensile (compressive) strain to the initially unstrained outer layers. The symmetry of the trilayer effectively means that the originally unstrained balancing layers could be on the top and bottom (as shown), or equal strained (stressor) layers could be on the top and bottom while the middle layer is initially unstrained.

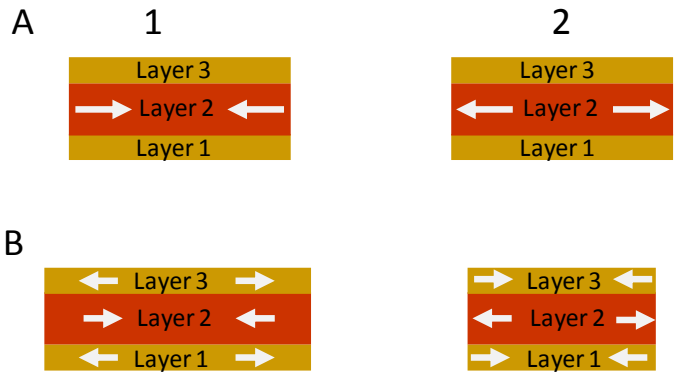

Figure 2-6. (A) Initial state of a trilayer system for a compressive film (1) and a tensile film (2). All of the strain in the system is in layer 2 and layers 1 and 3 are identical in thickness and composition. The handle substrate is holding the trilayer in this state. (B) After the trilayers are released, they are allowed to reach mechanical equilibrium. Compressive (tensile) strain in layer 2 transfers as tensile (compressive) strain to layers 1 and 3. The only mechanism for elastic strain relaxation is strain sharing between layers; no bending occurs because the forces are balanced through the thickness of the NM.

The amount of strain transfer is determined by a balance of forces [13]:

$$\begin{aligned}\Sigma F = 0 &= M_1\varepsilon_1 t_1 + M_2\varepsilon_2 t_2 + M_3\varepsilon_3 t_3 \\ &= M_1\varepsilon_1 t_{13} + M_2\varepsilon_2 t_2\end{aligned}, \qquad (2\text{-}6)$$

where M_i is the biaxial modulus of the material, ε_i is the strain in that layer, and t_i is the thickness of the layer. Assuming a balanced trilayer mathematically reduces the trilayer

problem to a bilayer problem: the force contributions from the top and bottom layers are equal and I only need to consider mismatch strain at one interface. Using this assumption the new thickness $t_{13} = t_1 + t_3$. I am also assuming that the layers are adherent so that the mismatch strain must stay constant (Eq. 2-2). Then the strain in each of the layers is:

$$\varepsilon_1 = -\varepsilon_m \frac{\eta\Sigma}{1+\eta\Sigma} \tag{2-7}$$

$$\varepsilon_2 = \varepsilon_m \frac{1}{1+\eta\Sigma} \tag{2-8}$$

where $\eta = t_2/t_{13}$ and $\Sigma = M_2/M_1$ are defined the same way as in the previous section. The strain transferred to the outer layers is determined by the thickness ratio, the biaxial modulus ratio, and the mismatch strain. Figure 2-7 illustrates the degree to which trilayer NMs will strain share for different thickness ratios and modulus ratios.

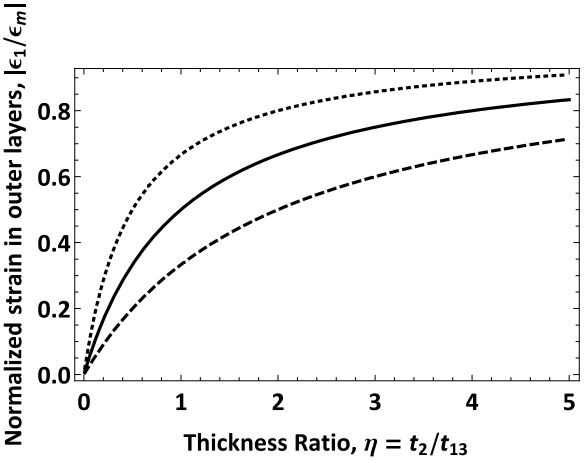

Figure 2-7. Normalized strain transferred to outer layers as a function of thickness ratio, $\eta = t_2/t_{13}$, for freestanding trilayer NMs. The three curves represent different biaxial modulus ratios: $\Sigma = M_2/M_1$ = 0.5 (dashed), 1.0 (solid), 2.0 (dotted). The strain through the thickness of each layer is constant because there is no bending to relieve any strain. The in-plane strain is isotropic because of the isotropic materials properties and the isotropic in-plane mismatch strain.

Figure 2-7 shows that the strain transferred to the outer layers (initially unstrained) approaches the mismatch strain ($\varepsilon_1/\varepsilon_m \rightarrow 1$) for large thickness ratios ($t_2 >> t_{13}$). The limitation here is that layer 2 must elastically accommodate all of the mismatch strain. This means that the thickness of layer 2 is limited by the critical thickness for a given mismatch strain. I discussed the critical thickness of strained SiGe epitaxial films in section 1.3.4, but polycrystalline and amorphous films will relieve strain though plastic deformation as a function of strain energy in the film as well. Using a Si/SiGe/Si trilayer NM as an example, the maximum strain transfer to the Si layers is shown in Figure 2-8 for four different Si layer thicknesses, $t_{Si} = t_{13}$.

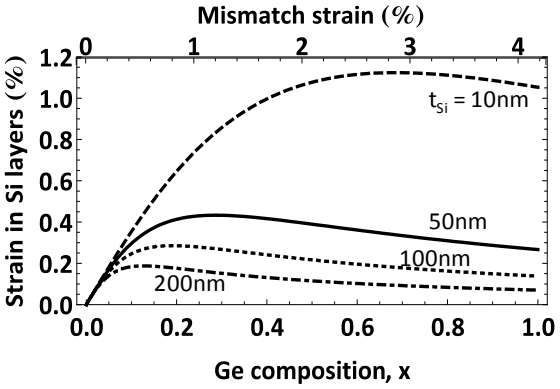

Figure 2-8. Strain transferred to the Si layers of a freestanding $Si/Si_{1-x}Ge_x/Si$ balanced trilayer NM for four different Si thicknesses: t_{Si} = 10nm (dashed), 50nm (solid), 100nm (dotted), and 200nm (dashed-dotted). Less strain is transferred to the Si layers as the thickness ratio is decreased (t_{Si} is increased). There is an optimum Ge composition (mismatch strain) for each Si thickness that results in maximum strain transfer. The Si thickness, t_{Si}, is the combined thickness of both Si layers (top and bottom).

The thickness of the SiGe layer (layer 2) is limited to the kinetic critical thickness for a given composition. There is a maximum strain transfer because the thickness ratio is varying; the

critical thickness decreases with increasing SiGe composition. This results in an optimum Ge composition (mismatch strain) for maximum strain transfer to Si layers of a given thickness. This result will be similar for other materials systems in which a critical thickness is known for the initially strained layer.

2.4 Generalized anisotropic elastic strain sharing for balanced trilayer heterostructures

When considering elastic strain sharing among several layers, considerations of the symmetry of the elastic constants of each layer and the initial mismatch strain distribution determine the detailed ultimate strain distribution in in-plane directions when the trilayer structure is released and the strain is shared. In the previous section I discussed elastic strain sharing in a freestanding trilayer NM assuming isotropic materials properties and an equibiaxial mismatch strain. In this section, I will provide a general treatment of elastic strain sharing in trilayer NM systems to demonstrate the influence of elastic anisotropies on the resulting strain distributions. I use anisotropic linear elastic theory to properly describe the strain in each layer in three dimensions. The results lead to the ability to create unique strain distributions in thin sheets, something that in turn can lead to unique electronic, photonic [22] and dielectric [23] properties.

I have already shown that the strain sharing in multilayer NM systems will depend on the relative thicknesses of each of the layers, differences in elastic constants of the materials, and the magnitude of the original mismatch strain. The generalization of this problem will add significant complexity to the strain sharing results; crystalline orientation, original mismatch

strain distribution, twist angle of bonded layers, plastic deformation, and so on will also alter the strain sharing between layers. To simplify this problem I will consider only balanced systems, as described above, such that I can ignore any bending moment in the trilayer NM. This means that the top and bottom layers of the trilayer NM are always identical in composition, orientation, and thickness.

Similar to the isotropic case described above, a force balance model is used to determine the strain distributions in freestanding trilayer NMs based on two states: the initial state, in which the trilayer NM is attached to a handling substrate and the balancing layers contain no strain, and the final state, a free-standing trilayer NM that has been allowed to come to equilibrium. Figure 2-9 is an illustration describing mathematically equivalent models for this multilayer system; the initially strained layer can be the middle layer (Figures 2-9A and B) or the outer layers can be similarly strained to produce the same results (Figures 2-9C and D).

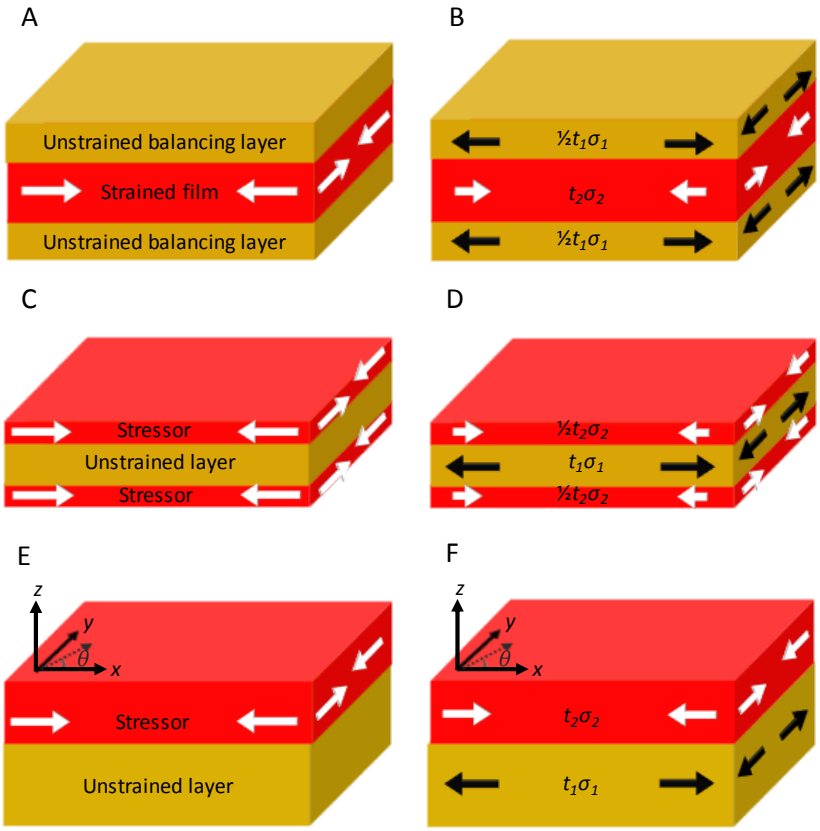

Figure 2-9. Mathematically equivalent models of balanced trilayer NMs. The arrows represent the relative magnitude and direction of the strain in each layer. The initially unstrained layers can be on the top and bottom (A), or the initially unstrained layer can be sandwiched between two stressor layers (C). Both of these cases are mathematically equivalent to a bilayer system in which the two outer-layer thicknesses are added and represented as one layer (E). The figures on the left (A, C, E) show the initial state of each system: all the strain remains in the stressor layer while attached to the initial handling substrate. The figures on the right (B, D, F) show the final state of the heterostructures after the NM has been allowed to strain share. The coordinate system is defined in the same way for all layers; however, the crystallographic directions in the stressor and initially unstrained layer need not be aligned. Layer 1 represents the combined properties of the initially unstrained layer(s) and layer 2 represents the initially strained (stressor) layer(s).

For simplicity I will take the initial, or as-grown, state of the trilayer to have all of the strain in the stressor or middle layer; this is the mismatch strain in the system (Eq. 2-2). The

mismatch strain distribution will depend on growth, deposition, or bonding conditions and is written in tensor notation as [13]:

$$\varepsilon_m = \varepsilon_2 - \varepsilon_2 = \begin{pmatrix} \varepsilon_{xx} & \varepsilon_{xy} & \varepsilon_{xz} \\ \varepsilon_{xy} & \varepsilon_{yy} & \varepsilon_{yz} \\ \varepsilon_{xz} & \varepsilon_{yz} & \varepsilon_{zz} \end{pmatrix} \quad (2\text{-}9).$$

I use tensor quantities here to describe fully the strain in each of the layers of the trilayer NM, such that I can use any mismatch strain distribution; I am not restricted to assuming an equibiaixal mismatch strain distribution. Once the trilayer structure is allowed to share the strain elastically, the freestanding NM will equilibrate (Figure 2-9C). The total force in the top and bottom layers must be equal and opposite to the force in the middle layer; the sum of the forces in the trilayer NM structure should equal zero:

$$C_2\varepsilon_2 t_2 + C_1\varepsilon_1 t_1 = 0 \quad (2\text{-}10).$$

The force in each layer is taken to be the stress, $\sigma_i = C_i\varepsilon_i$, multiplied by the thickness (t_i) of each layer [13], where C_i is the fourth-rank stiffness tensor and ε_i is the strain tensor for the respective layer. We are assuming that there is negligible thickness variation of the layer such that t_i is a constant scalar quantity. An expression for the strain in the outer balancing layers is obtained by combining Equations 1 and 2, and dividing through by the balancing-layer thickness (t_1):

$$\eta C_2\varepsilon_m + \eta C_2\varepsilon_1 + C_1\varepsilon_1 = 0 \quad (2\text{-}11).$$

η is defined the same as above: the thickness ratio between the strained film (or stressor layer) and the balancing layers, t_2/t_1.

To solve for each of the components of the balancing layer strain tensor in Eq. 2-11 I use the reduced form of the stiffness and strain tensors. In general, the fourth-rank stiffness tensor can be mathematically reduced to a 6x6 matrix based symmetry on elastic constants [24]. At most there will be 21 unique elastic constants (C_i is a symmetric matrix). I will only be considering cubic materials such that there are only 3 unique elastic constants and the stiffness tensor can be reduced to the following 6x6 matrix for NMs in which the Cartesian coordinate system is oriented along <100> type crystalline directions:

$$C_i = \begin{pmatrix} c_{11} & c_{12} & c_{12} & 0 & 0 & 0 \\ c_{12} & c_{11} & c_{12} & 0 & 0 & 0 \\ c_{12} & c_{12} & c_{11} & 0 & 0 & 0 \\ 0 & 0 & 0 & c_{44} & 0 & 0 \\ 0 & 0 & 0 & 0 & c_{44} & 0 \\ 0 & 0 & 0 & 0 & 0 & c_{44} \end{pmatrix} \quad (2\text{-}12),$$

where c_{ij} are the elastic constants for the respective layer [13]. For systems in which the <100> type crystalline directions do not align on the xyz-Cartesian coordinate system (z-direction always oriented along surface normal), the stiffness matrix was transformed to reflect the new, rotated coordinate system [24]. The details of the coordinate transformations are in Appendix A. Based similar symmetry arguments, the second rank strain tensor can be reduced to:

$$\varepsilon_i = \begin{bmatrix} \varepsilon_{xx} \\ \varepsilon_{yy} \\ \varepsilon_{zz} \\ 2\varepsilon_{xz} \\ 2\varepsilon_{yz} \\ 2\varepsilon_{xy} \end{bmatrix} \quad (2\text{-}13).$$

Using the reduced matrix forms of the strain and stiffness tensors, Equation 3 is effectively a system of 6 equations and 6 unknowns (one for each of the components of the strain tensor for layer 1 [balancing layer]).

It is apparent from Eq. 2-11 that the strain transferred to the outer balancing layers when the trilayer NM is released from the handling substrate will depend on the symmetry of the initial strain distribution in the stressor layer (ε_m), the relative stiffness differences between the balancing layers and the stressor layer (C_1 and C_2, respectively), and the ratio of thicknesses of each of the layers (η). I consider four situations. I start 1) with the outer balancing layers and the stressor layer both having 4-fold elastic symmetry with equibiaxial mismatch strain ($\varepsilon_{xx} = \varepsilon_{yy} = \varepsilon_m$), 2) change the elastic symmetry of the entire system while maintaining an equibiaxial mismatch strain, and then 3), 4) consider mixed-elastic-symmetry systems with equibiaxial strain and anisotropic biaxial strain ($\varepsilon_{xx} \neq \varepsilon_{yy} \neq 0$), respectively.

The goal of the work in this section is to investigate the changes in the transferred-strain distribution as a function of in-plane direction in freestanding trilayer NMs based on differences in elastic symmetry of the materials in the heterostructure. For simplicity, I use materials with 4-fold elastic symmetry (biaxially isotropic) and materials with 2-fold elastic symmetry (biaxially anisotropic), but Eq. 2-11 can be used for any balanced trilayer NM system if the crystalline orientation of the materials, elastic constants, and mismatch strain distribution are known. I used the specific materials as examples to obtain the results in the following sections, but the discussion of strain sharing between multilayer heterostructures is not limited to the example materials used here. I provide experimental proof of cases 1 and 2.

2.4.1 Case 1

First I consider the case where all layers in the trilayer heterostructure are biaxially elastically isotropic and the mismatch strain is equibiaxial. This is identical to the discussion of isotropic strain sharing in the previous section. I include this case for completeness and to show that I obtain the same result with this method. I use an (001)-oriented trilayer heterostructure system with an epitaxial mismatch strain as an example [15]. An isotropic biaxial mismatch strain would also result from a deposited amorphous or polycrystalline stressor layer (with an inherent stress from deposition) that has isotropic elastic symmetry. Figure 2-10A shows the normal in-plane strain distribution in the balancing layers [Si (001)] upon elastic strain sharing with a stressor layer [$Si_{0.8}Ge_{0.2}$(001)] with an initial mismatch strain of ~0.8% (red) for various thickness ratios, η. Here, the normal in-plane strains of the balancing layer are equal ($\varepsilon_{xx} = \varepsilon_{yy}$) and there is no shear strain ($\varepsilon_{xy} = 0$). Recall that the mismatch strain is the original strain in the stressor layer before release of the trilayer NM, but that the sign of the strain transferred to the outer balancing layers is opposite to the original strain in the stressor layer. Notice that as the stressor layer gets thicker and the balancing layers thinner (η increases), more strain is transferred to the balancing layers. The thickness of the stressor layer, however, must be kept below the critical thickness for plastic strain relaxation to maintain the original mismatch strain. This is also true for all of the following cases. The final strain sharing result for an equibiaxial mismatch strain and biaxially isotropic layers agrees with the result obtained assuming isotropic materials discussed in the previous section.

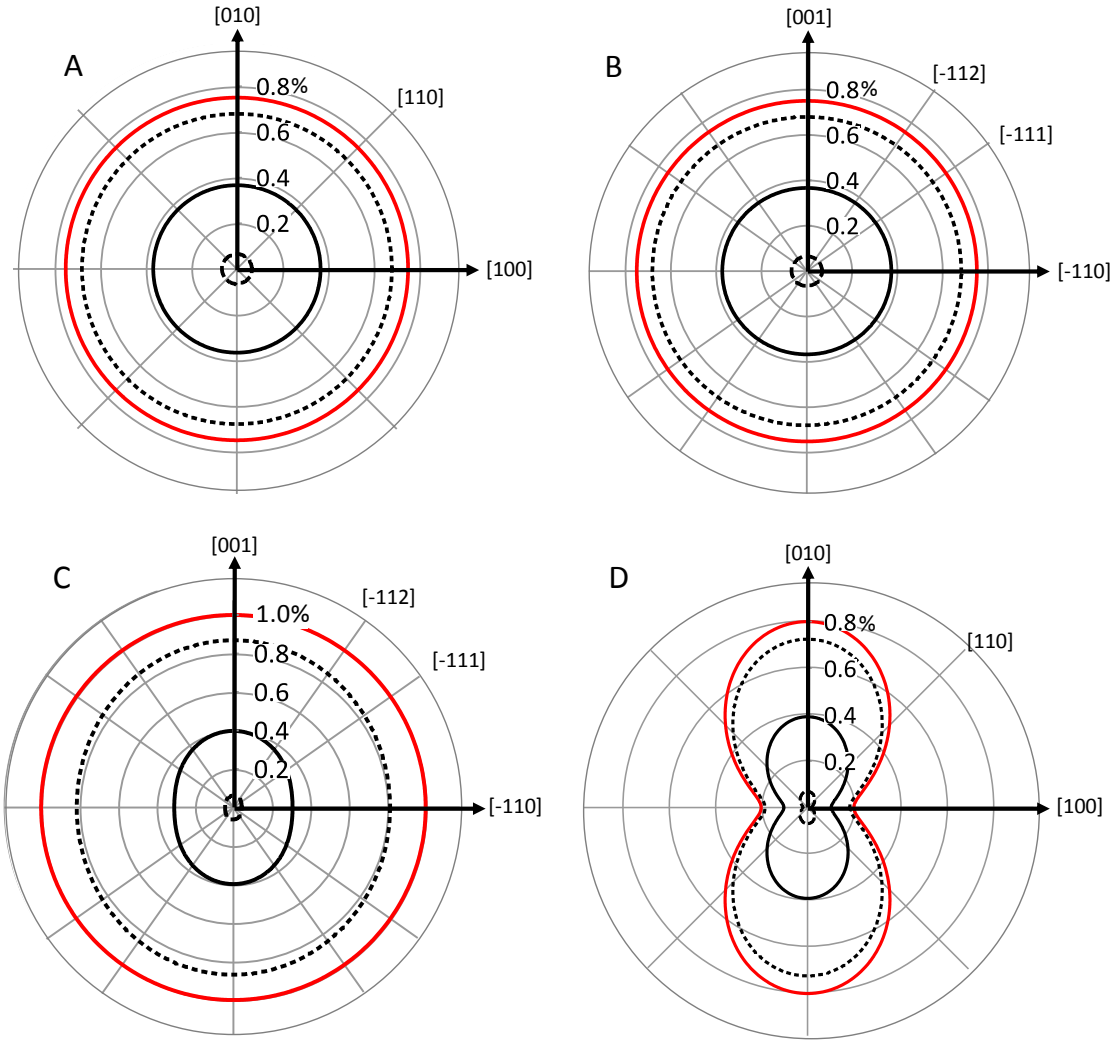

Figure 2-10. In-plane strain distributions in the balancing layers of trilayer NMs after elastic strain sharing for (a) Case 1: biaxially isotropic balancing layers with a biaxially isotropic stressor layer, (b) Case 2: biaxially anisotropic balancing layers with a biaxially anisotropic stressor layer, (c) Case 3: biaxially anisotropic balancing layers with an isotropic stressor layer, and (d) Case 4: biaxially isotropic balancing layers with a biaxially anisotropic stressor layer. Each curve represents a different thickness ratio, $\eta = t_2/t_1$: $\eta = 10$ (solid), $\eta = 1.0$ (dashed), and $\eta = 0.1$ (dotted). The mismatch strain in the system is also shown (red solid); this corresponds to the strain in the stressor layer before strain sharing occurs and is of opposite sign as the strain transferred to the outer balancing layers. The elastic constants for Si are used for the balancing layers, and the elastic constants of the stressor layer vary with each case (see text for details).

Strain sharing between biaxially elastically isotropic layers with an equibiaxial mismatch strain has been done many times and the experimental results agree well with the expected strain sharing based on isotopic elastic theory [1, 2, 15, 16, 25, 26]. Here I will provide one example of a 48nm Si/80nm $Si_{0.795}Ge_{0.205}$/46nm Si(001) trilayer NM. This heterostructure was fabricated by epitaxially growing SiGe and Si layers on SOI with MBE. The top Si layer thickness is nearly matched to the Si template thickness of the SOI to create a balanced trilayer. In the "as-grown" state all the strain in the trilayer is in the SiGe. The compressive strain in the SiGe layer is set by the alloy composition (see section 1.1) and the thickness is below the kinetic critical thickness for plastic relaxation (see section 1.3). I verified that the SiGe is strained to the Si lattice constant with an off-axis XRD reciprocal space map (RSM) near the (044) reflection [Figure 2-11A]. Any relaxation of the SiGe alloy would appear as intensity along the relaxation line: as the SiGe relaxes, the out-of-plane lattice constant decreases and the in-plane lattice constant increases. Here the in-plane SiGe lattice constant matches that of the Si, and the composition of the alloy is extracted from the out-of-plane spacing between the Si and SiGe peaks. I extracted the thicknesses of each of the layers by fitting a simulation to a $\theta/2\theta$ XRD line scans around the (004) reflection of the as-grown trilayer. More details concerning the sample fabrication are presented in Chapter 3.

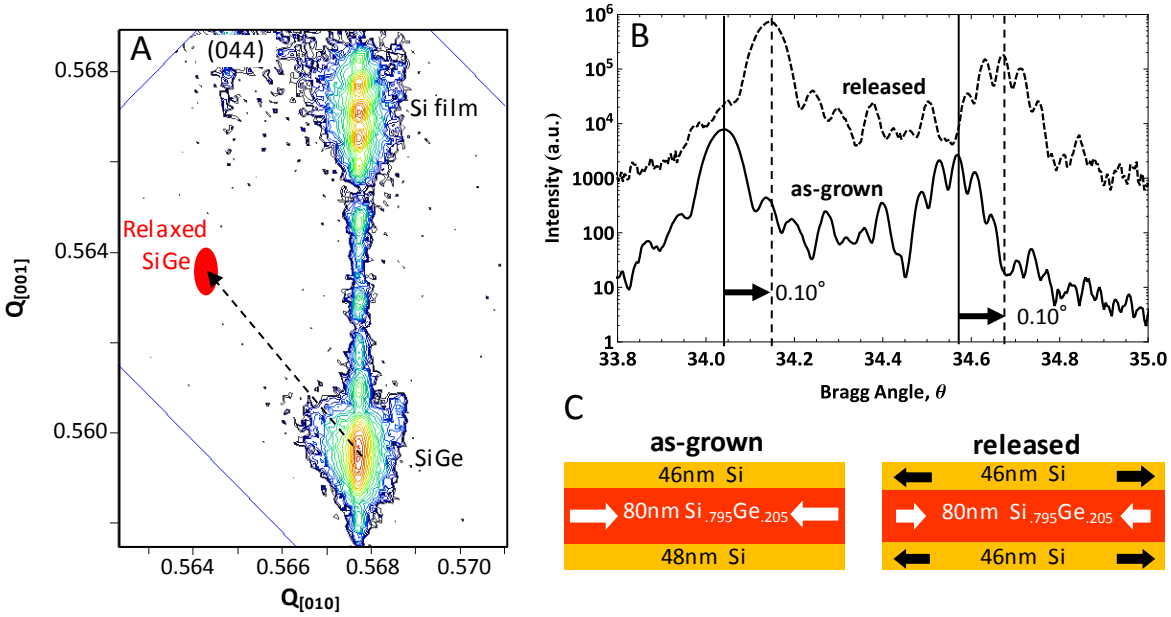

Figure 2-11. (A) XRD RSM around the (044) reflection of the as-grown 48nm Si/80nm $Si_{0.795}Ge_{0.205}$/46nm Si(001) trilayer heterostructure (left schematic in C). The SiGe film is fully strained to the Si lattice constant; the in-plane SiGe and Si peaks are at the same in-plane reciprocal lattice units. Any plastic strain relaxation of the SiGe would appear as intensity along the relaxation line (dashed arrow). The position of a fully relaxed alloy of the same composition is shown with a red dot. (B) High-resolution XRD θ/2θ triple-axis line scans around the (004) reflection before (left schematic in C) and after release (right schematic in C) of the same Si/SiGe/Si NM. All features in the scan shift to a higher Bragg angle (+0.1°) indicating a reduction in the out-of-plane lattice constant and an increase in the in-plane lattice constant of the entire trilayer heterostructure:

$\Delta\varepsilon_{\perp} = -0.26\pm0.01\% \rightarrow \Delta\varepsilon_{\parallel} = 0.34\pm0.01\%$. **This is consistent with elastic strain sharing.**

Once the initial strain state of the trilayer is verified, the trilayer is released from the handle substrate by selective removal of the BOX layer; the freestanding Si/SiGe/Si heterostructure is allowed to strain share. Figure 2-11B shows high-resolution θ/2θ triple-axis XRD line scans around the (004) reflection of the trilayer before and after release. The main peak in these scans is from the SiGe layer. The change in out-of-plane lattice spacing is

extracted from the shift in the SiGe peak from the as-grown state to the released state. An increase in the SiGe Bragg angle indicates that the out-of-plane lattice spacing decreased; the in-plane lattice spacing thus increases indicating a relaxation of the compressive strain in the SiGe layer. The change in strain in the SiGe layer will be equal to the amount of strain transferred to the outer Si layers. The mismatch strain must be conserved throughout the strain sharing process. The out-of-plane strain is related to the equibiaxial in-plane strain by:

$$\Delta\varepsilon_{\parallel SiGe} = \frac{-c_{11}}{2c_{12}}\Delta\varepsilon_{\perp SiGe} = \varepsilon_{\parallel Si} \qquad \text{(2-14)},$$

where $\Delta\varepsilon_{\parallel SiGe}$ and $\Delta\varepsilon_{\perp SiGe}$ are the changes in the in-plane equibiaxial strain and out-of-plane strain in the SiGe layer, respectively, c_{ij} are the constants of the elastic stiffness tensor of the SiGe layer (see section 1.1), and $\varepsilon_{||Si}$ is the equibiaxial strain in the Si layer. The expected strain transfer to the Si layers for the 48nm Si/80nm $Si_{0.795}Ge_{0.205}$/46nm Si(001) trilayer NM is 0.33% based on the measured thicknesses and composition of the layers. The equibiaxial strain in the Si layer extracted from the out-of-plane lattice constant measurement is 0.34 ± 0.01%. The presence of thickness fringes before and after release, as well as the uniform shift of all the peaks indicates that the layers remain coherent through strain sharing and that the strain sharing is elastic.

2.4.2 Case 2

As a next limit I consider a heterostructure system in which all the layers have 2-fold elastic symmetry, but with an equibiaxial mismatch strain distribution. An example of this type of heterostructure is coherent epitaxial growth and release of a (110)-oriented trilayer

heterostructure: Si(110)/$Si_{0.8}Ge_{0.2}$(110)/Si(110) [27, 28]. The mismatch strain is isotropic in-plane because I am using balancing layers and stressor layers with similar crystalline structures where the same in-plane orientations align during epitaxial growth [*e.g.,* SiGe (110) on Si(110)]. This means that the mismatch strain is defined in a similar way as a trilayer grown on (001)-oriented cubic materials ($\varepsilon_{xx} = \varepsilon_{yy}$, $\varepsilon_{xy} = 0$). Recall, for example, from section 1.1 that the biaxial modulus of Si(110) is biaxially anisotropic; however, the similar crystal structures of Si and Ge result in similar elastic-constant anisotropies. The implication is that, strain transfer between (110)-oriented materials of similar crystalline structures remains biaxially isotropic [Figure 2-10B]. *I believe there is no other way to make such strain distributions;* attempts to make plastically relaxed SiGe(110) substrates have failed due to anisotropic relaxation of the (110)-oriented alloy [29, 30]. These biaxially isotropic strain distributions are only enabled by elastic strain engineering in NMs.

Case 2 is experimentally exhibited in Si(110)/$Si_{(1-x)}Ge_x$(110)/Si(110) trilayer NMs. The (110) orientation of Si and SiGe is structurally and elastically 2-fold symmetric (section 1.1). This heterostructure is fabricated the same way as the Si/SiGe/Si(001) trilayer NMs (section 2.4.1), however, the SOI template layer is (110) oriented. Similar to the Si/SiGe/Si(001) trilayer, I measured the strain state of the trilayer (110) NM before and after release from the handle substrate. I characterized layer thicknesses, Ge composition, and the out-of-plane strain change with high-resolution $\theta/2\theta$ triple-axis line scans around the (220) reflection (Figure 2-12C). Off-axis reciprocal-space maps (RSMs) taken around the (331) and (260) reflections measured in-plane lattice constants in the [001] and [-110] directions, respectively (Figures 2-12A and B).

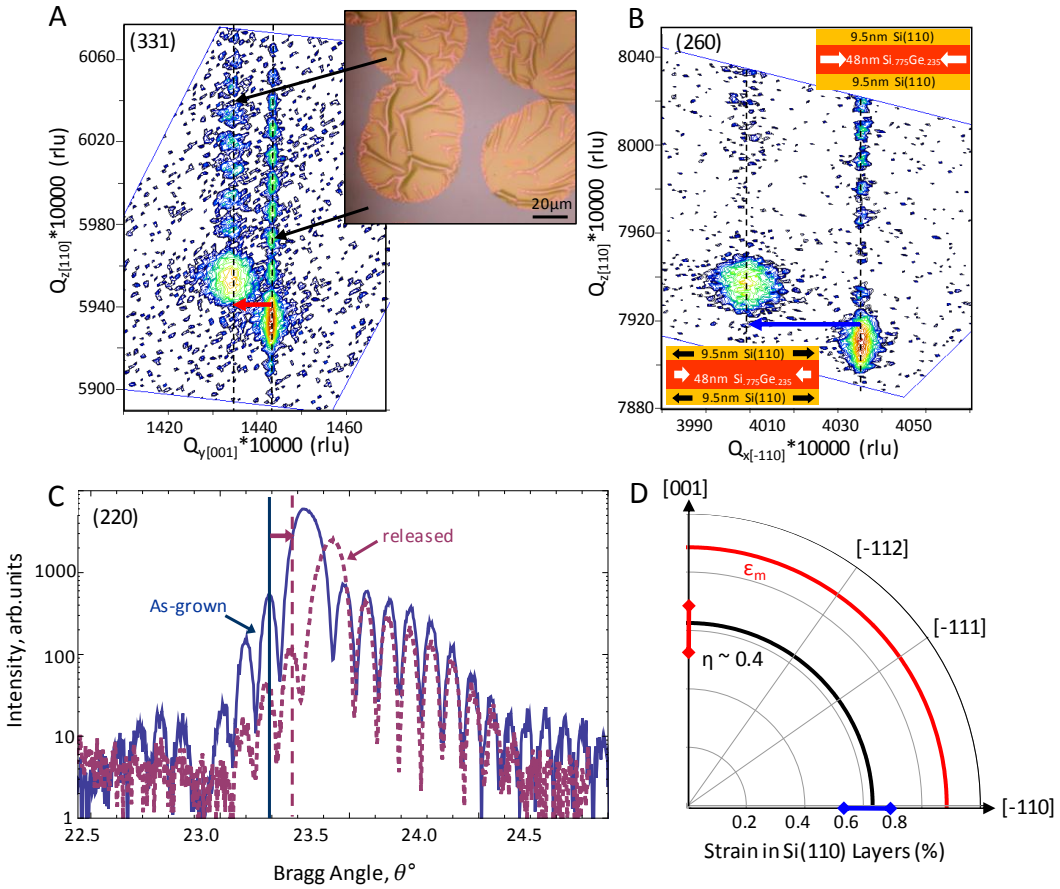

Figure 2-12. Off-axis reciprocal-space maps (RSMs) around the (A) (331) and (B) (260) reflections for the partially released trilayer Si(110) NM. An optical micrograph of the partially released trilayer Si(110) NM is shown in the inset of (A). At the center of each of the pink circular regions there is a 5-μm hole to allow the etchant access to the underlying SiO_2 layer: these regions are free to strain share (expansion causes wrinkles in the NM) as the supporting SiO_2 has been removed. A schematic diagram of the heterostructure is shown in the inset of (B) [upper is as-grown state, lower is released state]. The RSMs indicate that the alloy layer lattice constant becomes larger in-plane (decrease in reciprocal lattice units) and becomes smaller out-of-plane (increase in reciprocal lattice units). The amount of in-plane strain in each in-plane direction, {[001] (red arrow), [-110] (blue arrow)} is the change in in-plane lattice constant over the initial in-plane lattice constant $\Delta a_{//}/a_{//} = 0.6 \pm 0.1\%$. (C) (220) θ/2θ XRD scan of the same trilayer before release (solid) and after a full release (dashed). The uniform shift (0.08°) indicates elastic strain sharing and an out-of-plane strain relaxation, $\varepsilon_{\perp} = 0.32 \pm 0.04\%$, which translates into an in-plane strain, $\varepsilon_{//} = 0.64\% \pm 0.09\%$. The measurements closely agree with the expected strain transfer as calculated from Equation 3 for this heterostructure (D).

Figure 2-12C shows an example of θ/2θ (220) line scans before and after release [a θ/2θ scan around the (004) reflection of the Si(001) bulk substrate is used as reference]. Again, the main peak, from the SiGe layer, shows a shift to a higher Bragg angle, indicating a reduction in the out-of-plane lattice constant and thus an expansion in the in-plane lattice constant. For elastic strain sharing, the expansion in the in-plane lattice constant of the SiGe will be equal to the tensile strain transferred to the Si layers after strain sharing occurs. The relationship between the out-of-plane strain change and the in-plane equibiaxial strain is different for (001) and (110) oriented films (see Appendix A for details):

$$\Delta\varepsilon_{\parallel SiGe} = \frac{c_{11} + c_{12} + 2c_{44}}{c_{11} + 3c_{12} - 2c_{44}} \Delta\varepsilon_{\perp SiGe} = \varepsilon_{\parallel Si} \tag{2-15}$$

Table 2-1 shows the strain transferred to the Si(110) layers of several Si/SiGe/Si(110) NMs after release from the initial handle substrate. The expected strain transfer is calculated based on the thicknesses of the layers and the Ge composition of the alloy layer. The measured in-plane strain is extracted from measuring the out-of-plane lattice constant change in the SiGe layer.

Table 2-1. Structure of Si(110) NMs. The expected strain is calculated from Equation 3. The measured strain is extracted from the shift in the out-of-plane lattice constant.

Sample	Expected ε_{Si}	Measured ε_{Si}
9.5nm Si/49nm $Si_{.77}Ge_{.23}$/9.5 nm Si	0.63%	0.64 ± 0.09%
15nm Si/61nm $Si_{.83}Ge_{.17}$/14nm Si	0.43%	0.43 ± 0.08%
9nm Si/81nm $Si_{.88}Ge_{.12}$/10nm Si	0.33%	0.28 ± 0.05%
14nm Si/36nm $Si_{.79}Ge_{.21}$/12nm Si	0.45%	0.46 ± 0.03%

The RSMs around the (331) and (260) reflections (Figures 2-12A and B) were used to confirm that the strain sharing in the Si(110) trilayer NMs is indeed biaxially isotropic. With these reflections, I directly measured the in-plane lattice constant change in the [001] and [-110] directions, respectively. I created a trilayer Si(110) NM in which some of the membrane was allowed to strain share, while a portion was still attached to SiO_2. The latter provides a reference of the intact as-grown structure. In both reflections there is little in-plane peak broadening and all the peaks align along the direction normal to the film surface, indicating that the in-plane lattice constant remains the same throughout the thickness of the film, *i.e.*, the SiGe in-plane lattice constants match those of the Si layers. Any relaxation of the alloy layer would be indicated by a broadening and in-plane shift of the SiGe peak toward the relaxed SiGe line. Figures 2-12A and B show that the membranes remain fully coherent (*i.e.*, an epitaxial relationship without interface dislocations is maintained) after the strain sharing process as well. If the strain in the Si layers were not a result of the strain sharing with the alloy layer, the in-plane lattice constants of the Si and SiGe would not match; two main peaks would be visible for both the released and as-grown portions of the RSMs, indicating one horizontal position for the Si layers and another position for the SiGe layer. The absence of a Si peak in the RSMs shown in Figures 2-12A and B indicates that the Si and SiGe layers have the same in-plane lattice constant (the Si peak lies along a line with the same horizontal position as the SiGe), thus indicating proper strain sharing between the three layers. I measured equal strain in the two dissimilar perpendicular in-plane directions, indicating that the SiGe undergoes isotropic strain relaxation upon release. This implies that the in-plane biaxial strain in the Si is also isotropic.

I have shown that it is possible to obtain equibiaxial in-plane strain with elastic strain sharing between materials with 2-fold structural and elastic symmetry: Si/SiGe/Si(110) NMs. Furthermore, I can tune the amount of *isotropic* in-plane strain in the Si balancing layers of a trilayer Si(110) NM up to ~0.7% [28] by changing the Ge composition (alters the mismatch strain, ε_m) of the alloy layer or the layer thickness ratio (η). This result is in distinct contrast to the anisotropic strain produced in Si epitaxially grown on conventional relaxed bulk SiGe(110) substrates: anisotropic strain relaxation of the SiGe(110) alloy results in anisotropic strain in the Si grown on top [30].

2.4.3 Case 3

The third situation for elastic strain sharing is that of an elastically isotropic stressor layer between layers of elastically 2-fold symmetric balancing layers. An example is a deposited amorphous thin film (a-Si) between two (110)-oriented cubic single-crystalline NMs [Si(110)]. Here I assume an equibiaxial mismatch strain ($\varepsilon_{xx} = \varepsilon_{yy}$, $\varepsilon_{xy} = 0$), and that the strain is constant through the thickness of the elastically-isotropic strained film. These are reasonable assumptions for a truly randomly-oriented polycrystalline or amorphous intrinsically strained metal thin film: the elastic properties of the film are isotropic and the force exerted by the film varies linearly with film thickness [19]. Recall that the mismatch strain remains constant for coherent films for any given strain-sharing condition (Eq. 2-2). In this case, coherency of the layers means that the atoms at the interface between the two materials do not slip or rearrange during strain sharing: the bonding points at the interfaces between the stressor layer

and balancing layers do not change. Because the mismatch strain is equibiaxial, any anisotropy in the strain distribution in the 2-fold-elastically-symmetric balancing layers after elastic strain sharing is a direct result of the elastic anisotropy of the balancing layers. I assume an in-plane mismatch strain of ε_o = 1% and choose elastic constants for the stressor layer that are similar in stiffness to the balancing layers (but isotropic) [Si(110)/a-Si/Si(110) trilayer]. The resulting strain distribution in the low-elastic-symmetry balancing layers after elastic strain sharing is shown in Figure 2-10C. The strain distribution in the low-elastic-symmetry balancing layers has varying degrees of anisotropy as a function of thickness ratio, η. The degree of anisotropy in the strain distribution is discussed in section 2.5.

2.4.4 Case 4

Finally, the fourth situation is a uniaxially mismatched system in which the stressor layer has 2-fold elastic symmetry and the outer balancing layers are elastically isotropic in-plane [*e.g.*, (001)-oriented cubic single-crystalline NM]. A uniaxially mismatched system is one in which the lattice mismatch is large in one in-plane direction and smaller perpendicular to that: the mismatch strain is now a function of in-plane direction. The strain can be introduced *via* growth or *via* bonding a pre-strained membrane between two unstrained ones, something that is feasible because membranes bond very well. A strain mismatch of this sort occurs for a hexagonal material growing in a [1-100] orientation on a (001)-oriented cubic surface [31], or by bonding a mechanically anisotropically deformed stressor layer between elastically biaxially isotropic balancing layers. For simplicity, I assume a mismatch strain in which the normal in-plane strains are $\varepsilon_{xx} = \varepsilon_m$, $\varepsilon_{yy} = a\varepsilon_m$, and $\varepsilon_{xy} = 0$. Where the x-direction in the film {[-110] on a

(110)-oriented surface} is aligned with the [110] direction on the cubic (001) surface. This scenario is reasonable either for well aligned NM transfer [32] or for epitaxial growth with a uniaxial mismatch, in which the direction of highest mismatch is aligned in only one of the <110> type directions (*i.e.*, no twins); a situation that can occur if the hexagonal film is grown on a patterned or vicinal (001)-oriented cubic surface [33]. In this description, the elastic constants for the stressor are arbitrarily chosen such that the soft direction (low elastic modulus) of the stressor layer is aligned in the direction of highest mismatch strain. The strain distribution in the balancing layers after strain sharing is shown in Figure 2-10D, assuming a ε_m = 0.2% and a = 4. The strain transferred to the balancing layers follows the symmetry of the mismatch strain closely. That is, we can take a 4-fold crystallographically symmetric surface orientation and apply strain to create a material with 2-fold crystallographic symmetry. Lattice deformation of this sort is equivalent to applying a small in-plane isotropic biaxial strain and a uniaxial strain at the same time. The ability to break the symmetry in highly crystallographically symmetric materials offers opportunities to exploit new materials properties not seen otherwise, such as demonstration of the linear electro-optic effect in Si [34] and antiferromagntism in certain dielectric oxides [35].

2.5 Optimizing strain and anisotropy

I have shown that the strain distributions in elastically strain-shared NMs depend on the elastic symmetry of the two materials and the initial mismatch strain distribution between the layers of a functional trilayer NM. Additionally, the magnitude of strain transferred to the outer

balancing layers can be tuned by varying the thickness ratio (η), similar to what was shown for the isotropic strain sharing case in section 2.3. Figure 2-10 shows that as the stressor layer thickness increases with respect to the balancing layer thickness (increasing η), more strain is transferred to the balancing layers. It is important to note that the above strain sharing analysis is only valid for *elastically* deformed layers. In order to avoid plastic relaxation of any of the layers during strain sharing, the absolute thickness of each of the layers is just as important as the relative thickness ratio. As the layers get thicker (more bulk like), less elastic strain is accommodated by the material before plastic deformation occurs; all the layers must remain below the kinetic critical thickness for plastic strain relaxation at all steps during the strain sharing process (see section 1.3.4 for details). The thinness of NMs enables elastic strain sharing. If the dimensions of all layers were scaled to the wafer level (*e.g.*, similar trilayers made with wafer bonding), delamination and fracture would occur for similar strain levels. This capability is of considerable importance when considering integration of epitaxially or thermally mismatched materials for high-performance applications where strain is desired, but where the presence of any materials defects will significantly decrease device performance. Examples include group IV strained quantum wells for quantum computing devices [36], strained superlattices for group IV quantum cascade lasers [37], and group III-N growth for solar-cell applications [38]. In such materials applications, strain profiles are currently controlled by defect generation (i.e., growing strained films on substrates fabricated via the graded buffer layer technique discussed in section 1.3.5), such that the magnitude, direction, and uniformity of the strain cannot be engineered for optimum materials properties.

While the thinness of NMs allows for the introduction of large amounts of strain without defects, the transferability of NMs allows one to incorporate materials with differing elastic constants to give another parameter to tune the strain transfer in trilayer NM systems. I have already demonstrated how varying the elastic symmetry of individual layers affects the transferred strain distributions. For clarity in Figure 2-10 I used stressor layers with elastic constants of similar magnitudes to those of the balancing layers to highlight the effects of varying thickness ratios and elastic symmetry. Because trilayer NM systems can be created by transfer processes, materials with different stiffnesses can be integrated to enhance strain transfer. By using stressor materials that are 'stiffer' (higher modulus) with balancing layers that are 'softer' (lower modulus) there is less resistance on the stressor layer such that it can relax more completely, thus transferring higher amounts of strain to the softer balancing layers. The effect of controlling the stiffness of layers is shown in Figure 2-13 for the trilayer systems described in Case 3. The second set of curves (blue) in both plots represents the same thickness ratio as the original curves (black), but the stiffness of the strained layer is increased by a factor of ~3. The strain transferred to the balancing layers increases with increasing stressor layer elastic modulus (Figure 2-13A), but the degree of anisotropy for this particular case (Case 3: 2-fold elastically symmetric balancing layers with elastically isotropic stressor layer) decreases (Figure 2-13B). Here I define the degree of anisotropy as the ratio of strain values in the balancing layers in orthogonal directions in-plane ($\varepsilon_{<001>}/\varepsilon_{<110>}$). As the thickness ratio decreases (thickness of stressor layer decreases, thickness of balancing layers increases), the degree of

anisotropy increases, but less strain is transferred to the balancing layers. The change in degree of anisotropy is a result of the average elastic properties of the system.

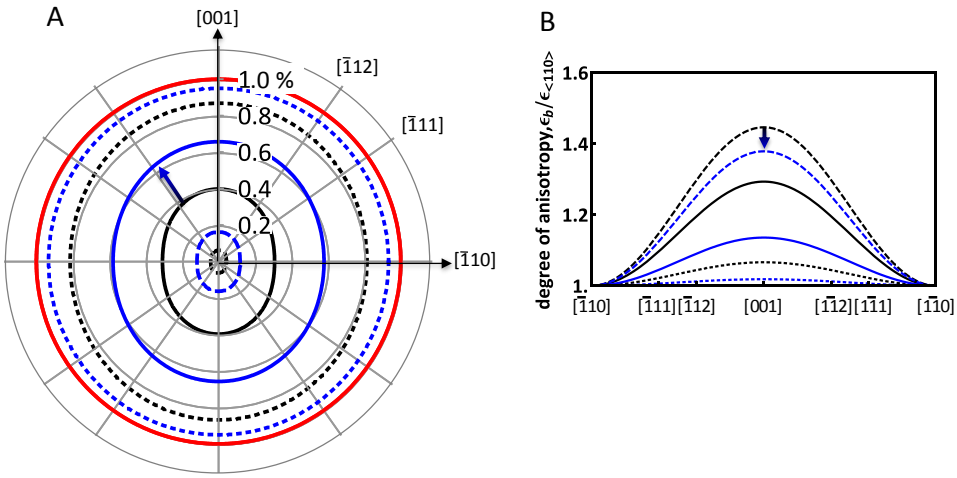

Figure 2-13. (A) Strain transferred to outer balancing layers for a heterostructure like Case 3: 2-fold elastically symmetric balancing layers with 4-fold elastically symmetric stressor layer. The mismatch strain is equibiaxial (red solid). The transferred strain is shown for three different thickness ratios: η = 0.1 (dashed), η = 1.0 (solid), and η = 10 (dotted) and two stiffnesses of the stressor layers (black curves and blue curves). The stressor layer (a-Ge) elastic modulus is slightly smaller than that of the balancing layers [crystalline Si(110)] for the black curves and is larger by about a factor of three (a-Cr as stressor layer) for the blue curves. The radial distance to any curve is the magnitude of the strain in that direction. The arrow indicates the increase in magnitude of the transferred strain for an increase in stressor layer elastic modulus for the same thickness ratio (example shown for η = 1.0). (B) The degree of anisotropy is taken to be the magnitude of the strain in a given direction normalized by the strain in the <110> type direction. The curve line types in (B) correspond to the same situations as the curves in (A). The magnitude of strain transfer is larger for stressor layers with larger elastic moduli, but the degree of anisotropy decreases (as shown by arrow for η = 0.1 curves).

When the elastic moduli are similar (black curves in Figure 2-13), the average elastic properties are scaled by the thickness ratio of the materials: thicker balancing layers means more anisotropic-like elastic properties, but also less strain transfer upon strain sharing. If the elastic

modulus of the stressor layer is increased (blue curves in Figure 2-13) then the average elastic properties of the system are also scaled by the effective stiffness differences between the materials. For the same thickness ratio, the overall system with the stiffer stressor will act more isotropic-like because the materials properties of the stressor dominate the system. This is an important consideration when combining dissimilar materials: semiconductors on polymers for flexible electronics [39] or dielectric oxides on semiconductors for nanoelectronics [40].

2.6 n-layer system

Thus far I only discussed elastic strain sharing in trilayer systems in which the top and bottom layers are identical in chemical composition, crystalline orientation, and mechanical properties, such that I can mathematically consider a bilayer system with one interface. This elastic strain sharing analysis can be extended to n-layer systems as long as the mismatch strain distribution at each interface and the elastic properties of each of the layers are known. For an n-layer system there will be n-1 coherency equations (one for each interface similar to Eq. 2-2). Assuming a balanced system, a freestanding NM heterostructure will remain flat and the forces in the heterostructure will still be in equilibrium. This condition produces an equation similar to Eq. 3 with a term ($t_i C_i \varepsilon_i$) for each layer.

As an example, consider the heterostructure shown in Figure 2-14A. There are three stressor layers and four balancing layers. The top and bottom stressor layers are identical (red)

and all the balancing layers (initially unstrained) are identical, thus the problem is reduced to a 3-layer system (n = 3) [Figures 2-14C and D].

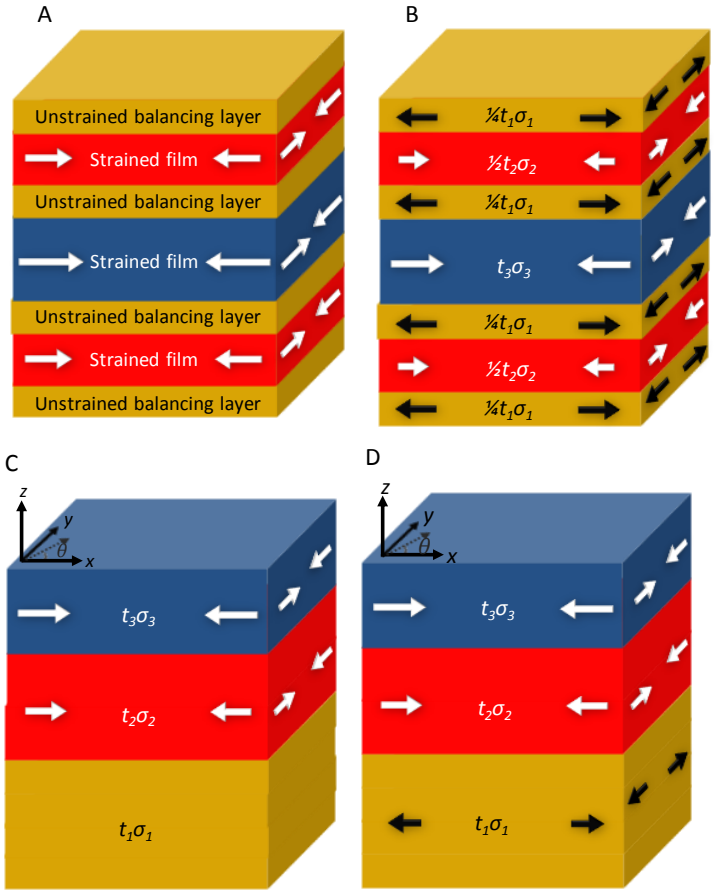

Figure 2-14. Mathematically equivalent models of balanced multilayer NMs. The arrows represent the relative magnitude and direction of the strain in each layer. The balancing layers and outer strained layers are identical in layer thickness, crystalline orientation, and composition. The balanced 7-layer heterostructure in (A) is mathematically equivalent to a trilayer system in which the balancing layer and outer strained layer thicknesses are added and represented as one layer (C). The figures on the left (A, C) show the initial state of each system: all the strain remains in the strained layers (red and blue) while attached to the initial handling substrate. The figures on the right (B, D) show the final state of the heterostructures after the NM has been allowed to strain share. Layer 1 represents the combined properties of the initially unstrained layers (yellow), layer 2 represents the outer initially strained (red) layers, and layer 3 represents the middle initially strained layer (blue).

The coherency conditions at the interfaces are:

$$\varepsilon_{m1} = \varepsilon_2 - \varepsilon_1 \quad \text{(2-16a)}$$

$$\varepsilon_{m2} = \varepsilon_3 - \varepsilon_1 \quad \text{(2-16b)},$$

where ε_{mi} is the mismatch strain at a given interface and ε_i is the strain in that layer. Both stressor layers are initially strained with respect to layer 1 (balancing layer). The forces must balance such that:

$$t_1 C_1 \varepsilon_1 + t_2 C_2 \varepsilon_2 + t_3 C_3 \varepsilon_3 = 0 \quad \text{(2-17)},$$

where t_i and C_i are the thickness and stiffness tensors for a given layer, respectively. Combining Eqs. 2-16 and 2-17, the strain transferred to the balancing layers can be calculated by evaluating:

$$C_1 \varepsilon_1 + \eta_1 C_2 \varepsilon_{m1} + \eta_1 C_2 \varepsilon_1 + \eta_2 C_3 \varepsilon_{m2} + \eta_2 C_3 \varepsilon_1 = 0 \quad \text{(2-18)},$$

where $\eta_1 = t_2/t_1$ and $\eta_2 = t_3/t_1$.

To ensure the n-layer system is balanced and will exhibit strain sharing without curling, the forces through the thickness of the structure must be equal and opposite. If this is not obvious from the symmetry of the heterostructure (like in Figure 2-14), the radius of curvature for the heterostructure in the freestanding state must be calculated (Eq. 2-4). If the radius is very large compared to the lateral size of the NM, or infinite, the structure will remain flat during strain sharing and the above analysis is valid. This type of analysis would be needed to calculate strain sharing in complex superlattice systems or if using dissimilar materials for balancing layers (top and bottom layers not identical).

2.7 Chapter summary

Nanomembranes are thin sheets of single-crystalline material that can be released from the host substrate with selective etching techniques. The thinness and the ability to release and transfer NMs make them uniquely suited to strain engineering. Strain can be incorporated by controlled deformation of a handle substrate or with elastic strain sharing techniques: the design of freestanding multilayer heterostructures. The magnitude, direction, and symmetry of strain in NMs can be tuned by integrating materials with different elastic and mismatch strain symmetries. I showed examples of strain sharing in epitaxial Si/SiGe/Si(001) and Si/SiGe/Si(110) NM systems, but elastic strain sharing techniques can be applied to any single crystalline NM material.

2.8 References

1. B. Tanto, Dislocation-Free Strain-Engineered Si and SiGe Nanomembranes. PhD Dissertation: Univ. of Wisconsin-Madison, (2009).
2. M. M. Kelly, Elastic Strain Sharing in Silicon/Silicon Germanium Nanomembranes. PhD Dissertation: Univ. of Wisconsin-Madison (2007).
3. M. A. Meitl, Z.-T. Zhu, V. Kumar, K. J. Lee, X. Feng, *et al.,* Transfer Printing by Kinetic Control of Adhesion to an Elastomeric Stamp. *Nature Mater.* **5** (2006) 33-38.
4. K. Zhang, J.-H. Seo, W. Zhou, Z. Ma, Fast Flexible Electronics using Transferrable Silicon Nanomembranes. *J. Phys. D: Appl. Phys.* **45** (2012) 143001.
5. A. M. Kiefer, D. M. Paskiewicz, A. M. Clausen, W. R. Buchwald, R. A. Soref, et al. Si/Ge Junctions Formed by Nanomembrane Bonding. *ACS Nano* **5** (2011) 1179-1189.
6. J. R. Sánchez-Pérez, C. Boztug, F. Chen, F. F. Sudradjat, D. M. Paskiewicz, *et al.,* Direct-Bandgap Light-Emitting Germanium in Tensilely Strained Nanomembranes. *P. Natl. Acad. Sci. USA* **108** (2011) 18893-18898.
7. A. Plößl, G. Kräuter, Wafer Direct Bonding: Tailoring Adhesion Between Brittle Materials. *Mater. Sci.*

Eng. **R25** (1999) 1-88.

8. Q.-Y. Tong, U. Gösele, Semiconductor Wafer Bonding: Recent Developments. *Mater. Chem. Phys.* **37** (1994) 101-127.

9. H.-J. Kim, Fracture Mechanics-Based Approaches to Understand and Control Adhesion in Thin Film Transfer Processes. PhD Dissertation: Univ. of Wisconsin-Madison (2011).

10. A. M. Kiefer, Silicon/Germanium Junctions Formed by Membrane Bonding. PhD Dissertation: Univ. of Wisconsin-Madison, (2011).

11. J.-H. Ahn, H-S. Kim, E. Menard, K. J. Lee, Z. Zhu, *et al.,* Bendable Integrated Circuits on Plastic Substrates by Use of Printed Ribbons of Single-Crystalline Silicon. *Appl. Phys. Lett*. **90** (2007) 213501.

12. F. Chen, C. Euaruksakul, Z. Liu, F. J. Himpsel, F. Liu, *et al.,* Conduction Band Structure and Electron Mobility in Uniaxially Strained Si via Externally Applied Strain in Nanomembranes. *J. Phys. D: Appl. Phys.* **44** (2011) 325107.

13. L. B. Freund, S. Suresh, *Thin Film Materials: Stress, Defect Formation, and Surface Evolution* Cambridge Univ. Press: Cambridge, MA, (2003).

14. G. A. Slack, S. F. Bartram, Thermal Expansion of Some Diamondlike Crystals. *J. Appl. Phys.* **46** (1975) 89-98.

15. M. M. Roberts, J. J. Klein, D. E. Savage, K. A. Slinker, M. Friesen, et al., Elastically Relaxed Free-Standing Strained-Silicon Nanomembranes. *Nat. Mater.* **5** (2006) 388-393.

16. S. A. Scott, M. G. Lagally, Elastically Strain-Sharing Nanomembranes: Flexible and Transferable Strained Silicon and Silicon-Germanium Alloys. *J. Phys. D: Appl. Phys.* **40** (2007) R75-R92.

17. C. Deneke, R. Songmuang, N. Y. Jin-Phillipp, O. G. Schmidt, The Structure of Hybrid Radial Superlattices. *J. Phys. D.: Appl. Phys.* **42** (2009) 103001.

18. M. Belyansky, M. Chance, O. Gluschenkov, J. Kemppisty, N. Klymko, *et al.,* Methods of Producing Plasma Enhanced Chemical Vapor Deposition Silicon Nitride Thin Films with High Compressive and Tensile Stress. *J. Vac. Sci. Technol. A* **26** (2008) 517-521.

19. R. Koch, The Intrinsic Stress of Polycrystalline and Epitaxial Thin Metal Films. *J. Phys. Condens. Matter* **6** (1994) 9519-9550.

20. J. Song, H. Jiang, Y. Huang, J. A. Rogers, Mechanics of Stretchable Inorganic Electronic Materials. *J. Vac. Sci. Technol. A* **27** (2009) 1107- 1125.

21. M. Huang, P. Rugheimer, M. G. Lagally, F. Liu, Bending of Nanoscale Ultrathin Substrates by Growth of Strained Thin Films and Islands. *Phys. Rev. B.* **72** (2005) 085450.

22. Y. S. Nam, S. W. Lee, K. S. Baek, S. K. Chang, J.-H. Song, *et al.,* Anisotropic Optical Properties of Free

and Bound Excitons in Highly Strained *A*-plane ZnO Investigated with Polarized Photoreflectance and Photoluminescence Spectroscopy. *Appl. Phys. Lett.* **92** (2008) 201907.

23. G. Bai, W. Ma, Phenomenological Analysis of Phase Transistions in Epitaxial Perovskite Ferroelectric Thin Films. *Physica B* **405** (2010) 1901-1907.

24. T. C. T. Ting, *Anisotropic Elasticity: Theory and Applications* Oxford Univ. Press: New York, (1996).

25. P. M. Mooney, G. M. Cohen, J. O. Chu, C. E. Murray, Elastic Strain Relaxation in Free-Standing SiGe/Si Structures. *Appl. Phys. Lett. **84** (*2004) **1**093.

26. D. L. Owen, D. Lackner, O. J. Pitts, S. P. Watkins, P. M. Mooney, In-place Bonding of GaAs/InGaAs/GaAs Heterostructures to GaAs (0 0 1). *Semicond. Sci. Technol. **24** (*2009) 035011.

27. A. C. Opotowsky, S. A. Scott, C. S. Ritz, D. E. Savage, G. K. Celler, M. G. Lagally, Structure of Elastically Strain-Sharing Silicon(110) Nanomembranes. *New J. Phys.* **7** (2007) 270.

28. D. M. Paskiewicz, S. A. Scott, D. E. Savage, M. G. Lagally, Elastically Strain-Sharing Si(110) Nanomembranes. *ECS Trans.* **33** (2010), 813-821.

29. K. Arimoto, J. Yamamamka, K. Nakagawa, K. Sawano, Y. Shiraki, N. Usami, K. Nakajima, Growth Temperature Dependence of Lattice Structures of SiGe/Graded Buffer Structures Grown on Si(110) Substrates by Gas-Source MBE. *J. Cryst. Growth* **301** (2007) 343-348.

30. V. Destefanis, D. Rouchon, J. M. Hartmann, A. M. Papon, L. Baud, A. Crisci, M. Mermoux, Structural Properties of Tensily Strained Si Layers Grown on SiGe (100), (110), and (111) Virtual Substrates. *J. Appl. Phys.* **106** (2009) 043508.

31. B. Z. Liu, J. A. Nogmai, Scanning Tunneling Microscopy Study of Dysprosium Silicide Nanowire Growth on Si(001). *J. Appl. Phys.* **93** (2003) 593-599.

32. S. Mack, M. A. Meitl, J. Baca, Z.-T. Zhu, J. A. Rogers, Mechanically Flexible Thin-Film Transistors that Use Ultrathin Ribbons of Silicon Derived from Bulk Wafers. *Appl. Phys. Lett*. **88** (2006) 213101.

33. B. Z. Liu, J. Nogmai, Growth of Parallel Rare-Earth Silicide Nanowire Arrays on Vicinal Si(001). *Nanotechnology* **14** (2003) 873-877.

34. R. S. Jacobsen, K. N. Andersen, P. I. Borel, J. Fage-Pedersen, L. H. Frandsen, *et al.,* Strained Silicon as a New Electro-Optic Material. *Nature* **441** (2006) 199-202.

35. F. H. Zhang, Z. Huang, G. Y. Gao, P. F. Chen, L. F. Wang, *et al.,* Anisotropic-Strain-Induced Antiferromagnetic-Insulating State with Strong Phase Instability in Epitaxial $(La_{0.8}Pr_{0.2})_{0.67}Ca_{0.33}MnO_3$ Films. *Appl. Phys. Lett.* **96** (2010) 062507.

36. M. A. Eriksson, M. Friesen, S. N. Coppersmith, R. Joynt, L. J. Klein, *et al.,* Spin-Based Quantum Dot Quantum Computing in Silicon. *Quantum Inf. Processing* **3** (2004) 133-146.

37. A. Borak, S. Tsujino, C. Falub, M. Scheinert, L. Diehl, *et al.,* Recent Results on the Road to a Si/SiGe Quantum Cascade Laser. *Mater. Res. Soc. Symp. Proc.* **832** (2005) F4.2.1.

38. B. R. Jampana, N. N. Faleev, I. T. Ferguson, R. L. Opila, C. B. Honsberg, Utilizing Polarization Induced Band Bending for InGaN Solar Cell Design. *Mater. Res. Soc. Symp. Proc.* **1167** (2009) 1167-O07-04.

39. Y. Sun, E. Menard, J. A. Rogers, H.-S. Kim, S. Kim, *et al.,* Gigahertz Operation in Flexible Transistors on Plastic Substrates. *Appl. Phys. Lett.* **88** (2006) 183509.

40. C. Dubourdieu, I. Gélard, O. Salicio, G. Saint-Girons, B. Vilquin, *et al.,* Oxide Heterostructures for Nanoelectronics. *Int. J. Nanotechnol.* **7** (2010) 320-347.

Chapter 3 Elastically relaxed SiGe nanomembranes

3.1 Fabrication of SiGe Nanomembranes

SiGe NM fabrication starts with epitaxial growth of thin SiGe alloy films on SOI(001) substrates. The alloy layer thickness is kept below the kinetic critical thickness for dislocation-mediated relaxation of SiGe grown on Si [1]. Because the kinetic critical thickness is higher at lower temperatures, I use a low growth temperature (≤ 450°C), which is only possible in MBE (see section 1.3 for details). Immediately following the SiGe film growth, a Si capping layer of similar thickness as the SOI template layer is grown on top. The resulting heterostructure is a Si/SiGe/Si trilayer, where the SiGe in-plane lattice parameter is strained to that of the Si lattice constant (Fig. 3-1A).

The NM size and shape is patterned with photolithography and plasma etching (identical to the process for the fabrication of unstrained NMs described in Chapter 2). The buried oxide (BOX) layer is selectively etched away in hydrofluoric acid (HF) to release the Si/SiGe/Si trilayer from the SOI handling substrate (Figure 3-1B). In this step, the compressively strained SiGe layer shares its strain with the sandwiching Si layers (as described in Chapter 2). The Si layers are then selectively etched away in a dilute potassium hydroxide (KOH) solution [45% KOH, dionized (DI) water, and isopropyl alcohol (IPA) at room temperature, with volume mixing ratio KOH:DI water:IPA = ~ 1:4:4 [2]], allowing the strain in the SiGe to relax elastically (Figure 3-1C), leaving a perfectly crystalline SiGe NM with a lattice constant appropriate to bulk SiGe at the appropriate composition suspended in the KOH solution. The SiGe NM is transferred to DI

water and then the wet transfer techniques described in Chapter 2 are used to transfer the SiGe NM to a new oxidized Si substrate (Figure 3-1D). The SiGe NMs are bonded to the new host substrate by annealing at 500°C.

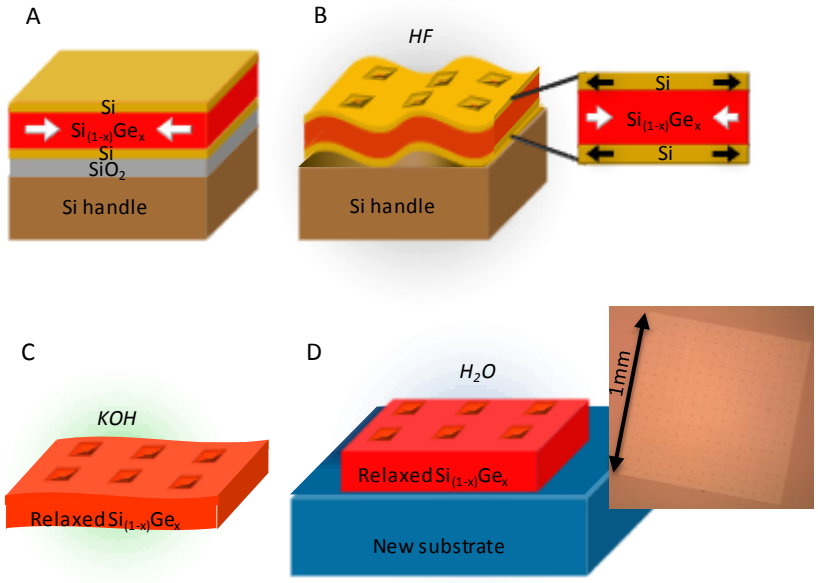

Figure 3-1. SiGe fabrication process. (A) SiGe and top Si layers are epitaxially grown on SOI. (B) Etchant access holes are patterned with photolithography and reactive ion etching (RIE). Then the BOX layer of the SOI is selectively etched in HF. (C) The top and bottom Si layers are selectively etched in a KOH solution. (D) The SiGe NM is transferred to a new host substrate in water and annealed to 500°C to encourage bonding. The inset is an optical micrograph of a typical SiGe NM that has been transferred to oxidized Si. The periodic dark specs in the image are 5µm wide etchant access holes.

$Si_{1-x}Ge_x$ NMs with 20% < x < 40% have been successfully fabricated with the above technique [2, 3]. The composition range is set by the KOH etch selectivity (low) and the kinetic critical thickness (high). For sufficiently high Ge content (x > 20%), the etch rate of the SiGe in KOH is ~200x slower than that of pure Si [4]. The etch selectivity increases with increasing Ge concentration. The upper limit for SiGe NM compositions is set by the kinetic critical thickness

because the initial SiGe films are grown on rigid Si substrates (SOI). The layers must be kept thin to avoid plastic relaxation, however, the layers must be thick enough to handle the resulting SiGe NMs (> 20nm) without breaking them. When growing the SiGe films with low-temperature MBE, ~20-30nm thick ~$Si_{0.6}Ge_{0.4}$ films can be grown without significant plastic strain relaxation (see section 1.3.2).

While the etch rate of SiGe is negligible (>200x slower depending on the Ge concentration) in comparison to Si in KOH, it is worth pointing out that it is not zero. For this reason, it is important to remove the SiGe NMs from the KOH solution very soon after the Si has been etched away (within ~5min) to avoid excess roughening of the SiGe NM. I use a room temperature, dilute (~5%) KOH solution to reduce the etch rate significantly (from >1μm/min at 80°C to ~25nm/min at room temperature for Si [5]). This is acceptable because the Si layers are very thin (< 50nm) and will still etch away within minutes. Figure 3-2 shows atomic force microscopy (AFM) images of similar SiGe films: one grown on bulk Si and thus strained to the Si lattice constant (Figure 3-2A) and one a SiGe NM elastically relaxed and transferred to a new oxidized Si substrate (Figure 3-2B). Both the film and the NM are below the kinetic critical thickness. The root-mean-square (rms) roughness of the SiGe NM is slightly higher than that of the strained SiGe film grown on the bulk Si substrate, which is to be expected from slight etching in the KOH solution. Overall surface morphology is similar for the two films and SiGe does not significantly roughen in the KOH solution.

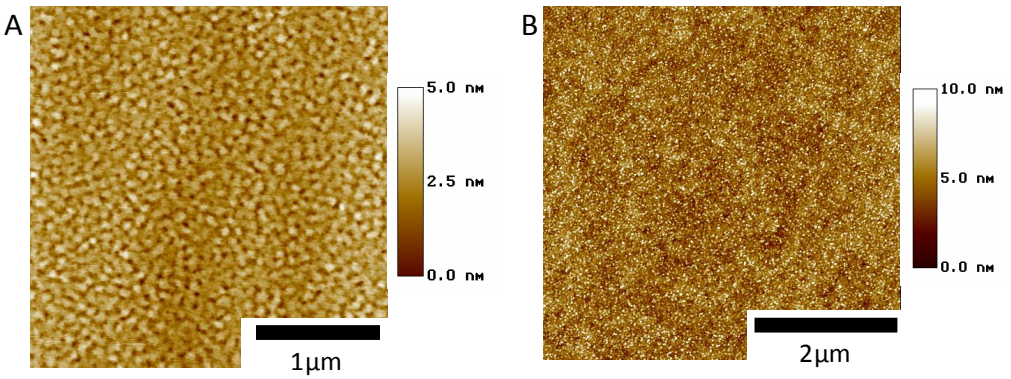

Figure 3-2. AFM images of the surface of (A) 40nm $Si_{0.75}Ge_{0.25}$ film pseudomorphically grown on a bulk Si substrate (0.6nm rms roughness) and (B) ~55nm $Si_{0.75}Ge_{0.25}$ NM transferred to an oxidized Si substrate (1.4nm rms roughness).

A typical SiGe NM fabricated with the above technique is shown in the inset of Figure 3-1D; the lateral dimensions are currently limited to ~1mm x 1mm. The lateral area is limited because the NMs curl into tubes during the second release step (Figure 3-1C). The bending is most likely caused by a difference between the top and bottom Si thicknesses during the etching process. The KOH etchant has full access to the top Si layer, but needs time to undercut the bottom Si layer. Recall that the Si/SiGe/Si trilayer has settled onto the original handle substrate after etching the SiO_2 layer. The difference in etchant access will lead to different Si thicknesses on the top and bottom of the SiGe during etching, thus the strain will not be balanced through the thickness of the heterostructure and the NM will curl. When left in the KOH for some time, the NM starts to uncurl because the remaining Si is etched away, and the elastically relaxed SiGe NM no longer has any strain to keep it curled. When the NMs are large laterally, they roll onto themselves many times. For a given mismatch strain and thickness ratio

(t_{Si}/t_{SiGe}) the radius of curvature will remain the same, therefore a larger NM will roll more times to reach the same radius of curvature as the smaller NM (see Figure 3-3).

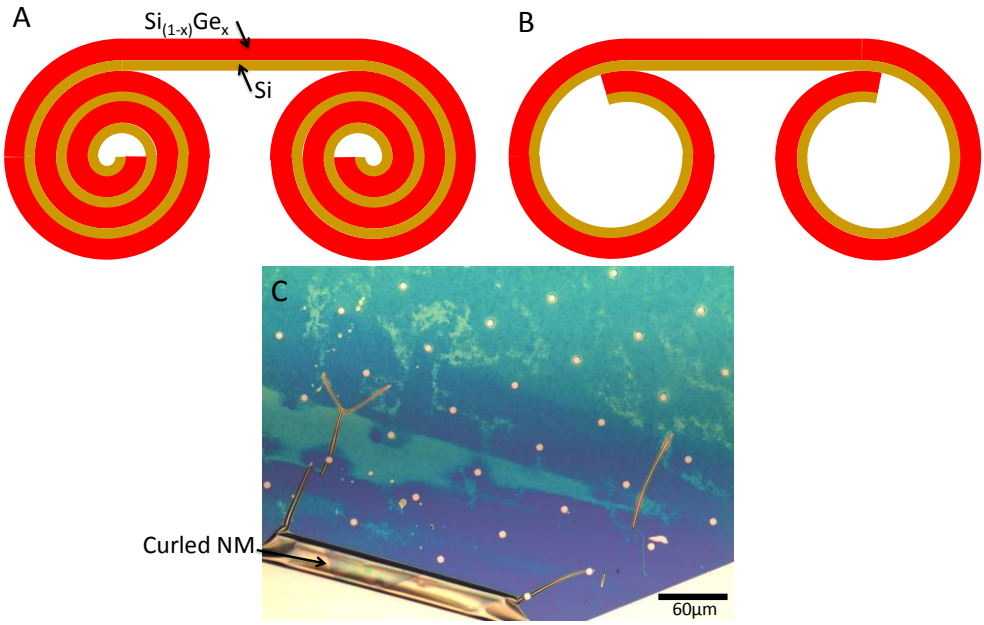

Figure 3-3. Schematic diagrams of hypothesized SiGe (red)/ Si (brown) bilayers curling in KOH for (A) large lateral area NMs, and (B) small lateral area NMs. The radius of curvature is similar for both structures because the mismatch strain and thicknesses of the films are similar. The number of times the NMs rolls is different because of the lateral size of the NM. (C) Optical micrograph of ~45nm $Si_{0.73}Ge_{0.27}$ NM after release and transfer to SOI(001). It is likely that not all the Si was etched away during the Si selective etch (note color variations on flat portion of NM). The NM is curled in the bottom left corner of the image where there is still enough Si to cause bending.

The likelihood of the rolled surfaces bonding together in the curled state is very high. The rolled structure may also restrict KOH etchant access to the Si layers, thus limiting the ability of the NM to unroll because the Si cannot be etched away properly. One way to circumvent this problem would be to grow the top Si layer thicker than the bottom template Si layer. If grown to the appropriate thickness the top Si layer and bottom Si layers would etch away at the same

time keeping the heterostructure balanced during the second etch step. The issue with this proposed change is that the trilayer is then unbalanced during the first etch step, (Figure 3-1B, etching of the SiO_2 layer) and the heterostructure will curl from the initial unbalanced strain before it reaches the KOH solution. The compromise for this fabrication technique is to limit the lateral area of the SiGe NMs to ~1mm x 1mm square; the yield for SiGe NMs of this size is ~80-90%.

3.2 Characterization of elastic strain relaxation

The strain state of the SiGe NMs is characterized at each step throughout the fabrication process to ensure that the alloy is elastically relaxing. In the initial stage of SiGe NM fabrication, the SiGe film is pseudomorphically grown on a Si substrate; the alloy is compressively strained to the Si lattice constant. After release of the SiGe NM, the strain must be measured again to ensure that there is no strain in the NM: all the strain has been elastically relaxed during the release process. I measured the strain state and uniformity of the strain in the layers with high-resolution x-ray diffraction (XRD), micro-Raman spectroscopy, or a combination of the two techniques. Both techniques were described in detail in chapter 1.

3.2.1 X-ray diffraction

The as-grown Si/SiGe/Si(001) trilayer heterostructures are characterized with θ/2θ XRD line scans through the (004) reflection. These scans (shown in Fig. 3-4) are fit to simulations to extract the Ge concentration and thickness of the alloy layer. The (004) reflection is a measurement of the out-of-plane lattice parameter; therefore I expect the SiGe peak to be at a

lower Bragg angle (larger plane spacing) than the Si peak. The SiGe will be compressively strained to the Si lattice parameter in-plane, and, as a consequence of the Poisson effect, will expand in the out-of-plane direction. The Ge composition extracted from these scans assumes that the alloy layer is fully strained to the Si lattice constant in-plane. The presence of well-defined thickness fringes implies smooth interfaces, a good indicator of high-quality, coherent epitaxial growth.

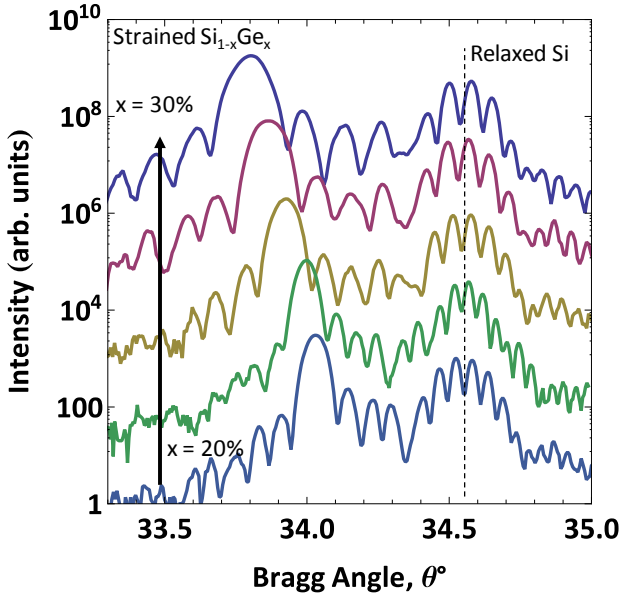

Figure 3-4. θ/2θ XRD line scans through the (004) reflection for five different $Si/Si_{1-x}Ge_x/Si$ heterostructures, 20% < x < 30%. The thickness and composition of the pseudomorphic SiGe are extracted from fits to simulations.

To verify that there is no plastic relaxation in the as-grown films, off-axis reciprocal-space maps (RSMs) are taken around the (224) reflection for the different trilayer heterostructures, as shown in Figure 3-5. All RSMs show that the SiGe is fully strained to the Si lattice constant; the in-plane lattice parameter is the same as that of Si. If the alloy layer were

starting to relax, the SiGe peak would not have the same in-plane lattice parameter as the Si layers (horizontal peak position); the SiGe peak would start to spread and move along the relaxation lines drawn in Figure 3-5. The peak broadening along the relaxation line for the 25%-Ge-concentration sample (Figure 3-5C) may be explained by the onset of plastic relaxation. This will be described in more detail in the next section. The measurements demonstrate that the SiGe NMs remain fully strained to the Si lattice constant in the as-grown state.

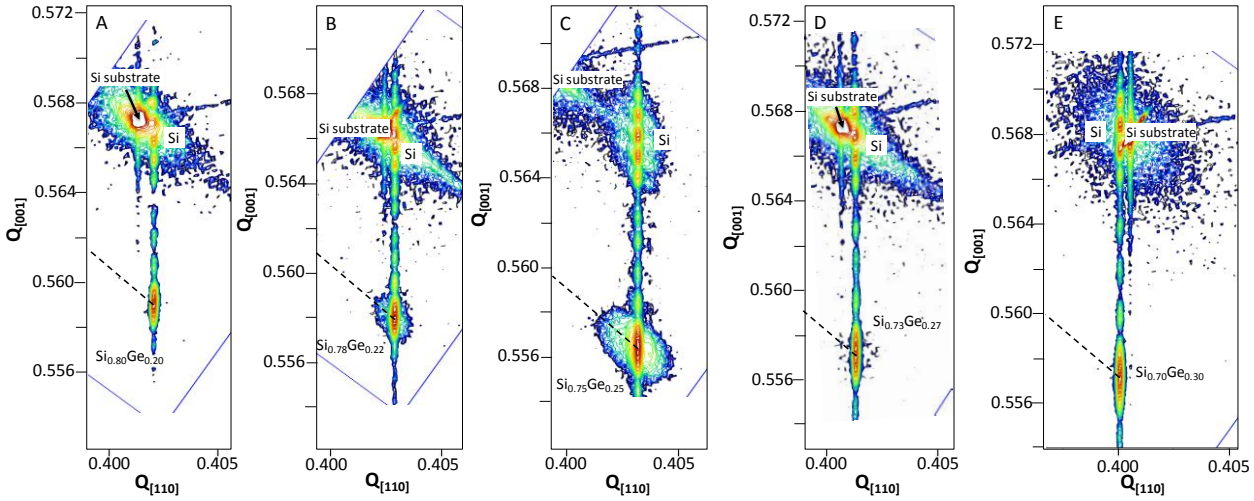

Figure 3-5. Off-axis RSMs around the (224) reflection for Si/SiGe/Si as-grown heterostructures. In all cases the SiGe film is strained to the Si lattice constant in-plane (horizontal position). Plastic relaxation of the alloy layers would be present as diffracted intensity along the relaxation line (dashed line). The very intense, Si substrate peak is separated from the Si/SiGe/Si heterostructure because the miscut of the Si template layer of the SOI is slightly different from that of the bulk Si handle wafer. The shift in the Si peak between the heterostructure and the Si substrate represents different tilt angles, not changes in the lattice constant.

Upon release of the SiGe NMs the strain in the alloy should approach 0%, meaning that the change in strain from the as-grown state to the released state of the NMs should be consistent with full relaxation of $Si_{1-x}Ge_x$. I measured the change in out-of-plane lattice constant

with strain relaxation of SiGe NMs with θ/2θ XRD line scans through the (004) reflection (Figure 3-6A).

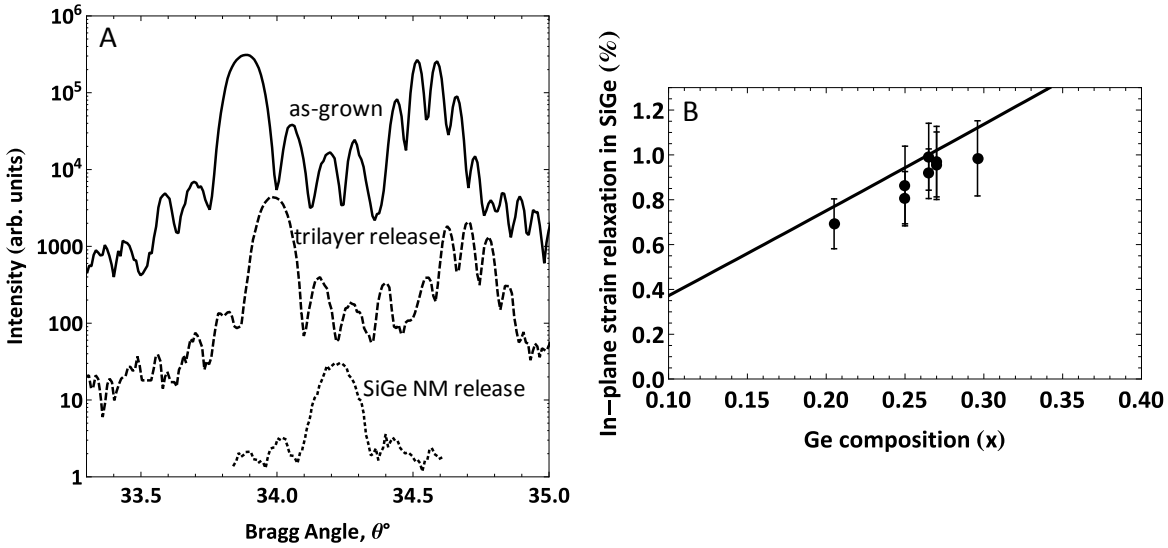

Figure 3-6. Strain relaxation in SiGe NMs as measured with θ/2θ XRD line scans through the (004) reflection. (A) Example of θ/2θ XRD line scans through the (004) reflection for $Si_{0.73}Ge_{0.27}$ NM fabrication process. The change in out-of-plane lattice constant for each step of the fabrication process is consistent with expectations. The out-of-plane strain change in the SiGe for the trilayer release is -0.28 ± 0.08% ($\varepsilon_{||}$ = 0.37 ± 0.10%) and the SiGe NM release is -0.79 ± 0.12% ($\varepsilon_{||}$ = 0.99 ± 0.15%). The expected in-plane strain relaxation for these steps is $\varepsilon_{||}$ = 0.43% and $\varepsilon_{||}$ = 1.00%, respectively. (B) Inferred in-plane strain relaxation (based on measurement of out-of-plane lattice constant) for SiGe NMs with 20% < x < 30%. The solid line is the expected strain relaxation based on Ge composition.

The shift in the SiGe peak represents the change in out-of-plane lattice constant at each step of the fabrication process. After release of the trilayer, the out-of-plane lattice constant decreases (increase in Bragg angle) to a strain state consistent with elastic strain sharing (chapter 2). Once the Si layers are removed, the SiGe relaxes to the bulk lattice constant consistent with the

appropriate Ge composition. The in-plane strain is inferred based on the Poisson relationship between out-of-plane strain and in-plane strain (Eq. 2-14) Figure 3-6B shows a summary of the in-plane strain relaxation for $Si_{1-x}Ge_x$ NMs 20% < x < 30%.

I also measured the in-plane strain relaxation in the SiGe NMs directly by combining the above out-of-plane lattice measurements with RSMs around the (224) reflection. Measurements of the magnitude of the (004) and (224) reciprocal-lattice vectors allow me to calculate the magnitude of the in-plane reciprocal-lattice vector, $|q_{220}|$ [Figure 3-7A].

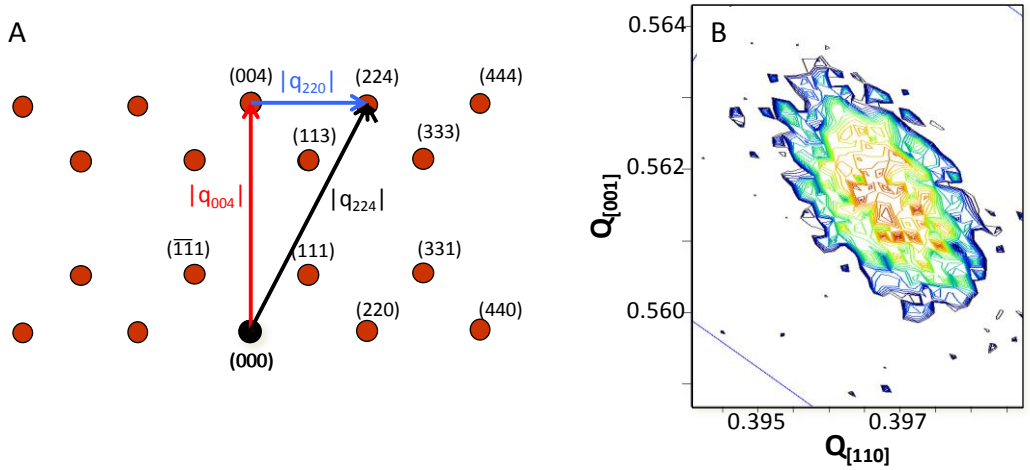

Figure 3-7. (A) Schematic representation of reciprocal space in the plane defined by [001] and [110]. The magnitude of the in-plane reciprocal-lattice vector, $|q_{220}|^2 = |q_{224}|^2 - |q_{004}|^2$. (B) RSM around the (224) reflection for a $Si_{0.73}Ge_{0.27}$ NM. The resulting in-plane strain from this measurement [and the (004) measurement of Figure 3-6] is -0.04 ± 0.10%.

The magnitude of the reciprocal-lattice vector, $|q_{hkl}|$, is related to the plane spacing, d_{hkl}, by:

$$|q_{hkl}| = \frac{\lambda}{2d_{hkl}} \tag{3-1}$$

where λ is the wavelength of the x-rays. The in-plane ($\varepsilon_{//}$) and out-of-plane ($\varepsilon_{\perp}$) strains relate the strained/measured plane spacing, d_{hkl}, to the unstrained plane spacing, d^{o}_{hkl}:

$$d_{004} = d^{o}_{004}\left(1+\varepsilon_{\perp}\right) = \frac{-2c_{12}}{c_{11}}\varepsilon_{\parallel} \tag{3-2a}$$

$$d_{220} = d^{o}_{220}\left(1+\varepsilon_{\parallel}\right) \tag{3-2b}.$$

Using the ratio of the unstrained plane spacings ($d^{o}_{220}/d^{o}_{004} = \sqrt{2}$) and Eqs. (3-2), the in-plane strain is:

$$\varepsilon_{\parallel} = \frac{d_{220} - \sqrt{2}d_{004}}{\frac{2c_{12}}{c_{11}}d_{220} + \sqrt{2}d_{004}} \tag{3-3}.$$

Figure 3-7B shows an example RSM around the (224) reflection for a $Si_{0.73}Ge_{0.27}$ NM (similar NM to that shown in Figure 3.6A). The diffracted intensity is very weak (the RSM intensity is on a Log scale from 1.5 – 8.0 cts/sec) because the sample size (~1mm x 1mm) is smaller than the x-ray beam size (~1mm x 1cm). This makes XRD measurements on SiGe NMs difficult and time consuming. The next section will describe how micro-Raman spectroscopy makes strain measurements on SiGe NMs more efficient and allows me to measure strain variations on the local scale, rather than averaging over the entire area of the sample.

3.2.2 Micro-Raman spectroscopy

I also use micro-Raman spectroscopy to monitor the strain state of the SiGe NMs throughout the fabrication process. With knowledge of the Ge composition in the SiGe NM from XRD measurements in the as-grown state, I can measure the strain change in the SiGe NM by measuring the frequency shift of the Raman peaks associated with SiGe going from the as-

grown state to the released state. There are three Raman modes in SiGe corresponding to the three types of bonds found in the random alloy: Si-Si (near 500cm^{-1}), Si-Ge (near 400cm^{-1}), and Ge-Ge (near 300cm^{-1}). The relative intensity of each of the three peaks is proportional to the number of that type of bond being measured at a given time. Alloys with more Si than Ge (like the SiGe described in this work) will have a strong Si-Si peak, a weaker Si-Ge peak, and a very weak Ge-Ge peak (if present at all). The exact Raman frequencies of the three modes are proportional to the Ge composition and strain. For biaxial strain in the (001) plane, the frequency shift (relative to the frequency for the unstrained material) is linearly proportional to strain: $\Delta\omega_{SiGe} = b_i\varepsilon_{SiGe}$ [6, 7], where ε_{SiGe} is the biaxial in-plane strain in the SiGe layer and b_i is a constant based on elastic constants and phonon deformation potentials of SiGe. The derivation of the strain coefficient was presented in chapter 1. There will be a different b_i for each of the three types of bonds. The linear coefficients ($b_{Si\text{-}Si}$, $b_{Si\text{-}Ge}$, $b_{Ge\text{-}Ge}$) that relate frequency shift ($\Delta\omega_{SiGe}$) and biaxial strain (ε_{SiGe}) in SiGe have been experimentally determined [7] and are given in Table 3-1. The coefficients do not significantly depend on Ge concentration.

Table 3-1. Experimentally determined strain coefficients for the three Raman modes of SiGe [7].

$b_{Si\text{-}Si}$	-730 ± 70cm^{-1}
$b_{Si\text{-}Ge}$	-570 ± 50cm^{-1}
$b_{Ge\text{-}Ge}$	-450 ± 30cm^{-1}

Raman spectra from five SiGe NM samples are shown in Figure 3-8 (20% < x < 32%). After release and transfer of the SiGe NMs, the Si-Si and Si-Ge peaks move to lower wavenumbers (details shown in insets of Figures 3-8A and E), implying an increase in the in-plane lattice parameter with respect to the initial as-grown compressively strained state. The

frequency shifts of the Si-Si peaks for several elastically relaxed SiGe NMs are shown in Figure 3-8H. The frequency shifts are consistent with full elastic relaxation of compressive strain from fully strained $Si_{(1-x)}Ge_x$ films grown pseudomorphically on Si with appropriate Ge compositions. The absence of a strained-Si peak in Figures 3-8A-E (this peak would appear between the peaks from the bulk Si and Si-Si mode of the SiGe) indicates that all of the Si was removed from the Si/SiGe/Si heterostructure during the fabrication of the SiGe NMs.

The frequency of the SiGe Raman modes is also dependent on the composition of the alloy. Ideally, if two of the three Raman modes for SiGe are measured, the strain and Ge composition can be determined from a single spectrum. The issue is that there are many empirical models for the Raman frequency shift dependence for relaxed alloys [8-11] and each model will result in a slightly different result. Using the model that best fits my data [8], I plotted the Raman frequency for the SiGe NMs in the as-grown state (Figure 3-8F) and after release (Figure 3-8G). In practice, the uncertainty in the peak position of the weak Si-Ge mode results in large errors in both Ge composition and strain. Details of this analysis can be found in Appendix B.

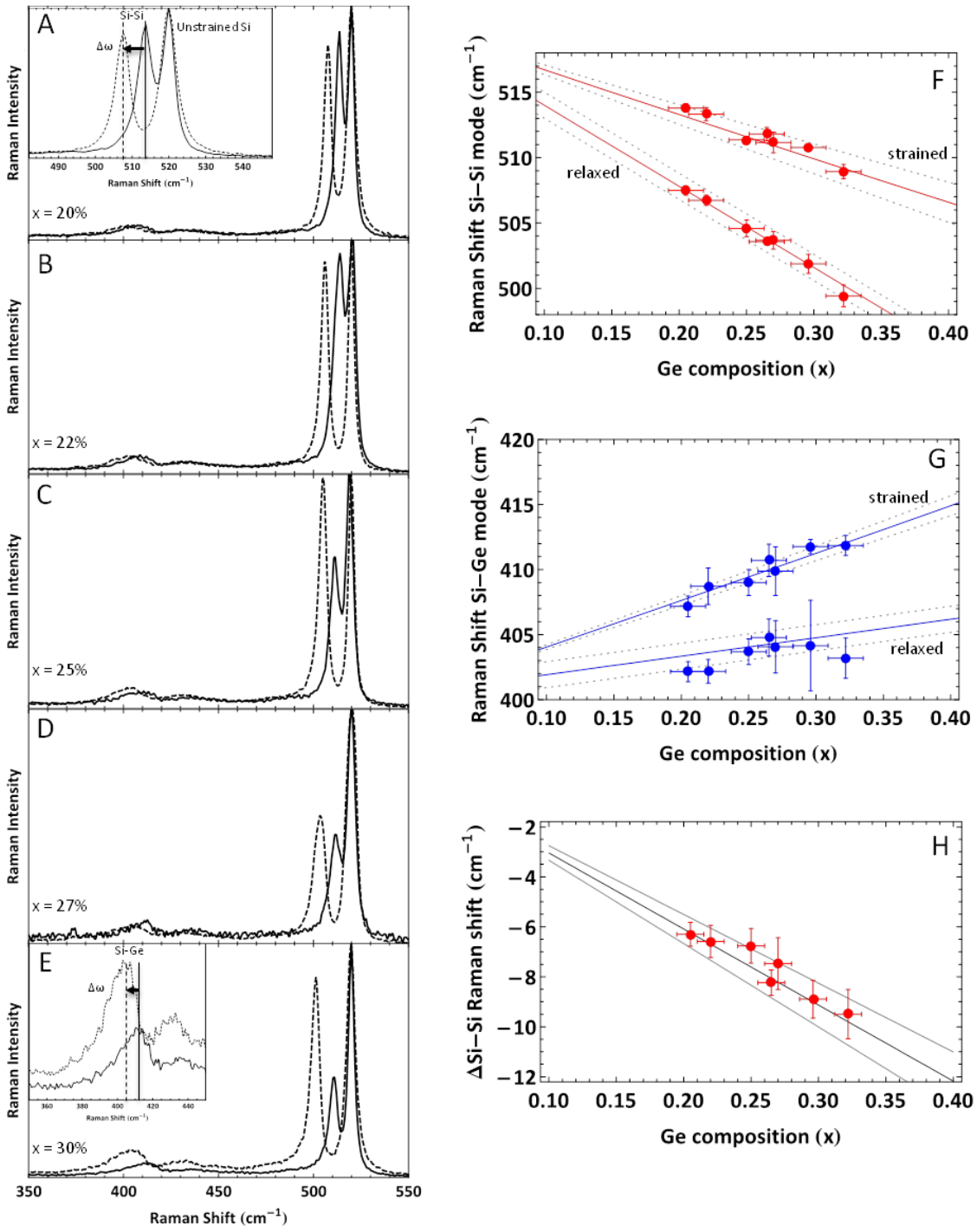

Figure 3-8. Raman spectroscopy results of SiGe NMs. (A-E) Example Raman spectra from SiGe strained to the Si lattice constant (solid lines) and after fabrication of elastically relaxed SiGe NMs (dashed lines). The frequency shift of both the Si-Si mode (details in inset of A) and the Si-Ge mode (details in inset of E) to lower wavenumbers indicates an expansion in the in-plane lattice constant. The intensity

is plotted on a linear scale and the spectra are normalized to the intensity of the bulk-Si peak. The unstrained-Si peak in the as-grown spectra is from the Si layers of the Si/SiGe/Si trilayer. The unstrained-Si peak in the spectra from the released and transferred SiGe NMs is from the new host substrate (bulk Si). The 442nm laser used for this measurement will penetrate the SiGe NM and a portion of the underlying Si substrate. (F) Measured Raman frequencies for the strained (higher wavenumbers) and relaxed (lower wavenumbers) Si-Si modes. (G) Similar to (F) for the Si-Ge Raman modes. The lines are models from [8] for the unstrained-NM Raman frequency. The strain coefficient from [7] was applied to the unstrained-NM model to get the expected strained-NM Raman frequency for each of the modes. (H) The frequency shift of the Si-Si mode from the strained as-grown state to the unstrained, elastically relaxed state of the SiGe NMs. The line shows the expected Raman frequency shift as a function of composition. The gray lines in (F, G, H) represent the uncertainty in the aforementioned models.

As mentioned previously, an advantage of using micro-Raman spectroscopy to measure strain in SiGe NMs is that the measurement is local (laser spot size is ~1μm) and I can map the strain in SiGe NMs to check for spatial uniformity. Figure 3-9 shows Raman maps of the Si-Si Raman frequency over ~25μm x 25μm areas of two $Si_{1-x}Ge_x$ (x = 25% and 27%) films in the as-grown state (Figure 3-9A and C) and then after release and transfer of the SiGe NM (Figures 3-9B and D). The Raman maps show that there is little strain variation in the samples before and after SiGe NM fabrication. The *maximum* variation in the Si-Si frequency is ± 0.6cm^{-1} ($\Delta\varepsilon_{||SiGe}$ = ± 0.08%). This variation is just above the noise level of the instrument (± 0.3cm^{-1}) over the time frame in which the map was taken. The stability and signal-to-noise level of these Raman measurements are discussed in Appendix B.

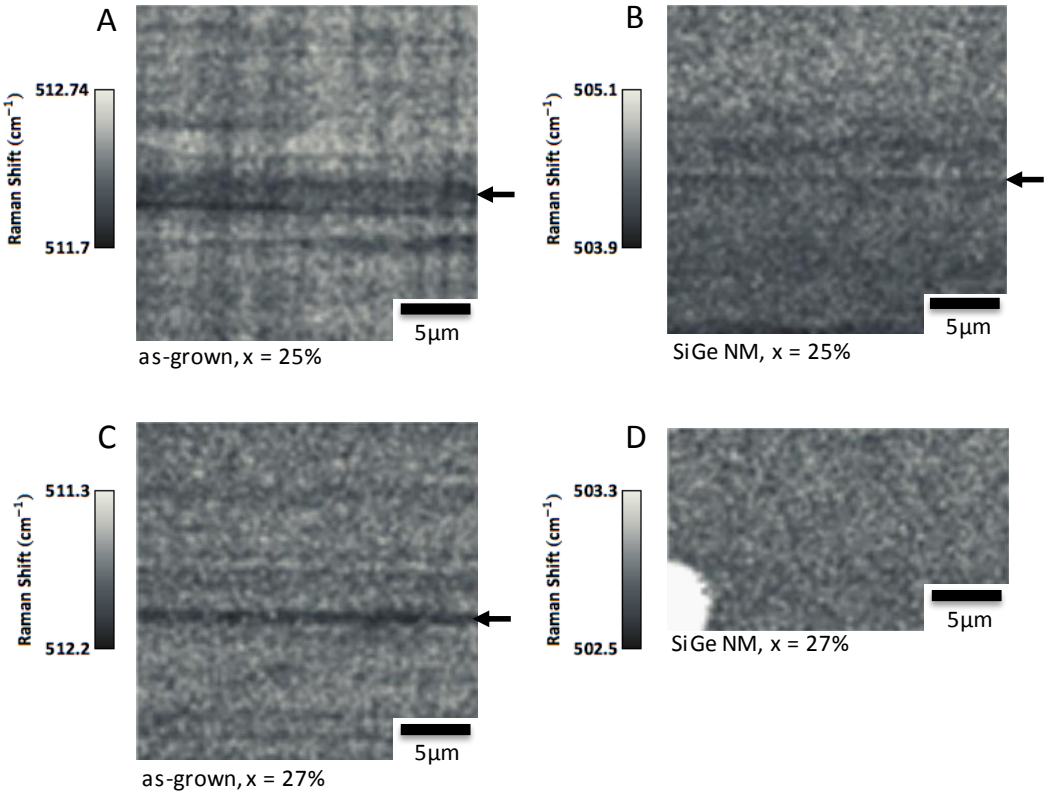

Figure 3-9. Micro-Raman maps of the frequency of the Si-Si mode in (A) 25%-alloy film and (C) 27%-alloy film grown on Si(001). (B) 25%-alloy SiGe NM and (D) 27%-alloy SiGe NM released and transferred to a Si substrate. The white area in the lower left corner of D represents an area where there is no SiGe; etchant access hole in the SiGe NM exposes the underlying Si substrate. Some of the variation in peak position (appear as horizontal lines and denoted by arrows) is from inconsistencies in the instrument and are not from variations in the sample.

I pointed out in the previous section that the SiGe peak in the off-axis RSM around the (224) reflection of the 25%-Ge-concentration sample had some peak broadening that may be due to the onset of plastic relaxation; the micro-Raman map in Figure 3-9A confirms this hypothesis. There are shifts in the Si-Si mode frequency that correspond to the signature crosshatch pattern of dislocation formation in SiGe films grown on Si substrates. The non-

uniform distribution of dislocations in the SiGe gives rise to strain variations and hence frequency shifts in the Raman spectra. Upon release of the SiGe NM, these strain variations disappear (Figure 3-9B). The misfit dislocations that form in SiGe grown on Si(001) are 'perfect' 60° dislocations; the Burgers vector is a full lattice translation vector. When the Si on either side of the SiGe film is removed, there is no longer material pinning the strain fields at the SiGe/Si interface in place. The result is formation of a double atomic step on both surfaces (top and bottom) of the SiGe NM [12]. While the partial plastic relaxation in the as-grown SiGe film may result in rougher SiGe NM surfaces, the strain fields from the misfit dislocations will be removed upon release and transfer of the SiGe NM.

3.3 Chapter summary

SiGe NMs are fabricated from coherent SiGe films grown on SOI substrates. The SiGe films are elastically relaxed by releasing the alloy from the SOI substrate as freestanding nanomembranes. The strain in the SiGe NMs is characterized with XRD and micro-Raman spectroscopy at every step throughout the fabrication process. Transferred SiGe NMs are uniform in strain and composition, and the crystalline quality of the alloy is maintained though the release and transfer process.

3.4 References

1. D. C. Houghton, Strain Relaxation Kinetics in $Si_{1-x}Ge_x$/Si Heterostructures. *J. Appl. Phys*. **70** (1991) 2136-2151.

2. B. Tanto, Dislocation-Free Strain-Engineered Si and SiGe Nanomembranes. PhD Dissertation: Univ. of Wisconsin-Madison, (2009).

3. D. M. Paskiewicz, B. Tanto, D. E. Savage, M. G. Lagally, Defect-Free Single-Crystal SiGe: A New Material from Nanomembrane Strain Engineering. *ACS Nano* **5** (2011) 5814-5822.

4. J. T. Borenstein, N. D. Gerrish, R. White, M. T. Currie, E. A. Fitzgerald, Silicon Germanium Epitaxy: A New Material for MEMs. *Mat. Res. Soc. Symp*. **657** (2001) EE7.4.1.

5. H. Siedel, L. Csepregi, A. Heuberger, H. Baumgartel, Anisotropic Etching of Crystalline Silicon in Alkaline Solutions, *J. Electrochem. Soc.* **137** (1990) 3612-3632.

6. I. De Wolf, Micro-Raman Spectroscopy to Study Local Mechanical Stress in Silicon Integrated Circuits. *Semicond. Sci. Technol*. **11** (1996) 139-154.

7. F. Pezzoli, E. Bonera, E. Grilli, M. Guzzi, S. Sanguinetti, *et al*. Phonon Strain Shift Coefficients in $Si_{1-x}Ge_x$ Alloys. *J. Appl. Phys*. **103** (2008) 093521.

8. J. C. Tsang, P. M. Mooney, F. Dacol, J. O. Chu, Measurements of Alloy Composition and Strain in Thin Ge_xSi_{1-x} Layers. *J. Appl. Phys.* **75** (1994) 8098-8108.

9. F. Pezzoli, L. Martinelli, E. Grilli, M. Guzzi, S. Sanguinetti, *et al.,* Raman Spectroscopy of Si1-xGex Epilayers. *Mater. Sci. Eng. B* **124-125** (2005) 127-131.

10. M. Z. Hossain, H. T. Johnson, Effects of Composition, Strain, and Atomic Disorder on Optical Phonon Frequencies in $Si_{1-x}Ge_x$, *J. Appl. Phys.* **107** (2010) 073515.

11. T. S. Perova, J. Wasyluk, K. Lyutovich, E. Kasper, M. Oehme, *et al.,* Composition and Strain in thin $Si_{1-x}Ge_x$ Virtual Substrates Measured by Micro-Raman Spectroscopy and X-Ray Diffraction. *J. Appl. Phys.* **109** (2011) 033502.

12. C. Euaruksakul, Strain-Band Structure Relationship in Strained Silicon Nanomembranes. PhD Dissertation: Univ. of Wisconsin-Madison (2009).

Chapter 4 Elastically relaxed SiGe NMs as growth substrates

After confirming full elastic relaxation in SiGe NMs after release and transfer to new handling substrates (clean Si with chemical oxide), I use these new substrates for subsequent growths to demonstrate the viability of the SiGe NMs as realistic high-quality substrates for additional epitaxy. The formation of strained-Si quantum wells (QWs) for quantum electronics [1] is one area in which high-crystalline-quality SiGe substrates are needed to improve strain uniformity and mosaic structure (crystalline tilt) in SiGe/Si/SiGe heterostructures. I demonstrate here the ability to grow thick lattice matched SiGe layers and thin strained Si QW layers on SiGe NM 'substrates'. I compare the strain uniformity and mosaic structure of heterostructures grown on SiGe NMs to those grown on plastically relaxed SiGe graded-buffer-layer substrates.

4.1 Preparation of SiGe NM substrates

In general, even though Si and Ge have similar crystalline structures and mechanical properties, cleaning the surfaces of these two materials is very different [2, 3]. The standard pre-growth chemical clean for Si surfaces before growth in the UW MBE or CVD systems is as follows: (1) 10min ultrasonication in acetone and then methanol, (2) 10min UV exposure, (3) 20sec in 10% HF, (4) 10min in piranha (~80°C H_2SO_4 + H_2O_2 solution), (5) 15min in standard clean 1 [SC1] (~80°C H_2O + NH_4OH + H_2O_2 solution), and (6) 20sec in 10% HF (with a 5-min DI water rinse between each step after step (2), before putting the sample directly into the high-vacuum growth chamber. This procedure removes particulates, any organic and some metallic impurities on the surface of the Si through oxidation (piranha and SC1) and minimal etching

(SC1) of the surface. The HF dips remove the oxide and leave the surface H-terminated. The thin (~50nm), high-Ge-concentration (x > 20%) SiGe NMs, however, are completely etched away in 15min of SC1. This is because the etch rate of Ge (~200nm/min) in SC1 is much higher than that of Si (<1Å/min) [2, 3]. I modify the chemical clean for the SiGe NM samples by using 1-2 cycles of: 20sec in 10% HF + 10min in Piranha solution. This cleaning procedure only etches away a few nanometers of the SiGe NM (though oxidation). The last step in the cleaning process is a 20-sec 10% HF dip to remove any oxide that formed during the cleaning process and H-terminate the surface before inserting the sample into the high-vacuum growth chamber.

I investigated the surface morphology of the SiGe NMs before and after the chemical clean (before growth) to ensure that the cleaning procedure was not introducing significant changes in the surface roughness. Figure 4-1 shows atomic force microscopy (AFM) images of the surface of a $Si_{0.75}Ge_{0.25}$ NM before the chemical clean (but after release and transfer) [Figure 4-1A] and after the modified chemical clean described above (Figure 4-1B). The surface morphology does change after the clean but the rms roughness does not significantly increase over the rms roughness of the released and transferred NM (1.4nm before to 1.6nm after). Some change in the surface morphology (i.e., the correlation length of the roughness) is expected as the SiGe NM had time to oxidize before the AFM measurement; the measurement took place months after the SiGe NM had been released, transferred, and bonded to the Si substrate. The surface morphology of the chemically cleaned NM surface was measured within 1 hour of H-termination so there should be minimal oxide formation on the surface. The surface

of the NM with native oxide is fundamentally different (amorphous SiO_2 vs. H-terminated single-crystalline material) from that of the chemically cleaned NM that has been slightly etched in solution (~1-2nm of material etches away during each Piranha/HF cleaning cycle). The timing of the AFM measurements was intentional because I wanted to replicate the fabrication and chemical cleaning procedure a typical sample would go through before epitaxial overgrowth.

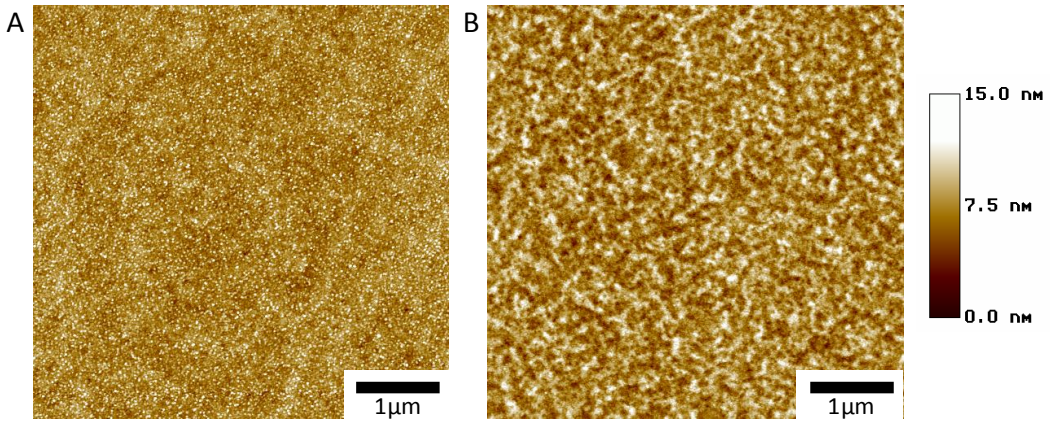

Figure 4-1. (A) AFM of the SiGe NM surface after release, transfer, and bonding to a new oxide-terminated Si substrate (rms roughness = 1.4nm). (B) AFM of the SiGe NM after the modified chemical cleaning procedure described in the text (rms roughness = 1.6nm). The measurement was taken within 1 hour of H-termination. The intensity and length scales are the same for both images.

There are two potential problems with the modified chemical cleaning procedure described above. (1) The piranha solution does not remove all impurities from the surface of the SiGe NM, and (2) multiple 10% HF dips increase the probability of the SiGe NMs delaminating/debonding from the new host substrate. The cleanliness of the surface is paramount for epitaxial growth in general, but is of particular concern when using CVD for the epitaxial layers grown on top of the SiGe NMs; any contamination, particularly carbon, will

prevent epitaxial growth leaving holes/pits in the epitaxial film. This is clearly shown in Figure 4-2. Figure 4-2A shows an optical micrograph of an epitaxial film grown on polished, plastically-relaxed, graded SiGe substrate. The standard pre-growth chemical clean was used here because the SiGe was thick enough to withstand some etching in the SC1 solution. A thick (~1µm) lattice matched SiGe layer followed by a thin (~10nm) strained Si layer, and a SiGe capping layer was grown on this substrate.

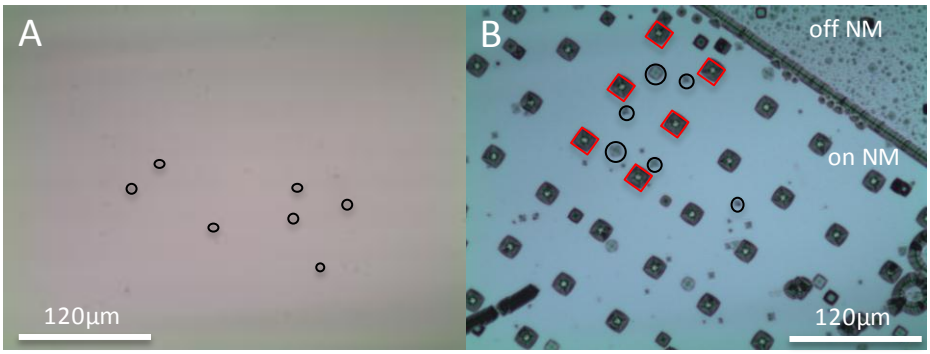

Figure 4-2. Optical micrographs of CVD epitaxial films on SiGe substrates cleaned with the standard chemical clean and the modified chemical clean. (A) ~80nm $Si_{0.71}Ge_{0.29}$/10nm Si/1µm $Si_{0.71}Ge_{0.29}$/$Si_{0.71}Ge_{0.29}$ polished, relaxed graded buffer layer substrate cleaned with the standard pre-growth chemical clean. The pits are small black dots in the image and a few are highlighted by black circles. (B) ~80nm $Si_{0.73}Ge_{0.27}$/10nm Si/2µm $Si_{0.73}Ge_{0.27}$/50nm $Si_{0.73}Ge_{0.27}$ NM substrate cleaned with one cycle of the modified pre-growth chemical clean (HF/piranha/HF). In the upper right corner of the image there is no NM; the heterostructure also grows on the exposed portion of the Si substrate. The original SiGe NM had etchant access holes for release, these appear as a rectangular array of discolored regions on the surface (a few highlighted by red squares). The pits (black circles) created from contamination on the surface of the NM appear between the regular array. Note: In order to see pits created by CVD epitaxy with an optical microscope the film must be very thick < ~1µm. The lateral size of the pits will typically be ~2x thickness of the film.

For comparison, a similar heterostructure was grown on a SiGe NM that was cleaned via the modified chemical clean described above (Figure 4-2B). Only one HF/piranha/HF sequence was used here. It is clear from Figure 4-2 that the pit density is higher on the SiGe NM sample.

The pits created by impurities on the surface of the substrate represent areas on the sample where no epitaxial growth took place or growth stopped before the heterostructure was complete: they represent discontinuities in the epitaxial film. The crystalline quality of the surrounding film is not affected, however, these areas must be avoided during device fabrication; the pits act as electrical shorts to the substrate, thus redirecting the desired current path (epitaxial layers). One way to eliminate pits is to use MBE growth of the epitaxial layers rather than CVD growth. Because MBE is a physical deposition process, any dirt/impurities on the surface of the growth substrate will be covered by the growth rather than preventing growth altogether. The impurities may still be present, but the growth is uniform over the surface making it easier to find places on the sample for device fabrication. The thickness of the constant-composition SiGe buffer layer is limited with MBE growth because of the lower growth rates (~5nm/min for MBE versus 10-20nm/min for CVD). Both MBE and CVD are used to grow heterostructures on SiGe NM substrates in this work.

The second issue with the modified chemical cleaning process is delamination or debonding of the SiGe NMs during the chemical clean. The cause is most likely from multiple 10% HF baths and that the SiGe NMs are typically transferred to Si substrates with some form of native or chemical oxide. Even after annealing to encourage bonding (~500°C), there will still be a thin layer of SiO_2 at the SiGe NM/Si substrate interface. This interface region may then be

etched away during multiple HF treatments and is likely the cause of SiGe NM delamination during chemical cleaning. When transferring and bonding the SiGe NMs to the new Si handle substrate it is important to ensure there are no wrinkles and/or bubbles in the NM where the HF etchant could gain access to the SiGe NM/substrate interface. It is inevitable that during the transfer process not all NMs will lie flat: the thin NMs are difficult to handle and some will have wrinkles and/or bubbles like the one shown in the optical micrograph in Figure 4-3A. During ultrasonic cleaning, however, the wrinkled and bubbled portions of the NM will break off leaving only the well-bonded regions of the NM for subsequent cleaning and epitaxial growth (Figure 4-3B).

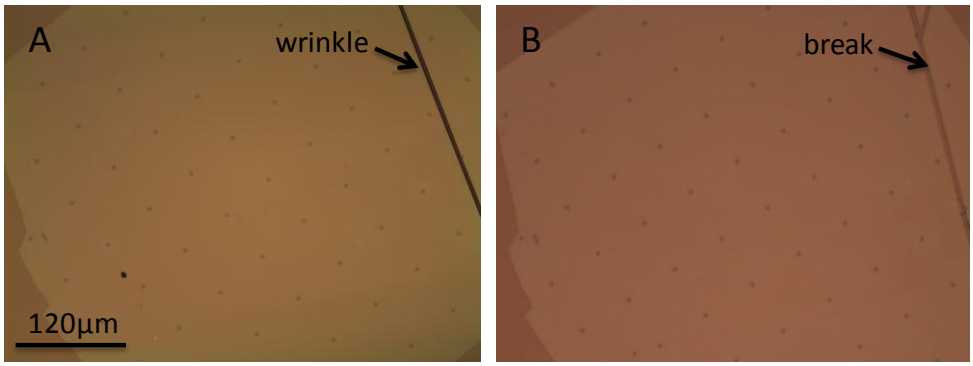

Figure 4-3. Optical micrographs of a SiGe NM transferred to a hydrophilic (oxide-terminated) Si substrate. (A) Wrinkles produced in the transfer process break during ultra-sonic cleaning leaving (B) breaks in the NM. The rectangular array of dots in the NMs are etchant access holes. The scale bar is the same for both images.

Once the SiGe NMs are properly cleaned and prepared, SiGe/strained Si/SiGe epitaxial heterostructures are grown on them with CVD or MBE to form strained Si quantum wells (QWs). The SiGe composition of the epilayer is matched to the composition of the NM. Constant-composition buffer layers range in thickness from 300nm to 2µm. The strained-Si QW

layer is kept thin (< 12nm) to avoid plastic strain relaxation. Because the SiGe NMs are often transferred to Si host substrates, the SiGe/Si/SiGe heterostructure is also grown on the surrounding bulk Si. The epilayers grown on the bulk Si are plastically relaxed and very rough (see area "off NM" in Figure 4-2 above). Only the films grown on the SiGe NMs are characterized; the layers grown on the bulk Si do not affect the growth of the heterostructure on the SiGe NM 'substrate'.

4.2 Analysis of average strain states

Similar to measuring the strain state of SiGe NMs before and after release, I measure the strain state of the epitaxial films grown on the SiGe NM substrates with XRD and Raman spectroscopy. The composition of the SiGe epilayer must match the SiGe NM composition to avoid strain build up in the film and the strained Si layer should be tensilely strained to the relaxed SiGe lattice constant. Figure 4-4 shows XRD data from a ~1µm $Si_{0.73}Ge_{0.27}$/10nm εSi/77nm $Si_{0.73}Ge_{0.27}$ heterostructure grown on a ~45nm $Si_{0.73}Ge_{0.27}$ NM. The θ/2θ line scan around the (004) reflection is fit to simulation to extract the thicknesses of the Si QW and the SiGe capping layer. The on-axis (004) and off-axis (224) RSMs show that the SiGe epilayer is compositionally matched to the SiGe NM. Two SiGe peaks would appear in the diffraction pattern if the compositions did not match, one for the epilayer and one for the SiGe NM. Small deviations in composition in the epitaxial layer would produce small amounts of strain in the SiGe; however, the critical thickness for dislocation formation for such strains is several

microns. The growth of a thick lattice matched SiGe layer demonstrates that it is in fact possible to grow macroscopic lattice-matched crystals on SiGe NMs.

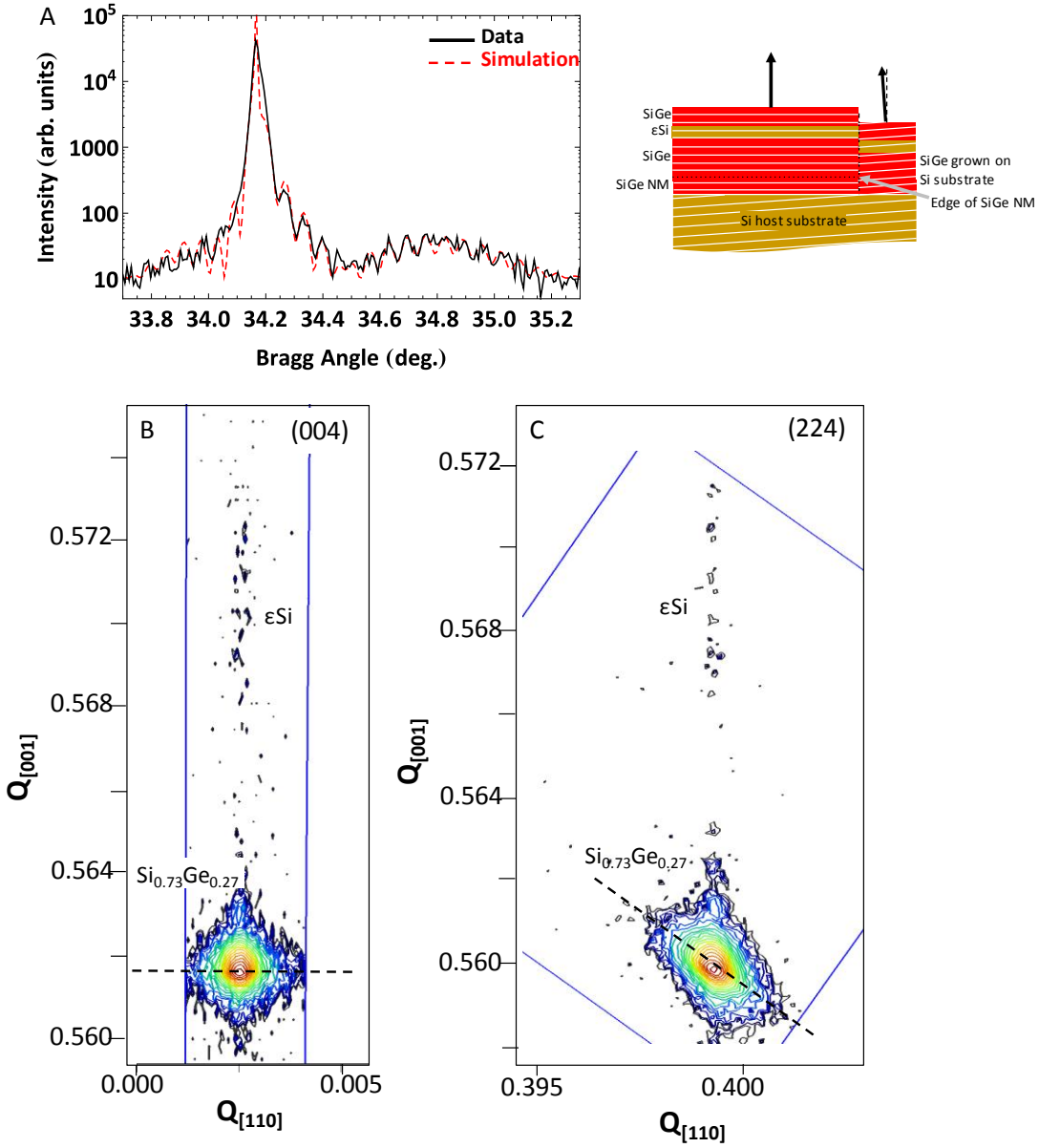

Figure 4-4. XRD from a 77nm $Si_{0.73}Ge_{0.27}$/10nm εSi/~1µm $Si_{0.73}Ge_{0.27}$/45nm $Si_{0.73}Ge_{0.27}$ NM heterostructure. (A) θ/2θ line scan through the (004) reflection (black) fit to simulation (red) to extract the thicknesses of the Si QW and SiGe capping layers. Diffraction from the heterostructure grown on the SiGe NM can be separated from diffraction of the heterostructure grown on the surrounding bulk Si substrate because the substrate orientation is tilted relative to that of the SiGe

NM (inset). RSMs around the (B) (004) and (C) (224) reflections indicate that the Si is strained to the SiGe lattice constant and that the SiGe epilayer composition matches that of the SiGe NM. The dashed lines indicate a constant θ value; peak spreading along this line signifies variation in crystalline tilt, otherwise known as mosaic broadening.

I have grown up to ~2μm of lattice matched material on SiGe NM substrates with little-to-no mosaic broadening in the SiGe epilayer (example shown in section 4.5). The RSMs also indicate that the Si layer is strained to the SiGe lattice constant; the peak spacing in the (004) map is appropriate for Si strained to the $Si_{0.73}Ge_{0.27}$ lattice constant and the Si peak aligns to the same in-plane lattice constant in the (224) map. The diffraction intensity from the Si QW is weak because the layer is very thin (~10nm) and the lateral size of the sample is smaller than the x-ray beam.

Diffraction from the epilayers grown on the NM can be separated from the layers grown on the surrounding Si substrate; in this case the Si substrate has a ~2° miscut relative to the SiGe NM (inset of Figure 4-4A). The diffraction intensity from the film grown on the substrate is therefore tilted in reciprocal space relative to the film grown on the SiGe NM. I chose Si substrates with miscuts different from those of the SOI used to make the SiGe NMs such that I could characterize the strained Si layers in the heterostructures grown on the SiGe NMs. The diffraction intensity from the bulk Si substrate typically masks the diffraction from the thin strained Si layer, making it difficult to detect the strained-Si layer with on-axis XRD. Off-axis diffraction from the heterostructure grown on the SiGe NM is very far away from anything grown on the Si substrate because the NM is oriented in a different in-plane direction than the

Si substrate; the [110] in-plane direction of the NM is typically rotated by >10° from the Si substrate in-plane [110] direction.

I also used Raman spectroscopy to measure the average strain states of the heterostructures grown on SiGe NMs. The overall strain state of the film is a result of averaging several Raman measurements (>5) over a large area of the sample (~1mm x 1mm). I continued to use the 442nm laser for these measurements such that I was only measuring the epitaxial heterostructure grown on the NMs and not the underlying Si substrate; the strained-Si peak would not be visible near an intense bulk-Si peak from the substrate. Recall that the penetration depth for 442nm light in Si is ~300nm. This depth will decrease with increasing Ge composition in SiGe alloys. Figure 4-5 shows example Raman spectra from three different Si/SiGe heterostructures grown on SiGe NM substrates. As the thickness of the Si layer increases and gets closer to the surface (thinner SiGe capping layer) the signal intensity increases. This makes sense as the Raman signal intensity is proportional to the number of excited bonds within the measurement area. A summary of the Raman frequency shifts is shown in Figure 4-5D. The frequency shift of the strained-Si peak relative to the bulk-Si peak ($\Delta\omega_{\varepsilon Si}$) is in excellent agreement with the frequency shift of the Si-Si peak in the alloy layer from the as-grown compressive state of SiGe to the released and overgrown state of the SiGe NM (filled squares and filled circles in Figure 4-5D, respectively). This agreement is expected, as the frequency strain shift coefficients, *b*, agree within experimental uncertainty for the Si-Si mode of SiGe ($b_{Si\text{-}Si}$ = 730 ± 70cm^{-1} [4]) and for strained Si ($b_{\varepsilon Si}$ = 723 ± 15cm^{-1} [5]). The agreement in strain states means that we have grown coherently strained Si on a fully elastically relaxed Si

NM substrate. The Si-Si mode frequency shift between the compressively strained state of SiGe to relaxed SiGe is similar for the SiGe NM (open squares) and the SiGe epilayer (closed squares), indicating that the epilayer is compositionally matched to the SiGe NM.

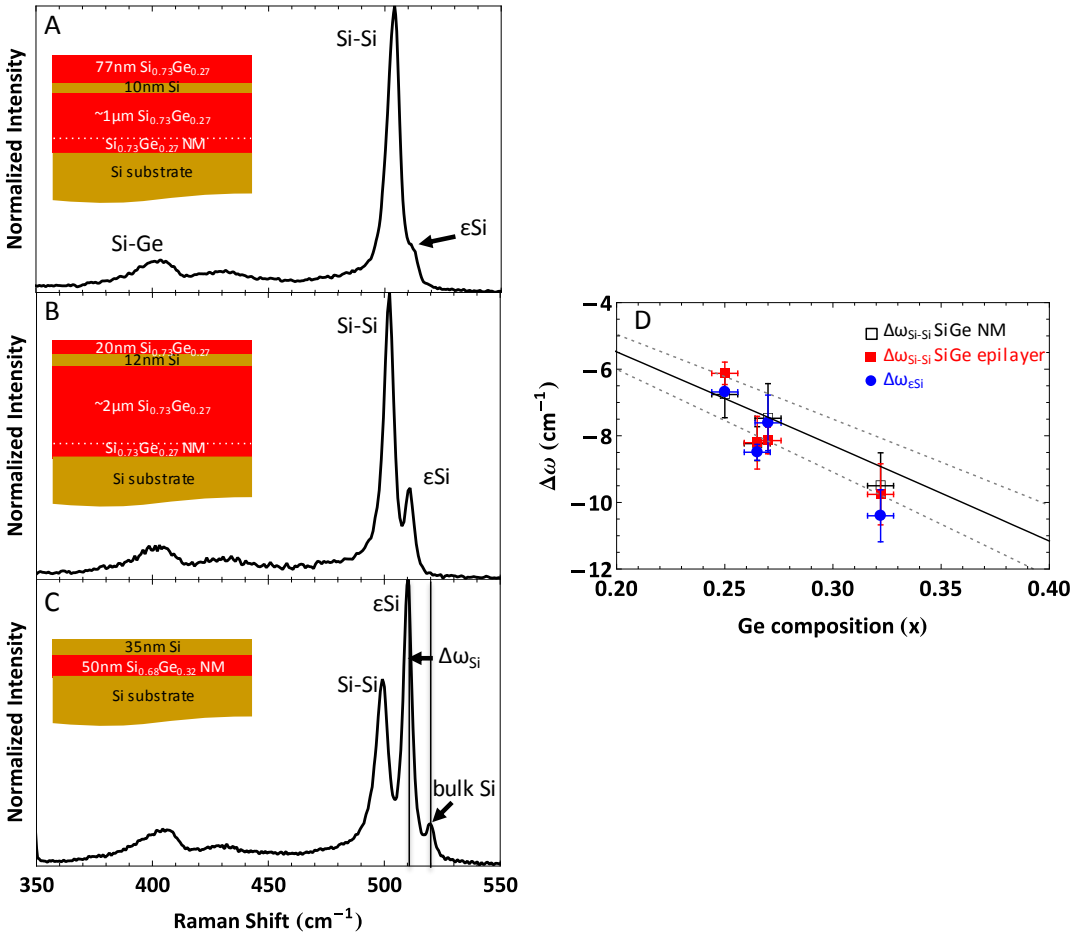

Figure 4-5. (A-C) Example Raman spectra for the heterostructures shown in the insets. The intensity is normalized to the most intense peak [Si-Si for (A) and (B), and εSi for (C)]. (D) Summary of frequency shifts for Si-Si mode within SiGe and the Si mode of the strained-Si layer. The Si-Si mode frequency shift ($\Delta\omega_{Si\text{-}Si}$) is with respect to the compressively strained as-grown state of the alloy. The strained Si mode frequency shift is ($\Delta\omega_{\varepsilon Si}$) with respect to the unstrained bulk Si peak (ω_o = 520 cm^{-1}, as shown in C). The expected frequency shift for SiGe alloys from the compressively strained state (grown on Si) to the relaxed state is shown as a line. The dotted gray lines on either side represent the uncertainty in the strain shift coefficient [4].

4.3 Local strain variations

Similar to mapping the strain relaxation in the released and transferred SiGe NMs, I measured the local strain variations in the heterostructures grown on the SiGe NMs with micro-Raman spectroscopy. Figure 4-6 shows the Si-Si mode and strained-Si mode frequency shifts as a function of position over a 37nm $Si_{0.75}Ge_{0.25}$/12nm Si/~1µm $Si_{0.75}Ge_{0.25}$/50nm $Si_{0.75}Ge_{0.25}$ NM heterostructure.

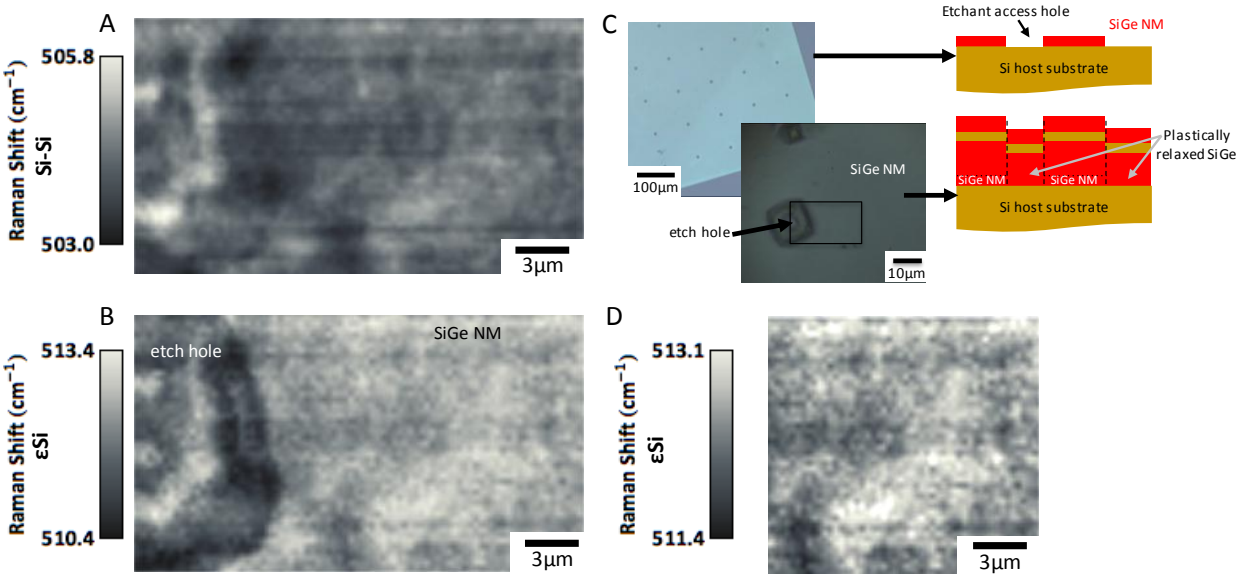

Figure 4-6. Micro-Raman maps of the (A) Si-Si mode within the SiGe epilayer and (B) Si mode in the strained Si QW. (C) Optical micrographs of the $Si_{0.75}Ge_{0.25}$ NM after release and transfer (upper) and after overgrowth of ~1µm SiGe/12nm Si/37nm SiGe (lower). The rectangle in the lower image represents the micro-Raman mapping area of A and B. (D) Part of the same map as B replotted on a different intensity scale to highlight the variations in the Si QW grown on the SiGe NM only.

The Raman map is taken over an area with a NM etchant access hole. Optical images of the sample before overgrowth and after overgrowth are shown in Figure 4-6C. The area of the Raman map is highlighted with a black rectangle. Because the SiGe NM is transferred to a Si

substrate, epitaxial growth takes place on the NM and on the surrounding Si substrate. The SiGe grown on the Si substrate will plastically strain relax via dislocation formation, while the SiGe grown on the SiGe NM substrate will grow nominally defect-free because the lattice constants are matched. The Si-Si Raman mode does not vary significantly over the two regions because the SiGe grown on the Si substrate is nearly fully plastically relaxed to the bulk SiGe lattice constant. If the SiGe were compressively strained (i.e., not fully plastically relaxed), the Si-Si peak would be shifted to higher wavenumbers similar to what is seen near the edge of the map (near the center of the etch hole). The maximum variation of the Si-Si peak on the NM portion of the map (right half of map) is ~1.5cm^{-1}, implying that the strain in the SiGe epilayer varies by ±0.10% from the average. The strain variation shown in this map is large compared to other Si/SiGe heterostructures grown on SiGe NM substrates (see section 4.5). The strain variation does not follow the typically crosshatch pattern of plastically relaxed films so it is unlikely that dislocation formation is the cause of the strain inhomogeneity. Compositional variations in the alloy, growth inhomogeneities, and roughness and/or delamination at the NM/substrate bonded interface are all potential sources of the strain variation. Compositional and growth inhomogeneities may be a result of non-uniform heating over the sample surface. The samples are resistively heated so the temperature uniformity is only as good as the current path through the sample. If the NM is not in good contact with the underlying Si substrate, the temperature variation over the sample could cause large compositional and thickness variations in CVD grown samples. Strain variations from NM transfer and/or bonding will be discussed in more detail in the following sections of this chapter.

The variation in the strained-Si peak is mapped out in Figure 4-6B. The strained Si peak moves to lower wavenumbers where the heterostructure is grown within the etch hole. This indicates that there is an increase in tensile strain in the Si layer grown in this region. From the average Raman strain measurements, I know that the Si grown on the SiGe NM is strained to the relaxed SiGe lattice constant. The variations in the Si mode are similar to the variations in the Si-Si mode in the heterostructure grown on the SiGe NM (right half of Figure 4-6A and B). This indicates that the strained Si layer is coherent with the underlying SiGe in this region. If the Si layer were plastically relaxing in the region grown over the etch hole the peak shift should be to higher wavenumbers, not lower. The complicated strain variation in the heterostructure grown within the etch hole may be from growth on the sidewalls of the NM meeting with growth on the bottom Si substrate to form complicated grain boundaries. The important point here is that the heterostructure grown on the exposed Si substrate does not significantly effect the heterostructure grown on the SiGe NM; the transition between the two regions is sharp (< 1μm) such that crystalline defects in the plastically relaxed regions should not propagate very far into the regions where the heterostructure was grown on the elastically relaxed SiGe substrate.

4.4 Crystalline-tilt analysis

Another indicator of crystalline quality in Si/SiGe heterostructures is the variation (or lack thereof) in crystalline tilt over a given sample area. A large spread in crystalline tilt could indicate dislocation formation, strain driven roughening of the sample surface, or the

introduction of growth defects (stacking faults, Nagai tilt [6], or the inclusion of impurities). On average, the spread in the crystalline tilt can be extracted from peak broadening of the film as measured in RSMs. I showed on-axis (004) and off-axis (224) RSMs of a Si/SiGe heterostructure grown on a SiGe NM in Figure 4-4. The peak broadening along the constant θ line indicates the variation of crystalline tilt; the lattice constant of the crystal is constant along this line so any diffraction intensity comes from changes in tilt, not strain variations. In the (004) map it is difficult to tell if the peak broadening in the constant θ direction is from tilt or from finite-crystal-size effects (the size the NM is smaller than the x-ray beam size). From the (224) map, however, there is a very small spread of the peak along the constant-θ line; any spread from finite-size effects would be parallel to the axes (horizontal and vertical). It is difficult to infer what may be causing the slight mosaic spread seen in the SiGe peak in the lab-source XRD and very little information about the strained-Si QW can be extracted because the diffraction peak is so weak.

To gain a better understanding of the mechanism causing tilt in the heterostructures grown on SiGe NM substrates, I measured the crystalline tilt on the local scale with micro/nano x-ray diffraction (μXRD). The basics of this measurement were discussed in section 1.5; diffraction from a very small (~50nm), highly brilliant (synchrotron source) x-ray beam is used to construct a two-dimensional map of the crystalline tilt. The diffraction condition (θ/2θ setting) is constant when mapping the tilt. This measurement is in contrast to any of the lab source XRD measurements, in which the diffraction condition is swept over large ranges to construct a line scan or a map in reciprocal space. Figure 4-7A shows a θ/2θ μXRD line scan around the (004)

reflection taken from one spot (~1μm) on the sample. This scan was also fit to simulation to extract the thicknesses of the SiGe capping layer and strained-Si QW layer, and the strain in the Si QW. This scan was used to determine the optimum diffraction condition for measuring tilt variation in the heterostructure. Because it is difficult to extract any information about the Si QW from lab source XRD measurements, we chose to set the diffraction condition near the strained-Si QW peak to gain insight into the tilt in the Si QW layer. The dashed box in Figure 4-7A indicates the angular divergence of the x-ray beam and thus the measurement area in reciprocal space of each point for this diffraction condition.

The tilt is extracted from variation in the diffracted intensity on a two-dimensional charge coupled detector (CCD) [Figure 4-7B]. Tilt in the scattering plane is labeled as x-tilt and tilt perpendicular to the scattering plane is labeled as y-tilt. Variations in crystalline tilt in the x-direction will result in changes in the diffraction condition (see inset of Figure 4-7B and Figure 1-24). Each pixel in the x-direction on the CCD indicates a different point in reciprocal space and can be converted as such (see Appendix C for details). The result is that the x-tilt is equal to the change in the Bragg angle and the y-tilt is proportional to the change in position in diffracted intensity along the y-direction of the CCD. Together, the x-tilt and y-tilt define the tilt magnitude, γ:

$$\cos[\gamma] = \cos[x_{tilt}]*\cos[y_{tilt}] \qquad (4\text{-}1).$$

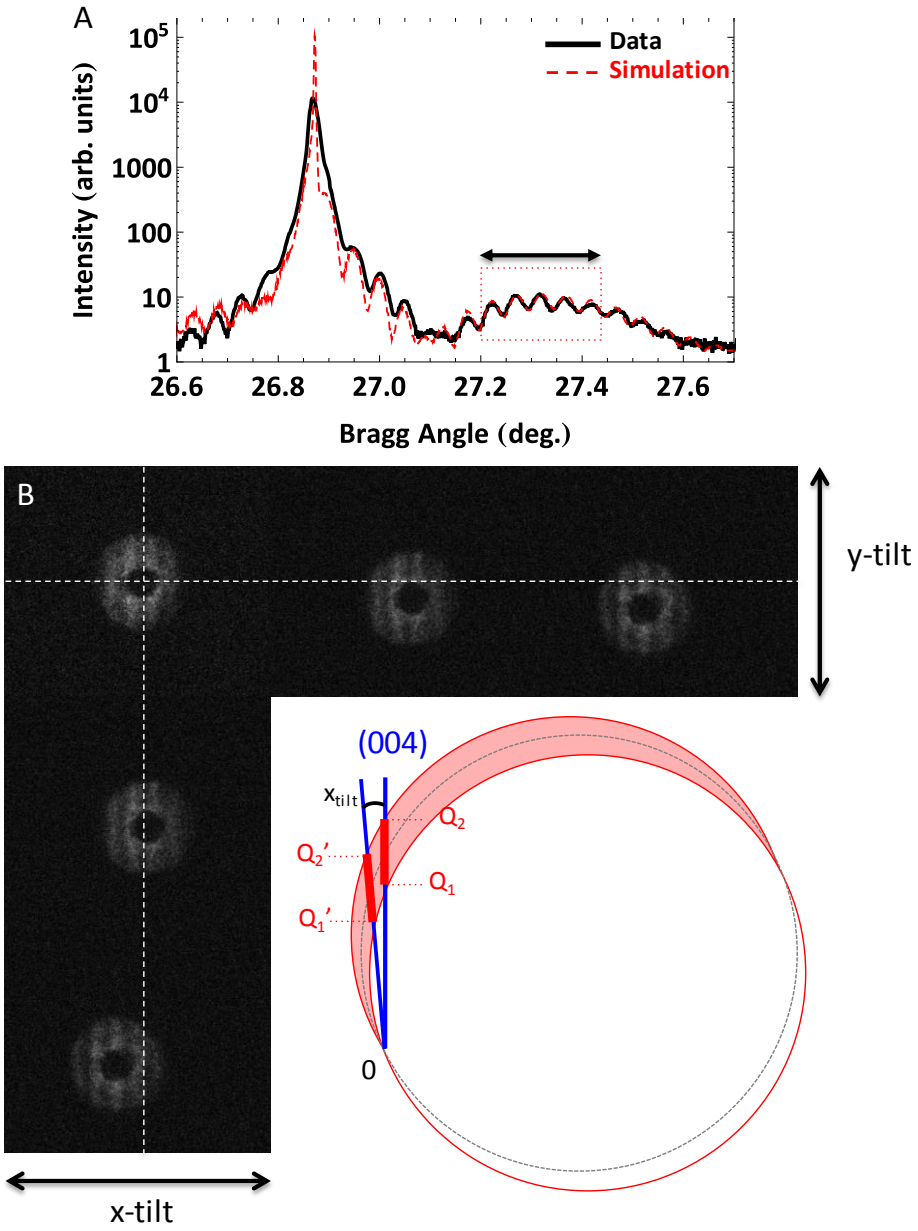

Figure 4-7. µXRD data from a 77nm $Si_{0.73}Ge_{0.27}$/10nm εSi/~1µm $Si_{0.73}Ge_{0.27}$/45nm $Si_{0.73}Ge_{0.27}$ NM heterostructure (same sample as that shown in Figure 4-4). (A) θ/2θ line scan around the (004) reflection at one spot (~1µm). (B) Example data from tilt analysis. The measured intensity on the CCD corresponds to the diffraction condition highlighted in the dashed box in (A). The y-tilt is proportional to the change in diffraction intensity in the y-direction on the CCD. The x-tilt is equal to the change in Bragg angle as measured directly by changes in the diffracted intensity along the x-direction of the CCD.

Figure 4-8A shows the variation of the crystalline-tilt magnitude within the strained-Si QW layer of a Si/SiGe heterostructure grown on a SiGe NM over a 10µm x 10µm area. The maximum variation (0.06°) agrees with the mosaic spread seen on average as measured with lab source XRD indicating that this area is representative of the entire sample. It is clear that the tilt mechanism is much different from that of the plastically relaxed graded buffer layers shown in Chapter 1 (Figure 1-17B). For plastically relaxed layers, the tilt follows a crosshatch pattern and is a result of dislocation formation and multiplication mechanisms. The lack of the crosshatch-like pattern for the tilt magnitude of the heterostructure grown on the SiGe NM leads me to believe that the tilt originates from something other than crystalline defects. Because the SiGe NMs are very thin and flexible they conform to variations (particulates and asperities) on the surface of the new host substrate. One likely source of tilt variation in the heterostructure may be from bending of the SiGe NM 'substrate' after transfer. If the new host substrate is not very clean or the surface is rough, the SiGe NM will conform to the inhomogenities on the surface (Figure 4-8C). The result is a 'substrate' that has tilt variation due to bending of the crystalline SiGe NM template and any epitaxial film grown on top will have similar changes in tilt over the sample area. The bending of the SiGe NM does not have to be large to produce the tilts seen in this measurement. For example, a miscut of 0.05° on Si produces terrace widths of ~150nm for single-atomic step heights. The ~1.5µm area on the sample with the largest tilt variation (~horizontal line of maximum intensity in Figure 4-8A) would require a step height of ~1.3nm to produce a 0.05° tilt over this area. Hence the 'wrinkles' or bending of the SiGe NM would not be visible with an optical microscope.

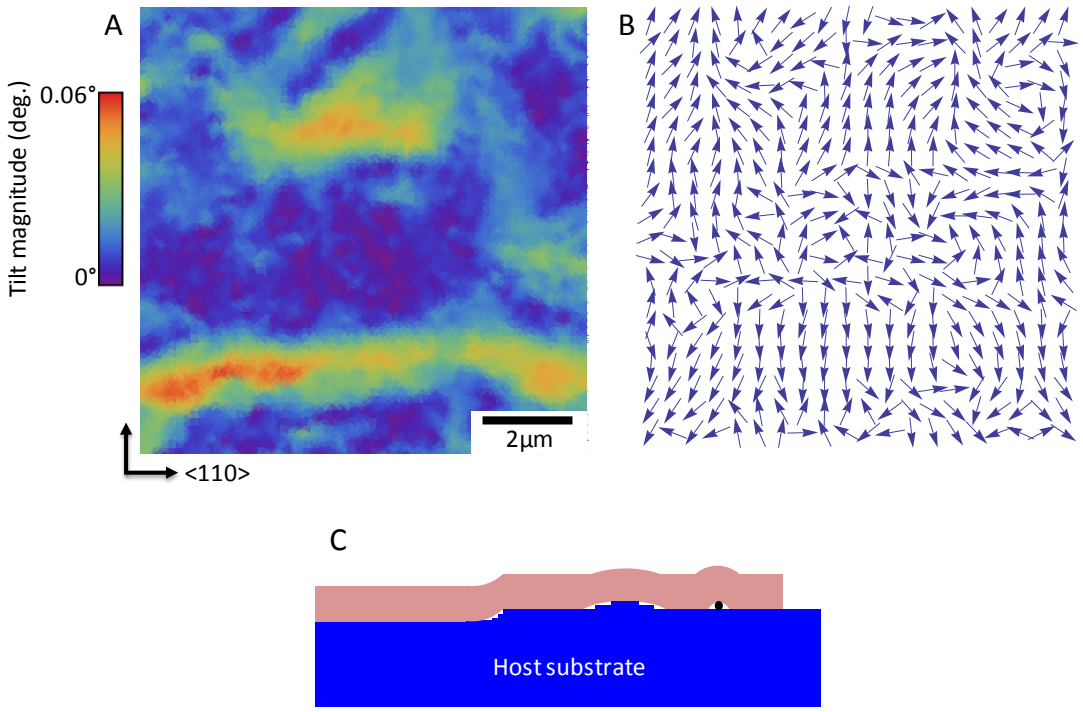

Figure 4-8. (A) Crystalline tilt magnitude for the strained Si QW layer of a 77nm $Si_{0.73}Ge_{0.27}$/10nm εSi/~1µm $Si_{0.73}Ge_{0.27}$/45nm $Si_{0.73}Ge_{0.27}$ NM heterostructure. (B) Vector plot of the tilt direction. (C) Schematic diagram of the possible tilt mechanisms for SiGe NM substrates. The SiGe NM can conform to surface roughness and particulates on the surface of the new host substrate causing the single crystal to bend. Any heterostructure grown on top of the bent SiGe NM substrate will follow the tilt of the substrate.

If the SiGe NM is bending to conform to the new substrate surface, it is possible that this mechanism also accounts for the strain variations seen in the micro-Raman measurements of section 4.3. The strain will vary depending on the radius of curvature and/or the initial bonding points of the SiGe NM. Strain in the NM can result from bending alone: the SiGe NM conforms to the surface when transferred. The NM can also stretch as a result of capillary forces: the NM can be suspended over a valley and attached on either side, while capillary forces pull the NM into the valley causing stretching and bending.

The variation in crystalline tilt (and potentially strain variation) of the heterostructures grown on SiGe NMs is most likely from inhomogeneities at the NM/host substrate bonding interface. Currently, I use a wet transfer technique to transfer the SiGe NMs to Si that has been terminated with chemical oxide (Piranha and AHP cleaning). Steps to improve this interface may include transferring SiGe NMs to H-terminated Si or finding dry transfer methods to improve the bond formation and interface quality of transferred NMs.

4.5 Comparison of heterostructures grown on SiGe NM substrates vs. plastically relaxed graded buffer layer substrates

In the previous sections I discussed the crystalline quality and local strain inhomogeneities in Si/SiGe heterostructures grown on SiGe NM substrates. Here I provide a comparison of these results with those obtained for heterostructures grown on plastically relaxed, compositionally graded SiGe buffer layer substrates. To date, the relaxed graded buffer layer substrates are the best SiGe substrates available. I show here that SiGe NM substrates match or exceed the material quality of graded SiGe substrates.

The most obvious example of contrasting crystalline quality between the SiGe NM substrates and the SiGe graded buffer layer substrates is the magnitude of the crystalline tilt over large areas (>10μm). Figure 4-9 shows off-axis (224) RSMs for similar heterostructures grown on the two different substrates. Thick, (~2μm) compositionally matched SiGe layers were grown on both substrates before growth of a ~12nm strained Si layer, followed by a 20nm SiGe capping layer. The mosaic broadening in the heterostructure grown on the SiGe NM is negligible, while the broadening of the constant-composition SiGe layer on the graded buffer

layer substrate is ~0.2°. The magnitude of the mosaic broadening in the graded buffer layer sample is typical and is a result of the plastic relaxation of the SiGe grown on the Si substrate [7].

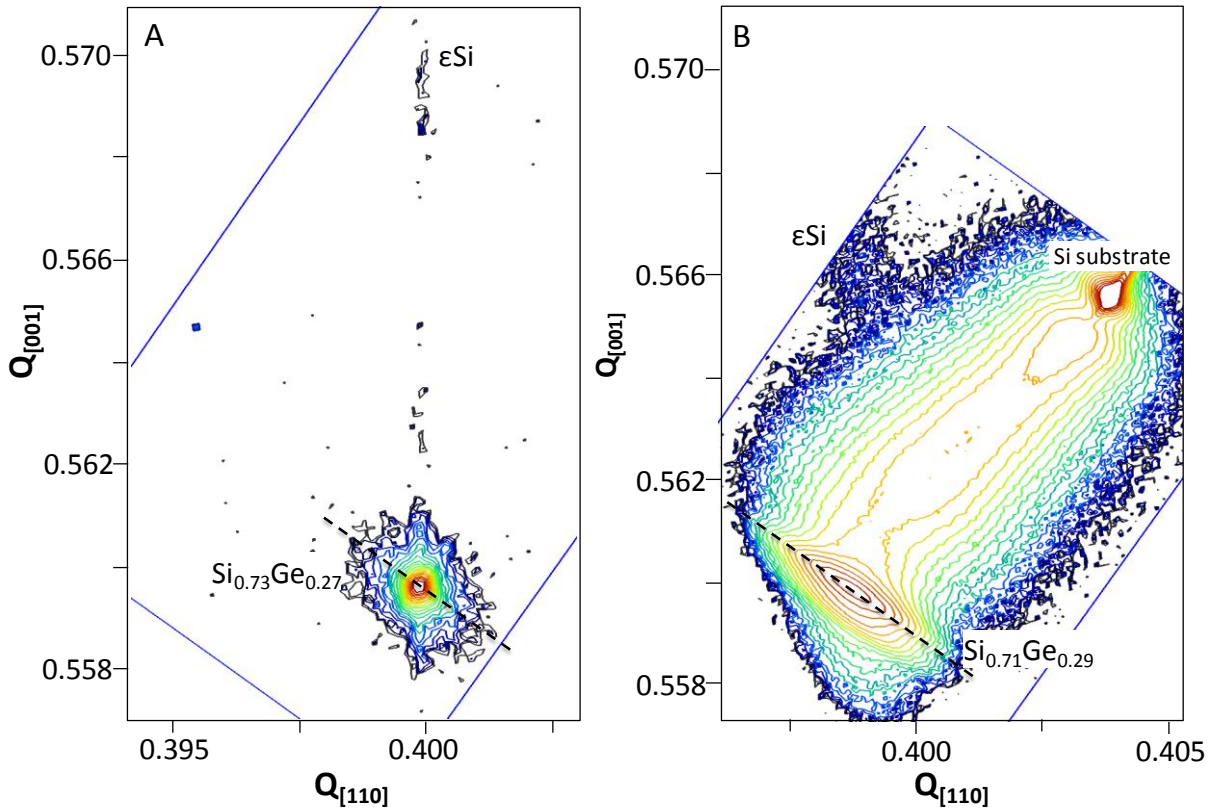

Figure 4-9. Off-axis (224) reciprocal space maps (RSMs) for (A) 20nm $Si_{0.73}Ge_{0.27}$/12nm Si/~2µm $Si_{0.73}Ge_{0.27}$/45nm $Si_{0.73}Ge_{0.27}$NM and (B) 20nm $Si_{0.71}Ge_{0.29}$/12nm Si/~2µm $Si_{0.71}Ge_{0.29}$/polished $Si_{0.71}Ge_{0.29}$ graded buffer layer substrate. The dashed line in both images is the constant θ line and peak broadening along this line represents variations in crystalline tilt.

Figures 4-10A and B show a comparison of the local tilt in heterostructures grown on SiGe NM substrates and graded buffer layer substrates, respectively. I hypothesized in the previous section that the tilt in the heterostructure grown on the SiGe NM originates from bending of the SiGe NM after transfer to the new host substrate. The magnitude of crystalline

tilt in the constant-composition SiGe layer grown on the graded buffer layer substrate (Figure 4-10B) is ~0.2° and follows the crosshatch pattern of the plastic relaxation in the graded substrate. This magnitude agrees with the average results shown in Figure 4-9B. Because dislocations multiply by the Frank-Read mechanism described in Chapter 1, dislocations will pile up near intersecting misfit segments creating the crosshatch block pattern. The blocks produced by the dislocation pileups will have slightly different crystalline tilts (Figure 4-10D). On smaller length scales (<5µm), however, the crystalline tilt decreases [~0.02°] (Figure 4-10C).

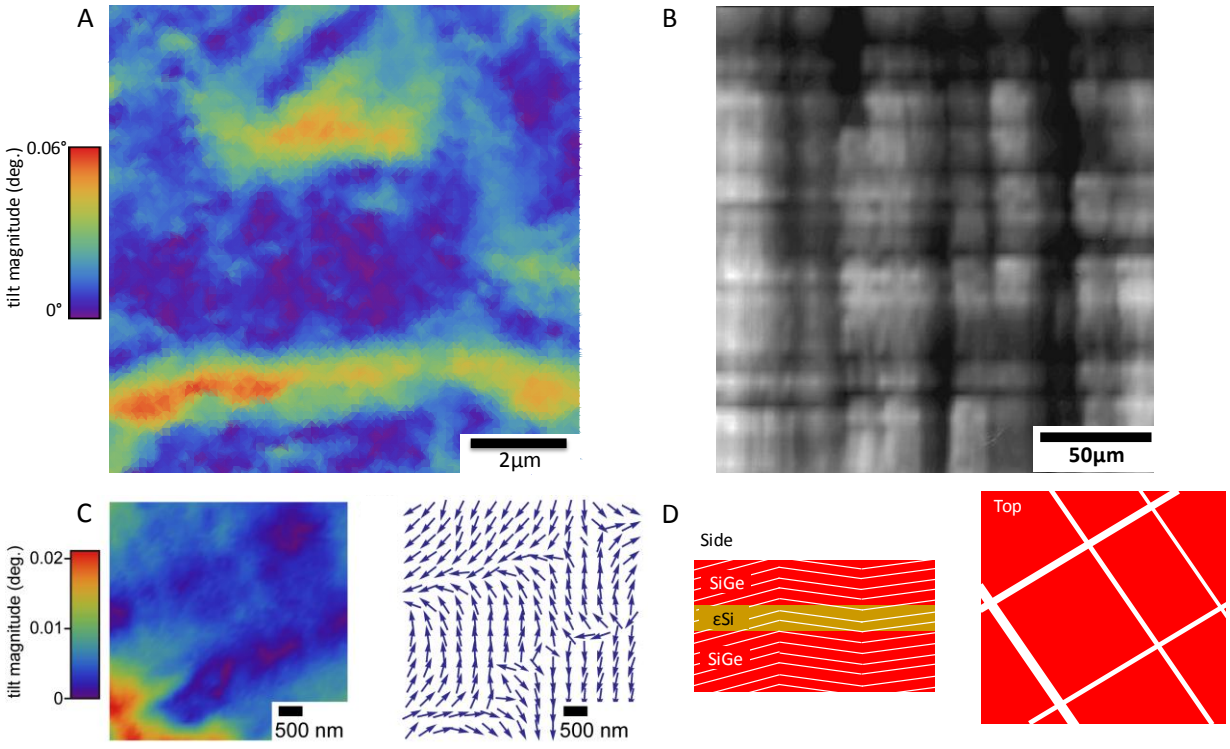

Figure 4-10. µXRD maps of crystalline tilt magnitude for the (A) strained Si QW layer of a 77nm $Si_{0.73}Ge_{0.27}$/10nm εSi/~1µm $Si_{0.73}Ge_{0.27}$/45nm $Si_{0.73}Ge_{0.27}$ NM heterostructure, (B) constant composition $Si_{0.83}Ge_{0.17}$ layer grown on a relaxed $Si_{0.83}Ge_{0.17}$ graded buffer layer substrate [7], and (C) strained-Si QW layer of a ~80nm $Si_{0.71}Ge_{0.29}$/10nm εSi/~1µm $Si_{0.71}Ge_{0.29}$/polished $Si_{0.71}Ge_{0.29}$ graded buffer layer heterostructure [8]. (D) Schematic diagrams of the mosaic blocks created by plastic relaxation in graded SiGe substrates.

One likely explanation for this decrease is that the measurement in Figure 4-10C is within one crystalline 'block,' thus reducing the tilt variation. On average, the tilt is still ~0.2° as shown in Figure 4-9B. The large crystalline tilt produced in samples grown on graded buffer layer substrates can increase charge carrier scattering (near "grain boundaries") in devices fabricated on these materials, a significant source of device failure for single-electron devices made from strained Si/relaxed SiGe heterostructures.

I also compared the local strain variations in the starting SiGe substrates and in the heterostructures grown on the SiGe substrates with micro-Raman spectroscopy. The strain variation in the SiGe and in the strained Si QW is reduced by a factor of two for the SiGe NM substrates as compared to the SiGe graded buffer layer substrates; the strain variation on the SiGe NM substrates is ±0.05% and it is ±0.10% on the SiGe graded buffer layer substrates. The strain variations remain approximately the same after overgrowth of SiGe/strained Si QW heterostructures. The graded buffer substrates (Figure 4-11B) and the heterostructures grown on them (Figures 4-12C and D) exhibit the crosshatch pattern indicative of plastic relaxation via dislocations. This pattern is absent on the SiGe NM substrates (Figure 4-11A) and the heterostructures grown on the NMs (Figures 4-12A and B). In Figure 4-12, the areas in which the strain variation in the SiGe layer (Si-Si mode) matches that of the strain variation of the strained Si layer (εSi mode) are areas where the Si is coherent with the SiGe (Si strained to the SiGe lattice constant). There is one area in the strained Si layer grown on the SiGe NM where the patterns of the two layers do not match (arrows in Figure 4-12B). The εSi mode moves to higher wavenumbers with respect to the Si-Si mode within the SiGe layer. This indicates

retraction of the Si lattice constant and is most likely due to plastic relaxation in the Si QW; the crosshatch-like pattern is oriented along <110> directions similar to that for the plastically relaxed SiGe buffer layer substrates. This result illustrates the versatility of the micro-Raman measurements in analyzing what is happening in both the relaxed SiGe layers and in the strained Si layers.

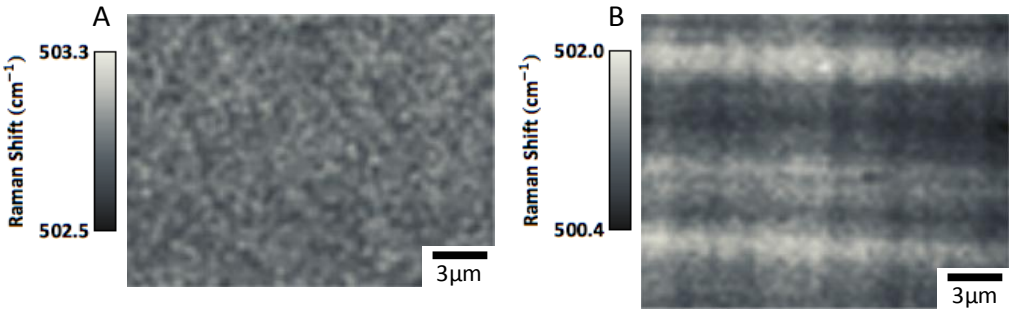

Figure 4-11. Micro-Raman maps of the Si-Si mode in (A) an elastically relaxed $Si_{0.73}Ge_{0.27}$ NM substrate and (B) a plastically relaxed, polished $Si_{0.71}Ge_{0.29}$ graded buffer layer substrate.

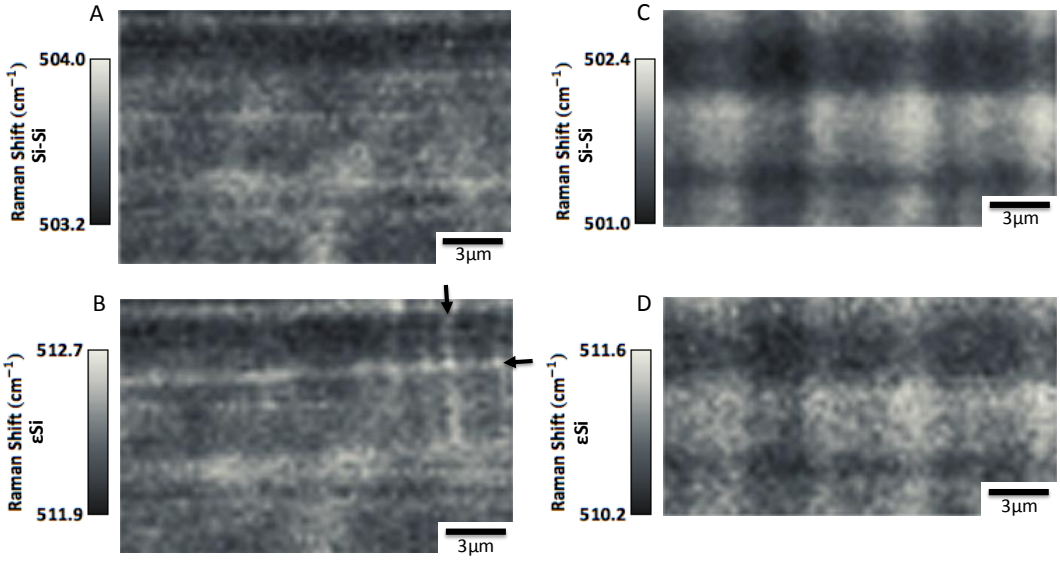

Figure 4-12. Micro-Raman maps of (A) the Si-Si mode and (B) the εSi mode of a 20nm $Si_{0.73}Ge_{0.27}$/12nm Si/~2µm $Si_{0.73}Ge_{0.27}$/45nm $Si_{0.73}Ge_{0.27}$NM heterostructure, and the (C) Si-Si mode and (D) εSi of a 20nm $Si_{0.71}Ge_{0.29}$/12nm Si/~2µm $Si_{0.71}Ge_{0.29}$/polished $Si_{0.71}Ge_{0.29}$ graded buffer layer heterostructure. The arrows in B point to areas where the strained-Si layer appears to be plastically relaxing.

4.6 Chapter Summary

Elastically relaxed SiGe NMs were used as substrates for epitaxial growth of high-crystalline-quality strained Si/SiGe heterostructures. Thick compositionally matched SiGe buffer layers were grown on the SiGe NMs to show that macroscopic single crystals could be grown on the thin transferred NMs. The strain and crystalline tilt of the strained Si/relaxed SiGe heterostructures were examined on macroscopic and microscopic length scales and compared to similar heterostructures grown on plastically relaxed graded buffer layer substrates. The strain and tilt variations in the heterostructures grown on the SiGe NMs were less than those of the heterostructures grown on the graded buffer layer substrates. Ideally the SiGe NM substrates should show little, if any, tilt and strain variation over the sample area. One of the current limitations of using SiGe NMs as growth substrates is the transfer method; the compliancy of the SiGe NM highlights any inhomogeneities at the NM bonded interface. Even with these inhomogeneities the SiGe NM substrates show promise as substrates for growth of high-crystalline quality strained Si/SiGe heterostructures.

4.7 References

1. M. A. Eriksson, M. Friesen, S. N. Coppersmith, R. Joint, L. J. Klein, *et al.,* Spin-based Quantum Computing in Silicon. *Quantum Inf. Process.* **3** (2004) 133-146.

2. D. P. Brunco, B. De Jaeger, G. Eneman, J. Mitard, G. Hellings, *et al.* Germanium MOSFET Devices: Advances in Materials Understanding, Process Development, and Electrical Performance. *J. Electrochem. Soc.* **155** (2008) H552 – H561.

3. S. Sioncke, D. P. Brunco, M. Meuris, O. Uwamahoro, J. Van Steenbergen, *et al.,* Etch rates of Ge, GaAs, and InGaAs in Acids, Bases, and Peroxide Based Mixtures, *ECS Trans.* **16** (2008) 451 – 460.

4. F. Pezzoli, E. Bonera, E. Grilli, M. Guzzi, S. Sanguinetti, *et al*., Phonon Strain Shift Coefficients in Si_{1-}

$_x$Ge$_x$ Alloys. *J. Appl. Phys*. **103** (2008) 093521.

5. S. Nakashima, T. Mitani, M. Ninomiya, K. Matsumoto, Raman Investigation of Strain in Si/SiGe Heterostructures: Precise Determination of the Strain-Shift Coefficient of Si Bands. *J. Appl. Phys*. **99** (2006) 053512.

6. H. Nagai, Structure of Vapor-Deposited $Ga_xIn_{1-x}As$ Crystals. *J. Appl. Phys*. **45** (1974) 3789-3794.

7. P. M. Mooney, J. O. Chu, SiGe Technology: Heteroepitaxy and High-Speed Microelectronics. *Annu. Rev. Mater. Sci.* **30** (2000) 335-362.

8. P. G. Evans, D. E. Savage, J. R. Prance, C. B. Simmons, M. G. Lagally, *et al.,* Nanoscale Distortions of Si Quantum Wells in Si/SiGe Quantum-Electronic Heterostructures. *Adv. Mater*. **24** (2012) 5217-5221.

Chapter 5 Conclusions

5.1 Dissertation summary and outlook

In this dissertation I have discussed several ways to strain engineer thin, freestanding Si and SiGe nanomembrane materials. Strain is in essence the ability to tune the lattice constant of a material, and elastic strain engineering in NMs offers a unique way to deform and elastically relax single-crystal materials in sheet form in order to harness potential advantages from strain without the introduction of crystalline defects.

With the freedom of materials integration that NMs offer, I showed that strain distributions not easily achieved with other methods can be incorporated into NM materials with proper elastic strain engineering. Expanding on basic isotropic elastic strain sharing theory, I used anisotropic linear elastic theory to calculate strain distributions between materials with different elastic symmetries. The calculations in Chapter 2 show that by combining materials with 2-fold and 4-fold elastic symmetry one can produce and tune anisotropic biaxial strain distributions in biaxially isotropic materials, and isotropic biaxial strain distributions in biaxially anisotropic elastic materials. This type of elastic strain sharing is only possible in thin NM materials because thicker, bulk-like materials will fail under similar strains.

NM materials also provide a means to fabricate elastically relaxed materials that cannot be easily made by conventional bulk crystal growth techniques. I demonstrated the fabrication and use of elastically relaxed, single-crystalline $Si_{(1-x)}Ge_x$ NMs. The SiGe NMs are epitaxially grown below the critical thickness for defect-mediated relaxation on silicon-on-insulator

substrates and subsequently released through two selective etching processes. I confirm with multiple characterization methods that the SiGe layers are fully strained to the Si lattice constant before release of the NM and fully elastically relaxed to the SiGe lattice constant after release. Once transferred and bonded to new handling substrates, the SiGe NMs can be used as templates for growth of new materials. I have demonstrated the growth of thick lattice matched SiGe alloy and Si coherently strained to the underlying SiGe NM. The uniformity of strain and crystalline tilt was examined in the heterostructures grown on SiGe NM substrates. The results show that the crystalline quality and strain uniformity of heterostructures grown on SiGe NMs are improved over heterostructures grown on plastically relaxed SiGe graded buffer layer substrates. These experiments show that the SiGe NMs are suitable for growth of high-crystalline-quality materials for use in high-performance applications.

The fabrication of elastic relaxed single-crystalline SiGe also facilitates the integration of other semiconducting materials into existing Si technology. With a tunable-lattice-constant substrate, III-V and II-VI alloys can in principle be grown with a matching lattice constant to incorporate direct-band-gap materials onto Si without the problems associated with lattice mismatched epitaxial growth. Control over the lattice constant of direct-band-gap materials allows tunability of the band gap to fabricate various optical devices, each operating at a different wavelength.

The strain engineering procedures described in this dissertation are quite naturally extendable to other materials systems where strain significantly modifies materials properties. NMs from any materials (single-crystalline or not) can be fabricated with proper selective etching of

release layers. Elastic strain sharing will take place between multilayer NMs where at least one layer is initially strained, and elastic relaxation of NMs will take place upon release of a single strained layer. The released NM can then be transferred to a new host substrate and used for materials integration or as a substrate for subsequent growth of new materials. In particular, a whole menagerie of compound-semiconductor materials, as well as various complex ferroic and superconducting oxides, fits into this category. We can therefore expect that many new or better materials will become possible based on nanomembrane strain engineering.

5.2 Future directions

Based on the results of this work, there are several future research opportunities that would aid in the development and understanding of strain engineered Si and SiGe NM materials. I highlight a few such topics here.

5.2.1 Electrical characterization

I focused on the crystalline quality and strain uniformity in relaxed SiGe/strained Si heterostructures grown on elastically relaxed SiGe NM substrates. The structural uniformities within heterostructures grown on SiGe NM substrates were improved compared to similar heterostructures grown on plastically relaxed graded buffer layer substrates. Conventionally, relaxed SiGe/strained Si QW heterostructures are grown on the plastically relaxed SiGe substrates to form a two-dimensional electron gas (2DEG) in the strained Si QW layer. Further gating of this 2DEG allows for the formation of single-electron quantum dot devices to

investigate spin coherence times for quantum computing applications [1]. Previous research has shown that the mobility limiting mechanism in low-temperature 2DEGs created in such heterostructures grown on the best graded buffer layer substrates (threading dislocation density ~$10^5/cm^2$) was background impurities, not structural imperfections [2]. We have reason to believe, however, that in these single-electron devices any nonuniformities in the crystalline film will cause variation from device to device. Strain variations will change the energy of the QW barrier and dislocations within the device may scatter charge. It is important then to investigate the electrical properties of Si/SiGe heterostructures grown on SiGe NMs to: (1) confirm that low-temperature 2DEG performance in these materials matches that of the materials grown on the graded buffer layer substrates, and (2) compare multiple devices on a single sample to investigate if device uniformity improves with the improvement in strain and crystalline tilt uniformity in heterostructures grown on SiGe NMs.

5.2.2 Defect density analysis

Throughout this work, I emphasized *elastic* strain engineering in NMs. I confirmed elastic strain sharing and elastic strain relaxation by measuring the strain in NMs at several stages of the fabrication process with multiple techniques (XRD and Raman spectroscopy). Within the resolution of the strain measurements there are no strain relieving crystalline defects in the NMs. To obtain an accurate measurement of the defect density in such NMs, methods that are able to measure very low defect densities are needed: defect etching or x-ray topography. In defect etching, chemical etching of the material occurs much faster at crystalline defects like threading dislocations, misfit dislocations, and stacking faults leaving pits or

trenches in the material. Once the material is etched properly, the defect density is obtained from counting the etch pits created by the defects. The difficulty with using this technique to obtain defect densities in NMs is that the NMs are very thin; the entire NM is etched away in a few seconds of the typical etchant solutions, even after diluting the solutions [3]. Defect etching could be used on thick heterostructures grown on released and transferred NMs, but the defect density may be a reflection of the quality of the epitaxial growth and not of the quality of the NM. X-ray topography is a more promising technique and does not require destroying the sample; it measures deviation from a Bragg condition over a large sample area (wafer size). Irregularities in the crystalline structure will appear as dark areas on a 2D detector because the Bragg condition is not met in that area (diffracted x-rays scatter at a different angle). X-ray topography may be difficult on NMs as well because of the transfer process. In Chapter 4 I discussed how the crystalline tilt in heterostructures grown on SiGe NM is most likely from a bending of the SiGe NM after the transfer process (NM conforms to the new substrate surface). This bending in the film will also show up as a deviation from the Bragg condition in x-ray topography.

5.2.3 Improving transferred NM interfaces

In order to use elastically strain engineered NMs, the NMs must be freestanding at some point in the fabrication process to allow strain to share between multiple layers or to allow the strain in a single layer to relax. The NMs must then be transferred to new host substrates for further processing (epitaxial growth, device fabrication, etc.). The bonded interface between the NM and the new host substrate is thus important; the NM must stay bonded to the new

host substrate through further processing and the bonding interface must not change the desired materials properties of the NM. Because NMs are very compliant, they will conform to the surface of the new substrate. In some cases, it is desirable to have a NM conform to nonuniform surfaces to advantageously change the materials properties [4]. In other cases, for example when growing epitaxial heterostructures on transferred NMs, it is desirable to have the NMs as flat as possible. Investigation and control of the bonded interface of unstrained transferred NMs is an active area of study. Dry-transfer processes dominate this literature because NM placement is more controlled compared to wet-transfer processes [5-7]. The issue with strain engineered NMs is that they must be freestanding at some point to allow strain sharing or strain relaxation to occur; the entire NM must expand or contract in the freestanding state to come to equilibrium. Wet-transfer techniques allow full expansion or contraction of the NM, while dry-transfer processes often result in wrinkles or breaking of the strained NM during transfer [8]. Wet-transfer techniques typically have lower yields and placement of the NM on the new host substrate is often random. There is also always a layer of water (or solution) that is trapped at the interface, introducing a source of contamination at the bonded interface. It is therefore important to develop transfer techniques for better control over transferred strained-engineered NM interfaces. One such alternative could be employing a multiple release and transfer technique: (1) release and transfer the strain-engineered NM with conventional wet processes but transfer the NM to a host substrate with a release layer, (2) release the NM in place (it has already strain shared so it will remain flat) and use dry transfer processes to place the NM onto the final host substrate. A second option is to fabricate a tethered NM window

(freestanding NM attached on all sides by a thick handle substrate 'frame'), and fabricate the strain-engineered NM in the freestanding portion by growing or depositing multiple layers. The final NM can then be transferred by breaking the freestanding area away from the handle substrate 'frame' [9].

5.3 References

1. C. B. Simmons, J. R. Prance, B. J. Van Bael, T. S. Koh, Z. Shi, *et al*. Tunable Spin Loading and T_1 of a Silicon Spin Qubit Measured by Single-Shot Readout. *Phys. Rev. Lett*. **106** (2011) 156804.

2. D. Monroe, Y.H. Xie, E. A. Fitzgerald, P. J. Silverman, G. P. Watson, Comparison of Mobility-Limiting Mechanisms in High-Mobility $Si_{1-x}Ge_x$ Heterostructures. *J. Vac. Sci. Technol., B* **11** (1993) 1731-1737.

3. E. Escobedo-Cousin, S. H. Olsen, A. G. O'Neill, H. Coulson, Defect Identification in Strained Si/SiGe Heterolayers for Device Applications. *J. Phys. D: Appl. Phys*. **42** (2009) 175306.

4. A. I. Fedorchenko, H. H. Cheng, G. Sun, and R. A. Soref, Radiation Emission from Wrinkled SiGe/SiGe Nanostructures. *Appl. Phys. Lett.* **96** (2010) 113104.

5. H.-J. Kim, Fracture Mechanics-Based Approaches to Understand and Control Adhesion in Thin-Film Transfer Processes. PhD Dissertation: Univ. of Wisconsin-Madison (2011).

6. A. M. Kiefer, D. M. Paskiewicz, A. M. Clausen, W. R. Buchwald, R. A. Soref, et al. Si/Ge Junctions Formed by Nanomembrane Bonding. *ACS Nano* **5** (2011) 1179-1189.

7. M. A. Meitl, Z.-T. Zhu, V. Kumar, K. J. Lee, X. Feng, *et al.,* Transfer Printing by Kinetic Control of Adhesion to an Elastomeric Stamp. *Nature Mater.* **5** (2006) 33-38.

8. S. A. Scott, M. G. Lagally, Elastically Strain-Sharing Nanomembranes: Flexible and Transferable Strained Silicon and Silicon-Germanium Alloys. *J. Phys. D: Appl. Phys.* **40** (2007) R75-R92.

9. U.S. Patent Application No. 13/13367600, (submitted Feb. 7, 2012) (Max G. Lagally, Deborah M. Paskiewicz, Boy Tanto, applicants).

Appendix A Coordinate transformations and anisotropic linear elastic theory

Tensor mathematics and anisotropic elastic theory was used extensively in this dissertation to calculate anisotropic strain distributions in elastically strain shared nanomembrane systems. A brief review of these concepts is presented in this Appendix.

A.1 Coordinate transformations

A coordinate transformation will transform a vector from one coordinate system to another without loss of information; the vector magnitude and direction do not change, just the basis to which it is referenced. The vector **a** is transformed to the vector **a*** by the transformation matrix Q:

$$\mathbf{a}^* = Q.\mathbf{a} \tag{A-1}.$$

a is a vector in the universal coordinate system with basis unit vectors: $e = \{\hat{e}_1, \hat{e}_2, \hat{e}_3\}$**,** and **a*** is the same vector transformed into a new coordinate system with basis unit vectors: $m = \{\hat{m}_1, \hat{m}_2, \hat{m}_3\}$**.** The transformation matrix Q is defined as:

$$Q = \begin{pmatrix} \hat{m}_1\hat{e}_1 & \hat{m}_1\hat{e}_2 & \hat{m}_1\hat{e}_3 \\ \hat{m}_2\hat{e}_1 & \hat{m}_2\hat{e}_2 & \hat{m}_2\hat{e}_3 \\ \hat{m}_3\hat{e}_1 & \hat{m}_3\hat{e}_2 & \hat{m}_3\hat{e}_3 \end{pmatrix} \tag{A-2}.$$

Because $\hat{m}_i$ and $\hat{e}_i$ are both unit vectors, the product is just the cosine of the angle between them (from dot product): $\hat{m}_i\hat{e}_i = \cos\theta$. The columns of the transformation matrix, Q, are the **x***, **y***, and **z*** vectors defined by the x-, y-, and z-directions in the universal coordinate system.

Consider transforming a matrix from the universal Cartesian coordinate system to the one shown in Figure A-1. Here $e = \{[100],[010],[001]\}$ is the universal Cartesian coordinate system, and $m = \left\{\frac{1}{\sqrt{2}}[\bar{1}10],[001],\frac{1}{\sqrt{2}}[110]\right\}$ is the transformed coordinate system (starred). This transformation is needed when considering (110)-oriented cubic crystalline materials. Then

$$Q = \begin{pmatrix} \frac{-1}{\sqrt{2}} & \frac{1}{\sqrt{2}} & 0 \\ 0 & 0 & 1 \\ \frac{1}{\sqrt{2}} & \frac{1}{\sqrt{2}} & 0 \end{pmatrix} \qquad \text{(A-3).}$$

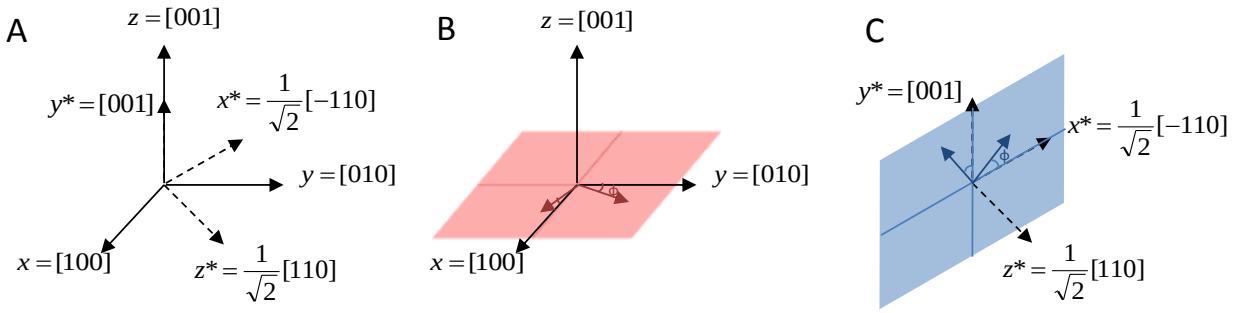

Figure A-1. (A) The universal coordinate system (solid lines): x = $\hat{e}_1$ = [100], y = $\hat{e}_2$ = [010], z = $\hat{e}_3$ = [001]. The new coordinate system (dashed lines): x* = $\hat{m}_1$ = $\frac{1}{\sqrt{2}}[\bar{1}10]$, y* = $\hat{m}_2$ = [001], z* = $\hat{m}_3$ = $\frac{1}{\sqrt{2}}[110]$. Rotation of the (B) universal coordinate system and the (C) new coordinate system about the z- and z*-axes by angle φ, respectively.

The x- and y-directions are often rotated about the z-axis to calculate anisotropic materials properties as a function of direction in the x-y plane. We can rotate the original x- and y-axes in the universal coordinate system by making the transformation matrix a function of

rotation about the z-axis. For the universal coordinate system shown in Figure A-1B, the x- and y-directions will rotate (red arrows) about the z-axis as a function of ϕ (red plane):

$$Q_{(001)} = \begin{pmatrix} \cos\phi & \sin\phi & 0 \\ -\sin\phi & \cos\phi & 0 \\ 0 & 0 & 1 \end{pmatrix} \quad \text{(A-4).}$$

A similar transformation can be done in the new coordinate system:

$$Q_{(110)} = \begin{pmatrix} \frac{-1}{\sqrt{2}}\cos\phi & \frac{1}{\sqrt{2}}\cos\phi & \sin\phi \\ \frac{1}{\sqrt{2}}\sin\phi & \frac{-1}{\sqrt{2}}\sin\phi & \cos\phi \\ \frac{1}{\sqrt{2}} & \frac{1}{\sqrt{2}} & 0 \end{pmatrix} \quad \text{(A-5).}$$

For any rectangular coordinate system the three basis vectors must form an orthonormal basis (basis vectors are orthogonal to one another), which makes the transformation matrix Q orthogonal ($Q^{-1} = Q^{T}$).

A.2 Linear elastic theory

In linearly elastic materials, there is a region of the stress vs. strain curve that is linear; the stress is linearly proportional to strain. Linear elastic theory applies up to the elastic limit and Hooke's law can be used to determine stress as a function of strain (and vice versa). In simple isotropic materials, the stress that results from a uniaxial strain (deformation in one direction) is:

$$\sigma = E\varepsilon \quad \text{(A-6),}$$

where E is the Young's (or elastic) modulus of the material. It is also the slope of the stress/strain curve for uniaxial loading. An isotropic material, by definition, is one in which the

elastic properties are the same in all directions: the response of an isotropic material is the same no matter which direction the stress or strain is applied.

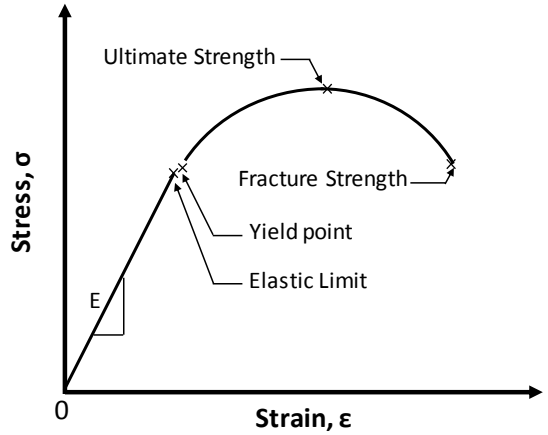

Figure A-2. Stress-strain curve. Linear elastic theory applies up to the elastic limit. The slope of the linear region of the curve is the elastic (or Young's) modulus, E.

Elastic strain in a material is defined as the change in length of the material divided by the original length. In other words the percentage of length gained or lost with the deformation. For crystalline materials we can define strain as a change in lattice constant:

$$\varepsilon = \frac{a_{new} - a_o}{a_o} \qquad \text{(A-7)}.$$

A positive strain indicates the material gets larger (tensile strain), and a negative strain means the material got shorter (compressive strain).

To fully characterize elastic deformation in isotropic materials, two elastic constants must be known. Many times the engineering constants are given: Young's modulus (E), biaxial modulus (M), shear modulus (μ or G), or Poisson's ratio (v). The Young's modulus is the response of the material to uniaxial loading, the biaxial modulus is the response of the material

to biaxial loading (plane strain), the shear modulus is the response of the material to shear loading, and Poisson's ratio is the ratio of the transverse strain to the axial strain for uniaxial loading. For isotropic materials, all of these quantities are related and only two need to be known independently:

$$E = \frac{1}{s_{11}}, \quad \nu = -\frac{s_{12}}{s_{11}} = -\frac{\varepsilon_{trans}}{\varepsilon_{axial}}, \quad M = \frac{E}{1-\nu},$$
$$\mu = \frac{E}{2(1+\nu)} = c_{44} = \frac{1}{2}(c_{11} - c_{12}) = \frac{1}{s_{44}} = \frac{1}{2(s_{11} - s_{12})} \qquad \text{(A-8).}$$

The constants c_{ij} and s_{ij} make up the stiffness and compliance tensors, respectively. These will be discussed in more detail below.

In most crystalline materials the response to a given strain is anisotropic; the response of the material is dependent on the crystallographic direction of the applied force. The engineering elastic constants are now a function of crystallographic orientation. Hooke's law can still be used in the linear elastic region of anisotropic crystalline materials, but we must account for anisotropy. Now the stress/strain relations are:

$$\sigma_{ij} = c_{ijkl}\varepsilon_{kl}$$
$$\varepsilon_{ij} = s_{ijkl}\sigma_{kl} \qquad \text{(A-9).}$$

The stress and strain are both second rank tensors, which can be written as:

$$\sigma = \begin{pmatrix} \sigma_{11} & \sigma_{12} & \sigma_{13} \\ \sigma_{21} & \sigma_{22} & \sigma_{23} \\ \sigma_{31} & \sigma_{32} & \sigma_{33} \end{pmatrix}, \qquad \varepsilon = \begin{pmatrix} \varepsilon_{11} & \varepsilon_{12} & \varepsilon_{13} \\ \varepsilon_{21} & \varepsilon_{22} & \varepsilon_{23} \\ \varepsilon_{31} & \varepsilon_{32} & \varepsilon_{33} \end{pmatrix} \qquad \text{(A-10a)}$$

$$\sigma = \sigma_{ij} = \begin{bmatrix} T^{(e_1)} \\ T^{(e_2)} \\ T^{(e_3)} \end{bmatrix} = \begin{pmatrix} \sigma_{11} & \sigma_{12} & \sigma_{13} \\ \sigma_{21} & \sigma_{22} & \sigma_{23} \\ \sigma_{31} & \sigma_{32} & \sigma_{33} \end{pmatrix} \equiv \begin{pmatrix} \sigma_{xx} & \sigma_{xy} & \sigma_{xz} \\ \sigma_{yx} & \sigma_{yy} & \sigma_{yz} \\ \sigma_{zx} & \sigma_{zy} & \sigma_{zz} \end{pmatrix} \equiv \begin{pmatrix} \sigma_{xx} & \tau_{xy} & \tau_{xz} \\ \tau_{yx} & \sigma_{yy} & \tau_{yz} \\ \tau_{zx} & \tau_{zy} & \sigma_{zz} \end{pmatrix} \qquad \text{(A-10b),}$$

where each of the components is described in Figure A-3.

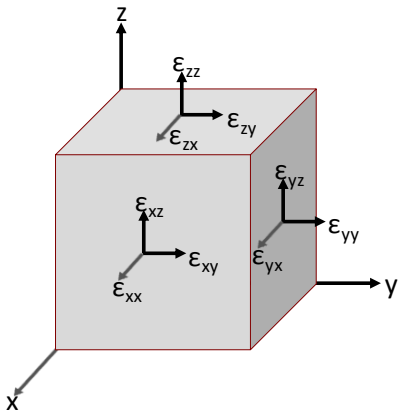

Figure A-3. The strain tensor components defined in the universal coordinate system. The stress tensor components are defined in a similar way.

The stiffness and compliance of the material are both represented by fourth rank tensors. The stiffness tensor (the compliance tensor has the same form) is:

$$c = \begin{pmatrix} \begin{pmatrix} c_{1111} & c_{1112} & c_{1113} \\ c_{1121} & c_{1122} & c_{1123} \\ c_{1131} & c_{1132} & c_{1133} \end{pmatrix} & \begin{pmatrix} c_{1211} & c_{1212} & c_{1213} \\ c_{1221} & c_{1222} & c_{1223} \\ c_{1231} & c_{1232} & c_{1233} \end{pmatrix} & \begin{pmatrix} c_{1311} & c_{1312} & c_{1313} \\ c_{1321} & c_{1322} & c_{1323} \\ c_{1331} & c_{1332} & c_{1333} \end{pmatrix} \\ \begin{pmatrix} c_{2111} & c_{2112} & c_{2113} \\ c_{2121} & c_{2122} & c_{2123} \\ c_{2131} & c_{2132} & c_{2133} \end{pmatrix} & \begin{pmatrix} c_{2211} & c_{2212} & c_{2213} \\ c_{2221} & c_{2222} & c_{2223} \\ c_{2231} & c_{2232} & c_{2233} \end{pmatrix} & \begin{pmatrix} c_{2311} & c_{2312} & c_{2313} \\ c_{2321} & c_{2322} & c_{2323} \\ c_{2331} & c_{2332} & c_{2333} \end{pmatrix} \\ \begin{pmatrix} c_{3111} & c_{3112} & c_{3113} \\ c_{3121} & c_{3122} & c_{3123} \\ c_{3131} & c_{3132} & c_{3133} \end{pmatrix} & \begin{pmatrix} c_{3211} & c_{3212} & c_{3213} \\ c_{3221} & c_{3222} & c_{3223} \\ c_{3231} & c_{3232} & c_{3233} \end{pmatrix} & \begin{pmatrix} c_{3311} & c_{3312} & c_{3313} \\ c_{3321} & c_{3322} & c_{3323} \\ c_{3331} & c_{3332} & c_{3333} \end{pmatrix} \end{pmatrix} \quad \text{(A-11).}$$

From symmetry, $c_{ijkl} = c_{jikl} = c_{klij}$ and similarly for s_{ijkl}. This also makes the stress and strain tensors symmetric, $\sigma_{ij} = \sigma_{ji}$ and $\varepsilon_{ij} = \varepsilon_{ji}$. Now the 81 components of the compliance and stiffness tensors

have been reduced to 21, and the 9 components of the stress and strain tensors have been reduced to 6. The reduction in the number of independent components reduces Hooke's law to:

$$\begin{aligned} \sigma_i &= C\varepsilon_i \\ \varepsilon_i &= S\sigma_i \end{aligned} \tag{A-12}$$

where,

$$\sigma_i = \begin{pmatrix} \sigma_{11} \\ \sigma_{22} \\ \sigma_{33} \\ \sigma_{23} \\ \sigma_{13} \\ \sigma_{12} \end{pmatrix}, \quad \varepsilon_i = \begin{pmatrix} \varepsilon_{11} \\ \varepsilon_{22} \\ \varepsilon_{33} \\ 2\varepsilon_{23} \\ 2\varepsilon_{13} \\ 2\varepsilon_{12} \end{pmatrix}, \quad C = \begin{pmatrix} c_{11} & c_{12} & c_{13} & c_{14} & c_{15} & c_{16} \\ c_{12} & c_{22} & c_{23} & c_{24} & c_{25} & c_{26} \\ c_{13} & c_{23} & c_{33} & c_{34} & c_{35} & c_{36} \\ c_{14} & c_{24} & c_{34} & c_{44} & c_{45} & c_{46} \\ c_{15} & c_{25} & c_{35} & c_{45} & c_{55} & c_{56} \\ c_{16} & c_{26} & c_{36} & c_{46} & c_{56} & c_{66} \end{pmatrix} \tag{A-13},$$

and S has a similar form as C. The subscript *i* denotes the reduced vector form of the stress or strain tensor. The number of independent elastic constants (c_{ij} or s_{ij}) can be further reduced depending on the symmetry of the crystalline material. For isotropic materials the stiffness tensor reduces to:

$$C = \begin{pmatrix} c_{11} & c_{12} & c_{12} & 0 & 0 & 0 \\ c_{12} & c_{11} & c_{12} & 0 & 0 & 0 \\ c_{12} & c_{12} & c_{11} & 0 & 0 & 0 \\ 0 & 0 & 0 & \frac{1}{2}(c_{11} - c_{12}) & 0 & 0 \\ 0 & 0 & 0 & 0 & \frac{1}{2}(c_{11} - c_{12}) & 0 \\ 0 & 0 & 0 & 0 & 0 & \frac{1}{2}(c_{11} - c_{12}) \end{pmatrix} \tag{A-14}.$$

Recall that only two independent materials constants are needed to describe deformation in isotropic materials. In cubic crystalline materials three independent materials constants are needed to describe deformation, and the stiffness matrix can be written as:

$$C = \begin{pmatrix} c_{11} & c_{12} & c_{12} & 0 & 0 & 0 \\ c_{12} & c_{11} & c_{12} & 0 & 0 & 0 \\ c_{12} & c_{12} & c_{11} & 0 & 0 & 0 \\ 0 & 0 & 0 & c_{44} & 0 & 0 \\ 0 & 0 & 0 & 0 & c_{44} & 0 \\ 0 & 0 & 0 & 0 & 0 & c_{44} \end{pmatrix} \quad \text{(A-15).}$$

Other forms of the stiffness tensor and the number of independent elastic constants needed to describe deformation in other types of crystalline materials are outlined in [1].

The constants c_{11}, c_{12}, c_{44}, s_{11}, s_{12}, and s_{44} are tabulated for many cubic crystalline materials. Table 2 gives the elastic constants for select materials, some of which were used in chapter 2 as examples of strain sharing between isotropic and anisotropic nanomembrane materials. For isotropic materials only two of the three materials constants are given.

Table A-1. Elastic constants for select materials.

Material	c_{11}	c_{12}	c_{44}	s_{11}	s_{12}	s_{44}
	(GPa)			(GPa^{-1} x 10^{-3})		
Si[1]	166.2	64.4	79.8	7.67	-2.14	12.54
$Si_{(1-x)}Ge_x$[2]	166.2 - 37.8x	64.4 - 16.2x	79.8 - 13.1x	7.67+2.13x	-(2.14+0.54x)	12.54+2.46x
GaAs	118.8	53.7	59.4	11.72	-3.65	16.82
SiO_2[4]	75.6	14.4		14.1	-2.25	
Si_3N_4[4]	320	90.1		3.57	-0.79	
a-Si[3]	131	64	37	11.2	-3.69	27.0
a-Ge[3]	110	43	34	11.7	-3.27	29.4
a-Cr[4,5]	314	83.4		3.58	-0.75	
poly-Au[4]	253	199		12.8	-5.64	

[1]Si was used as the balancing layers in cases considered in chapter 2 [2].
[2]Linear combination of Si and Ge elastic constants based on alloy concentration. This is valid based on reference [3]. $Si_{0.80}Ge_{0.20}$ was used as the stressor layer in cases 1, 2, and 4.
[3]Amorphous Si [4] was used as the stressor layer in case 3 and a-Ge was used as the "softer" stressor layer in section 2.5.
[4]Elastic constants are calculated values assuming an isotropic material based on elastic modulus and Poisson's ratio [2]. For ideal isotropic materials, there are only two unique elastic constants: $c_{44} = ½(c_{11} – c_{12})$
[5]a-Cr was used as the "stiffer" stressor layer in section 2.5.

It is useful to know how to transform the stress and strain vectors and the compliance and stiffness matrices in reduced form to different coordinate systems. As they are written above they are referenced to the universal Cartesian coordinate system, with basis vectors $e = \{[100],[010],[001]\}$. The derivation of the transformations is done in [1]. The result is shown here. The starred quantities are in a new reference system.

$$\begin{aligned} \sigma_i^* &= K\sigma_i, & \sigma_i &= K^{-1}\sigma_i^* \\ \varepsilon_i^* &= \left(K^{-1}\right)^T \varepsilon_i, & \varepsilon_i &= K^T\varepsilon_i^* \\ \sigma_i &= C\varepsilon_i, & \varepsilon_i &= S\sigma_i \\ \sigma_i^* &= C^*\varepsilon_i^*, & \varepsilon_i^* &= S^*\sigma_i^* \end{aligned} \qquad \text{(A-16)}$$

$$C^* = KCK^T, \qquad S^* = \left(K^{-1}\right)^T SK^{-1} \tag{A-17},$$

where

$$K = \begin{bmatrix} K_1 & 2K_2 \\ K_3 & K_4 \end{bmatrix} \tag{A-18}$$

$$K_1 = \begin{bmatrix} Q_{11}^2 & Q_{12}^2 & Q_{13}^2 \\ Q_{21}^2 & Q_{22}^2 & Q_{23}^2 \\ Q_{31}^2 & Q_{32}^2 & Q_{33}^2 \end{bmatrix} \tag{A-18a}$$

$$K_2 = \begin{bmatrix} Q_{12}Q_{13} & Q_{13}Q_{11} & Q_{11}Q_{12} \\ Q_{22}Q_{23} & Q_{23}Q_{21} & Q_{21}Q_{22} \\ Q_{32}Q_{33} & Q_{33}Q_{31} & Q_{31}Q_{32} \end{bmatrix} \tag{A-18b}$$

$$K_3 = \begin{bmatrix} Q_{21}Q_{31} & Q_{31}Q_{32} & Q_{23}Q_{33} \\ Q_{31}Q_{11} & Q_{32}Q_{12} & Q_{33}Q_{13} \\ Q_{11}Q_{21} & Q_{12}Q_{22} & Q_{13}Q_{23} \end{bmatrix} \tag{A-18c}$$

$$K_4 = \begin{bmatrix} Q_{22}Q_{33} + Q_{23}Q_{32} & Q_{23}Q_{31} + Q_{21}Q_{33} & Q_{21}Q_{32} + Q_{22}Q_{31} \\ Q_{32}Q_{13} + Q_{33}Q_{12} & Q_{33}Q_{11} + Q_{31}Q_{13} & Q_{31}Q_{12} + Q_{32}Q_{11} \\ Q_{12}Q_{23} + Q_{13}Q_{22} & Q_{13}Q_{21} + Q_{11}Q_{23} & Q_{11}Q_{22} + Q_{12}Q_{21} \end{bmatrix} \tag{A-18d}.$$

Q_{ij} are the components of the transformation matrix defined above.

The engineering elastic constants (as a function of crystallographic direction) can be extracted from the stiffness and compliance matrices by applying certain stress or strain conditions. For instance, the anisotropic Young's modulus, E, is the response of the material to a uniaxial stress in a given direction. Where the biaxial modulus, M, is the response of a material to an equal biaxial stress in a given plane. A uniaxial stress along the x-direction in Cartesian coordinates is:

$$\sigma = \begin{pmatrix} \sigma_o & 0 & 0 \\ 0 & 0 & 0 \\ 0 & 0 & 0 \end{pmatrix} \quad \text{(A-19)},$$

and equibiaxial stress in the xy-plane in Cartesian coordinates is:

$$\sigma = \begin{pmatrix} \sigma_o & 0 & 0 \\ 0 & \sigma_o & 0 \\ 0 & 0 & 0 \end{pmatrix} \quad \text{(A-20)}.$$

The compliance tensor may need to be transformed to find the anisotropic response of a material; it is most convenient to define a coordinate system in which the applied stress or strain is along one of the basis directions. If the stress is acting along the [110] direction of the crystal, compliance tensor must be transformed such that the x-direction now lies along [110]. To find E or M as a function of in-plane direction the coordinate transformation must sweep the x-y plane (make x and y axes transformations functions of ϕ as shown above). This is especially useful to determine characteristics of sheets of crystalline materials (i.e. membranes). The Young's modulus, Poisson's ratio, and biaxial modulus were shown for crystalline Si and Ge in the (001), (110), and (111) planes in chapter 1.

The above theory was applied when solving for anisotropic strain distributions in elastically strain shared NM systems (chapter 2). Table 2 shows the components of the mismatch strain used for each of the cases described in chapter 2. Recall that cases 1-3 assumed an equi-biaxial mismatch strain and case 4 assumed an anisotropic mismatch strain. The differences in the z-components of the strain tensor are due to differences in crystallographic direction of the NMs.

Table A-2. Components of the mismatch strain tensor for each of the cases considered in chapter 2.

	ε_{xx}	ε_{yy}	ε_{zz}
Case 1[1]	ε_m	ε_m	$-\frac{2c_{12}}{c_{11}}\varepsilon_m$
Case 2[1]	ε_m	ε_m	$-\frac{c_{11}+3c_{12}-2c_{44}}{c_{11}+c_{12}+2c_{44}}\varepsilon_m$
Case 3[2]	ε_m	ε_m	$-\frac{2c_{12}}{c_{11}}\varepsilon_m$
Case 4[3]	ε_m	$a\varepsilon_m$	$-\frac{c_{11}+3c_{12}-2c_{44}-2ac_{12}}{c_{11}+c_{12}+2c_{44}}\varepsilon_m$

[1] ε_m = mismatch strain between Si and $Si_{0.8}Ge_{0.2}$
[2] ε_m = 1.0%
[3] ε_m = 0.2%, a = 4

A.3 References

1. T. C. T. Ting, *Anisotropic Elasticity: Theory and Applications* Oxford Univ. Press: New York (1996).

2. L. B. Freund, S. Suresh, *Thin Film Materials: Stress, Defect Formation, and Surface Evolution* Cambridge Univ. Press: Cambridge, MA (2003).

3. J. A. Floro, E. Chason, S. R. Lee, G. A. Petersen, Biaxial Moduli of Coherent $Si_{1-x}Ge_x$ Films on Si(001). *Appl. Phys. Lett.* **71** (1997) 1694-1696.

4. C. Mathiondakis, P. C. Kelires, Softening of Elastic Moduli of Amorphous Semiconductors. *J. Non-Cryst. Solids* **266-269** (2000) 161-165.

Appendix B Micro-Raman spectroscopy data analysis

The Raman shift or frequency of the measured Raman modes in Si and SiGe crystals is very sensitive to strain and composition. It is therefore important to accurately determine exact frequencies of the peaks in each Raman spectrum. This requires appropriate peak fitting, proper calibration, and knowledge of the stability and sensitivity of the instrument. I used the LabRAM Aramis Horiba Jobin Yvon Confocal Raman Microscope in the Materials Science Center at the University of Wisconsin for all of the Raman measurements in this work. Here I discuss some of the data and uncertainty analysis required to obtain accurate peaks shifts of less than 1cm^{-1} for the HeCd 442nm laser. Other wavelengths are available on this instrument but were not used for a significant portion of the data collected in this work.

B.1 Peak fitting

I used a weighted linear combination of Gaussian and Lorentzian line forms to fit symmetric Raman peaks. This approximation is an alternative to the Voigt profile (convolution of Gaussian and Lorentzian functions); the weighted linear combination is less computationally intensive and reduces the time it takes to fit large data sets (two-dimensional maps can have over 5000 points). The functional form used in the peak fitting of symmetric peaks is:

$$I = y + A\left(\frac{(1-c)e^{-\frac{(x-x_o)^2}{2\sigma^2}}}{\sqrt{2\pi}\sigma} + \frac{c}{\pi\sigma\left(1+\frac{(x-x_o)^2}{\sigma^2}\right)}\right) \qquad \text{(B-1)}$$

where y is the magnitude of the constant background, A is the amplitude, σ is the peak width, x_o is the peak position, and c is the weighted proportion of the function that is Lorentzian-like (I used c = 0.8). Figure B-1 shows how well this functional form fits the Raman data from a bulk Si sample. The Raman peak near 520cm^{-1} is from the bulk Si. The Raman signal shown in Figure B-1 is raw data and has not been adjusted for proper calibration; peak fitting puts the bulk Si peak at 516.37 ± 0.01cm^{-1}. Bulk Si is often used as a calibration sample by setting ω_o = 520cm^{-1}. All other peaks are then referenced from bulk Si.

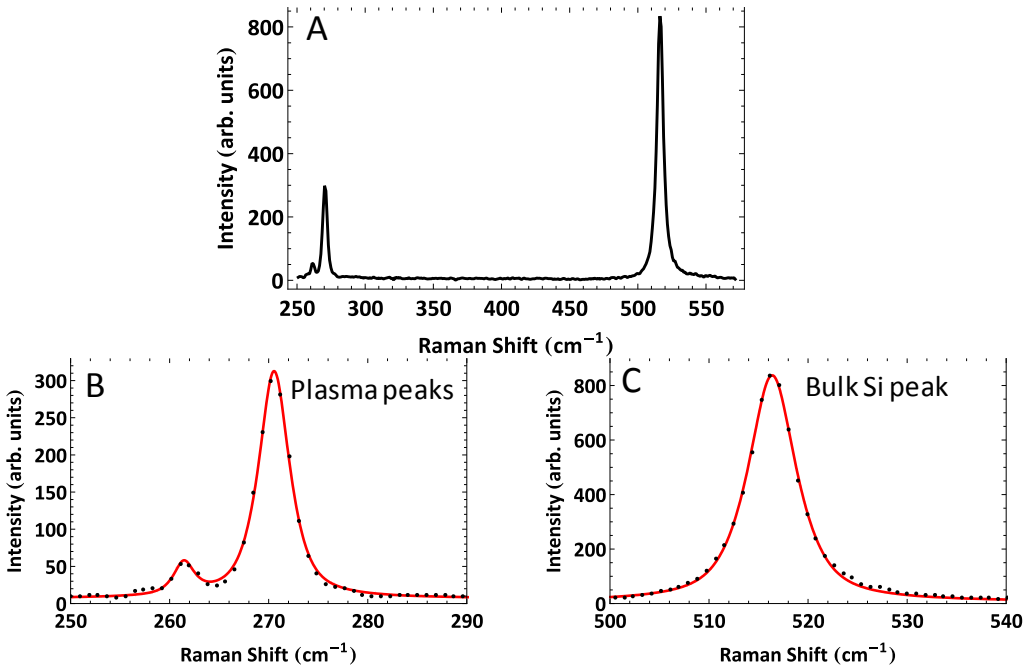

Figure B-1. Example Raman spectrum of bulk Si. The peak near 520cm^{-1} is from the LO phonons in Si and the peak near 270cm^{-1} is the plasma peak from the HeCd laser (442nm). The entire spectrum is shown in (A); (B) and (C) show the peak fitting (solid line) results using Eq. B-1 for the plasma peaks and the bulk Si peak, respectively. Data acquisition information: 442nm laser, 100x obj., D1 filter, 2400 grating, 55µm confocal hole, 10sec acquisition time, averaged over 2 cycles.

The plasma peak shown in Figure B-1 is an additional wavelength generated in the gas laser (weak intensity compared to laser wavelength) and elastically scattered off of the sample. The plasma peak is often used as an internal calibration when bulk Si is not present to measure small shifts in the Si Raman mode due to strain [10, 11]. The plasma peak will shift with changes in the instrument over time (small deviations in alignment due to heat, humidity, and instabilities of the laser). If the positions of the bulk Si peak and the main plasma peak are known, small shifts (< 0.5cm^{-1}) can be accurately measured (more details on this below).

The profile in Eq. B-1 is used for symmetric Raman peaks (pure Si and Ge Raman modes). The profile must be altered to accurately determine the peak positions in SiGe alloys; the Si-Si, Si-Ge and Ge-Ge peaks of SiGe alloys are asymmetric and must be fit with an asymmetric profile [1]. The functional form used to fit peaks from SiGe is a two-sided Lorentzian:

$$I = \frac{1}{2}\left[y_1\left(1-sign(x-x_o)\right)+y_2\left(1-sign(x_o-x)\right)\right]+\frac{A}{2}\left[\frac{1-sign(x-x_o)}{1+\frac{(x-x_o)^2}{\sigma_1^2}}+\frac{1-sign(x_o-x)}{1+\frac{(x_o-x)^2}{\sigma_2^2}}\right] \quad \text{(B-2)}$$

where A is the amplitude, x_o is the peak position, y_1 and y_2 represent the background of the low and high wavenumber side of the peak, respectively, and σ_1 and σ_2 represent the peak width of the low and high wavenumber side of the peak, respectively. The sign function returns a +1 if the argument is positive and a -1 if the argument is negative. An example of peak fitting for SiGe films is shown in Figure B-2. The spectrum in Figure B-2 is from a 45nm $Si_{0.73}Ge_{0.27}$ film grown on SOI with a ~25nm Si capping layer. The alloy is strained to the Si lattice constant. The

Si-Si and Si-Ge peaks are present in the spectrum. The Ge-Ge peak is not visible because the Ge concentration is rather low (peak intensity is proportional to number of Ge-Ge bonds).

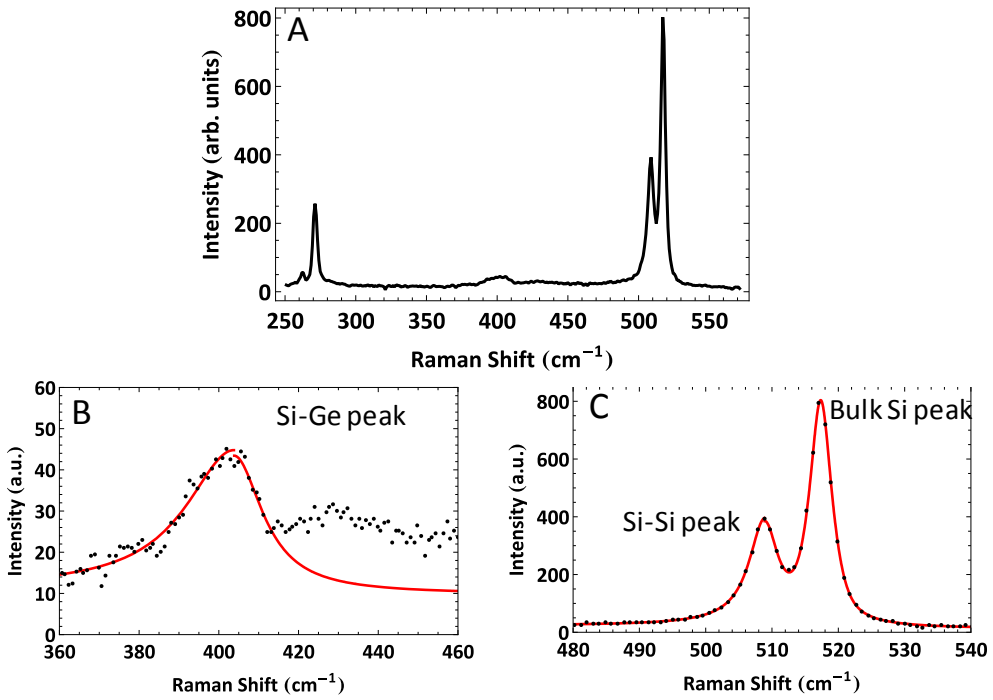

Figure B-2. Example Raman spectrum of SiGe: 27nm Si/45nm $Si_{0.73}Ge_{0.27}$/22nm SOI. The bulk Si peak is fit with the symmetric form of B-1 and the Si-Si and Si-Ge peaks are fit with the asymmetric form of B-2. (A) shows the entire spectrum, and (B) and (C) show the peak fitting (solid line) near the Si-Ge peak, and Si-Si and bulk Si peaks, respectively. Data acquisition information: 442nm laser, 100x obj., D1 filter, 2400 grating, 55µm confocal hole, 10sec acquisition time, averaged over 2 cycles.

Figure B-3 shows an example of the difference between fitting a Si-Ge peak with the symmetrical form of Eq. B-1 and the asymmetrical form of Eq. B-2. It is clear that the asymmetric form extracts the peak position with less uncertainty. The weak peak near the Si-Ge peak (higher wavenumbers) is not used during peak fitting. It is speculated that this peak is

from Si-Si bond motion near Ge atoms [2]. The peak is often very weak and broad, and is thus not used to accurately determine strain or composition in SiGe alloys.

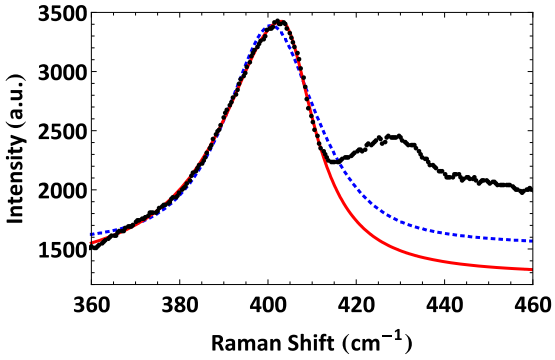

Figure B-3. Raman spectrum near the Si-Ge of a ~50nm $Si_{0.68}Ge_{0.32}$ elastically relaxed NM. The Si-Ge peak is fit with the asymmetric form of Eq. B-2 (solid, red) and the symmetric form of Eq. B-1 (dashed, blue). Data acquisition information: 442nm laser, 100x obj., D1 filter, 2400 grating, 55µm confocal hole, 30sec acquisition time, averaged over 2 cycles, with 2 subpixels.

B.2 Sample heating

The incident laser light in micro-Raman spectroscopy is focused through an optical microscope objective. This reduces the incident laser spot size and thus reduces the measurement area on the sample. The reduction in spot size means that the intensity of the laser is focused into a small area and increases the likelihood heating up the sample in the measurement area. If the heating is significant, the lattice will expand due to thermal expansion and cause the Raman peak to shift accordingly; expansion of the lattice constant causes the Raman modes to shift to lower wavenumbers. To reduce heating effects during measurement, neutral density filters can be placed in the optical path to reduce the intensity of the laser and thus the effective laser power that reaches the sample. Figure B-4A shows an example of laser

heating changing the Raman frequency shift of a freestanding, tethered 22nm Si NM. The Si NM is freestanding in the center where measurement is taken, and tethered on all edges like a window by the bulk Si substrate. The Raman peak position moves to lower wavenumbers with no filter indicating that there is sample heating during the measurement. The appropriate filter is selected when the Raman peak no longer shifts to higher wavenumbers with decreasing laser power. Figure B-4B shows the laser power measured at the sample for three lasers on the UW MSC Raman microscope.

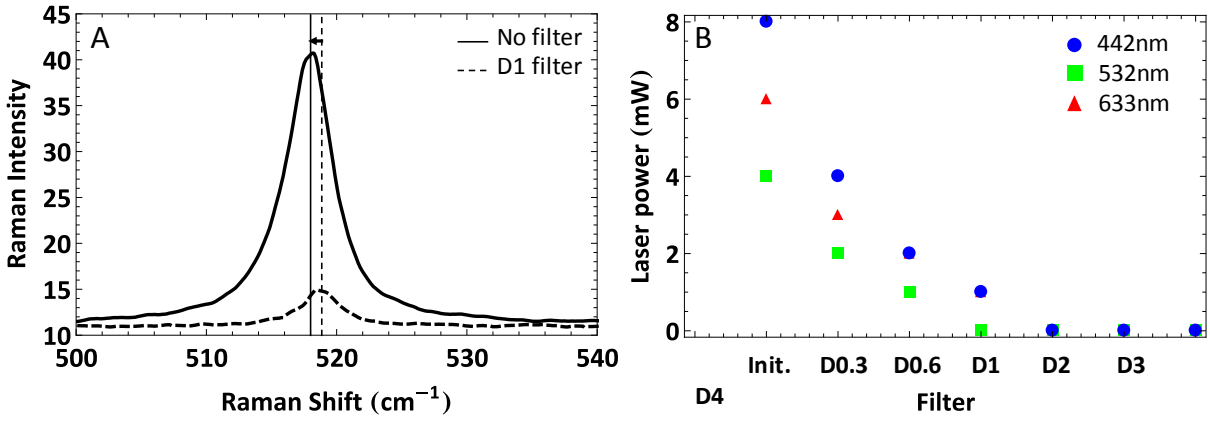

Figure B-4. (A) Raman spectrum of a 22nm freestanding Si NM (sample provided by Anna Clausen). The peak is shifted to lower wavenumbers when no filter (solid) is present indicating that the laser is heating the sample. The intensity of the Raman spectrum taken with the D1 filter in place (dashed) is lower because the incident intensity is much lower. (B) Laser power versus filter setting measured at the sample for the 442nm (circles), 532nm (squares), and 633nm (triangles) lasers on the UW MSC Raman microscope. Init. indicates no filter. Jose Sánchez-Pérez measured the laser power as a function of the filter setting. The power meter used has a 1mW resolution. Data acquisition information: 442nm laser, 50x obj., 2400 grating, 40µm confocal hole, 30sec acquisition time, averaged over 5 cycles, with 6 subpixels.

B.3 Instrument stability

The most important quantity in determining strain from Raman measurements is the relative peak shift from the unstrained material to the strained material. The peak shift can be small (< 1cm^{-1}) for small strains in Si (< 0.14%), so it is important to determine peak shifts within ±0.5cm^{-1} or less. While the peak positions can be determined to within ±0.05cm^{-1} with peak fitting, the stability of the instrument significantly increases this uncertainty. To determine the stability of the instrument over time, I measured the frequency of the bulk Si Raman mode and the elastically scattered plasma peak (from the 442nm laser) over a 24 hour time period. I used the D1 filter to ensure there was no sample heating and measured the same spot on the sample every time. The bulk Si peak position as a function of time is plotted in Figure B-5A; the raw data is plotted in black and the adjusted Si Raman frequency is plotted in red. The adjusted bulk Si Raman frequency takes into account shifts in the plasma peak position (peak fitting shown in Figure B-1B). The plasma peak serves as a reference point in all Raman spectra such that most instabilities in the instrument can be accounted for. Ideally, the plasma peak position should not change relative to the bulk Si peak position. After this adjustment, the uncertainity in the bulk Si peak position is ±0.1cm^{-1}. The normalized intensity of the peaks and the ambient temperature near the sample are plotted in Figures B-5B and C, respectively. Temperature changes can cause thermal expansion (or retraction) of the sample resulting in real shifts in the Raman frequency. Other changes in the environment (including temperature, humidity, vibrations, etc) can cause apparent changes in the Raman frequency because of slight variations in the optical path of the incident or scattered Raman light. The stability of the instrument over

many hours is important when acquiring maps, some of which can take up to 48 hours to acquire.

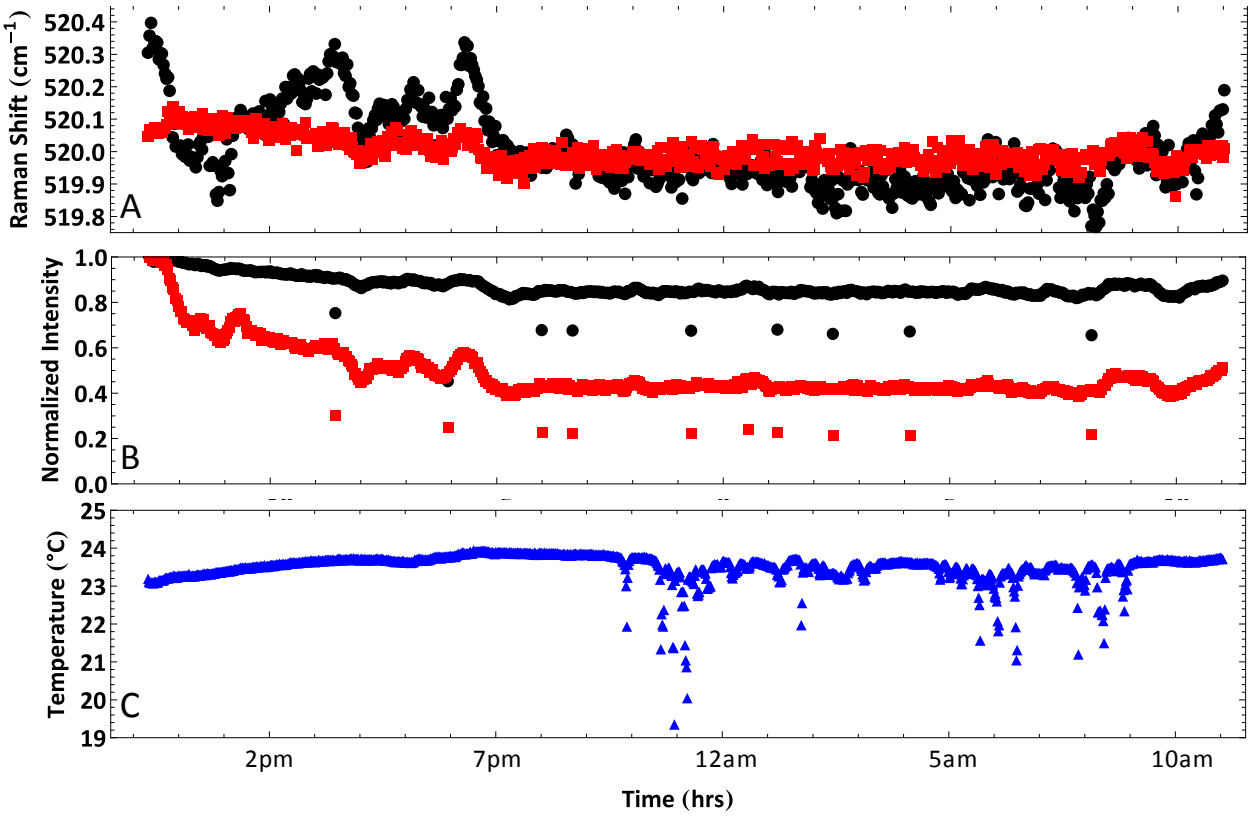

Figure B-5. (A) Bulk Si Raman frequency as a function of time: raw data (black circles) and frequency shift using the plasma peak as reference (red squares). (B) Normalized peak intensity of Si peak (black circles) and plasma peak (red squares). (C) Ambient temperature near the sample. Data acquisition information: 442nm laser, 100x obj., D0.6 filter, 2400 grating, 55µm confocal hole, 30sec acquisition time, averaged over 2 cycles, with 2 subpixels.

From Figure B-5, there appears to be a correlation between the intensity of the Raman signal and the Raman frequency. The signal intensity and the relative change in frequency between the bulk Si peak and the plasma peak are very sensitive to the optical path of the incident laser and the scattered Raman signal. **It is therefore paramount to focus the laser on**

the sample in the same way every time. If the laser is not focused on the sample properly, the scattered Raman signal may be shifted in frequency relative to the elastically scattered plasma peak. To show this effect, I acquired Raman data from bulk Si as a function of distance between the surface of the sample and the objective lens (z-height). Figure B-6A shows the peak intensity of the bulk Si peak (black circles) and the plasma peak (red squares). The z = 0 position is the optical focus of the surface of the sample (with a white light source). A negative z means the stage is moving away from the sample. Raman spectra for four different focus positions are shown in Figure B-6D: (1) the optical focus of the surface of the sample (red), (2) where the plasma peak intensity is greatest (red dotted), (3) at the relative maxima of Si signal for z-heights smaller than the optical focus (blue), (4) the maximum intensity of the Si signal (best focus). Figures B-6E and F show the same spectra as Figure B-6D near the plasma peak and the Si peak, respectively. The difference in peak position between the bulk Si peak and the plasma peak is Δ and is plotted as a function of z-height in Figure B-6B. From these measurements is it easy to see that slight changes in focus appear to change Δ. If the Raman signal is maximized before every measurement, the plasma peak will be in the correct position and small frequency shifts can be measured accurately. The optimum Raman focus is slightly different from the optical focus of the surface of the sample or the focus of the laser spot because scattering is wavelength dependent. From the data shown in Figure B-6C (Δ as a function of Si peak intensity near the best focus position), $\Delta = 246.03 \pm 0.24 cm^{-1}$. The uncertainty in Δ comes from the uncertainty in the intersection of the fitting of the two lines to the data.

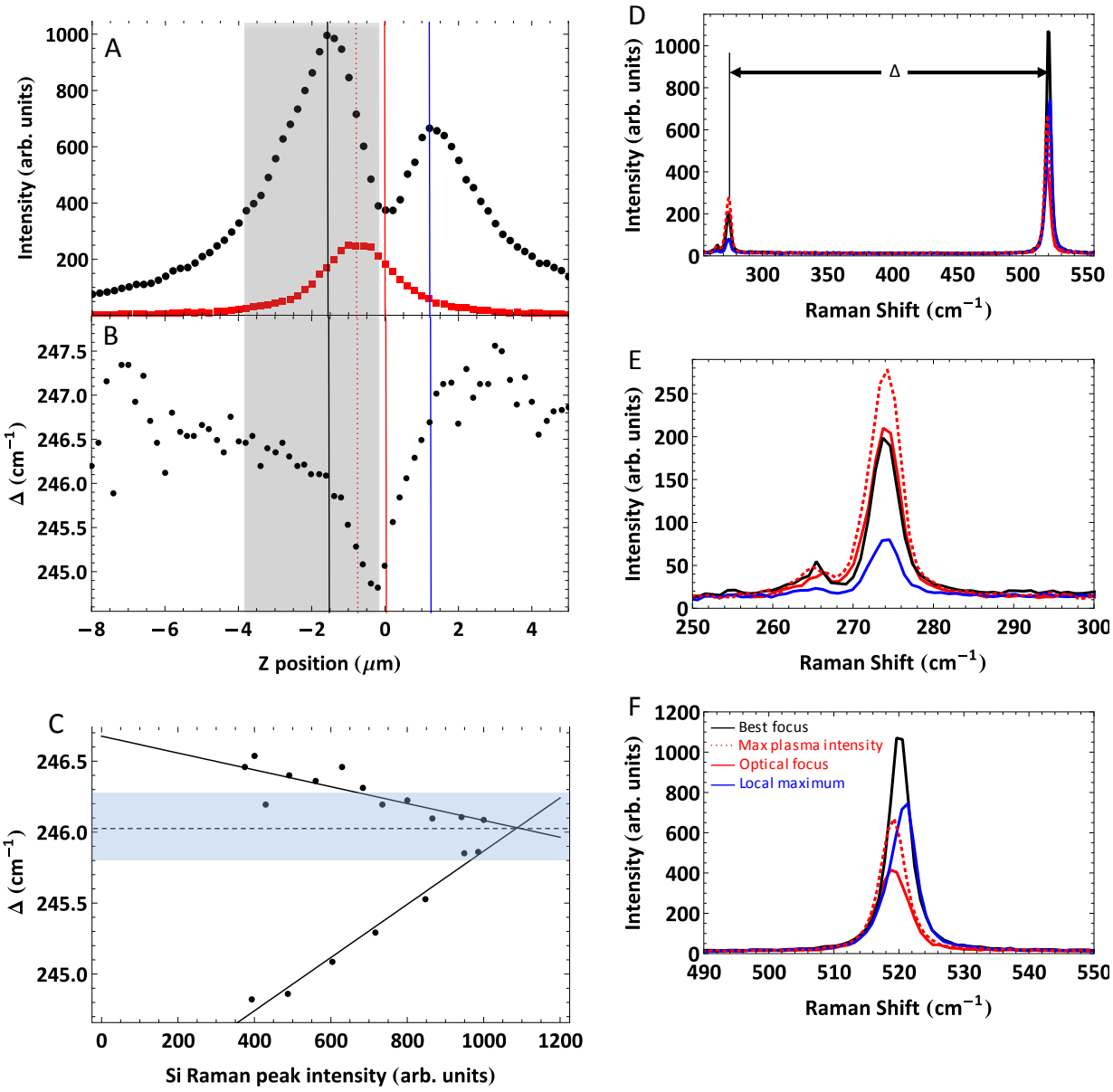

Figure B-6. (Electonic copy in color) (A) Maximum intensity of Si Raman peak (black circles) and plasma peak (red squares) as a function of z-height (negative z indicates an increase in distance between sample surface and objective lens). (B) Δ as a function of z-height. (C) Δ as a function of Si peak intensity for points near the best focus (maximum Si peak intensity, points within the gray shaded region in A and B). The solid lines show the best linear fit through the data on either side of the maximum. The dashed line is the intersection of the two models and represents the true value of Δ: Δ = 246.03 ± 0.24cm^{-1}. The uncertainty in Δ comes from uncertainty in the linear regression. (D) Raman spectra of the best focus (black), the optical focus (red), the maxima of plasma peak intensity

(red dotted), and the local maxima in Si peak intensity for positive z (blue). (E) Same spectra as D near plasma peaks. The spectra were shifted so that the plasma peaks aligned. (F) Same spectra in D near bulk Si peaks. Data acquisition information: 442nm laser, 100x obj., D1 filter, 2400 grating, 55µm confocal hole, 10sec acquisition time, averaged over 2 cycles.

The change in Δ with z-height (focus position) most likely comes from differences in optical path lengths between the Raman signal and the plasma line. If the laser is focused inside the sample rather than on the surface, the Raman scattered signal is originating from a different location than the plasma line that is reflected off the surface of the sample (Figure B-7). When the light goes through the spectrometer grating the difference in path length will appear as a difference in frequency.

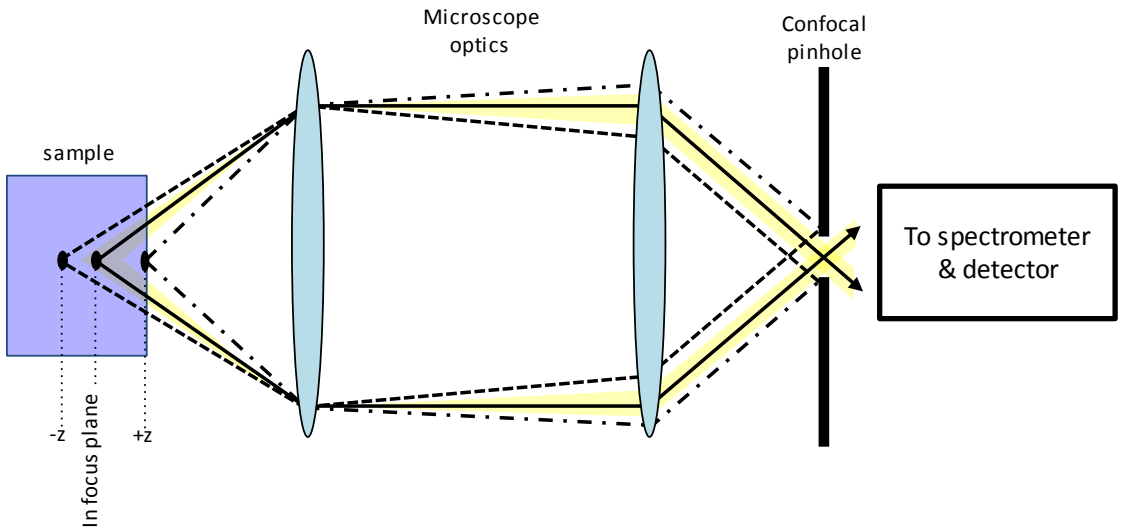

Figure B-7. Ray diagram of the scattered Raman signal from three sample depths through a confocal microscope. The confocal pinhole size can be set to reject the Raman signal coming from different sample depths. There will be Raman signal from a range of depths that make it through the optical system to the spectrometer (shaded area).

Use of a confocal microscope allows one to block most scattered light originating from different optical paths, such that when the laser is focused well inside the sample the plasma peak should be blocked. The range of scattered light that gets to the detector is set by the size of the confocal hole. Even for very small confocal hole sizes, there will be some uncertainty in the frequency of the plasma peak relative to the Raman scattered signal.

If using the plasma peak as a reference, the optimum focus position must be used to avoid false peaks shifts when acquiring maps. Examples of 2D Raman maps are shown in Figures B-8 and B-9. The map of bulk Si in Figure B-8 was lightly off of the best focus for the Raman signal. The variations in the Raman frequency correspond to changes in the peak intensity (Figures B-8A and B, respectively). It may be tempting to try to correct a map based on the linear relationship between delta and the signal intensity (Figure B-6C), however, there are other factors that contribute to variations in signal intensity. The corrected map shown in Figure B-8C does reduce the magnitude of the peak variation (range in Δ goes from ~1.0cm^{-1} to ~0.5cm^{-1} after the correction), but the long-range variations (horizontal lines) do not completely disappear. It is thus *not* recommended to 'correct' a map based on the variation in the Raman signal intensity. It is better to find the optimum focus for the Raman signal when acquiring a map (Figure B-9). There may be some variations from the optimum focus based on changes in the optical elements over time (environmental factors), however, these variations will be slowly varying over time and should be obvious in the map. All the Raman maps presented in this work were taken at the optimum focus; however, there may be slight variations that appear as horizontal lines (scan direction) because of changes in the instrument over time.

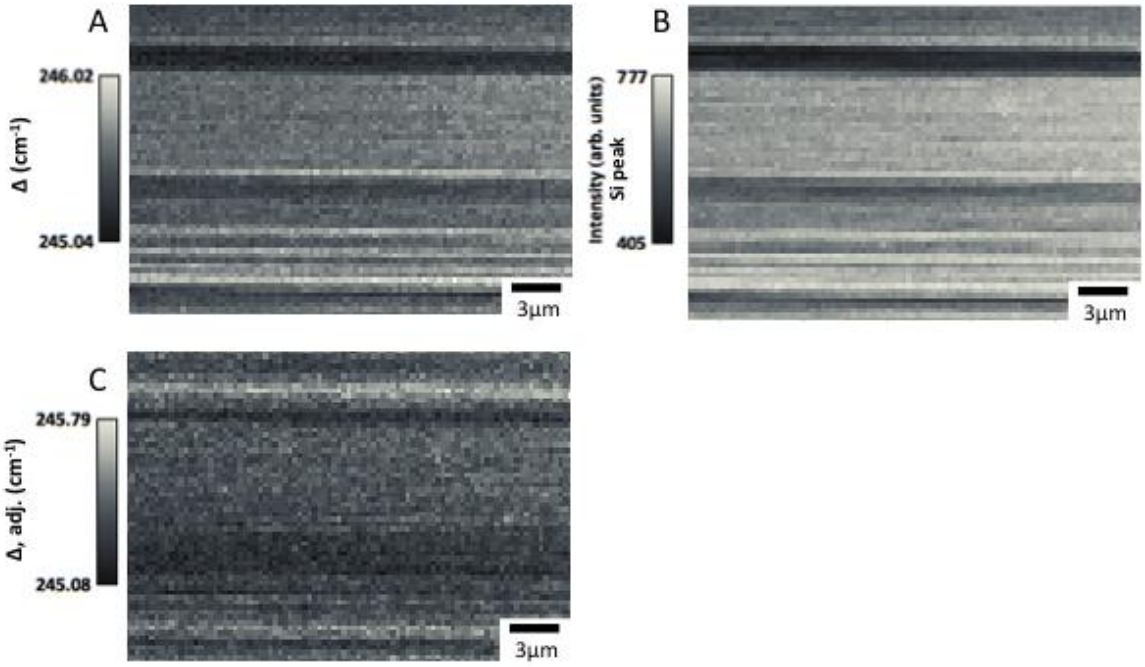

Figure B-8. Raman map of bulk Si. (A) Map of the measured difference in frequency between the bulk Si peak and the plasma peak, Δ. (B) Map of the intensity of the bulk Si peak. (C) Map of Δ based on the linear relationship between Δ and the intensity of the bulk Si Raman signal (Figure B-6C). The linear relationship for Δ values below the optimum focus could be used because the Δ values in A were below the optimum value. Data acquisition information: 442nm laser, 100x obj., D1 filter, 2400 grating, 55μm confocal hole, 10sec acquisition time, averaged over 2 cycles, 0.3μm/step.

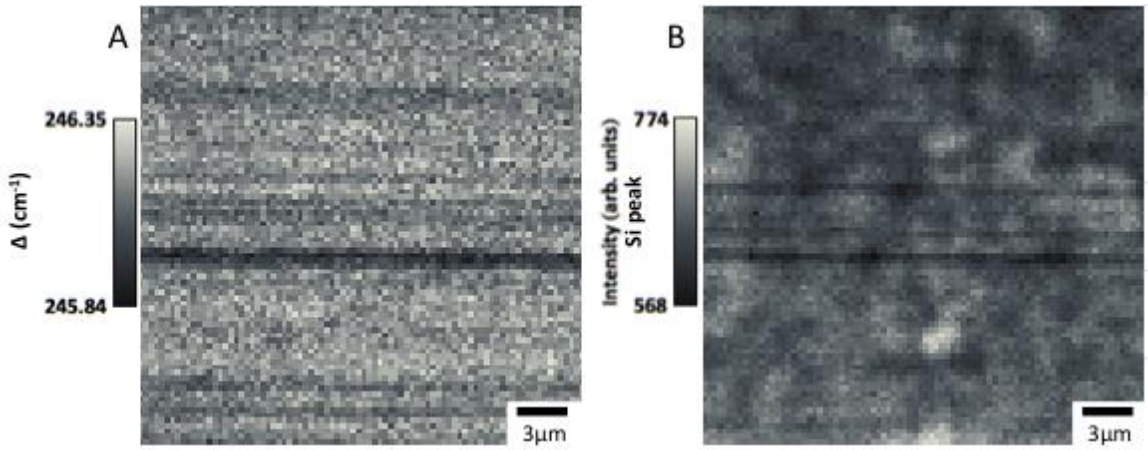

Figure B-9. Raman map of an as-grown Si/SiGe/Si heterostructure. (A) Frequency difference between the unstrained Si peak and the plasma peak, Δ. The maximum variation is within the uncertainty of the expected value of Δ. (B) Raman signal intensity of the unstrained Si peak. The variation in intensity that appears as speckles is most likely from changes in thickness of the epitaxial layers and results in changes in the amount of Si being measured. Data acquisition information: 442nm laser, 100x obj., D1 filter, 2400 grating, 55μm confocal hole, 10sec acquisition time, averaged over 2 cycles, 0.3μm/step.

The optimum Δ value, the frequency difference between the bulk Si peak and the plasma peak, will change with alignment of the instrument (changes in position of mirrors and/or CCD alignment relative to the spectrometer) and thus needs to be determined after each course alignment. Figure B-10 shows the change in Δ over months. Changes in alignment are apparent by large differences in Δ. The uncertainty in Δ on a given day is from (Figure B-10A) small deviations from the optimum focus.

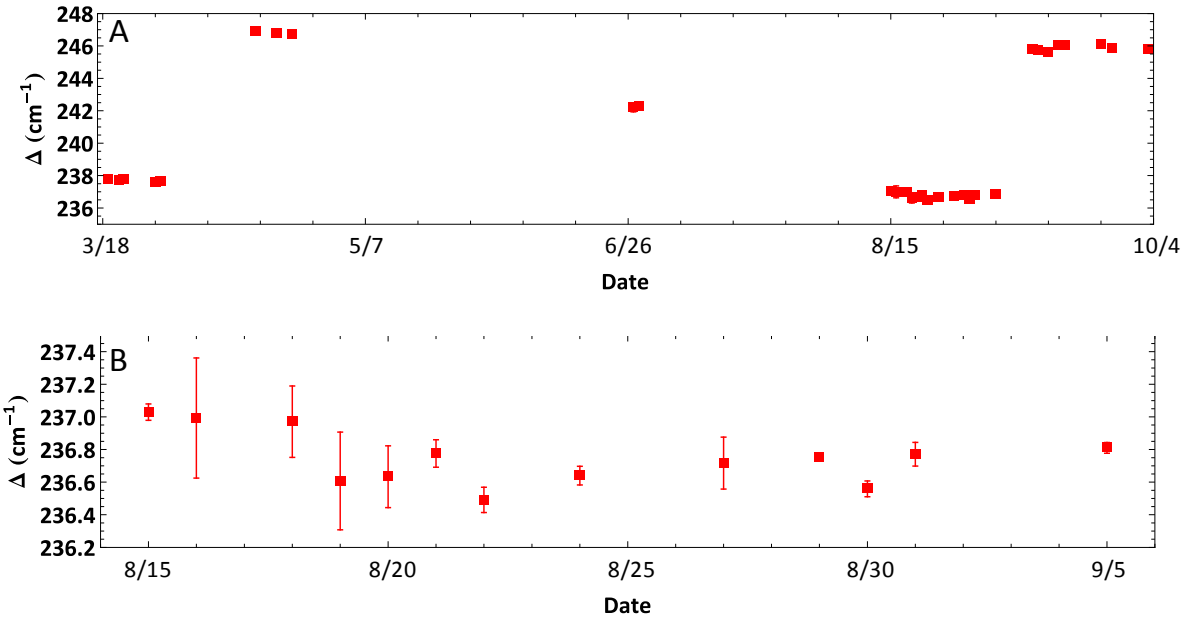

Figure B-10. Average Δ by acquisition date (A) over several months (each alignment condition is at a different average Δ value) and (B) over the course of one alignment condition. The error bars are from several bulk Si measurements averaged together and most likely from slight deviations from the optimum focus. The user sets the focus.

Changes in alignment of the instrument, and therefore Δ, will cause the shift in measured Raman frequency from strain to change. For example, consider a Si sample with 1.0% biaxially tensile strain. From the accepted strain shift coefficient [3], $b_{\varepsilon Si}$ = -723cm^{-1}, the Raman frequency shift should be ~-7.2cm^{-1}. Let's say this corresponds to the average Δ = 242cm^{-1} from Figure B-10. If, from changes in alignment over time, Δ changes to 246cm^{-1} (a change of less than 2%) the strain shift coefficient will change similarly. The Raman frequency shift for the 1.0% biaxially will now be -7.3cm^{-1}. Uncertainty in the strain shift coefficient reported in the literature is most likely from variation in alignment from instrument to instrument. The range of Δ values reported here will result in an uncertainty in the strain shift coefficient of ± ~2%,

resulting in an uncertainty in the strain shift coefficient similar to what is reported in the literature (-723 ± 15cm^{-1} [3]). The uncertainty in strain as measured with the Raman frequency shift is shown in Figure B-11. Above I discussed how the Raman frequency shift due to strain needs to be measured within ±0.5cm^{-1} to see relative changes in the material when acquiring Raman maps. This can be done under one alignment condition. In general, strain measurements taken under different alignment conditions can still be compared to one another based on the uncertainty in the strain shift coefficient.

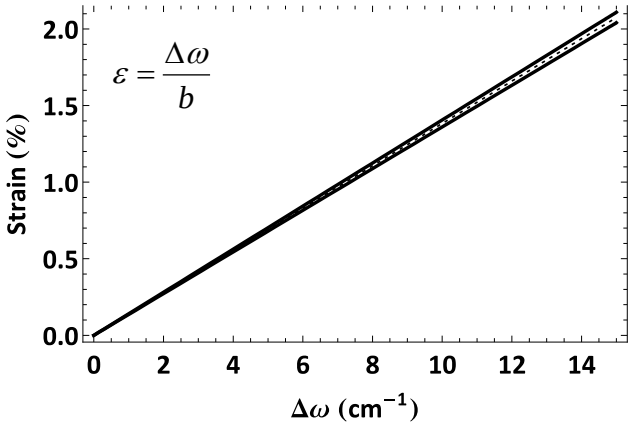

Figure B-11. Biaxially strain in Si vs. Raman frequency shift in wavenumbers. The two solid lines represent the change in the strain shift coefficient, b, for the range of Δ values shown in Figure B-9A. Here, the magnitude of Δω is plotted against the strain magnitude. A positive Δω represents a compressive strain and a negative Δω represents a tensile strain (b is negative).

B.4 Raman analysis of SiGe alloys

There have been many studies dedicated to determining the shift in Raman frequency as a function of composition and strain in SiGe alloys [1, 2, 4-7]. The relationship between Raman frequency and composition is inconsistent in these studies, perhaps based on

considerations of instrument stability or inconsistencies in peak fitting as discussed above. Figure B-12 shows four different models for the Raman frequency of the Si-Si and Si-Ge modes versus Ge composition for low-Ge-composition, relaxed $Si_{1-x}Ge_x$ alloys. Assuming that the strain of the alloy is known from some other independent measurement, the uncertainty in the composition based on the Si-Si mode is ±1.5% and based on the Si-Ge mode is ±7%. The uncertainty in the Si-Ge mode will be naturally larger in alloys for this composition range because the signal-to-noise for the Si-Ge peak is worse than that of the Si-Si peak. In order to use Raman spectroscopy to determine both the strain and composition, the relationship between composition and frequency shift of the Si-Si peak and Si-Ge peak must be known.

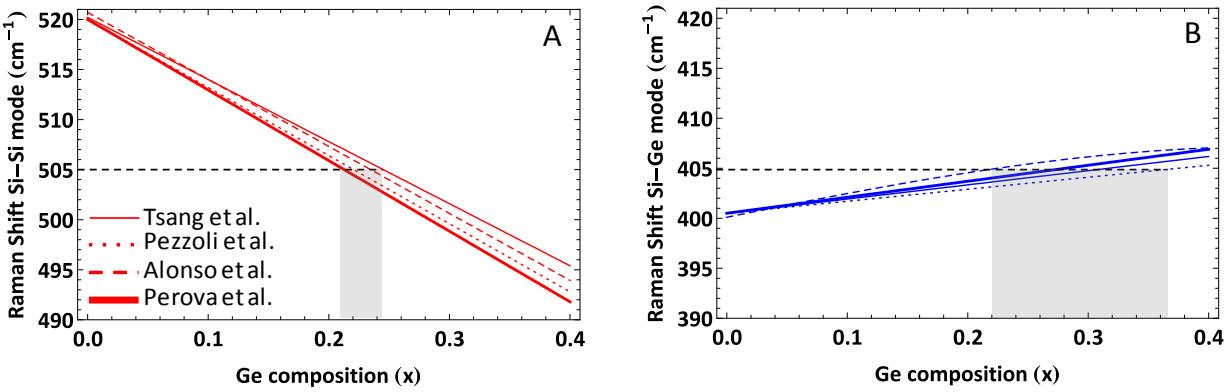

Figure B-12. Four different models for the Raman frequency of (A) the Si-Si mode and (B) the Si-Ge mode as functions of Ge composition in SiGe alloys. The shaded region represents the uncertainty in composition taking into account all the models.

The strain shift coefficient for each of the Raman modes for SiGe alloys (Si-Si, Si-Ge and Ge-Ge) has been experimentally determined much like that for strained Si. Again, I am only considering the strain shift coefficient for biaxially strained films. Figure B-13 shows the range in the strain coefficient for each of the SiGe Raman modes based on a linear combination of

elastic constants (dotted lines) and experimental values from several sources. I used the strain shift coefficients in [6] (solid horizontal lines with uncertainty represented by shaded areas), since these seem to encompass most of the values reported in the literature.

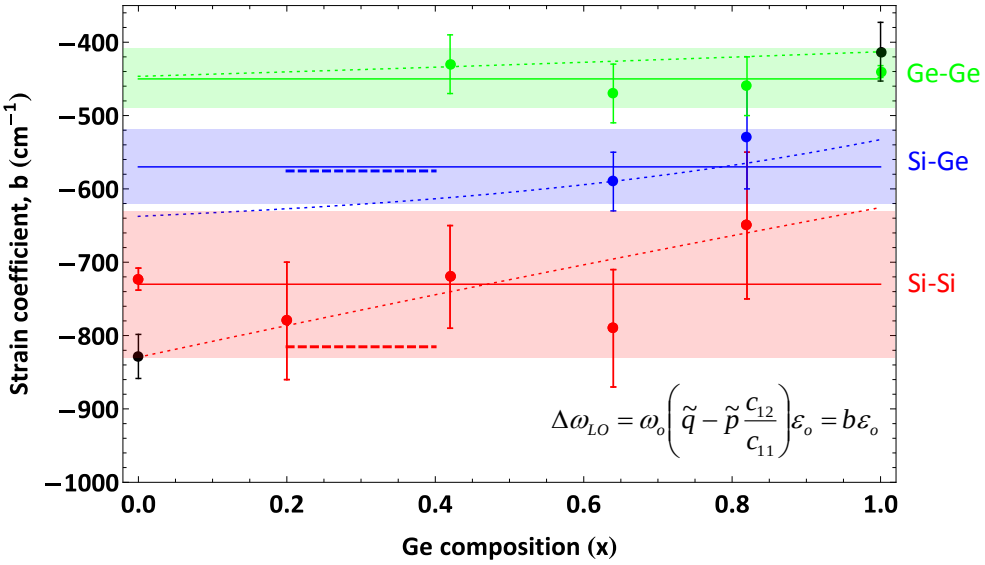

Figure B-13. The biaxial strain shift coefficient for Si-Si (red), Si-Ge (blue) and Ge-Ge (green) Raman modes in SiGe alloys. The dotted lines are calculated based on a linear combination of elastic constants (see equation in inset). The black dots are calculated based on experimental determination of p and q (phonon deformation potentials) [8, 9]. Other experimental values are represented by dots [3, 6] and dashed lines [4]. The average of several experimentally determined values of b are represented by a solid line and the uncertainty by the shaded region for each mode.

Figures B-14A and B show the Raman frequency shift of the Si-Si and Si-Ge modes as a function of Ge composition (relaxed models at lower wavenumbers) and strain (SiGe strained to Si lattice constant at higher wavenumbers). The Raman data from SiGe films grown on Si substrates and elastically relaxed SiGe NMs taken in this work is also shown. The Raman frequency as a function of composition should have the linear relationship:

$$\omega(x) = \omega_o + cx \qquad \text{(B-3)},$$

where ω_o is the Raman frequency at x = 0 and c is the slope of the line of the Raman frequency versus composition. The Raman frequency as a function of composition and biaxial strain is:

$$\omega(x) = \omega_o + cx + b\varepsilon_{||} \qquad \text{(B-4)},$$

where b is the strain shift coefficient defined in Figure B-13 and $\varepsilon_{||}$ is the biaxial strain. For SiGe alloys strained to the Si lattice constant, $\varepsilon_{||}$ can be approximated as the composition of the alloy times the mismatch strain between Si and Ge (-0.0417x). Equation B-4 then becomes:

$$\omega(x) = \omega_o + (c - 0.0417b)x \qquad \text{(B-5)}.$$

Linear models through the data are shown in Figures B-13C and D and the results are in Table B-1. The Raman frequency at x = 0, ω_o, is set to 520cm^{-1} for the Si-Si mode and 400cm^{-1} for the Si-Ge mode. The Raman frequency as a function of relaxed and strained SiGe alloys from this work most closely matches the relaxed SiGe models from [4] using the strain coefficients reported in [6].

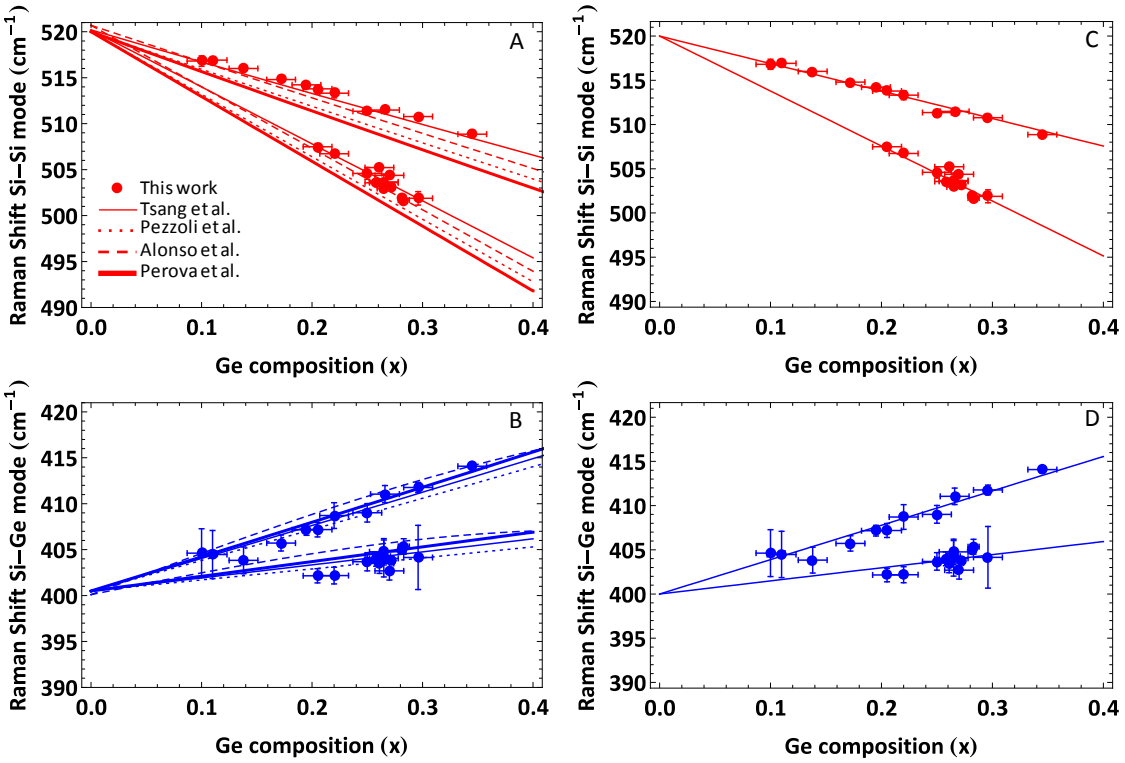

Figure B-14. Raman frequency of (A) Si-Si mode and (B) Si-Ge mode as a function of relaxed alloy composition (lower wavenumbers) and SiGe strained to the Si lattice constant (higher wavenumbers). The data collected in this work is shown as dots. The Ge composition is measured with XRD. The same experimental data plotted in A and B is shown in C and D with the best linear fit to the strained and relaxed alloys.

Table B-1. Coefficients of linear models for Raman frequency of relaxed and strained SiGe alloys (Eqs. B-3 and B-5, respectively). The value of c is taken from the reference shown and the value of b is from [6] for all cases.

	Si-Si		Si-Ge	
	c	**(c - 0.0417b)**	**c**	**(c – 0.0417b)**
Tsang et al.	-62.0	-31.6	14.2	38.0
Pezzoli et al.	-66.9	-36.5	(24.5 -4.5x-33.5x^2)	-(5.9 +4.5x+33.5x^2)
Alonso et al.	-68.0	-37.6	12.0	35.8
Perova et al.	-70.5	-40.1	16.0	39.8
This work	-62.1 ± 0.6	-31.1 ± 0.4	14.8 ± 0.9	38.9 ± 1.2

B.5 References

1. T. S. Perova, J. Wasyluk, K. Lyutovich, E. Kasper, M. Oehme, *et al.,* Composition and Strain in Thin $Si_{1-x}Ge_x$ Virtual Substrates Measured by Micro-Raman Spectroscopy and X-Ray Diffraction. *J. Appl. Phys.* **109** (2011) 033502.

2. M. I. Alonso, K. Winer, Raman Spectra of c-$Si_{1-x}Ge_x$ Alloys. *Phys. Rev. B* **39** (1989) 10056-10062.

3. S. Nakashima, T. Mitani, M. Ninomiya, K. Matsumoto, Raman Investigation of Strain in Si/SiGe Heterostructures: Precise Determination of the Strain-Shift Coefficient of Si Bands. *J. Appl. Phys.* **99** (2006) 053512.

4. J. C. Tsang, P. M. Mooney, F. Dacol, J. O. Chu, Measurements of Alloy Composition and Strain in Thin Ge_xSi_{1-x} Layers*. J. Appl. Phys.* **75** (1994) 8098-8108.

5. F. Pezzoli, L. Martinelli, E. Grilli, M. Guzzi, S. Sanguinetti, *et al.* Raman Spectroscopy of $Si_{1-x}Ge_x$ Epilayers. *Mater. Sci. Eng. B* **124-125** (2005) 127-131.

6. F. Pezzoli, E. Bonera, E. Grilli, M. Guzzi, S. Sanguinetti, *et al.,* Phonon Strain Shift Coefficients in $Si_{1-x}Ge_x$ Alloys, *J. Appl. Phys*. **103** (2008) 093521.

7. M. Z. Hossain, H. T. Johnson, Effects of Composition, Strain, and Atomic Disorder on Optical Phonon Frequencies in $Si_{1-x}Ge_x$. *J. Appl. Phys*. **107** (2010) 073515.

8. E. Anastassakis, A. Cantarero, M. Cardona, Piezo-Raman Measurements and Anharmonic Parameters in Silicon and Diamond. *Phys. Rev. B* **41** (1990) 7529-7535.

9. F. Cerdeira, C. J. Buchenauer, F. H. Pollak, M. Cardona, Stress-Induced Shifts of First Order Raman Frequencies of Diamond-and Zinc-Blende-Type Semiconductors. *Phys. Rev. B* **5** (1972) 580-593.

10. I. De Wolf, Micro-Raman Spectroscopy to Study Local Mechanical Stress in Silicon Integrated Circuits. *Semicond. Sci. Technol.* **11** (1996) 139-154.

11. N. C. Craig, I. W. Levin, Calibrating Raman Spectrometers with Plasma Lines from the Argon Ion Laser. *Appl. Spectro.* **33** (1979) 475-476.

Appendix C X-ray microdiffraction data analysis

As discussed in Chapters 1 and 4, x-ray microdiffraction was used to map changes in crystalline tilt in the strained Si layer of a relaxed SiGe/strained Si heterostructure grown on SiGe NMs. A highly brilliant x-ray beam (synchrotron generated) is focused onto the sample using a Fresnel zone plate (~50nm). The focused x-ray beam has a range of incident angles (angular divergence ~0.24°), and thus results in simultaneously measuring through a small range of diffracting conditions. An example of the data collected is shown in Figure C-1B. Intensity in the x-direction represents diffraction along the out-of-plane direction [001] (schematic diagram shown in Figure C-3B), and intensity along the y-direction is from diffraction perpendicular to the scattering plane (in and out of the paper as drawn in Figure C-3B). The donut shaped pattern represents the allowed incident angles as focused by the zone plate. The vertical lines within the donut shaped pattern are intensity fluctuations from the heterostructure (thickness fringes). The CCD image in Figure C-1B is from one point on the sample and one diffracting condition. The horizontal profile in Figure C-1C represents the diffraction along the [001] direction. A collection of horizontal profiles from data taken at different θ/2θ conditions can be stitched together to form the θ/2θ line scan near the (004) reflection shown in Figure C-1A.

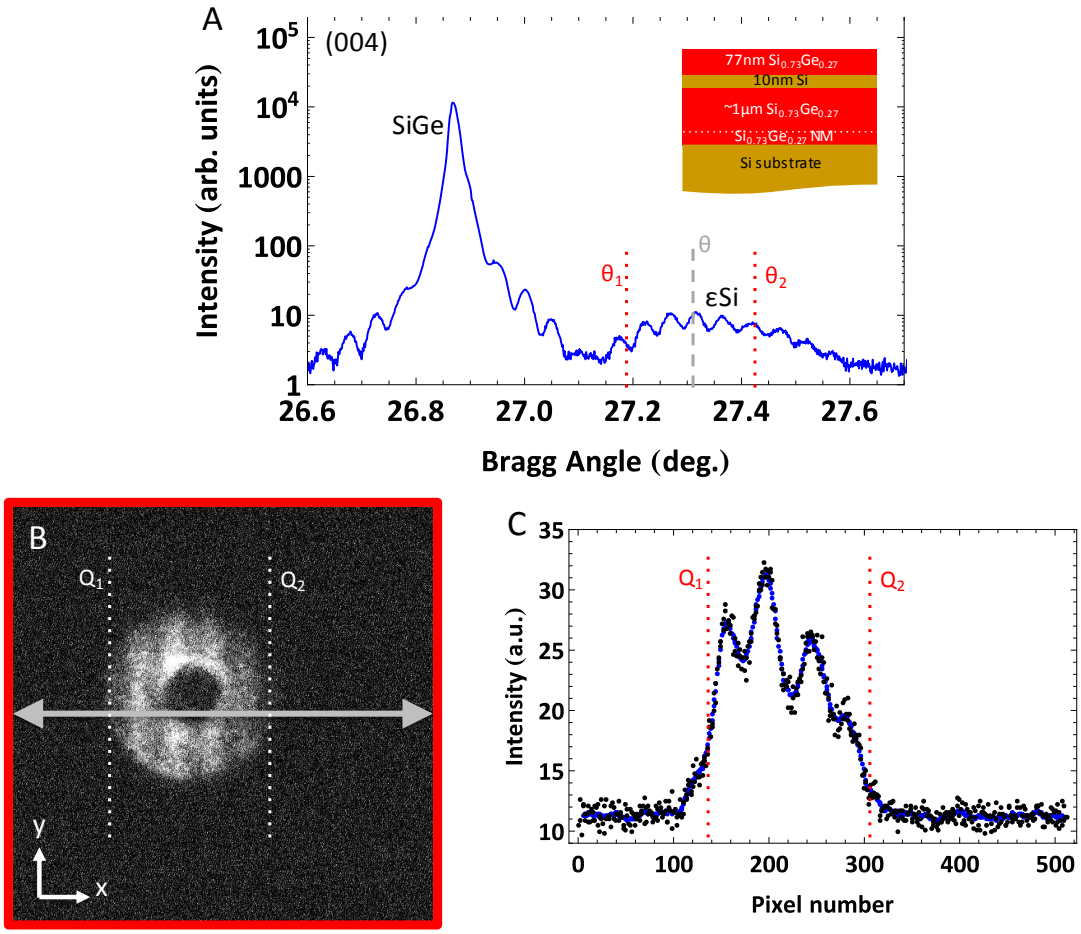

Figure C-1. (A) θ/2θ line scan at one point (~1µm area) on a 77nm SiGe/10nm εSi/~1µm SiGe heterostructure grown on an elastically relaxed SiGe NM (schematic shown in inset). (B) Example of diffracted data for a given diffraction condition. Only a cropped 512x512 pixel area is shown, but the CCD is 1024x1024 pixels. (C) The horizontal intensity profile of the data in B (blue arrow in B). The intensity profile is extracted by summing the values in the vertical direction. The blue line represents the profile after 11-point smoothing. The points Q_1 and Q_2 represent the range of reciprocal lattice vectors in a given measurement. θ_1 and θ_2 in A represent the Bragg angles that correspond to Q_1 and Q_2, respectively, in B and C.

To construct the θ/2θ line scan shown in Figure C-1A, a conversion from pixel number on the 2D CCD to Bragg angle (or reciprocal lattice vector, Q) must be found. The step size between the Bragg conditions (θ) of each of the points for the scan in Figure C-1A is less than

the angular divergence of the diffracted x-rays. This means that there are several CCD images that contain the same Q vector. Figure C-2 shows the horizontal profiles that contain the sharp SiGe peak. I fit these peaks with a Gaussian line form to extract the exact peak position in pixel number. From knowledge of the change in Bragg angle, θ, and the Q vector of the SiGe (from lab source XRD measurements), I obtained a conversion factor from pixel number to Bragg angle. The relative change in diffraction angle (in degrees) from the relative change in pixel number is: 0.00110°/pixel = ~4 arcseconds/pixel.

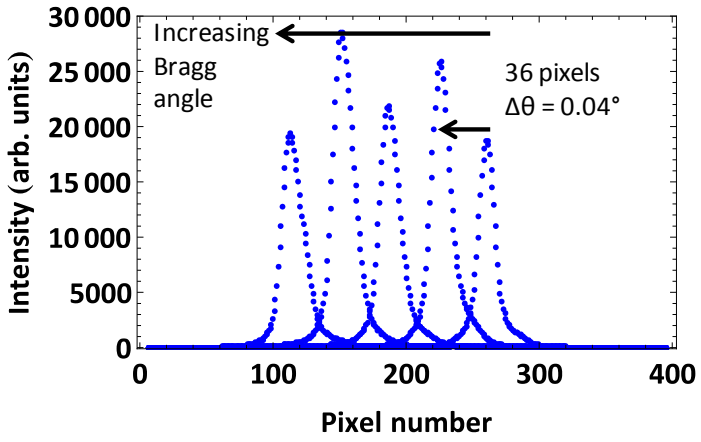

Figure C-2. Profiles in the x-direction on the CCD for five different Bragg conditions near the SiGe diffraction peak. The shift in pixel number of the SiGe diffraction peak with changes in Bragg condition give the conversion from pixel number to the magnitude of the reciprocal lattice vector, Q: 0.04°/36 pixels = 0.000110°/pixel.

From the above analysis, changes in the diffracted intensity on the CCD can be converted to changes in tilt angle. One diffracting condition is used to measure tilt variation over a 2D area on the sample by translating the sample over the area to be measured. Relative changes in tilt perpendicular to the scattering plane will cause the diffracted intensity to shift in

the y-direction on the CCD, and tilt in the scattering plane will cause the diffracted intensity to shift in the x-direction on the CCD (Figure C-3D). Tilt in the scattering plane (x_{tilt}) will result in a change in the Bragg angle equal to the x_{tilt} (Figure C-3C).

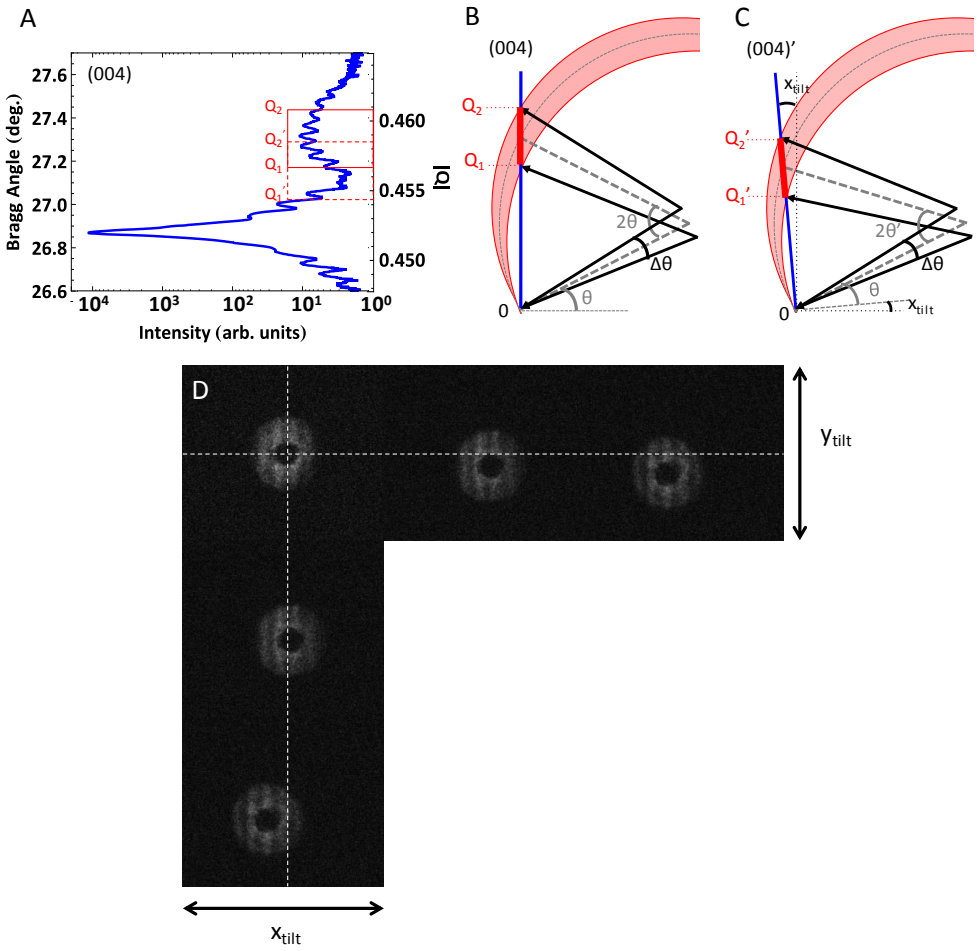

Figure C-3. (A) θ/2θ line scan around the (004) reflection (same data as shown in Figure C-1A). (B) Diffraction geometry with Ewald sphere construction for a range of incident x-ray angles (centered at θ with a range Δθ). Diffraction near the (004) reflection is shown as a solid blue line. The area highlighted in red (between Q_1 and Q_2) is what is measured. (C) When the crystal is tilted in the scattering plane by x_{tilt}, the Bragg angle changes by the same amount (θ + x_{tilt}) and the measured diffraction is between Q_1' and Q_2'. The schematics are not drawn to scale. (D) The diffracted intensity near the εSi peak at three different points on the sample. The x_{tilt} and y_{tilt} is extracted by measuring changes in the position of the intensity on the detector.

I extract the relative changes in tilt by using the center of mass measurement in ImageJ. To obtain the correct value for the shift in intensity on the CCD in this way, a few things must be considered. The first is that the background of each CCD image is subtracted properly. The raw data includes a non-uniform background. I used the Image Calculator in ImageJ to subtract (pixel-by-pixel) a 'dark' CCD image (Figure C-4A) from each of the diffraction images collected (Figure C-4C). A threshold value was also used to subtract any constant background noise remaining (Figure C-4D).

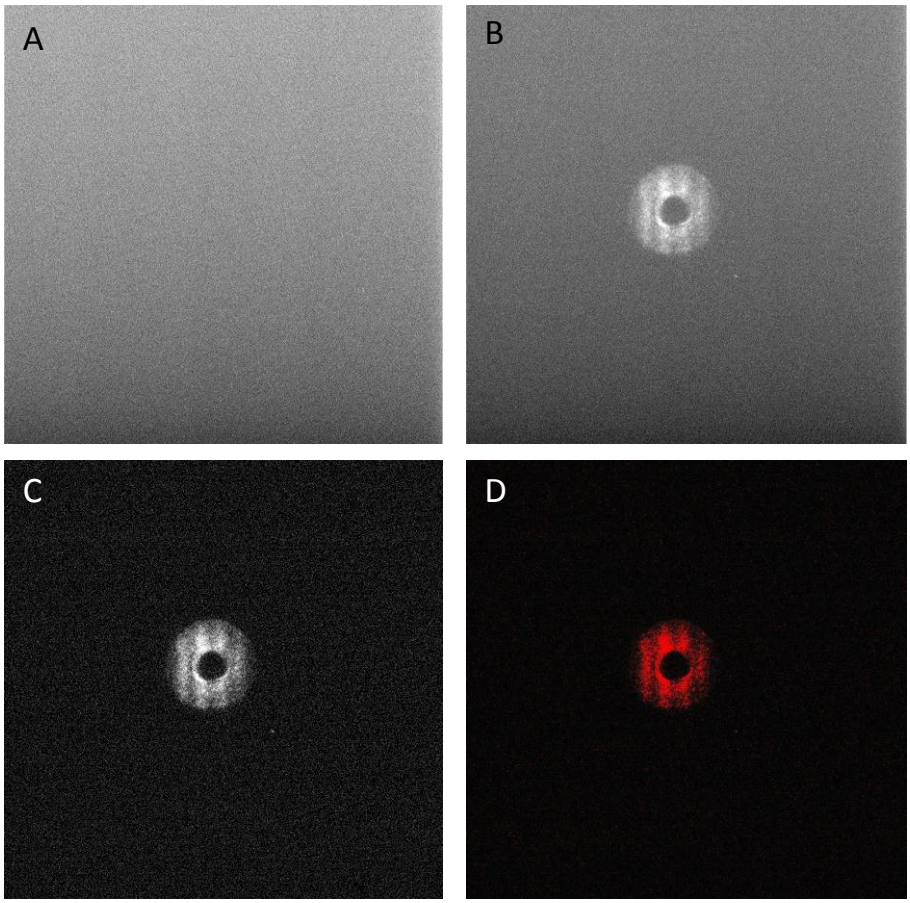

Figure C-4. (A) 20sec background image. (B) Example of raw diffraction data near the εSi (004) reflection. (C) Data minus the background image (B – A). (D) Threshold image to remove of constant background noise.

The center of mass measurement will be very sensitive to large intensity fluctuations from apparent changes in the heterostructure. If for instance the diffraction condition was set near the intense SiGe peak or in the region between the SiGe peak and the strained Si peak, small changes in the x_{tilt} will result in deviations from the Bragg angle. Small deviations from the Bragg angle where the intensity is varying because of heterostructure configuration will result in large shifts in the center of mass calculation because of the intensity variation, not because of the location of the diffracted intensity on the CCD. For this reason, I used a diffraction condition near the top of the strained Si peak, where small shifts in the x_{tilt} will not cause large intensity fluctuations from changes in the Bragg angle. Figures C-5A and B show the x_{tilt} and y_{tilt}, respectively, (relative to the average center position) for a 1µm x 1µm area on the strained Si/relaxed SiGe heterostructure shown in the inset of Figure C-1A. The magnitude and direction of the tilt are shown in Figures C-5C and D, respectively. These figures are similar to those shown in Chapter 4 for the large 10µm x 10µm area.

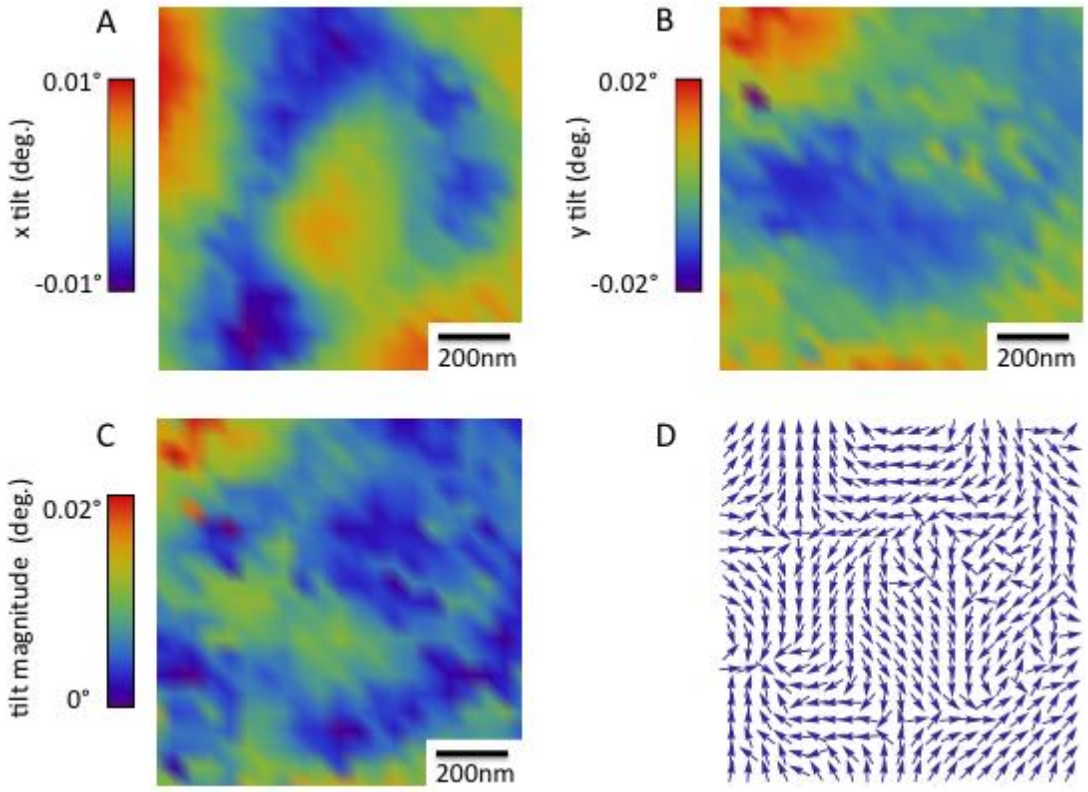

Figure C-5. 1µm x 1µm (21 x 21 points) map of (A) x_{tilt}, (B) y_{tilt}, (C) tilt magnitude, and (D) tilt direction.